



1. Report No. FHWA/TX-91+1123-5		2. Government Accession No.		3.	
4. Title and Subtitle EXPERIMENTAL STUDY OF FACTORS AFFECTING THE SPECTRAL-ANALYSIS-OF-SURFACE-WAVES METHOD				5. Report Date February 1991	
				6. Performing Organization Code	
7. Author(s) Glenn J. Rix, Kenneth H. Stokoe, II, and Jose M. Roesset				8. Performing Organization Report No. Research Report 1123-5	
9. Performing Organization Name and Address Center for Transportation Research The University of Texas at Austin Austin, Texas 78712-1075				10. Work Unit No. (TRAIS)	
				11. Contract or Grant No. Rsch. Study 2/3-18-87/9-1123	
12. Sponsoring Agency Name and Address Texas State Department of Highways and Public Transportation; Transportation Planning Division P. O. Box 5051 Austin, Texas 78763-5051				13. Type of Report and Period Covered Interim	
				14. Sponsoring Agency Code	
15. Supplementary Notes Study conducted in cooperation with the U. S. Department of Transportation, Federal Highway Administration. Research Study Title: "Non-Destructive Test Procedures for Analyzing the Structural Conditions of Pavements"					
16. Abstract <p>Three series of seismic tests were performed to investigate factors which affect the Spectral-Analysis-of-Surface-Waves (SASW) test method. In the first series, the source of seismic waves was studied. Until recently, transient input motion has been used almost exclusively as the source with often unpredictable results. Random and sinusoidal input motions were investigated to evaluate if either could provide more consistent results. The investigation revealed that sinusoidal input attained substantially higher signal-to-noise ratios than either transient or random motions. The improved signal-to-noise ratio may be very helpful in situations where transient motion fails to provide acceptable results.</p> <p>A basic assumption of the SASW method is that only fundamental mode surface waves exist in the field. This assumption was investigated in the second series of tests using measurements of particle motion versus depth to calculate the relative contribution of the first several modes of surface wave propagation. The results were somewhat inconclusive because of the inability to model the subsurface accurately. However, theoretical results indicated that fundamental-mode surface waves comprised between 72 and 86 percent of the total motion. In addition, a qualitative comparison of theoretical mode shapes and experimental displacements also indicated that fundamental-mode motion dominates.</p> <p>Finally, the third series of surface wave tests was performed on a concrete test slab to assess the influence of the relative stiffness of adjacent layers and the relative spacing of source and receivers on measured dispersion. Results of this test series indicated that a large stiffness ratio between adjacent layers can adversely affect measured dispersion curves for wavelengths which are between approximately 0.7 and 1.8 times the thickness of the slab. The influence of the relative source-receiver spacing was more difficult to determine because of the lack of a "true" dispersion curve with which to compare results. Based on selected records, receiver spacings with a ratio of d_2/d_1 greater than two appeared to yield improved dispersion curves.</p>					
17. Key Words non-destructive testing, experimental study, Rayleigh waves, surface waves, seismic testing, pavements, subgrades			18. Distribution Statement No restrictions. This document is available to the public through the National Technical Information Service, Springfield, Virginia 22161.		
19. Security Classif. (of this report) Unclassified		20. Security Classif. (of this page) Unclassified		21. No. of Pages 188	22. Price

EXPERIMENTAL STUDY OF FACTORS AFFECTING THE SPECTRAL-ANALYSIS-OF-SURFACE-WAVES METHOD

by

Glenn J. Rix
Kenneth H. Stokoe, II
Jose M. Roesset

Research Report Number 1123-5

Research Project 2/3-18-87/9-1123

Non-Destructive Test Procedures for Analyzing the Structural Conditions of Pavements

conducted for

**Texas State Department of Highways
and Public Transportation**

in cooperation with the

**U. S. Department of Transportation
Federal Highway Administration**

by the

CENTER FOR TRANSPORTATION RESEARCH

Bureau of Engineering Research

THE UNIVERSITY OF TEXAS AT AUSTIN

February 1991

NOT INTENDED FOR CONSTRUCTION, PERMIT, OR BIDDING PURPOSES

K. H. Stokoe, II, P.E. (Texas No. 49095)

Research Supervisor

The contents of this report reflect the views of the authors, who are responsible for the facts and the accuracy of the data presented herein. The contents do not necessarily reflect the official views or policies of the Federal Highway Administration or the State Department of Highways and Public Transportation. This report does not constitute a standard, specification, or regulation.

PREFACE

Research Project 1123 is a joint project between the Center for Transportation Research, The University of Texas at Austin, and the Texas Transportation Institute, Texas A&M University. The project deals with the development of experimental and analytical techniques for nondestructive testing of pavements. This report is the first of three reports from the Center for Transportation

Research. The report deals with continued development of the Spectral-Analysis-of-Surface-Waves (SASW) Method for in situ testing of pavements, bases, and subgrades. The work builds on earlier work conducted on Project 437 and contributes to on-going work on Project 1175.

LIST OF REPORTS

(Note: Research Reports 1123-1, 1123-2, 1123-3, and 1123-4F have been submitted through the Texas Transportation Institute of Texas A&M University on that agency's part of the joint Project 1123. The reports listed below are the reports submitted through the Center for Transportation Research of The University of Texas at Austin.)

Research Report 1123-5, "Experimental Study of Factors Affecting the Spectral-Analysis-of-Surface-Waves Method," by Glenn J. Rix, Kenneth H. Stokoe, II, and Jose M. Roesset, presents the results of field studies of source types, source-receiver configurations, stiffness ratios between adjacent layers, and the vertical distribution of surface wave motion on SASW measurements. February 1991.

Research Report 1123-6, "Effect of Finite Width on Dynamic Deflections of Pavements," by Yumin Vincent Kang, Jose M. Roesset, and Kenneth H. Stokoe, II, presents the results of analytical studies of the effects of the finite width of the pavement and the relative location of nondestructive testing devices on predicted dynamic deflections. January 1991.

Research Report 1123-7F, "The Falling Weight Deflectometer and Spectral Analysis of Surface Waves for Characterizing Pavement Moduli: A Case Study," by R. F. Miner, K. H. Stokoe, II, and W. R. Hudson, presents the results of a comprehensive field and laboratory study conducted during the construction of an overpass ramp in Austin, Texas. February 1991.

ABSTRACT

Three series of seismic tests were performed to investigate factors which affect the Spectral-Analysis-of-Surface-Waves (SASW) test method. In the first series, the source of seismic waves was studied. Until recently, transient input motion has been used as the source, often with unpredictable results. Random and sinusoidal input motions were investigated to evaluate if either one could provide more consistent results. The investigation revealed that sinusoidal input attained substantially higher signal-to-noise ratios than either transient or random motions. The improved signal-to-noise ratio may be very helpful in situations where transient motion fails to provide acceptable results.

A basic assumption of the SASW method is that only fundamental mode surface waves exist in the field. This assumption was investigated in the second series of tests using measurements of particle motion versus depth to calculate the relative contribution of the first several modes of surface wave propagation. The results were somewhat inconclusive because of the inability to model the subsurface accurately. However, theoretical results indicated that fundamental-mode surface waves com-

prised between 72 and 86 percent of the total motion. In addition, a qualitative comparison of theoretical mode shapes and experimental displacements also indicated that fundamental-mode motion dominates.

Finally, the third series of surface wave tests was performed on a concrete test slab to assess the influence of the relative stiffness of adjacent layers and the relative spacing of source and receivers on measured dispersion. Results of this test series indicated that a large stiffness ratio between adjacent layers can adversely affect measured dispersion curves for wavelengths which are between approximately 0.7 and 1.8 times the thickness of the slab. The influence of the relative source-receiver spacing was more difficult to determine because of the lack of a "true" dispersion curve with which to compare results. Based on selected records, receiver spacings with a ratio of d_2/d_1 greater than two appeared to yield improved dispersion curves.

KEY WORDS: nondestructive testing, experimental study, Rayleigh waves, surface waves, seismic testing, pavements, subgrades

SUMMARY

An investigation of variables affecting measurements by the Spectral-Analysis-of-Surface-Waves (SASW) method is presented herein. The SASW method is used to determine the shear wave velocity and elastic modulus profiles of pavement sections and soil sites. With this method, a dynamic vertical load is applied to the surface, and a group of surface waves with different frequencies is generated in the medium. These waves propagate along the surface with velocities that vary with frequency and the properties of the different layers comprising the medium. Propagation of the waves is monitored with two receivers a known distance apart at the surface. By analysis of the phase information of the cross power

spectrum, and by knowing the distance between receivers, phase velocity, shear wave velocity and shear, and Young's moduli of each layer are determined.

This report contains a investigation of variables affecting these measurements for the nondestructive testing of pavements, bases and subgrades. Variables such as source types, source/receiver configurations, stiffness ratios between adjacent layers and vertical distribution of surface wave motion were studied experimentally. Much of the experimental work was conducted at the Hornsby Bend test site on the south side of Austin where testing of a curing concrete slab was performed after extensive testing of the soil site was conducted.

IMPLEMENTATION STATEMENT

The Spectral-Analysis-of-Surface-Waves (SASW) method potentially has many applications in material characterization of pavement systems. With this method, elastic moduli and layer thicknesses of pavement systems could be evaluated in situ. The method could also be utilized as a tool for quality control during construction and during regular maintenance inspections. The main drawbacks to utilizing the method are development of a rapid and automated field testing procedure and development

of an automated data reduction procedure. The key background information necessary to develop an automated field testing procedure is presented in Reports 437-3F, 1123-5 (this report), and 1175-2 (in progress). An automated data reduction procedure is being developed on Project 1243. However, the method can presently be used in a "manual" mode where field testing takes about 30 minutes at each site and data reduction takes about one hour in the office.

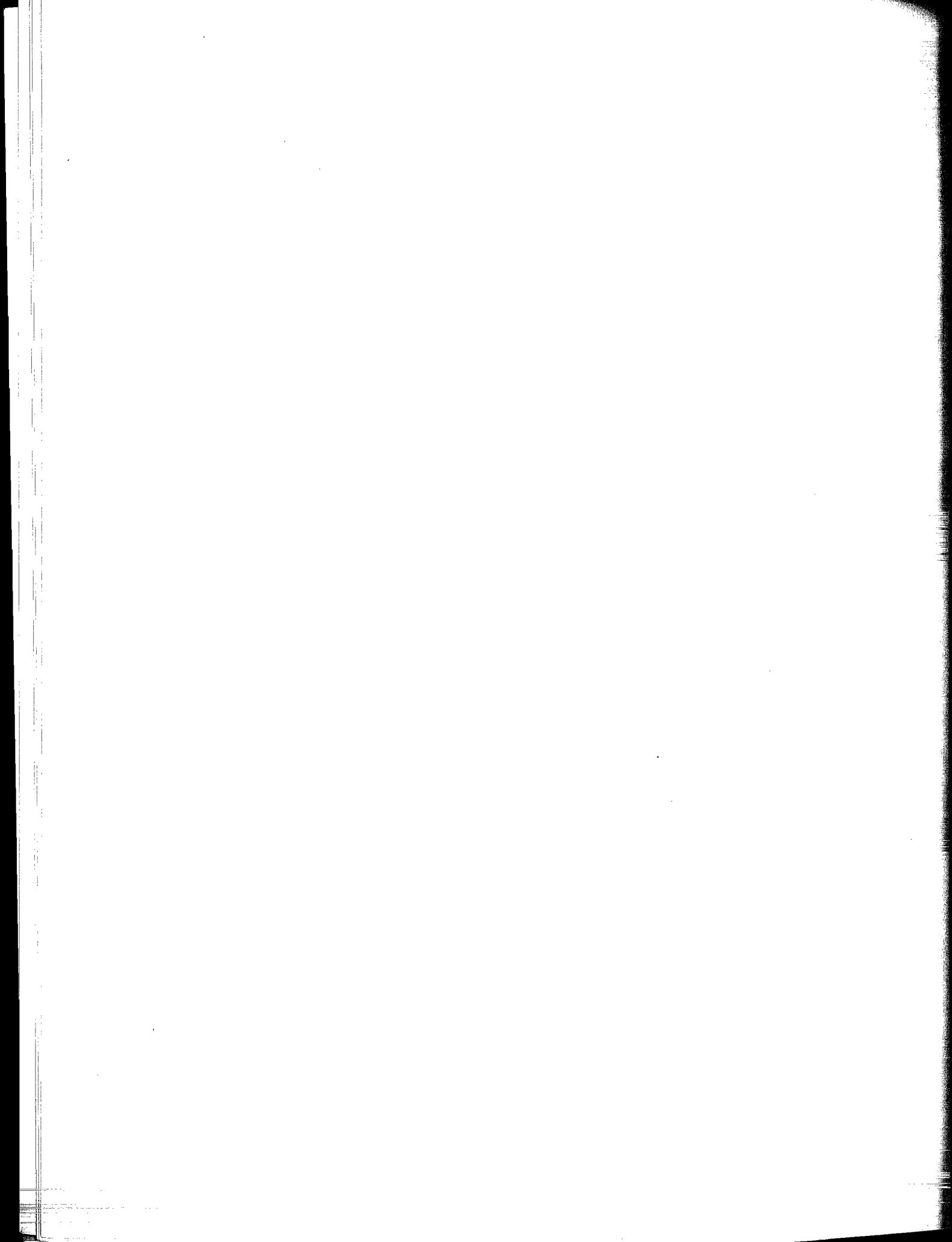


TABLE OF CONTENTS

PREFACE.....	iii
LIST OF REPORTS.....	iii
ABSTRACT.....	iv
SUMMARY.....	iv
IMPLEMENTATION STATEMENT.....	v
CHAPTER 1. INTRODUCTION	
1.1 Characteristics of Seismic Measurements.....	1
1.2 Characteristics of In Situ Test Methods.....	2
1.3 Purpose and Organization of the Report.....	3
CHAPTER 2. OVERVIEW OF SEISMIC METHODS USED FOR ENGINEERING PURPOSES	
2.1 Introduction.....	4
2.2 Seismic Methods Used for Engineering Purposes.....	4
2.3 Seismic Methods Involving Body Waves.....	4
2.3.1 Refraction Method.....	5
2.3.2 Reflection Method.....	6
2.3.3 Borehole Methods.....	6
Crosshole Method.....	7
Downhole Method.....	7
2.3.4 Surface Wave Methods.....	8
2.4 Engineering Applications of Seismic Methods.....	9
2.4.1 Profiling of Structural Features.....	9
2.4.2 Property Determination for Dynamic Analyses.....	10
2.4.3 Nondestructive Testing of Pavement Systems.....	10
2.4.4 Determination of Deformation Parameters.....	10
2.5 Summary.....	11
CHAPTER 3. THE SPECTRAL-ANALYSIS-OF-SURFACE-WAVES TEST METHOD	
3.1 Introduction.....	12
3.2 Surface Wave Propagation and Dispersion.....	12
3.3 Steady-State Rayleigh Wave Method.....	14
3.4 Spectral-Analysis-of-Surface-Waves Method.....	16
3.4.1 Field Testing.....	16
Equipment.....	16
Test Procedure.....	17
3.4.2 Dispersion Calculations.....	19
3.4.3 Inversion.....	22
3.5 Summary.....	24

CHAPTER 4. APPLICATION CONCEPTS FOR ACCELERATED PAVEMENT TESTING	
4.1	Introduction..... 26
4.2	Boring Logs and Basic Soil Data..... 26
4.3	Results of Previous Seismic Measurements..... 28
4.4	Concrete Test Slab..... 28
4.5	Summary..... 30
CHAPTER 5. COMPARISON OF SURFACE WAVE SOURCES AND INPUT MOTIONS	
5.1	Introduction..... 31
5.2	Description of Sources and Input Motions..... 31
5.2.1	Transient Input Motion..... 32
5.2.2	Random Input Motion..... 33
5.2.3	Sinusoidal Input Motion..... 33
5.2.4	Comparison of Transient, Random, and Sinusoidal Input Motions..... 33
5.3	Experimental Results Using Various Sources and Input Motions..... 36
5.3.1	Results Using Transient Input Motion..... 36
5.3.2	Results Using Random Input Motion..... 39
5.3.3	Results Using Sinusoidal Input Motion..... 41
5.3.4	Comparison of Results..... 41
5.4	Comparison of Other Sources and Input Motions..... 41
5.5	Comparison of Theoretical Phase Spectra..... 44
5.6	The Use of Transfer Functions to Measure Dispersion..... 46
5.7	Summary..... 48
CHAPTER 6. COMPARISON OF EXPERIMENTAL AND THEORETICAL WAVE MOTIONS	
6.1	Introduction..... 60
6.2	Measurement of Experimental Particle Motions..... 60
6.3	Comparison of Particle Motions in a Cased Borehole and in the Free Field..... 61
6.4	Comparison of Experimental and Theoretical Motions..... 63
6.4.1	Experimental Particle Displacements..... 63
6.4.2	Theoretical Particle Displacements..... 65
6.4.3	Comparison of Experimental and Theoretical Particle Displacements..... 66
6.5	Mode Contribution Calculations..... 68
6.5.1	Identification of Individual Surface Wave Modes..... 68
6.5.2	Calculation of Mode Participation Factors..... 71
6.5.3	Calculation of the Contribution of Individual Modes..... 72
6.5.4	Results..... 73
6.6	Summary..... 74
CHAPTER 7. INFLUENCE OF SOURCE-RECEIVER SPACING AND RELATIVE LAYER STIFFNESS ON SURFACE WAVE TESTS	
7.1	Introduction..... 76
7.2	Test Procedures..... 77
7.2.1	Surface Wave Tests..... 77
7.2.2	Compression Wave Tests..... 77
7.2.3	Supplemental Tests..... 77

7.3	Results of Surface Wave Tests.....	78
7.3.1	On Subgrade.....	78
7.3.2	On Curing Slab.....	80
7.4	Comparison of Surface Wave Test Results with Other Test Methods.....	86
7.4.1	Comparison of Laboratory and In Situ Values of Shear Wave Velocity.....	86
7.4.2	Comparison of In Situ Values of Shear and Compression Wave Velocity.....	87
7.4.3	Comparison of Shear Wave Velocity and Penetration Resistance.....	88
7.4.4	Comparison of In Situ Seismic Moduli and Moduli Derived from Cylinder Tests.....	88
7.5	Summary.....	90
CHAPTER 8. CONCLUSIONS AND RECOMMENDATIONS		
8.1	Summary.....	92
8.2	Alternative Sources and Input Motions.....	92
8.3	Comparison of Experimental and Theoretical Wave Motions.....	93
8.4	Influence of Source-Receiver Spacing and Relative Layer Stiffness on Surface Wave Results.....	94
8.5	Recommendations for Future Research.....	94
REFERENCES.....		96
APPENDIX A. THE INFLUENCE OF NOISE ON PHASE SPECTRA AND COHERENCE FUNCTIONS		
A.1	Introduction.....	102
A.2	Effect of Noise on Phase and Coherence: Simple Relationships.....	102
A.3	Effect of Noise on Phase and Coherence: Idealized Measurements.....	105
A.4	Summary.....	109
APPENDIX B. TABULATED DISPERSION CURVE.....		112
APPENDIX C. GEOPHONE CALIBRATION CURVES.....		118
APPENDIX D. PARTICLE DISPLACEMENT SPECTRA.....		120
APPENDIX E. SPECTRAL FUNCTIONS MEASURED DURING SURFACE WAVE TESTS ON CURING CONCRETE.....		137



CHAPTER 1. INTRODUCTION

1.1 CHARACTERISTICS OF SEISMIC MEASUREMENTS

Seismic measurements involve the introduction of stress (seismic) waves into a body of material and then monitoring the response of the body to the waves. In general, the strains induced by these waves are of such a magnitude that the body behaves in a linear, elastic fashion. For materials encountered in geotechnical engineering (e.g., natural soils or engineered fills), the linear, elastic range includes strains less than 0.001 percent. The maximum strain at which linear, elastic behavior is still valid is typically much greater for other engineering materials such as asphaltic or portland cement concrete.

Most often the response of a body to the introduction of seismic waves is measured in terms of the velocity of propagation of the waves. The propagation velocities of different types of waves are directly related to small-strain elastic moduli of the body. Small-strain moduli represent the slope of the stress-strain curve in the range of strain where linear, elastic behavior is valid (less than 0.001 percent for soils). The term *initial tangent moduli* is often used to refer to the small-strain moduli. This concept is illustrated in Fig 1.1. Moduli determined for higher levels of strain (greater than 0.001 percent for soils) where linear behavior is no longer valid are secant moduli, shown in Fig 1.2. Initial tangent moduli and secant moduli are plotted versus the logarithm of strain as shown in Fig 1.3 to emphasize the small-strain behavior of soils. The modulus is often normalized with respect to the initial tangent modulus as shown in Fig 1.4. The constant value of modulus at strains less than 0.001 percent is clearly shown in Figs 1.3 and 1.4.

For compression waves, waves in which the direction of particle motion is the same as the direction of propagation, the propagation velocity is related to the small-strain constrained modulus of the material by the relationship:

$$M_0 = \rho \cdot V_p^2 \quad (1.1)$$

where

$$\begin{aligned} M_0 &= \text{small-strain constrained modulus,} \\ \rho &= \text{mass density, and} \\ V_p &= \text{compression wave velocity.} \end{aligned}$$

The velocity of propagation of shear waves, which are waves in which the direction of particle motion is perpendicular to the direction of propagation, is related to the small-strain shear modulus of the material by the relationship:

$$G_0 = \rho \cdot V_s^2 \quad (1.2)$$

where

G_0 = small-strain shear modulus,

ρ = mass density, and

V_s = shear wave velocity.

Many times it is these values of constrained and shear moduli which are of interest to geotechnical engineers in situations where small-strain deformations are to be calculated (e.g., analyses of dynamically loaded machine foundations or site amplification studies). Frequently, however, other material parameters such as density or effective stress state are inferred from seismic measurements. Small-strain constrained and shear

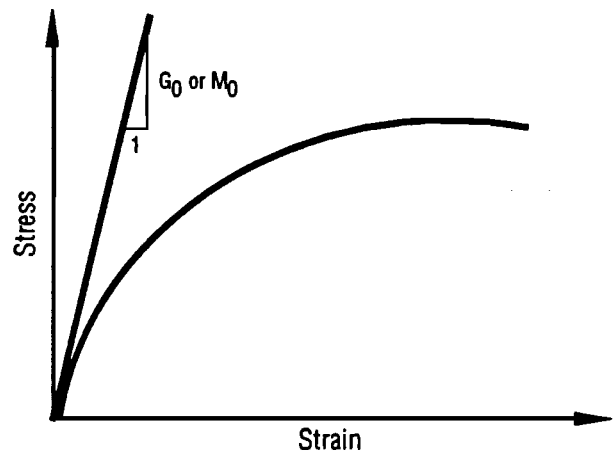


Fig 1.1. Illustration of small-strain or initial tangent modulus.

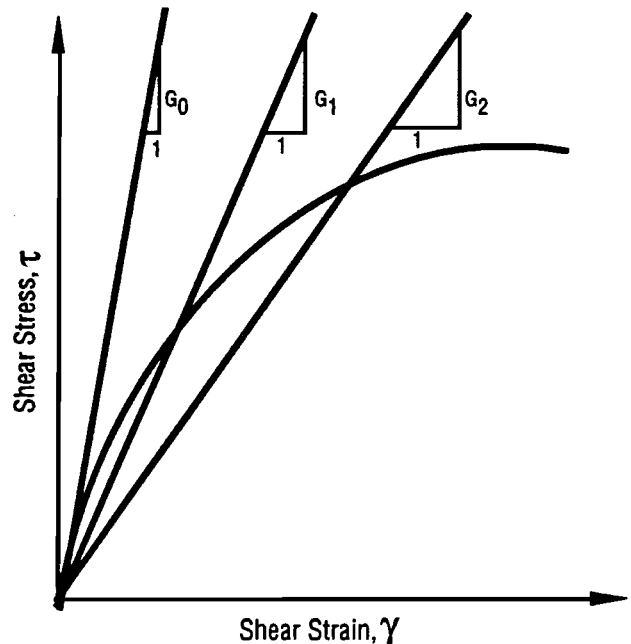


Fig 1.2. Illustration of secant moduli to characterize nonlinear behavior.

moduli are related to the void ratio and effective stress state of soils through relationships such as the one developed by Hardin (1978):

$$G_0 = \frac{A \cdot (\text{OCR})^k \cdot p_a^{1-n} \cdot \bar{\sigma}_m^n}{F(e)} \quad (1.3)$$

where

- G_0 = small-strain shear modulus,
- A = dimensionless coefficient,
- OCR = overconsolidation ratio,
- k = constant which depends on plasticity index,
- p_a = atmospheric pressure in the same units as G_0 and $\bar{\sigma}_m$,
- n = slope of the $\log G_0$ vs $\log \bar{\sigma}_m$ curve,
- $\bar{\sigma}_m$ = mean effective stress, and
- $F(e) = 0.3 + 0.7e^2$

or by Seed *et al* (1986) for cohesionless materials:

$$G_0 = 1000 \cdot K_2 (\bar{\sigma}_m)^{0.5} \quad (1.4)$$

where

- G_0 = small-strain shear modulus,
- K_2 = empirical constant reflecting density, and
- $\bar{\sigma}_m$ = mean effective stress.

Relationships like the ones presented in Eqs 1.3 and 1.4 form the basis for the use of seismic methods to infer material parameters such as density and stress state.

The model of the subsurface usually assumed in applying most in situ seismic methods in engineering is a one-dimensional model consisting of a layered, elastic half space with isotropic, homogeneous layers. New techniques are being developed (e.g., tomography) which will satisfy the demand for more realistic two- and three-dimensional models.

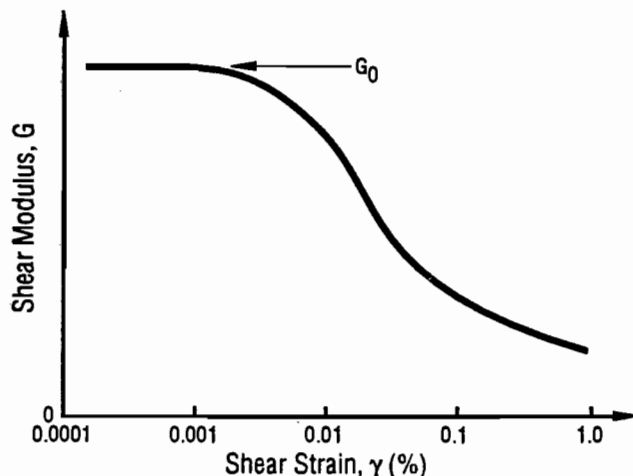


Fig 1.3. Typical variation of modulus with strain for soils.

1.2 CHARACTERISTICS OF IN SITU TEST METHODS

Since this report deals exclusively with in situ seismic methods, it is appropriate to briefly discuss some of the advantages of in situ test methods in general and in situ seismic methods in particular.

Two of the most common advantages associated with in situ methods in general are the avoidance of sample disturbance and the fact that tests are performed at the in situ stress state. Types of soil where sample disturbance can be critical are loose sands. Although elaborate methods have been devised to sample soils like loose sands, these methods are often too expensive to use on a production basis. In addition, it is extremely difficult (if not impossible) to eliminate sample disturbance completely. By definition, in situ methods avoid samples and sampling disturbance. Since materials are tested without removing a sample from the ground, there is no need to try to recreate complex states of stress in a triaxial cell, for example. This is particularly important when compacted fills and other *engineered soils* that have complex stress histories are to be tested.

There are other advantages which are specific to in situ seismic methods. One advantage which is often overlooked is the similarity between strain levels used in seismic testing and those experienced by geotechnical materials under actual loads. Recall from the previous section that strains associated with seismic testing are usually on the order of 0.001 percent or less. Using figures like the one shown in Fig 1.4, moduli determined by seismic methods can be easily extrapolated to strain levels encountered in the field (as discussed in Section 2.4.4). On the other hand, the strain levels associated with devices like the cone penetrometer far exceed those encountered in the field for working loads (Baligh, 1985). Deformation parameters measured by devices such as the pressuremeter or dilatometer are often significantly affected by the disturbance caused by advancing the device into the soil (Lacasse and Lunne, 1988).

Another advantage of in situ seismic methods is that larger (more representative) volumes of soil are tested than with other in situ methods. With the crosshole seismic method, the spacing between boreholes is usually 10 to 20 ft (3 to 6 m) resulting in a relatively large volume of soil which is being "sampled" by the seismic waves propagating between boreholes. The volume of soil sampled by the Spectral-Analysis-of-Surface-Waves (SASW) method is usually even larger. The ability to sample representative volumes of soil is particularly valuable when local variations in the material profile make it difficult to interpret the results of isolated measurements.

In situ seismic methods like the SASW test which are performed from the surface of the soil deposit make it possible to measure the in situ properties of hard-to-sample soils such as gravels and debris flows. It is often

extremely difficult to make use of techniques which require boreholes or penetration devices in these types of soils. Another area where so-called *nonintrusive, nondestructive* seismic methods have proven to be useful is in evaluation of the structural integrity of pavements. In pavement applications, the ability to avoid coring of the pavement structure is a practical requirement for production testing.

Finally, in situ seismic methods can often be incorporated into other in situ methods so that the two methods complement one another. An outstanding example of this type of combination is the seismic cone penetration test (Robertson *et al*, 1985). The cone penetrometer has proved itself a very useful tool for determining the layering of a site and the large-strain material parameters such as shear strength or angle of internal friction. In situ seismic methods are, in the author's opinion, the best method available for determining the small-strain moduli. The combination of these two methods can provide the user with a comprehensive set of strength and deformation parameters describing the material.

1.3 PURPOSE AND ORGANIZATION OF THE REPORT

The purpose of this research was to conduct an extensive experimental investigation of factors which affect surface wave testing in order to understand more fully the test results and to improve the test method.

Chapters 2 and 3 provide background information on in situ seismic methods used in engineering and on the SASW method, respectively. The emphasis in Chapter 2 is on describing the essential characteristics of the most commonly used engineering seismic methods and on presenting the relative advantages and disadvantages of each method. A detailed description of the equipment and test methodology used in the SASW method is the focus of Chapter 3 since the remainder of the report involves surface wave testing.

The test site which was used for much of the experimental work performed for this dissertation is described in Chapter 4. The Hornsby Bend test site was chosen because of the numerous well-documented studies which have been performed there in the past. The results of standard geotechnical test procedures including boring logs and standard penetration test (SPT) tests as well as the results of other seismic tests are presented in Chapter 4.

To date, the sources used in the SASW method have been primarily impact-type sources such as simple hammers or dropped weights. For many sites, these sources have worked well and have provided a convenient, portable means of generating surface wave energy. At several sites, however, impact-type sources have not performed well. Other types of sources are considered in Chapter 5 as alternatives to impact-type sources. The

most common type of alternative source is an electromechanical vibrator which, when controlled by a function generator, provides either sinusoidal or random signals. Chapter 5 focuses on the question of whether the relative inconvenience and lack of portability of the vibrator are overcome by the improved predictability and control and, therefore, improved test results associated with using the vibrator.

One of the important assumptions made when employing the SASW method is that primarily first mode (fundamental mode) surface waves are generated and measured in the field. Although this assumption is not inherent in the SASW method, it greatly simplifies the data reduction portion of the test. The purpose of Chapter 6 is to compare measured displacements with the theoretical displacements of individual surface wave modes to determine if the measured displacements are dominated by fundamental mode surface wave motion.

One of the factors which can influence the results of the SASW method is the relative stiffness of layers within the material profile. To understand better this effect, a concrete test slab was cast on the silty clay subgrade at the Hornsby Bend site to simulate a simple, two-layer profile. Surface wave measurements were made while the concrete cured (i.e., the stiffness was increasing) so that this simple system would appear to be many systems, each with a different ratio of stiffnesses between the surface layer and the lower "half space." The results of these measurements are discussed in Chapter 7. Other items which were studied using the test slab include the effect of different source-receiver combinations on measured surface wave dispersion and the relationship between the stiffness of the curing concrete and the times to initial and final set of the concrete.

Finally, the major findings of the report are summarized in Chapter 8. Recommendations for future studies are also discussed.

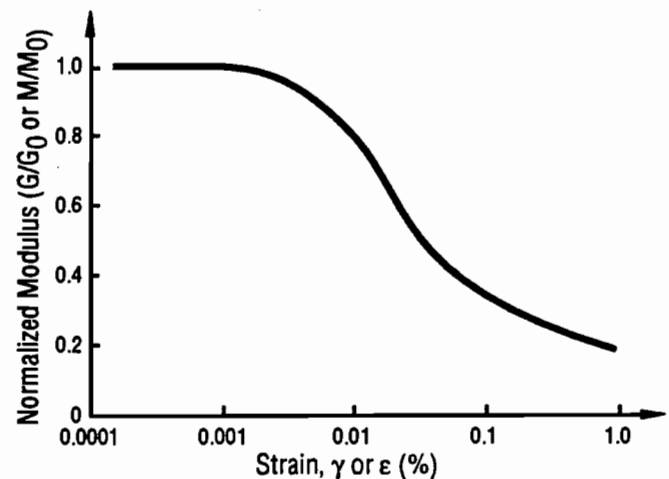


Fig 1.4. Typical variation of normalized modulus with strain for soils.

CHAPTER 2. OVERVIEW OF SEISMIC METHODS USED FOR ENGINEERING PURPOSES

2.1 INTRODUCTION

A wide variety of seismic methods are available for use in civil engineering. These methods range from very simple techniques used to extrapolate layering between soil borings to sophisticated methods intended to provide detailed information about various parameters of individual subsurface layers. The purposes of this chapter are: (1) to present an overview of the essential characteristics of several of the most widely used seismic methods for engineering purposes, and (2) to present some of the typical uses of these methods in civil engineering practice. For each of the methods discussed, the underlying principles, test configurations, and relative advantages and disadvantages of the method are presented.

2.2 SEISMIC METHODS USED FOR ENGINEERING PURPOSES

For the purposes of this report, one can consider three basic types of seismic (stress) waves which propagate in a layered, elastic half space: compression, shear, and Rayleigh waves. (Other wave types exist but are of relatively little importance when discussing seismic methods used in engineering.) Compression and shear

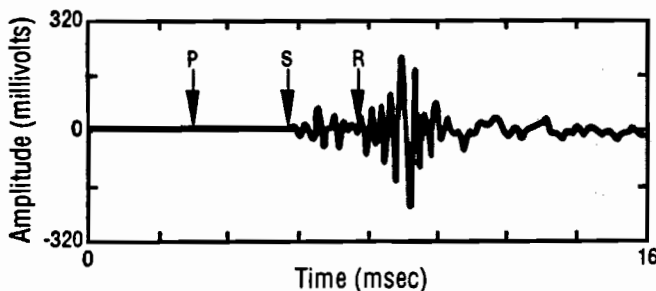


Fig 2.1. Time history recorded with a vertical receiver on the surface of a half space showing compression (P), shear (S), and Rayleigh (R) wave arrivals.

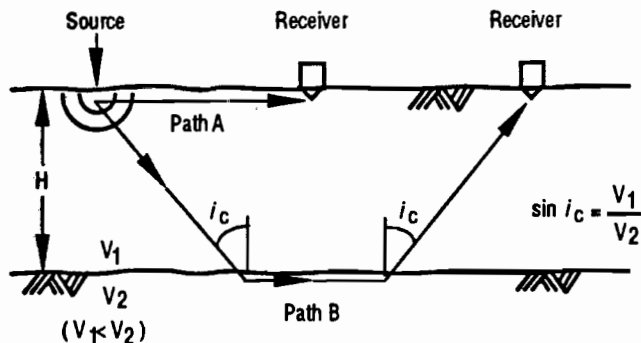


Fig 2.2. Typical test configuration used in the seismic refraction method.

waves are collectively called body waves because these waves propagate within the interior of the layered elastic half space as well as along its surface. Rayleigh waves are often referred to as surface waves because the propagation of these waves is guided by the surface of the half space. In a uniform half space, compression waves travel with the greatest velocity followed by shear waves and, finally, Rayleigh waves. All three velocities are related through the value of Poisson's ratio, ν , of the material. In a layered half space, the Rayleigh wave velocity is a complex function of the shear and compression wave velocities of each of the layers in the profile and varies with frequency (i.e., is *dispersive*). A typical time history recorded with a vertical receiver on the surface of a half space with the arrival of each type of wave indicated is presented in Fig 2.1.

The seismic methods available to civil engineers fall into two categories (i.e., body wave methods and surface wave methods) depending on the wave type which is utilized in the measurements. Body wave methods are more commonly used in civil engineering practice because, in general, these methods involve less complex data acquisition and analysis procedures than surface wave methods. However, methods based upon surface waves are becoming increasingly popular because these techniques can often overcome many of the shortcomings of body wave methods.

Both body wave and surface wave methods involve the measurement of the travel times of seismic waves. When body wave methods are used, the travel times are usually determined by identifying the first arrival of a particular wave type (compression or shear) at a receiver and measuring the time required for that wave to travel from the source to the receiver. The propagation velocity is the distance between the source and receiver divided by the measured travel time. Modern surface wave methods, on the other hand, rely upon more complex procedures to determine the travel time. These procedures are described in detail in Chapter 3. Generally, methods which only rely upon identification of the first arrival of a given wave type at a receiver are easier to interpret and less prone to error than methods which require more a complete analysis of the waveform.

2.3 SEISMIC METHODS INVOLVING BODY WAVES

Engineering seismic methods which utilize body waves can be subdivided into methods which are performed entirely from the surface (i.e., refraction and reflection methods) and methods which require the use of

one or more boreholes (i.e., crosshole and downhole methods). Each of these methods is described in the following sections.

2.3.1 REFRACTION METHOD

The refraction method was the first seismic test to be used extensively in civil engineering. Even today, refraction testing remains a popular way of determining structural features, such as the depth to bedrock, because of the availability of turn-key systems from vendors and the relatively simple data acquisition and analysis procedures involved.

An example of the test configuration used in the refraction method is presented in Fig 2.2. Body waves are generated by a source (e.g., explosives or a sledge hammer) impacting the surface of the material being tested. Refraction testing may be performed using either compression waves or horizontally polarized shear waves (SH waves). Compression waves are generated using a vertical impact on the ground surface while horizontally polarized shear waves are produced using a horizontal impact (usually transmitted through a plank to the ground surface).

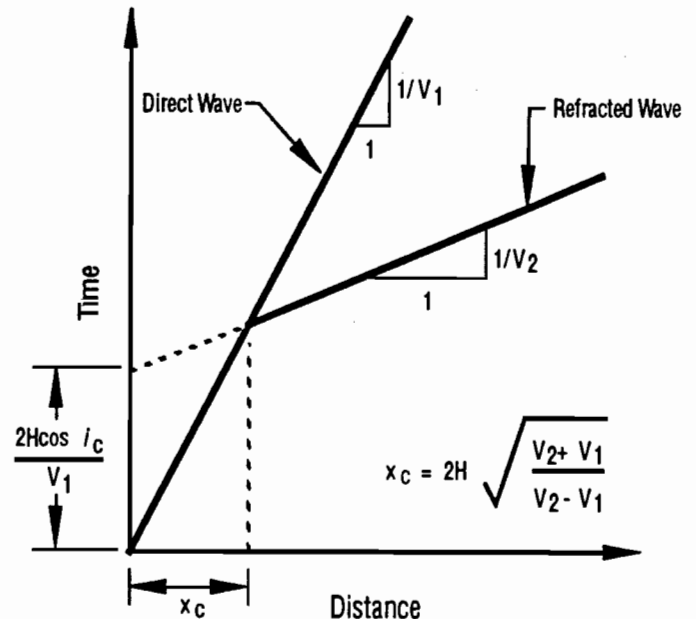
The compression or shear waves propagate throughout the medium and are measured by sensors placed on the ground surface at various distances from the source. If compression waves are being used, the sensors are oriented vertically. For horizontally polarized shear waves, horizontal sensors should be oriented perpendicularly to an imaginary line connecting the source and sensor.

In general, compression waves are used in refraction testing because these waves travel with the greatest velocity and will, therefore, be the first to arrive at the sensors. The arrival of horizontally polarized shear waves may be obscured by other wave types since they propagate with a slower velocity. Compression waves are considered in the following example. For a sensor placed relatively close to the source, the first wave to arrive will be the wave which travels directly from the source to the sensor (Path A in Fig 2.2). At some critical distance from the source, x_c , a wave which travels along Path B in Fig 2.2 will be the first wave to arrive at the sensor because the wave propagates more quickly in the underlying layer. By plotting the time of the first arrival at each sensor versus the distance from the source to that sensor, the thickness and velocity of each layer may be easily determined using simple relationships. An example of this type of plot is shown in Fig 2.3. Additional details of the method can be found in nearly all soil dynamics texts (e.g., Richart *et al*, 1970) or handbooks on seismic methods (e.g., Department of the Army, 1979).

The refraction method has a number of advantages which have helped to increase its popularity among civil engineers. The availability of turn-key systems and the relative ease of data acquisition and reduction (particularly for compression waves) are two factors

which have already been mentioned. Two other advantages are the fact that all of the measurements are performed from the surface (i.e., no boreholes are required) and that the determination of travel times is based on first arrivals at each sensor.

Unfortunately, the seismic refraction method suffers from several important disadvantages which prohibit its use at a wide variety of sites. The best known of these disadvantages involves the inability of the refraction method to resolve a layer with a wave velocity less than



Note: Travel time is based on identifying the initial arrival of the wave type of interest (P or SH wave)

Fig 2.3. Typical travel time plot from a seismic refraction test at a site composed of two layers.

the wave velocity in the layer located immediately above. This results from the absence of a critically refracted wave for this situation. (Since the surface layer is the almost always the stiffest layer in a pavement profile, the surface refraction method cannot be used on pavements.) A second disadvantage is the inability of the technique to locate thin layers of material in the profile accurately. This situation occurs because refracted waves from adjacent, underlying layers arrive at nearly the same time at the sensors and obscure the refracted wave arrival from a thin layer. Finally, since most refraction surveys utilize compression waves, saturated soils all exhibit nearly the same velocity (about 5,000 ft/sec or 1,500 m/sec) regardless of the compression wave velocity in the soil skeleton (Biot, 1956, and Allen *et al*, 1980). This is true as long as the compression wave velocity of the soil skeleton is less than the compression wave velocity through water. Although the surface refraction method is likely to remain popular in civil engineering, its uses are limited to a relatively small number of applications.

2.3.2 REFLECTION METHOD

The seismic reflection method has achieved widespread use in geophysics for the exploration of geologic formations believed to contain oil and natural gas. Efforts are currently underway to adapt this method for near-surface profiling to depths of interest to engineers (Hunter *et al.*, 1984, and Steeples, 1984).

As with the refraction method, an impulsive source is used to generate body wave energy which propagates throughout the medium and is monitored by sensors placed on the surface at known distances from the source. In the reflection method, however, the interest is in identifying the wave arrivals due to reflections from layer boundaries. Most reflection surveys utilize compression

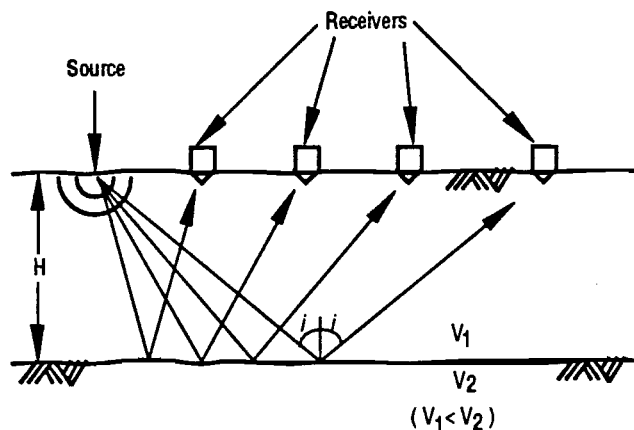


Fig 2.4. Typical test configuration used in the seismic reflection method.

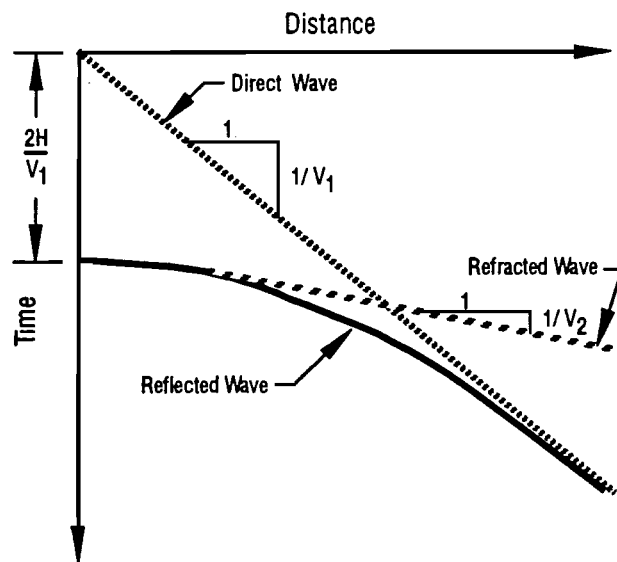


Fig 2.5. Typical travel time plot from a seismic reflection test at a site composed of two layers.

waves rather than shear waves. A typical test configuration is shown in Fig 2.4. The results are plotted in the form of curves of travel time versus offset (distance from the source). An example of such a plot is presented in Fig 2.5. Thicknesses and velocities of the layers can be determined using values obtained from the curves and simple relationships.

The example presented in the preceding paragraph has been oversimplified to illustrate the principles of the reflection method. Modern field procedures (e.g., Vibroseis), signal processing (e.g., filtering), and data analysis algorithms (e.g., migration and inversion) have progressed far beyond this simple example and have given geophysicists a powerful tool to use in resource exploration.

Several of the disadvantages of the refraction method are overcome by using the reflection method, including the problem of identifying slower-velocity layers beneath higher-velocity strata and the problem of locating thin layers. In addition, reflection surveys are also performed from the surface of the profile, thus eliminating the need for boreholes. However, the problem of measuring the compression wave velocity of water rather than the compression wave velocity of the material skeleton still exists because most reflection surveys rely upon compression waves. The use of shear waves (which are insensitive to the presence of water except as it affects the effective stress) is only now being investigated and implemented.

When using the reflection method, it can be difficult to distinguish the reflected wave arrivals from among the direct and refracted wave arrivals or from the surface wave arrivals. This is particularly true for the relatively small offsets required in engineering applications. Identification of reflected wave arrivals can become even more difficult when no strong reflecting boundaries are present, as is the case at many sites of interest to engineers. Finally, it has been necessary to develop powerful high-frequency sources which yield the desired spatial resolution and, at the same time, provide the penetration often required in engineering studies. Recent investigations of various sources (e.g., modified shotguns and rifles) for near-surface reflection tests have illustrated the benefits of developing such sources (Miller *et al.*, 1986).

Additional information about reflection testing can be found in any one of several texts on reflection seismology (e.g., Waters, 1984, and Dobrin, 1976).

2.3.3 BOREHOLE METHODS

The development of borehole seismic methods was spurred on by the need to determine detailed profiles of shear and compression wave velocities and shear and compression moduli at the relatively shallow depths (0 to 200 ft or 0 to 60 m) required in engineering studies. Two popular borehole techniques, the crosshole and downhole test methods, are discussed in the following paragraphs. (Another borehole technique, the uphole method, is rarely

used in engineering studies and is, therefore, not discussed.)

Crosshole Method

An example of the configuration typically used in a crosshole test is illustrated in Fig 2.6. Seismic waves are generated when a drop weight impacts on an in-hole wedge thereby creating a shearing motion on the wall of the borehole. Some sources also generate compression wave energy by expanding out against the wall of the borehole when the weight strikes the wedge. Three-dimensional geophones (vertical, radial, and transverse) located in adjacent boreholes at the same depth as the source are used to monitor the passage of the waves. The distance between each of the boreholes in a crosshole test is usually on the order of 10 ft (3 m). Each geophone is held tightly in place against the wall of the borehole through the use of some mechanism such as inflatable packers as shown in the figure or by pneumatic or hydraulic pistons. The most accurate measurements are usually determined by calculating the time required for the signal to travel from the first receiver (geophone) to the second (called true interval measurements or simply interval measurements), although direct measurements between the source and either receiver are also used. By moving the source and receivers down the borehole in unison, it is possible to generate detailed profiles of wave velocities and moduli. Additional information on basic crosshole test procedures can be found in Woods (1986) and Hoar and Stokoe (1978) or in published standards (ASTM, 1988c, and Department of the Army, 1979).

The crosshole method has several advantages with respect to other seismic testing techniques. Most sources used in crosshole testing offer increased control over the type of seismic wave which is generated. This additional control combined with the option of three geophones (vertical, radial, or transverse) to use as a receiver makes it possible to optimize the measurement of particular wave types. For example, if one desires to measure the compression wave velocity of the material, the radial geophone should be used since it responds primarily to compressional motion and is relatively insensitive to other types of motion. Vertically polarized shear waves (SV waves) are best measured using the geophone which is oriented vertically. New sources are currently under development (Hoar, 1982, and Camp, 1988) which generate horizontally polarized shear wave (SH wave) energy. SH waves can be best measured with a geophone which is mounted transversely. Increased control over the types of waves generated and measured can be valuable when trying to make measurements of stress-induced and structural anisotropy (Lee and Stokoe, 1986).

Advanced methods of data analysis have been developed which make it possible to get more information from the results of crosshole measurements. Recently, the crosshole method has been used to estimate material

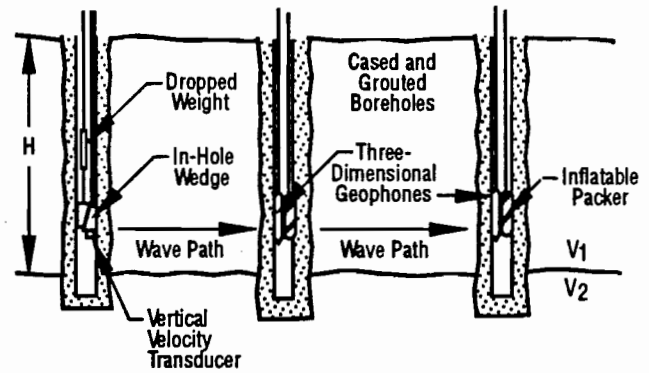


Fig 2.6. Typical test configuration used in the seismic crosshole method.

damping (Mok, 1987). Cross correlation and frequency domain techniques have been evaluated as means of making more detailed studies of body wave propagation and of automating the data reduction (Sánchez-Salineró, 1987). Finally, tomographic techniques have been used with the crosshole method, resulting in a detailed, two-dimensional profile rather than the one-dimensional profiles which result from the standard data analysis procedures (Dines and Lytle, 1979, and Roblee, 1988).

The primary disadvantage of the crosshole method is the need for two or more boreholes. (Although three boreholes are shown in Fig 2.5, the test is often performed with only two boreholes, one containing the source and the other containing the receiver.) Aside from the additional expense and time required to drill boreholes, in many instances it may not be possible to install boreholes as is the case when gravelly soils are to be tested. The need for boreholes has been overcome to some extent by incorporating sources and geophones into an electric cone penetrometer (Robertson *et al*, 1985). Although the seismic CPT was originally intended to function as the receiver in the downhole test (described next), two cone penetrometers (Baldi *et al*, 1988) working in tandem have been used to perform crosshole tests as well.

Other disadvantages of the crosshole method include the need to measure the deviation of the boreholes from vertical to obtain an accurate measurement of the distance between boreholes and the need to orient the three-dimensional geophone in the borehole to insure the accuracy of measurements made using the two horizontal geophones. Finally, a problem that may arise during crosshole testing is refraction of waves between boreholes. This situation can generally be avoided or minimized, however, by the appropriate choice of spacing between boreholes.

Downhole Method

The downhole method reduces the required number of boreholes to one and uses a source on the surface to

generate seismic waves. A typical test configuration used for the downhole method is shown in Fig 2.7. Several different procedures are available to determine the velocity profile when performing a downhole test including: (1) direct travel time measurements, (2) pseudo-interval measurements, (3) true interval measurements, and (4) application of inversion techniques to direct travel time measurements (Patel, 1981, and Mok, 1987). Each of these alternatives is discussed briefly in the paragraphs that follow.

When using direct travel time measurements, the time required for the wave to travel from the source on the surface to the receiver at depth is calculated. The velocities determined in this manner are, therefore, average velocities over the depth of the receiver. Because of this averaging, the ability to resolve changes in the wave velocity profile accurately is quickly lost as the depth of the receiver increases. The use of pseudo-interval measurements is an attempt to overcome this limitation by using the difference in travel time at two depths; the direct travel time to the receiver is determined at the first depth and is subtracted from the direct travel time to the receiver at the second depth. By using this procedure, it is usually possible to determine a more detailed profile than

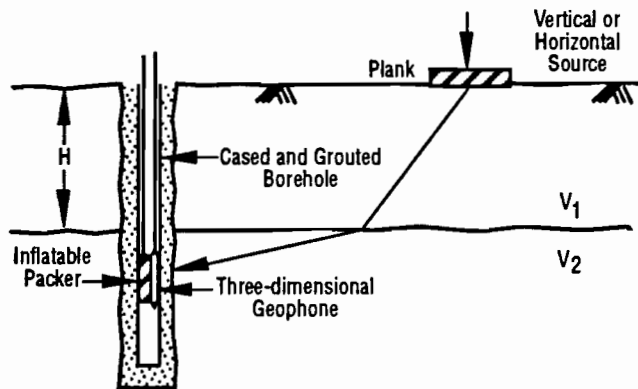


Fig 2.7. Typical test configuration used in the seismic downhole method.

by using direct travel times alone. It is important to note that pseudo-interval calculations involve two different "hits" from the source. This can sometimes be a source of error if the second hit does not generate the same types of waves as the first hit. The true interval measurement is similar to the pseudo-interval measurement, but the interval travel time is calculated directly from the waveforms recorded at two receivers for a single hit rather than using the difference in direct travel times from two separate hits. Since a single hit is involved, any problems which may arise from the use of two separate hits with the pseudo-interval technique are eliminated. Finally, the application of inversion methods to the reduction of

downhole data is a technique which has just been adapted to downhole tests for engineering purposes. Inversion methods retain the ease of direct travel time measurements as well as the accuracy of interval measurements. Mok (1987) provides a detailed explanation of inversion procedures.

One advantage of the downhole method with respect to the crosshole method is the simplicity and ease of use of surface sources in downhole testing. Liu *et al* (1988) have developed an air-powered source capable of generating strong, repeatable shear waves for downhole testing. Another improvement in the downhole method has come through the use of geophones incorporated into cone penetrometers as mentioned in the section on crosshole testing (Robertson *et al*, 1985). Use of the cone penetrometer eliminates the need for a cased borehole as well as improves the coupling between the soil and the receiver.

The primary disadvantage of the downhole method is the lack of penetration caused by the attenuation of high-frequency waves with depth. This limitation will undoubtedly be overcome as more powerful sources are developed (Liu *et al*, 1988). Another disadvantage is encountered when using compression waves and cased boreholes in the downhole method. Because compression waves often travel down the casing and arrive at the location of the receiver prior to compression waves travelling through the soil, the method cannot be relied upon to give accurate results in this situation.

In summary, both the crosshole and downhole methods (crosshole in particular) are well-developed seismic methods which can be used to provide reliable velocity and modulus profiles under a wide variety of site conditions.

2.3.4 SURFACE WAVE METHODS

Surface wave measurements have long been used by seismologists to estimate the structure of the earth using surface waves generated by earthquakes and nuclear explosions. However, the use of surface waves by engineers for near-surface measurements of wave velocities and moduli has not been nearly as popular as the seismic methods described in the previous sections. One possible reason for this is that, in the past, measurements using surface waves have involved bulky field equipment and empirical data analysis procedures which often resulted in significant errors. Until recently (late 1970's), the computers and dedicated field instrumentation which had the power to solve these problems were not readily available to implement more theoretically correct data analysis and reduction procedures. In the paragraphs which follow, a brief discussion of surface wave testing and the relative advantages and disadvantages of surface wave methods are presented. A more detailed discussion of surface wave methods is reserved for Chapter 3 because these

methods are the focus of this report. (Although the term *surface wave* may mean either Rayleigh or Love waves, Rayleigh waves are used exclusively in this report because Love waves do not exist in many soil profiles of interest to geotechnical engineers.)

A simplified example of the test configuration normally used for surface wave testing is presented in Fig 2.8. As indicated in the figure, all measurements are performed from the surface, eliminating the need for boreholes. Before the advent of sophisticated field instrumentation, the source was restricted to electromechanical vibrators operating at discrete frequencies. With the development of advanced signal recording and processing equipment, the source may now be an impact-type source such as a simple hammer or drop weight or an electromechanical or rotating mass vibrator with much more complex waveforms than the fixed-frequency sine waves used previously. (An in-depth comparison of the various type of sources is the subject of Chapter 5.) Velocity transducers (geophones) or accelerometers are usually employed as receivers. Surface waves generated by the source are monitored as they pass the receivers and are recorded on a dual-channel FFT analyzer with which the propagation velocity of surface waves of various frequencies is determined. Profiles of moduli and wave velocity may then be calculated using a procedure called inversion. Details of these procedures are discussed further in Chapter 3.

Surface wave testing combines many of the advantages of the other seismic methods presented earlier. Perhaps the most important advantage is that surface wave testing involves surface measurements of the predominant wave type generated by a source on the surface. Measurements made from the surface, aside from the fact that the expense and time required for boreholes are eliminated, make it possible to test hard-to-sample materials (e.g. gravels and loose sands) or perform tests on profiles such as pavements where nondestructive methods are a practical requirement (Stokoe *et al*, 1988, and Nazarian *et al*, 1983). Because surface waves are the predominant type of wave generated by a vertically-acting load on the surface, they are the most easily measured type of wave. The distribution of energy among the three types of waves for a vertically-acting source on the surface of a uniform half-space is given in the following table (Miller and Pursey, 1955):

TABLE 2.1. DISTRIBUTION OF WAVE ENERGY GENERATED BY A VERTICAL SOURCE ACTING ON A UNIFORM HALF SPACE

Wave Type	Total Energy (%)
Surface (Rayleigh)	67
Shear	26
Compression	7

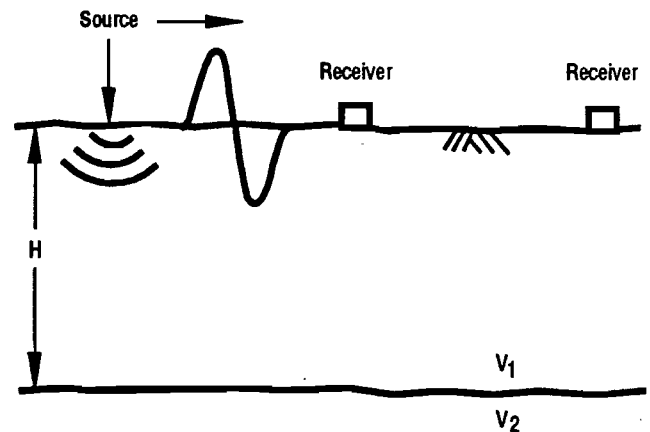


Fig 2.8. Typical test configuration used in surface wave (SASW) testing.

In addition, it can be shown (Ewing *et al*, 1957) that the geometric attenuation is much less for surface waves than for body waves. Along the surface of a half-space at large distances from the source (more than about two wavelengths), surface waves attenuate in proportion to $r^{-0.5}$ whereas body waves attenuate in proportion to r^{-2} . Other advantages of surface wave methods include the potential for very rapid testing and complete automation and the ability of method to be successfully used at sites where stiff layers are underlain by softer layers (e.g., pavement sites).

Disadvantages associated with surface wave testing lie primarily in the complexity of data analysis and reduction procedures. However, as field instrumentation and computers become more powerful as well as portable, these disadvantages are quickly being overcome.

In short, methods based upon surface waves possess many of the advantages of other seismic methods and very few of the disadvantages. As methods based on surface waves become more oriented to production type testing rather than research applications, the acceptance of these methods by geophysical engineers will undoubtedly increase.

2.4 ENGINEERING APPLICATIONS OF SEISMIC METHODS

The information provided by seismic tests has found increased use by engineers for a wide variety of purposes. In this section several of the more common uses of seismic test results are briefly discussed.

2.4.1 PROFILING OF STRUCTURAL FEATURES

The first uses of seismic methods (refraction in particular) were to extrapolate soil stratigraphy away from borings or to locate the soil-rock interface. In fact, these are still the only applications of seismic testing presented in many undergraduate engineering texts (e.g., Peck *et al*,

1974). More recent uses of seismic methods which fall into the category of structural profiling include tunnel and void detection surveys (Powers, 1984).

2.4.2 PROPERTY DETERMINATION FOR DYNAMIC ANALYSES

One of the most widespread uses of seismic tests has been to determine dynamic soil properties for dynamic soil-structure interaction problems. More specifically, low-amplitude shear modulus is an important input parameter in the design of dynamically-loaded machine foundations (Richart *et al.*, 1970, and Gazetas, 1982), response of structures to earthquake loads (ASCE, 1979), and in the analysis of liquefaction susceptibility using the strain-based approach (Dobry *et al.*, 1981).

2.4.3 NONDESTRUCTIVE TESTING OF PAVEMENT SYSTEMS

Seismic methods can provide a means of evaluating the structural integrity of pavement systems to determine the load-carrying capacity or remaining service life of pavements. A practical requirement of all methods used to evaluate the integrity of pavements is that the method be nondestructive. Nondestructive testing minimizes the interruption to traffic and permits the number of tests to be maximized because of the relatively short time needed to perform a single test. Furthermore, nondestructive testing permits sites to be reoccupied in the future for studies involving measurements made over a period of time.

One of the key parameters used in pavement evaluation is the modulus of each layer (including the subgrade) in the pavement profile (Haas and Hudson, 1978). The most commonly used methods used to determine the stiffness of layers within the pavement profile are the Dynaflect and Falling Weight Deflectometer (FWD). Both of these testing techniques utilize a dynamic load which causes the pavement to deflect. These deflections are measured by sensors located at preselected distances

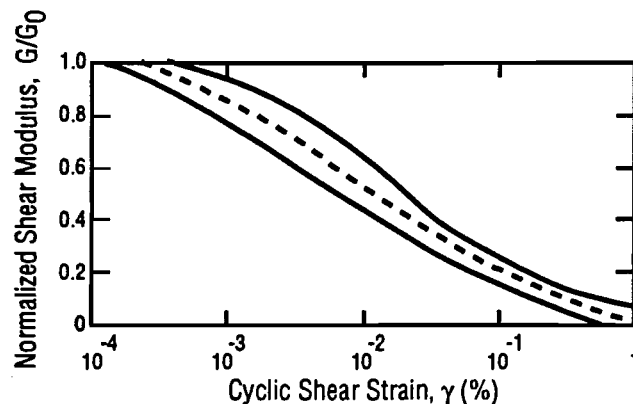


Fig 2.9. Variation of normalized shear modulus with shear strain for sands (after Seed and Idriss, 1970).

from the point on the pavement where the load is applied. Using linear, elastic theory, the moduli of the layers within the pavement system are back-calculated from the measured deflections.

Seismic methods are being developed as alternatives to deflection-based methods. Since seismic methods measure the stiffness directly (via the wave velocity), they are well-suited for determining the stiffness of layers in the pavement. Because a nondestructive test method is a practical requirement for the reasons discussed previously, surface wave methods are particularly useful as pavement evaluation tools. Unlike deflection-based methods, seismic methods can be used directly on the subgrade in addition to the pavement surface layer. This permits detailed modulus profiles to be obtained during each phase of pavement construction.

2.4.4 DETERMINATION OF DEFORMATION PARAMETERS

One area of research which has received attention for many years in geotechnical engineering is the development of constitutive models for soils. The results of seismic tests can provide valuable information in formulating these models. As discussed in Chapter 1, seismic measurements can be used to determine the initial slope (modulus) of the stress-strain curve. Initial shear modulus, G_0 , can be calculated using the measured shear wave velocity. If compression waves are used in unsaturated soils ($S_r < 99.5\%$), the initial constrained modulus, M_0 , is determined. G_0 and M_0 are important reference values in evaluating values of shear and constrained moduli, respectively, at levels of strain larger than those encountered in seismic testing (as illustrated in Fig 1.4). Once deformation parameters can be reliably estimated in the working strain range, it will become possible to develop alternatives to limit equilibrium design procedures which will be based upon allowable deformations.

One example of how small-strain shear modulus can be included in models of soil behavior has been presented by Hardin and Drnevich (1972). Hardin and Drnevich have proposed a modified hyperbolic relationship between shear stress and shear strain which takes the following form:

$$G = G_0 / (1 + \gamma/\gamma_r [1 + a \exp(-b(\gamma/\gamma_r))]) \quad (2.1)$$

where

- G = shear modulus at a given shear strain γ ,
- G_0 = small-strain shear modulus,
- γ = shear strain,
- γ_r = reference shear strain, τ_{\max}/G_0 ,
- τ_{\max} = shear stress at failure, and
- a, b = material parameters.

Relationships such as this can be used to estimate shear stress-shear strain curves in the working strain range.

Another approach for using small-strain shear modulus to estimate larger-strain behavior has been suggested by Seed and Idriss (1970). In this method, the variation of shear modulus with strain is determined using laboratory specimens or is estimated by empirical means. These results are plotted in the form of normalized shear modulus, G/G_0 , versus the logarithm of shear strain, γ , where G_0 is the small-strain shear modulus, γ is shear strain, and G is the secant modulus at a shear strain equal to γ . A typical relationship for sand is shown in Fig 2.9. The in situ value of G_0 is evaluated using seismic methods and is combined with the relationship in Fig 2.9 to calculate G at any level of strain.

Both the Hardin and Drnevich (1972) and Seed and Idriss (1970) approaches are well established methods which are widely used in geotechnical and earthquake engineering to evaluate the dynamic response of geotechnical materials.

2.5 SUMMARY

Seismic methods are finding increased use in civil engineering for a variety of purposes ranging from structural profiling to property evaluation. Seismic methods generally can be divided into two groups: methods based on body (compression and shear) waves and methods based on surface (Rayleigh) waves. Surface refraction was the first seismic method to be used extensively in civil engineering but suffers from a number of disadvantages which prevent its use at a large number of geotechnical sites and at all pavement sites. The most important of these limitations is the inability of the method to locate low-velocity layers underlying higher-velocity layers. Reflection methods have been developed primarily for use in the petroleum industry but

have recently been adapted to meet the needs of engineers. However, reflection methods still have several drawbacks, such as the problem of distinguishing reflected wave arrivals in the midst of other wave arrivals, which may make their application to engineering problems difficult. Body wave methods such as the crosshole and downhole tests which make use of boreholes have proven to be reliable methods of seismic testing. Unfortunately, the need for boreholes sometimes makes these methods either too expensive and time consuming to use or extremely difficult to use when site conditions prevent the installation of boreholes. The crosshole method has been used to a limited extent at pavement sites primarily for research purposes.

Methods based upon surface waves offer several important advantages (e.g., surface measurements of the predominant wave type) with respect to other methods. Although surface wave techniques generally require more complex data analysis procedures than do body wave methods, this disadvantage will diminish in importance as field instrumentation and computers become more powerful as well as portable. A complete description of a relatively new surface wave method, the Spectral-Analysis-of-Surface-Waves method, is presented in Chapter 3.

The uses of seismic testing in civil engineering range from relatively straightforward applications such as profiling of structural features to more advanced applications including in situ measurement of soil properties for dynamic analyses and determination of deformation parameters for use in constitutive modeling of soils and pavement materials. The number of uses will continue to grow as the ability to determine more detailed (i.e., two- and three-dimensional) profiles is developed and the demand for nondestructive test methods increases.

CHAPTER 3. THE SPECTRAL-ANALYSIS-OF-SURFACE-WAVES TEST METHOD

3.1 INTRODUCTION

Engineering seismic methods based upon surface waves were introduced in Chapter 2 as an alternative to other seismic methods. One advantage of surface wave methods is that all measurements are performed from the ground surface, thereby eliminating the expense and time required to install boreholes. Another advantage is that surface waves are the predominant wave type generated by a vertically-acting source on the surface and, therefore, are the most easily measured type of wave in terms of signal-to-noise ratios. The primary disadvantage associated with surface wave testing is the complexity of the data processing procedures.

The Spectral-Analysis-of-Surface-Waves (SASW) is a relatively new seismic method which has evolved within the last ten years. In that period of time, it has been used extensively to evaluate stiffness profiles at soil sites (e.g., Stokoe and Rix, 1988), to test pavement systems nondestructively (e.g., Nazarian *et al*, 1983) and to profile sites consisting of hard-to-sample materials such as gravelly deposits and debris blockages (e.g., Stokoe *et al*, 1988).

A comprehensive review of the SASW method will be presented in this chapter. Topics to be discussed include the nature of surface wave propagation and associated dispersion and various aspects of the SASW method such as field testing, dispersion calculations and inversion methodology. A summary of the predecessor to the SASW method, the steady-state Rayleigh wave method, is also presented so that one can better understand the recent advances in surface wave testing.

3.2 SURFACE WAVE PROPAGATION AND DISPERSION

To understand how surface waves can be used to determine the shear wave velocity profiles of geotechnical and pavement sites, it is first necessary to understand the nature of surface wave propagation in a layered half space. Unlike shear and compression waves which propagate along a spherical wave front, surface waves propagate along a cylindrical wave front as they spread out from the source. For most applications (including SASW testing) only plane surface waves are considered. The simplicity and convenience of working with plane waves far outweighs the slight loss in accuracy by not considering more complex forms of wave motion (Aki and Richards, 1980, and Sánchez-Salineró, 1987).

A plane surface wave has two components of motion: a vertical component and a radial component. A conceptual view of the displacements associated with surface wave propagation is presented in Fig 3.1. The vertical and radial motions combine to form an elliptical particle path as shown in the figure. A more detailed figure showing the variation of normalized vertical and radial displacement with normalized depth for various values of Poisson's ratio, ν , is shown in Fig 3.2. One important feature of surface wave propagation which may be observed in Fig 3.2 is the exponential decay of particle displacements with depth. Another feature which should be noted is that the particle displacements extend to greater depths as the wavelength increases. Both of these features contribute to the dispersive nature of surface waves as discussed below.

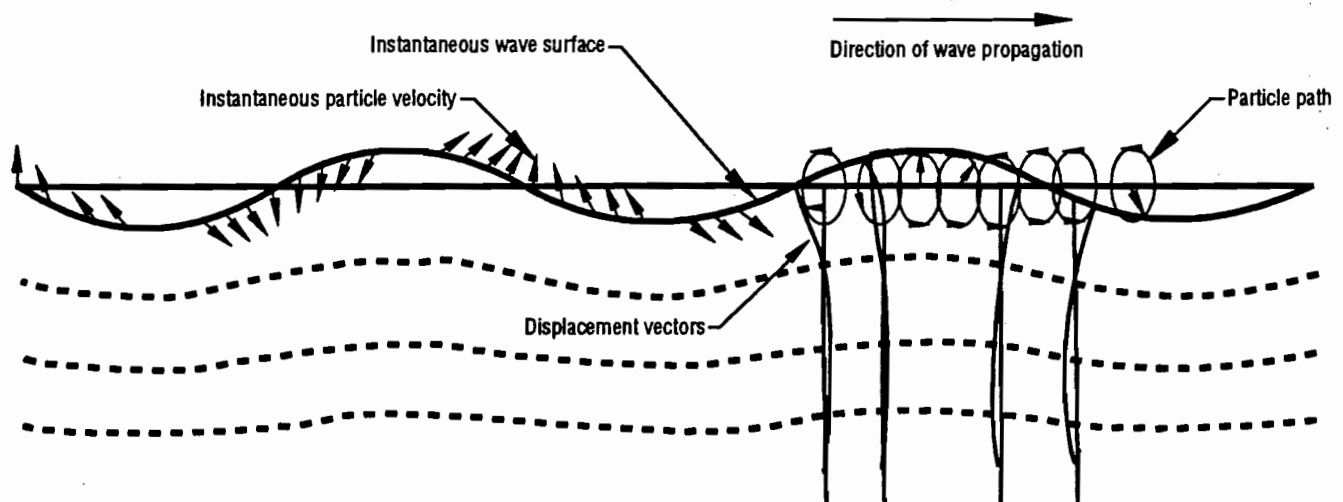


Fig 3.1. Conceptual view of surface wave propagation in a half space (from Fung, 1965).

A dispersive wave is one in which the velocity of propagation of the wave varies with the frequency or wavelength. (The velocity of propagation of a surface wave is often called the phase velocity, the apparent velocity or the apparent phase velocity. *Phase velocity* is used herein. Furthermore, the terms *frequency* and *wavelength* are used interchangeably since they are so closely related.) Surface waves in a layered half space are dispersive waves. To illustrate this behavior, consider the three examples shown in Figs 3.3 through 3.5. In Fig 3.3 the variation of phase velocity with wavelength (i.e., a dispersion curve) is shown for a uniform half space (i.e., V_s constant). For this case, surface waves are *nondispersive* (i.e., constant phase velocity) because all surface waves sample the same, uniform material, regardless of their wavelength. In Fig 3.4 the shear wave velocities of the layers in the profile increase with depth as shown in the inset of the figure. Many soil or rock sites exhibit this type of profile. The resulting surface wave

dispersion curve contains phase velocities which increase as the wavelength increases. This phenomenon occurs because as the wavelength increases the surface waves penetrate into layers with increasingly greater shear and compression wave velocities and the phase velocity increases as a result of the influence of these layers. (As discussed in Section 2.2, the phase velocity is a complex function of the shear and compression wave velocities of each of the layers in a layered half space.) Finally, the surface wave dispersion which results from a layered profile in which the shear wave velocities of the layers decrease with depth is shown in Fig 3.5. A common example of this type of profile is a pavement structure. The phase velocity decreases with increasing wavelength because the waves are influenced by layers with smaller shear and compression wave velocities as the wavelength increases.

The dispersive nature of surface wave propagation in a layered half space forms the basis of the SASW

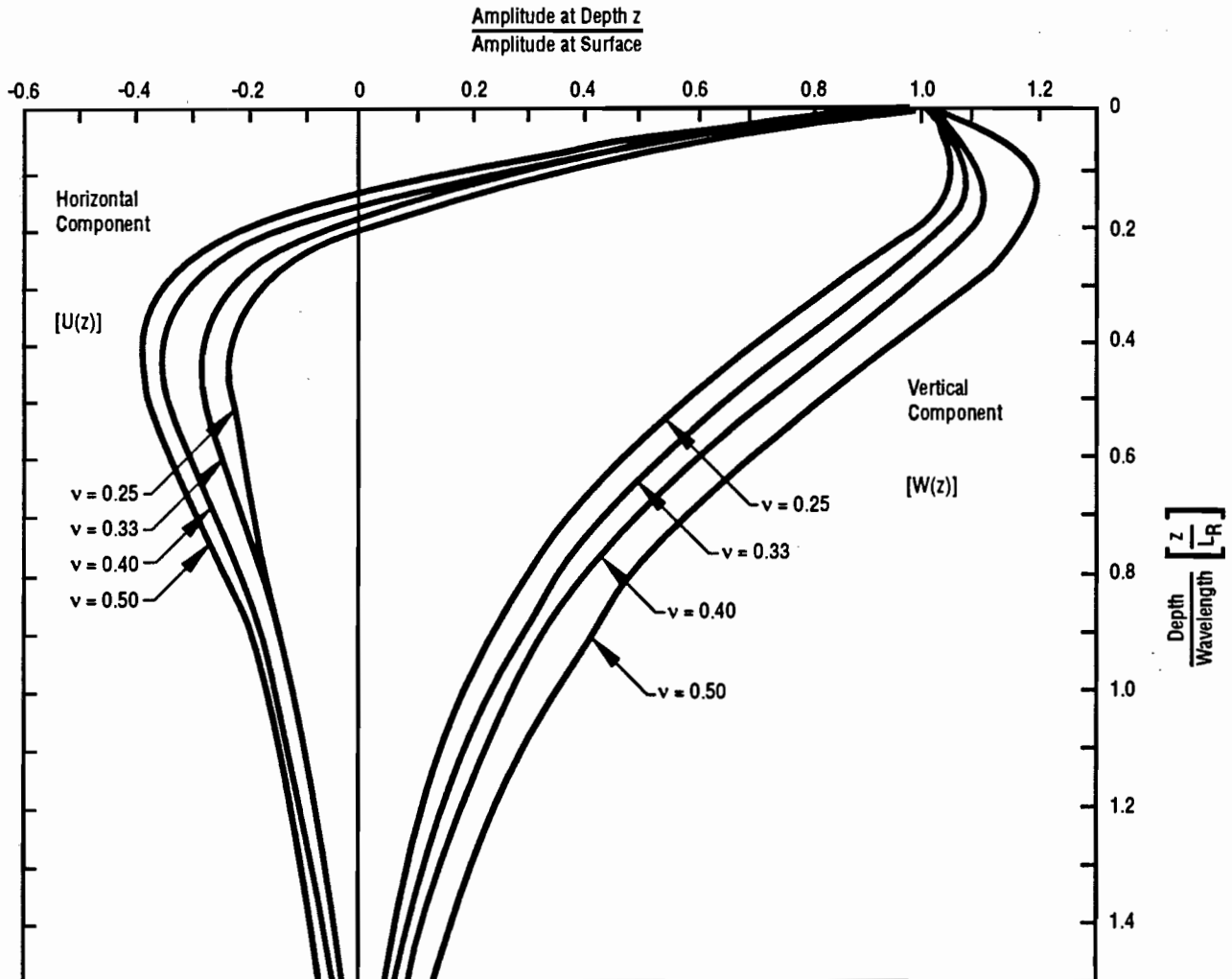


Fig 3.2. Variation of normalized vertical and radial displacement with normalized depth for a surface (Rayleigh) wave propagating in a uniform half space (from Richart *et al*, 1970).

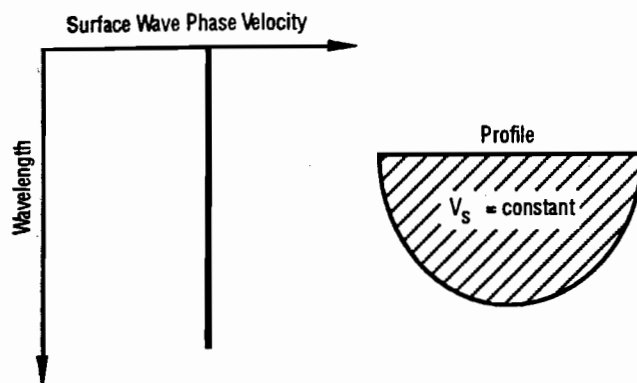


Fig 3.3. Surface wave dispersion in a uniform half space.

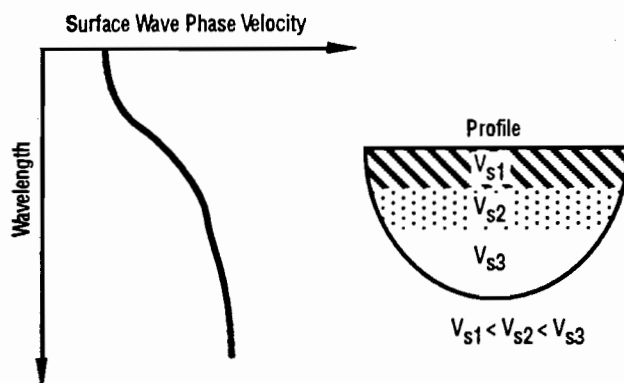


Fig 3.4. Surface wave dispersion in a layered half space in which velocity increases with depth.

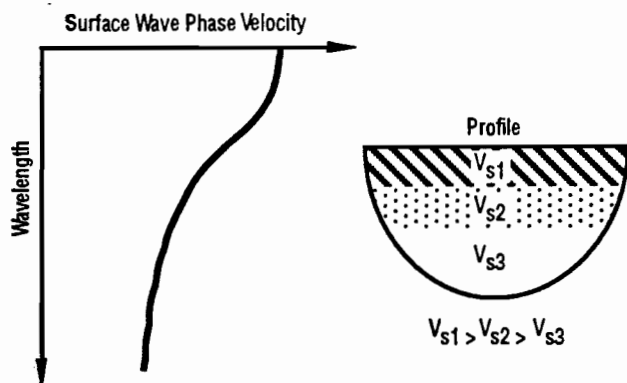


Fig 3.5. Surface wave dispersion in a layered half space in which velocity decreases with depth.

method. The objective in surface wave testing is to make experimental measurements of surface wave dispersion at geotechnical and pavement sites and to then estimate the shear and compression wave velocities of the layers in the profile using the complex relationship between the surface wave phase velocity and the shear and compression wave velocities of the layers. This back-calculation step, more properly called inversion, is conceptually illustrated in Fig 3.6. Several different algorithms are available to use in the inversion process. The first inversion algorithms used in engineering surface wave testing were empirical methods based upon observed relationships between surface wave dispersion and various types of material profiles. More modern, theoretically-based algorithms are currently used in SASW testing. Detailed descriptions of both methods of inversion are discussed later.

There are two basic assumptions made when utilizing the SASW method to determine the wave velocity profiles at geotechnical and pavement sites. The first assumption is that the only type of wave measured in the field is a plane surface wave. The effect of body waves on the measured surface wave dispersion is explicitly ignored in the SASW method as it exists at the present time. Sánchez-Salineró (1987) studied the implications of this assumption and determined that the effect of ignoring body waves is relatively minor as long as the spacing between the source and the first receiver relative to the wavelength is maintained within certain limits as discussed in Section 3.4.2. The second assumption is that only first mode (fundamental mode) surface wave energy is measured in the field. Surface waves generally consist of the summation of many modes of propagation. However, the first mode usually dominates when the source is located on the surface. An experimental assessment of the contribution of different modes of propagation to the overall surface wave motion is the subject of Chapter 6.

3.3 STEADY-STATE RAYLEIGH WAVE METHOD

The steady-state Rayleigh Wave method is the predecessor of the SASW method. The steady-state method is performed by placing a vertically-acting vibrator on the ground surface and operating the vibrator at a discrete frequency, f . A vertical receiver is moved away from the source along the ground surface until successive positions are found at which the vertical motion is in phase with the vibrator as shown in Fig 3.7. The distance between any two adjacent receiver positions is the wavelength, λ_R , of the surface wave at that frequency. The distance from the source to several of the in-phase points is plotted as shown in Fig 3.8 to determine the average wavelength at each frequency. The phase velocity, V_R , of the surface wave may then be calculated using the expression:

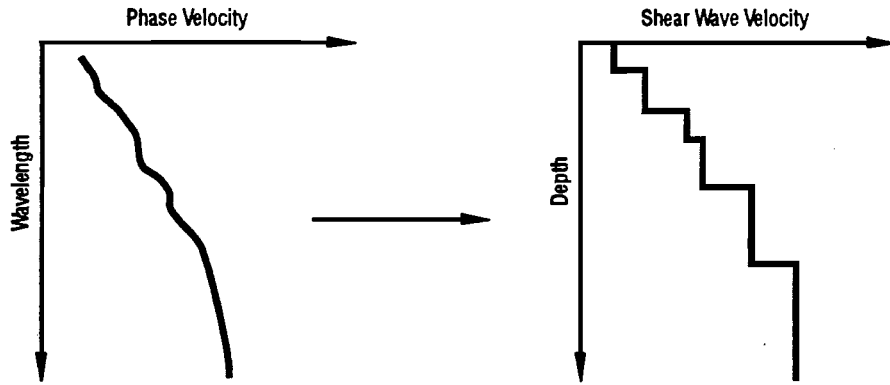


Fig 3.6. Conceptual illustration of the inversion process.

$$V_R = f \cdot \lambda_R \tag{3.1}$$

These steps are repeated for different discrete frequencies until a complete dispersion curve has been generated. Field measurements using the steady-state method are very time consuming because of the time required to perform the test for each frequency and the large number of points required to define a dispersion curve adequately.

Inversion of the measured surface wave dispersion data in the steady-state method is performed using an empirical procedure. In this procedure it is assumed that most of the surface wave energy is contained in the upper one-half to one-third wavelength (as illustrated in Fig 3.2 for a uniform half space) (Gazetas and Yegian, 1979). Therefore, it is also assumed that the phase velocity determined at a particular wavelength is representative of the material properties at a depth equal to one half (or one third) of the wavelength. In equation form:

$$z = \lambda_R/2 \tag{3.2}$$

where z denotes depth. Shear wave velocity is derived from the phase velocity using:

$$V_s \approx 1.1 \cdot V_R \tag{3.3}$$

since the shear wave velocity is about 10 percent greater than the Rayleigh wave velocity in a uniform half space. (The actual ratio of V_s/V_R depends on Poisson's ratio and varies from 1.05 to 1.14. Considering the empirical nature of the inversion process, this minor variation is often ignored and a value of 1.1 is used.) Even though pavement systems and most geotechnical profiles do not consist of uniform half spaces, this approximation is still used in this crude inversion procedure.

This empirical method of inversion appears to work reasonably well for sites at which the properties vary gradually with depth or are very uniform (Heukelom and Foster, 1960; Fry, 1963; and Ballard, 1964). However, this method can lead to significant errors at sites where

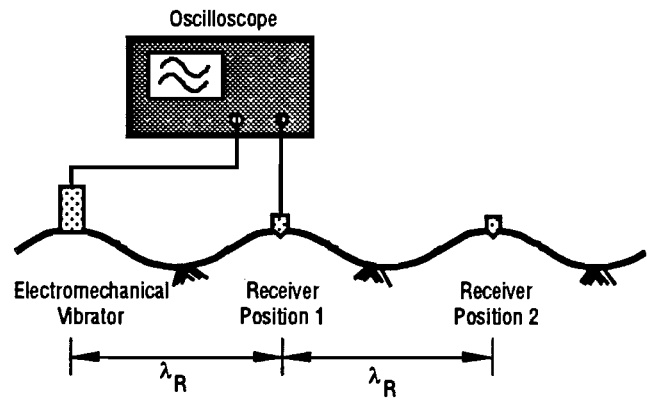


Fig 3.7. Illustration of the experimental procedure used with the steady-state Rayleigh wave method (after Richart *et al*, 1970).

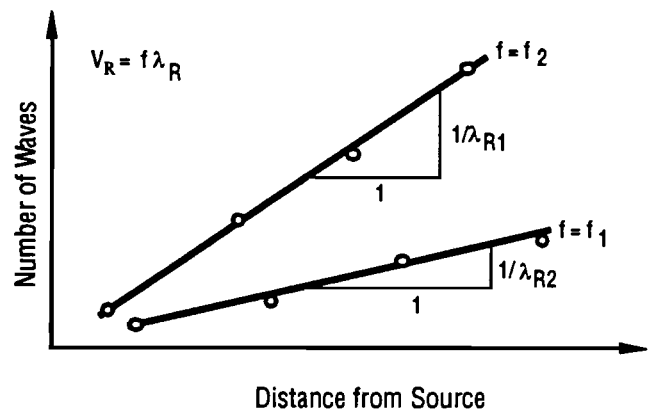


Fig 3.8. Determination of the average wavelength (after Richart *et al*, 1970).

these conditions do not exist. An example of this situation is a typical pavement profile where the contrast in stiffness between the pavement surface layer and the underlying base and subgrade materials is large. Theoretically-based inversion methods used with the SASW method overcome these limitations and allow surface wave testing to be performed at a wide variety of sites. These inversion methods are presented and discussed in Section 3.4.3.

The steady-state Rayleigh wave method was used in the late 1950's and early 1960's by researchers in the United States and England (Jones, 1958 and 1962; Heukelom and Foster, 1960; Fry, 1963 and 1965; Ballard, 1964; and Ballard and Casagrande, 1967). Unfortunately, the method never gained widespread acceptance due to the time-consuming test procedure involved and the empirically-based inversion algorithm.

3.4 SPECTRAL-ANALYSIS-OF-SURFACE-WAVES METHOD

Two factors led to the development of the SASW method in the late 1970's. The first of these factors was the availability of portable, digital electronic equipment which could be used to reduce the time required to perform field testing using the steps outlined in the following sections. The second factor was the increased availability of high-speed computers which could be used to implement theoretically-based inversion algorithms. These factors enabled the deficiencies of the steady-state Rayleigh Wave method to be overcome and have made the SASW method a viable engineering seismic method. SASW testing can be divided into three phases: (1) field testing, (2) dispersion calculations, and (3) inversion. In the following sections a detailed discussion of each of these phases of the SASW method is presented.

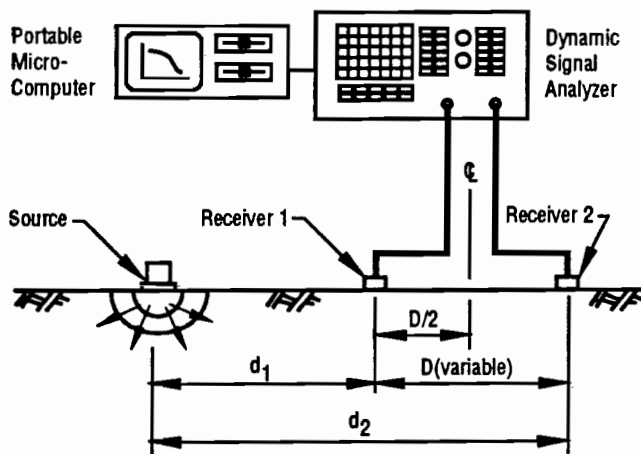


Fig 3.9. Configuration of equipment used in SASW testing.

3.4.1 FIELD TESTING

Field testing is one of two areas of surface wave testing (inversion is the other) where the greatest improvements have been made with respect to the steady-state method. These improvements have come in the form of sophisticated field instrumentation capable of performing real-time signal processing functions in the field as discussed below.

Equipment

The general configuration of source, receivers and recording equipment typically used in SASW testing is shown in Fig 3.9. A wide variety of sources has been used to generate surface wave energy over the desired frequency range. The most common types of sources used to date have been simple hammers or dropped weights which impact the ground surface and create a transient wave containing a broad range of frequencies. These sources, in addition to being reasonably portable, have worked well at numerous sites. There have been times, however, when impact-type sources have not been able to generate sufficient surface wave energy. In these cases, a source which approximates random noise excitation has worked well. A bulldozer or other piece of heavy construction equipment which simply idles in place or moves back and forth within a small area is, in fact, a good source of surface wave energy which approximates random noise. A detailed look at the variety of sources which are available for use in surface wave testing and the relative merits of each is the subject of Chapter 5.

The receivers which are used in SASW testing depend on the range of frequencies which will be used to profile the site. At most "soil" sites, where the objective is to develop a profile to depths of 50 to 200 ft (15 to 60 m), the frequencies used range from several hertz to several hundred hertz. In this case, vertical velocity transducers with a natural frequency of 1 Hz (Mark Products L-4C) have performed very well. An outstanding feature of these geophones is their large calibration constant (≈ 10 volts/in./sec or 4 volts/cm/sec) which allow small amplitudes of motion to be accurately measured. The maximum frequency at which the 1-Hz geophones may be used is about 300 Hz. Piezoelectric accelerometers (PCB Model 308B02) are typically used at sites where the objective is to determine a detailed profile only within the first few feet or meters and high frequencies (i.e. 1 kHz to 50 kHz) must be used. (This situation is the case for most pavement profiles.) In addition, accelerometers have been employed at sites where the receivers must be oriented in a position other than vertical such as on the wall of a tunnel. Velocity transducers with a natural frequency of 4.5 Hz have been found to work well when intermediate frequencies (100 Hz to 3,000 Hz) are used.

The recording equipment currently available for use in surface wave testing represents the single largest improvement over the equipment available for use in the late 1950's and early 1960's when the steady-state method was developed. Rather than using discrete frequencies to excite surface waves, impact, random noise or swept-sine sources may now be used resulting in a substantial decrease in the time needed for field testing. The use of sources such as these requires a portable field instrument which can perform frequency domain calculations (described in the next section) in real time. The instrument which has been used at The University of Texas for the past several years is a Hewlett-Packard Model 3562A Dynamic Signal Analyzer. The 3562A is a dual-channel Fast Fourier Transform (FFT) analyzer with a number of desirable features including a built-in source channel, waveform math and extensive control over input setup such as averaging and windowing.

Finally, a personal computer is connected to the dynamic signal analyzer via the GPIB (IEEE 488) interface bus to permit data to be transferred to the computer where the dispersion calculations (described in Section 3.4.2) are performed. This may either be done in the field using a portable computer or in the office using a desktop machine. Although portable computers have not been used extensively in the field to date, it is anticipated that the ability to calculate dispersion curves in the field will improve the quality of SASW test results by providing immediate feedback to the operator about the progress of the test.

Test Procedure

The general configuration of source and receivers used in SASW testing is presented in Fig 3.9. In theory, it should be possible to perform the entire test using one receiver spacing ($D = d_2 - d_1$ in Fig 3.9). However, practical considerations such as wave attenuation during propagation dictate that several different receiver spacings must be used and the results combined to evaluate each site. Receiver spacings which are typically used at soil sites range from 4 ft to 128 ft (1 m to 40 m). At pavement sites, spacings from 0.25 ft to 16 ft (0.1 to 5 m) are usually employed.

The source is usually placed such that the distance from the source to the first receiver (d_1 in Fig 3.9) is equal to the distance between receivers ($d_2 - d_1$ in Fig 3.9) resulting in a ratio of d_2/d_1 equal to two. Sánchez-Salinero *et al* (1988) analytically studied the effects of various ratios of d_2/d_1 on the measured dispersion curve and determined that $d_2/d_1 = 2$ was a good compromise between theoretical considerations, such as the reduction of near-field effects, and practical considerations, such as wave attenuation.

To begin a test, an imaginary centerline is established which will remain fixed throughout the test. The

receivers are placed equidistant from the centerline with the desired distance between the receivers for the first spacing. The source is then placed such that $d_2/d_1 = 2$ as discussed above. This arrangement is illustrated in Fig 3.10a. After obtaining data with this arrangement using procedures presented in the following paragraphs, the location of the source is reversed with respect to the receivers as shown in Fig 3.10b, and measurements are made using this arrangement. Once this has been completed, the source and receivers are moved to the next receiver spacing keeping the imaginary centerline midway between the receivers (Fig 3.10c). Finally, the

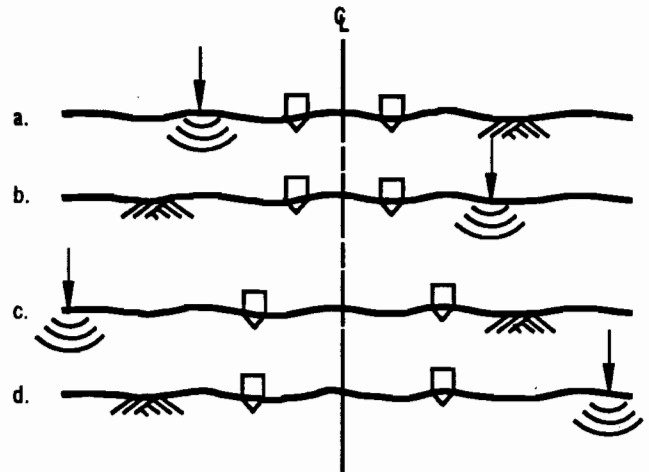


Fig 3.10. Arrangement of source and receivers illustrating the common receiver midpoint geometry.

source is once again reversed with respect to the receivers as shown in Fig 3.10d. This procedure is continued until the final receiver spacing has been completed. Generally, each new receiver spacing is twice that of the previous spacing. This arrangement of source and receivers is called the common receiver midpoint geometry (Nazarian, 1984) and has been found to work well for SASW testing. Other arrangements are, of course, possible if space limitations or other considerations prevent this geometry from being used.

For each source-receiver configuration, surface waves are generated by striking the ground with a hammer or dropped weight or by using one of the other types of sources available (see Chapter 5). An impact-type source (i.e., hammer or dropped weight) is used in the following example since it has been the most common type of source used to date. The surface waves resulting from the impact are sensed by the two receivers as they propagate away from the source, and the signals are recorded on the dynamic signal analyzer. Typical time histories, denoted $y_1(t)$ and $y_2(t)$, are shown in Fig 3.11 for receivers 1 and 2, respectively. Although at first it appears that the resolution in the time domain is poor

because the actual impulse occupies such a small fraction of the total time length, in fact, the mathematics of the FFT govern the total time length, and the resolution of the time records is more than adequate. To aid in understanding the nature of the time records, an expanded view of the records is presented in Fig 3.12. At this point, the operator may choose to accept or reject these time signals after viewing them on the display of the dynamic signal analyzer. Acceptable signals usually are very similar to those shown in Fig 3.11. These signals are characterized by an initial quiet period followed by the arrival of the impulse after which the ground surface

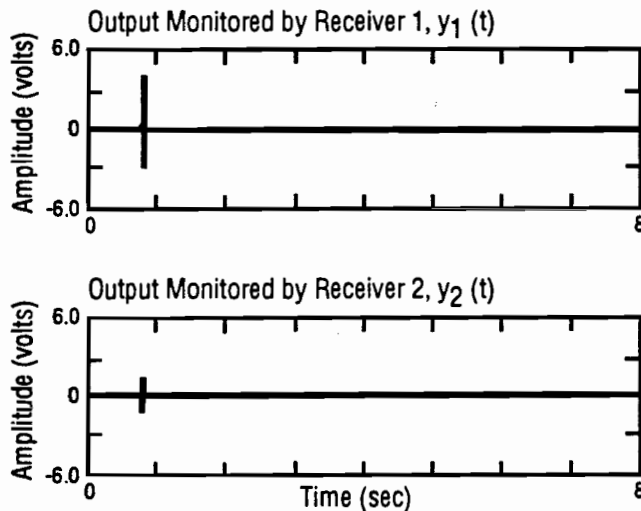


Fig 3.11. Typical time histories resulting from an impact-type source; source is a 500-lb (2.2-kN) weight dropped 6 ft (2 m) and receivers are 1-Hz geophones placed 26 ft (8 m) apart.

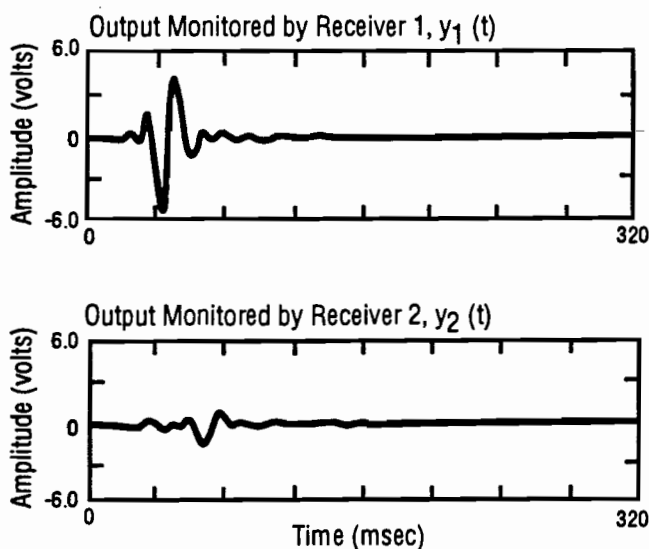


Fig 3.12. Expanded view of time histories from an impact-type source.

returns to its at rest position. Possible reasons for rejecting signals include the presence of extraneous noise, a "double hit," etc.

Once the operator has instructed the dynamic signal analyzer to accept the signals, the analyzer performs an FFT on both signals. The results are the linear spectra, $Y_1(f)$ and $Y_2(f)$, of $y_1(t)$ and $y_2(t)$, respectively. $Y_1(f)$ and $Y_2(f)$ are complex functions of frequency. The linear spectra are, in turn, used to calculate the cross power spectrum, coherence function and the auto power spectra of each receiver using the following relationships:

$$G_{y_1y_2} = Y_1(f)^* \cdot Y_2(f), \quad (3.4)$$

$$G_{y_1y_1} = Y_1(f)^* \cdot Y_1(f), \quad (3.5)$$

$$G_{y_2y_2} = Y_2(f)^* \cdot Y_2(f), \text{ and} \quad (3.6)$$

$$\gamma_{y_1y_2}^2 = |G_{y_1y_2}|^2 / (G_{y_1y_1} \cdot G_{y_2y_2}) \quad (3.7)$$

where

$G_{y_1y_2}$ = cross power spectrum between Receivers 1 and 2,

$G_{y_1y_1}$ = auto power spectrum of Receiver 1,

$G_{y_2y_2}$ = auto power spectrum of Receiver 2,

$\gamma_{y_1y_2}^2$ = coherence function between Receivers 1 and 2,

* denotes the complex conjugate, and

|| denotes the magnitude of a complex number.

It must be emphasized that all of these calculations are performed by the dynamic signal analyzer in real time and the results are immediately displayed on the screen of the analyzer. The ability to perform these calculations in the field is an essential part of SASW testing which permits the operator to monitor the progress of the test and thereby adjust any of the test parameters (type of source, receiver spacing, frequency range, etc.) to obtain the best possible results.

The impact is repeated and the results of the above calculations are averaged together with the results of previous impacts until a sufficient number of averages (usually five or more) have been obtained for each source-receivers configuration. Averaging is performed using the linear spectra of the signals rather than the time signals themselves because this eliminates the need for a synchronous trigger. Averaging in the frequency domain provides a statistical estimate of the spectra (i.e., each successive average reduces the variance of the calculated quantity) but does not improve the signal-to-noise ratio of the signals (Hewlett-Packard, 1982). Typical results are shown in Fig 3.13 which were obtained using a 52-ft (16-m) receiver spacing and five averages. The quantity displayed in Fig 3.13a is the phase of the cross power spectrum, denoted $\Theta_{y_1y_2}$, which is calculated:

$$\Theta_{y1y2} = \tan^{-1}(\text{Im}(G_{y1y2})/\text{Re}(G_{y1y2})) \quad (3.8)$$

where

$\text{Im}()$ denotes the imaginary part of a complex number, and

$\text{Re}()$ denotes the real part of a complex number.

The phase of the cross power spectrum (instead of the magnitude) is used to calculate the phase velocity as discussed in the next section and is, therefore, of more interest than the magnitude.

This process (which takes only several minutes to perform) is repeated for each source-receivers combination (see Fig 3.10). The cross power spectrum, coherence function and auto power spectra can be considered the "raw" data in SASW testing.

One of the advantages of the SASW method with respect to the steady-state method should now be apparent. With only several impacts from a hammer or dropped weight, it is possible to generate information over a broad range of frequencies rather than using discrete frequencies as in the steady-state method. This, in turn, makes it possible to determine more accurate wave velocity profiles.

3.4.2 DISPERSION CALCULATIONS

The next step in performing a surface wave test is to calculate the experimental dispersion curve using the data obtained from the various receiver spacings. For this purpose, the phase of the cross power spectrum is the most important of the records shown in Fig 3.13. The coherence function and the auto power spectra are used to help the operator decide what portions of the phase record may be contaminated by noise or spurious reflections or may be of poor quality because of low signal strength over part of the record. In a noise-free, linear system, the coherence function between receivers will be equal to one. If the coherence function is less than one, there are two possible explanations: (1) there is noise present in the measurement and/or (2) there are nonlinearities in the system (i.e., material profile) relating the two receivers (Bendat and Piersol, 1980). A study of the relationship between phase and coherence for a propagation model containing noise is presented in Appendix A. The auto power spectra can be used to determine what portion of the measured frequency range contained significant surface wave energy. Frequency ranges in which the auto power spectra contains relatively little energy might possibly coincide with ranges that are contaminated with noise because of low signal amplitudes.

The phase of the cross power spectrum shown in Fig 3.13a is reproduced in Fig 3.14. Frequencies less than 1.6 Hz have been removed from consideration (indicated by the cross hatching) because of the poor coherence (see Fig 3.13b). In this case the poor coherence probably results from noise in the measurement caused by low signal

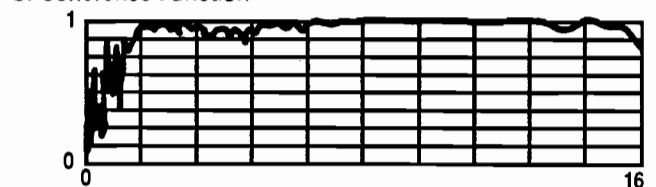
strength in that frequency range (see Fig 3.13c and d). The remainder of the record is used to calculate the experimental dispersion curve for this receiver spacing. (Additional editing to remove possible near-field effects is discussed later in this section.)

Before describing how the surface wave phase velocity is calculated, it is important to note the form in which the phase in Fig 3.14 has been plotted. The phase has been plotted from -180° to 180° and is called *wrapped*

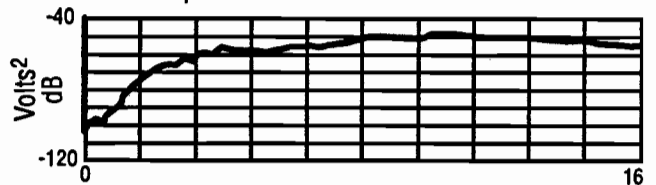
a. Phase of the Cross Power Spectrum



b. Coherence Function



c. Auto Power Spectrum of Receiver 1



d. Auto Power Spectrum of Receiver 2

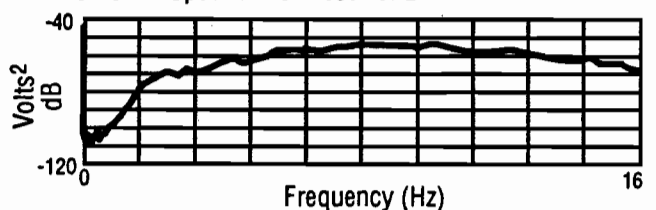


Fig 3.13. Typical spectral functions obtained during SASW testing (receiver spacing = 52 ft (16 m)).

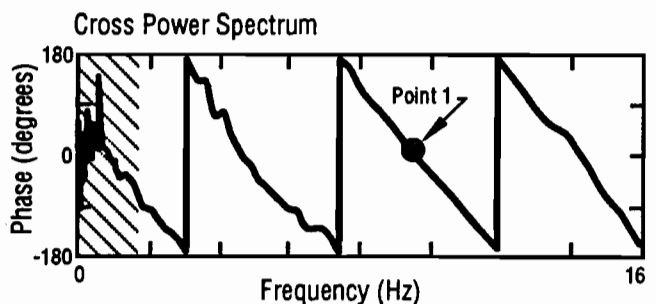


Fig 3.14. Editing the phase of the cross power spectrum shown in Fig 3.13a.

phase. To *unwrap* the phase, each segment is placed end-to-end as shown schematically in Fig 3.15. It is the unwrapped phase which is used to calculate the phase velocity.

The time delay between receivers as a function of frequency, $t(f)$, is calculated using:

$$t(f) = \Theta_{y_1 y_2}(f) / (360^\circ \cdot f) \quad (3.9)$$

where $\Theta_{y_1 y_2}(f)$ is expressed in degrees. The surface wave phase velocity as a function of frequency is then determined using:

$$V_R(f) = (d_2 - d_1) / t(f) . \quad (3.10)$$

The final step in calculating the surface wave dispersion curve is to determine the corresponding wavelength using:

$$\lambda_R = V_R / f . \quad (3.11)$$

Consider as an example the point designated as "Point 1" in Fig 3.14. Point 1 is at 9.6 Hz and has a phase equal to 720° ($180^\circ + 360^\circ + 180^\circ$). By using Eq 3.9, the time delay between receivers at this frequency is

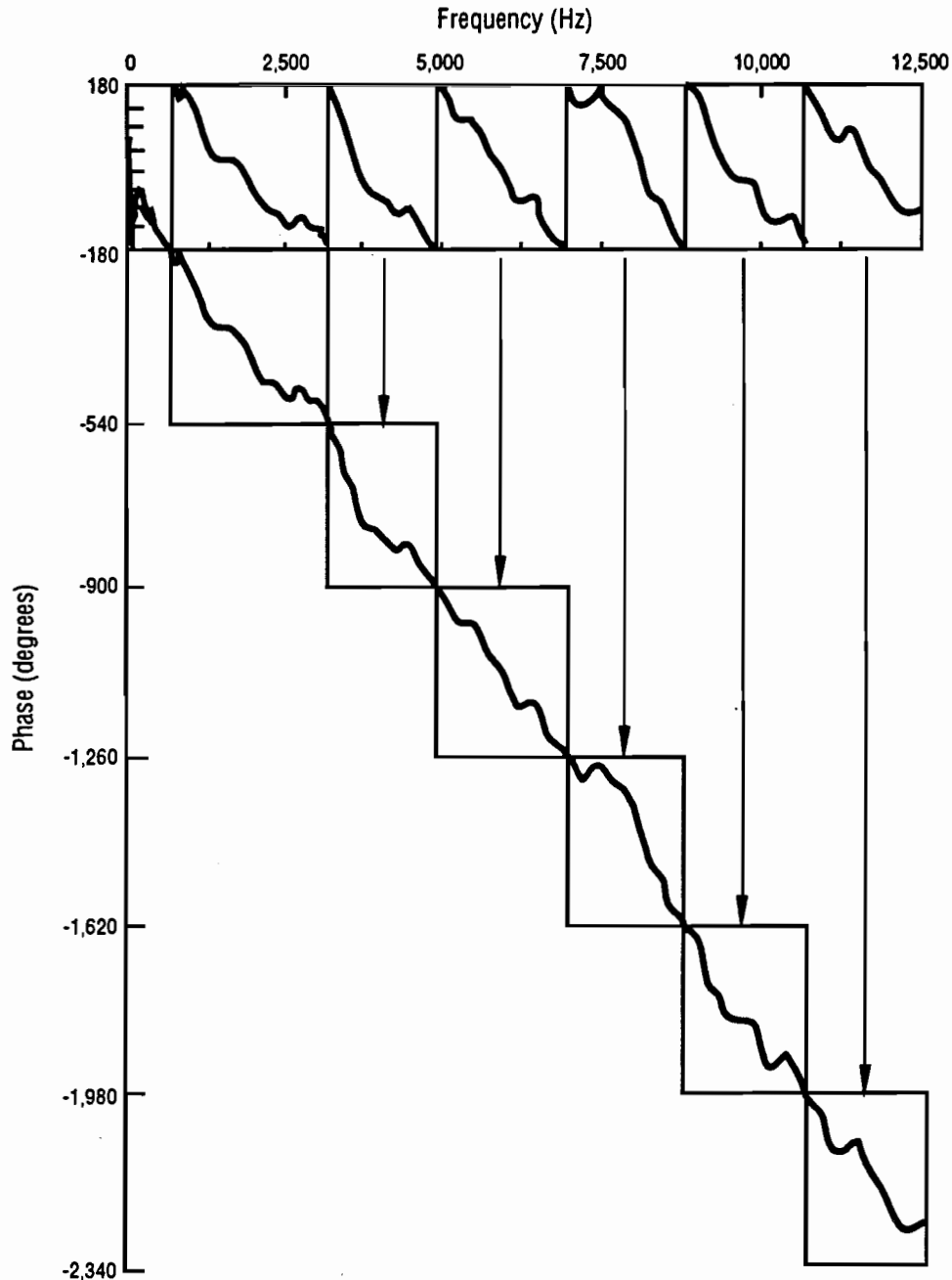


Fig 3.15. Illustration of the unwrapping process applied to the phase of the cross power spectrum (from Sheu, 1987).

208.3 msec. The distance between receivers is 52 ft (16 m) which results in a phase velocity (Eq. 3.10) of 250 ft/sec (77 m/sec). Finally, the corresponding wavelength from Eq. 3.11 is 26 ft (8 m). This series of calculations is repeated for each frequency in the phase record (except for those frequencies which have been removed from consideration by the operator because of noise, etc). These calculations are performed using an interactive program on the microcomputer once the data has been transferred to the computer.

Wavelengths longer than three times the distance from the source to the first receiver ($l_R > 3d_1$) are removed from the experimental dispersion curve to eliminate any significant near-field effects (Sánchez-Salineró, 1987). Although Sánchez-Salineró recommended that wavelengths greater than d_1 be discarded based upon an analytical study, practical experience indicates that the additional information gained by considering wavelengths between one and three times d_1 outweighs any loss of accuracy in this range of wavelengths.

The experimental dispersion curve corresponding to the phase of the cross power spectrum shown in Figs 3.13 and 3.14 is presented in Fig 3.16. The example dispersion point (Point 1) calculated previously is highlighted in Fig 3.16. There are approximately 700 points contained in the dispersion curve shown in Fig 3.16 ranging in frequency from 2.2 Hz to 16 Hz. It should be emphasized that all 700 points were collected simultaneously using only five impacts of a dropped weight.

Finally, the individual dispersion curves from each source-receivers configuration are combined to form the composite dispersion curve for the site. The composite dispersion curve for the site used in the example is presented in Fig 3.17 with the individual dispersion curve from the 52-ft (16-m) receiver spacing highlighted. The composite dispersion curve is repeated in Fig 3.18 with the contribution of each of the receiver spacings highlighted. A tabulated version of the dispersion curve is included in Appendix B for those who may wish to perform their own analyses on the dispersion data. When several receiver spacings are combined together, the total number of points in the composite dispersion curve can quickly approach an unmanageable number. Therefore, several hundred points are chosen to be statistically representative of the entire curve and these points are used in the inversion step. The user chooses the desired number of points to be contained in the reduced dispersion curve. A simple algorithm is used to choose the desired number of points such that the points are approximately evenly distributed between the minimum and the maximum wavelengths contained in the original dispersion curve. All of the points within one wavelength increment are averaged together to calculate one point which is representative of that increment. Other methods of selecting a reduced number of points are, of course, possible.

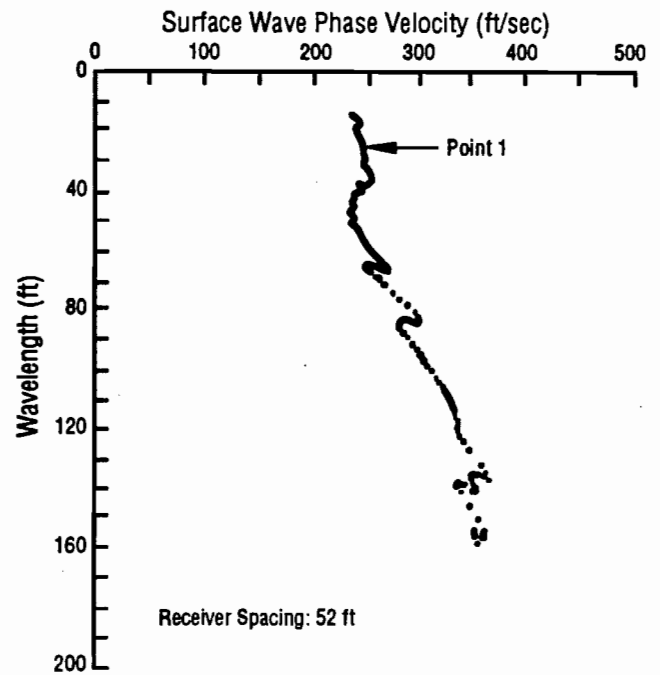


Fig 3.16. Experimental dispersion curve resulting from the phase of the cross power spectrum shown in Fig 3.14.

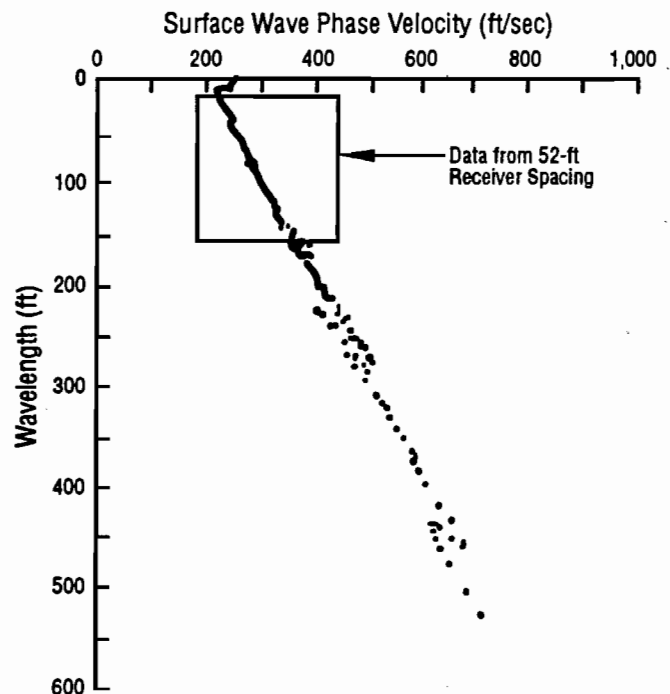


Fig 3.17. Composite dispersion curve.

Figures 3.17 and 3.18 and Appendix B contain the reduced number of points. For the dispersion curve used as an example in this section, the number of points was reduced from 7,796 in the original dispersion curve (from 16 receiver spacings) to 371 in the reduced version. Phase velocity values were averaged over wavelength increments which ranged from 0.3 ft (0.09 m) at short wavelengths to approximately 20 ft (6.1 m) at the longest wavelengths.

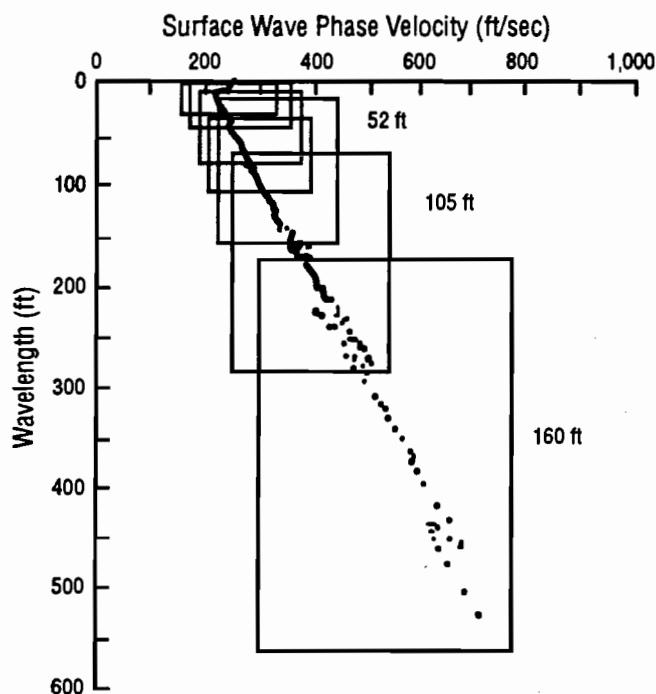


Fig 3.18. Composite dispersion curve with the contribution of each individual receiver spacing highlighted.

$v_{s,1}$	v_1	ρ_1	h_1
$v_{s,2}$	v_2	ρ_2	h_2
	\vdots		\vdots
$v_{s,n-2}$	v_{n-2}	ρ_{n-2}	h_{n-2}
$v_{s,n-1}$	v_{n-1}	ρ_{n-1}	h_{n-1}
$v_{s,n}$	v_n	ρ_n	

Fig 3.19. Site model used in inversion (after Nazarian, 1984).

3.4.3 INVERSION

Inversion is the other aspect of surface wave testing where significant improvements have been made in the SASW method relative to the steady-state Rayleigh wave method. Inversion was introduced earlier as the process of determining the shear wave velocity profile from the experimental dispersion curve obtained in the field. Unlike the empirical procedure used with the steady-state method, modern inversion methods rely upon theoretical solutions of surface wave propagation in a layered half space. The procedure currently used (Nazarian, 1984) is an iterative procedure in which the operator matches a theoretically-calculated dispersion curve to the experimental dispersion curve.

In the current procedure, the site is modelled as a stack of homogeneous layers overlying a half space as shown in Fig 3.19. The user begins by assigning initial values to the thickness, shear wave velocity, Poisson's ratio and mass density of each layer including the half space. (The half space is, of course, not assigned a thickness.) A modified Haskell-Thomson matrix solution (Thomson, 1959; Haskell, 1953; and Nazarian, 1984) is used to generate a theoretical dispersion curve for the assumed material profile. Once the theoretical curve has been calculated, it is graphically compared to the experimental curve.

To illustrate this process, consider the composite dispersion curve shown in Fig 3.17. The layering, initial shear wave velocity, initial Poisson's ratio and initial mass density profiles which have been chosen are shown in Fig 3.20. Using these initial values, a theoretical dispersion curve is calculated and compared with the experimental curve. An example of a comparison of this type is presented in Fig 3.21. At this point, the shear wave velocities and/or thicknesses of selected layers are adjusted in an attempt to obtain better agreement between the theoretical and experimental curves. Values of Poisson's ratio and mass density are rarely changed from their initial values since the influence of these parameters on the calculated dispersion curve is of secondary importance for reasonable initial estimates (Ewing *et al*, 1957). (In instances where saturated soils are present, the Poisson's ratio of saturated layers may be adjusted to maintain a compression wave velocity of 5,000 ft/sec (1,500 m/sec).) An example of the comparison between curves for the second iteration is presented in Fig 3.22. Iterations continue until satisfactory agreement is obtained between the two curves such as that shown in Fig 3.23. Once satisfactory agreement between the theoretical and experimental curves is obtained, it is assumed that the shear wave velocities and thicknesses of the layers in the model accurately represent the actual velocities and layering of the site. A flow chart summarizing the steps involved in the inversion process is presented in Fig 3.24.

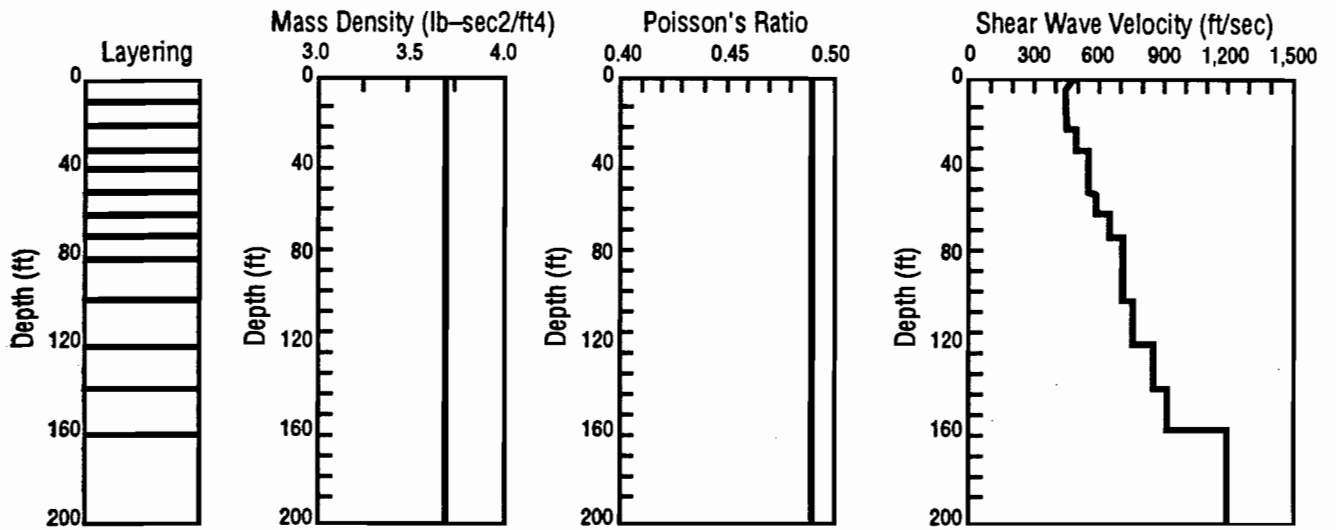


Fig 3.20. Initial layering and material parameter profiles used to invert the dispersion curve shown in Fig 3.17.

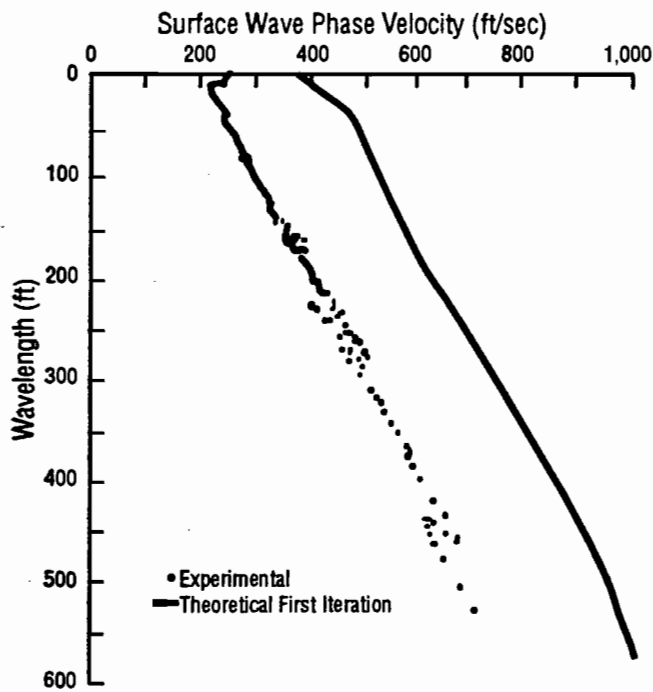


Fig 3.21. Comparison of theoretical and experimental dispersion curves: first iteration.

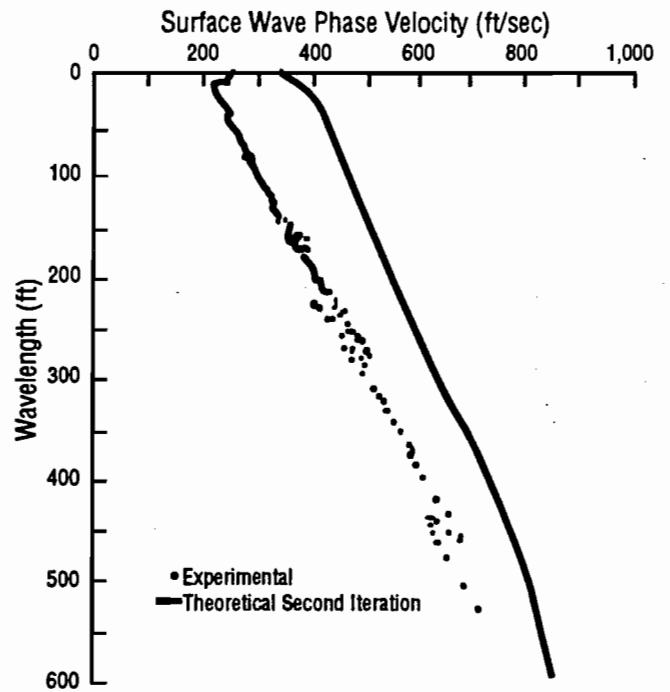


Fig 3.22. Comparison of theoretical and experimental dispersion curves: second iteration.

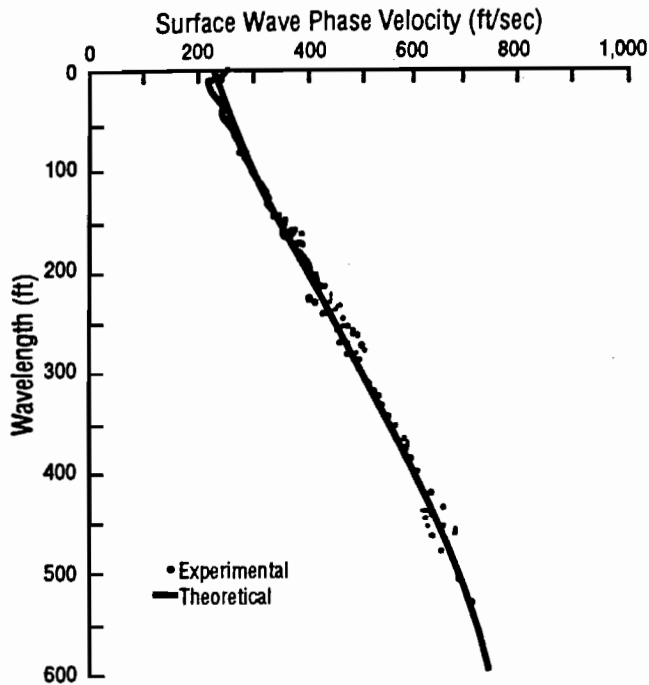


Fig 3.23. Comparison of theoretical and experimental dispersion curves: final iteration.

The final material parameter profiles (the most important of which is the shear wave velocity profile) which result from this procedure are presented in Fig 3.25. The use of theoretically-based inversion algorithms such as this one has significantly increased the accuracy of shear wave velocity profiles determined using surface waves and has expanded the number of sites where the SASW method can be successfully applied.

3.5 SUMMARY

The dispersive nature of surface wave propagation in a layered half space forms the basis for the Spectral-Analysis-of-Surface-Waves (SASW) method. Dispersion arises because the phase velocity of surface waves is affected by different layers in the material profile, depending on the wavelength of the surface wave with respect to the layering. For example, short-wavelength surface waves propagate only in the near-surface layers and, thus, are influenced the most by these layers. Waves with longer wavelengths propagate through deeper layers as well as the near-surface layers. Phase velocities of these waves are, therefore, influenced to a large extent by the deeper layers. The goal of SASW testing is to generate and measure surface wave dispersion and then to estimate (invert for) the shear wave velocities and thicknesses of the layers in the profile.

The steady-state Rayleigh wave method, the predecessor of the SASW method, was used with some success in the late 1950's and early 1960's. However, testing was

time consuming because measurements could only be made at discrete frequencies. Furthermore, empirical inversion procedures in use at the time severely limited the types of sites at which the method could be properly used.

Modern field instrumentation and computers have made it possible to overcome these two limitations and have resulted in the evolution of the SASW method to the point where it is competitive with other in situ seismic methods. Portable Fast Fourier Transform (FFT) analyzers have enabled the use of sources other than vibrators operating at discrete frequencies. It is now possible to gather information at hundreds (or thousands) of frequencies simultaneously in a fraction of the time it took to measure one frequency using the steady-state method. Another critical improvement incorporated into the SASW method is the use of theoretically-based inversion algorithms which make it possible to determine more accurate shear wave velocity profiles than was possible with empirically-based algorithms.

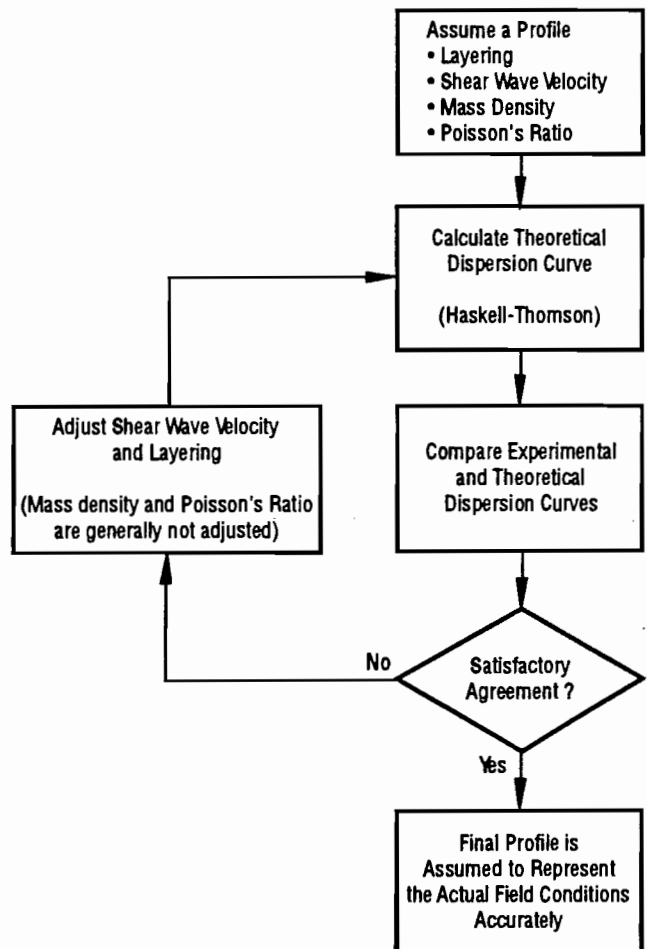


Fig 3.24. Flow chart summarizing the inversion procedure.

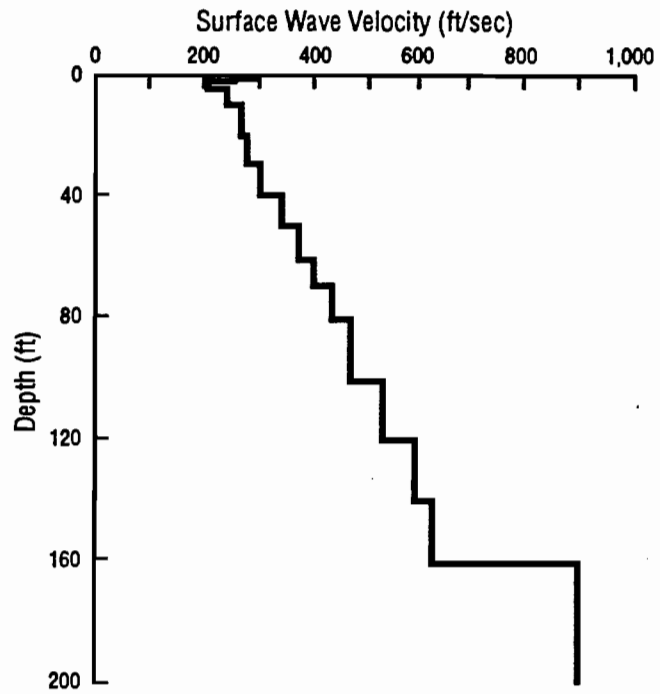


Fig 3.25. Final layering and material parameter profiles resulting from inversion.

CHAPTER 4. HORNSBY BEND TEST SITE

4.1 INTRODUCTION

The Hornsby Bend test site was selected as the site at which to perform much of the experimental work required for this report because of the extensive series of in situ tests which have been performed at the site in the past and because of the proximity of the site to The University of Texas. The site is located on land owned by the City of Austin situated in the southeast portion of the city. In September of 1985, Southwestern Laboratories, Inc., performed a routine geotechnical investigation of the site for a proposed waste-to-energy plant which was to be constructed at the site (Southwestern Laboratories, 1985). In conjunction with the investigation for the proposed plant, a series of crosshole tests was performed at the site in September of 1985 by personnel from The University of Texas. In September of 1986, a graduate soil dynamics class from the University performed a second crosshole test series using the same cased boreholes which had been used previously. During 1986 and 1987, Mok (1987) also conducted extensive studies using the crosshole and downhole seismic methods at the site.

This chapter summarizes these previous studies. Results of the routine geotechnical investigation and previous in situ seismic tests are presented in the following sections. A description of the concrete test slab constructed at the site and used to perform surface wave tests is also included.

4.2 BORING LOGS AND BASIC SOIL DATA

A plan view of the Hornsby Bend test site is presented in Fig 4.1 showing the locations of the numerous boreholes used in the investigation for the waste-to-energy plant. The boreholes used for the crosshole tests performed in 1985 and 1986 were located near Boring B3-03 in the central portion of the proposed plant. (Boring B3-03 is indicated with an arrow in Fig 4.1.) These borings were drilled with a hollow-stem auger and continuous sampling system. A log of Boring B3-03 is shown in Fig 4.2. There are four layers which may be distinguished from the boring: (1) a hard silty clay layer extending from the surface to 13.5 ft (4.1 m);

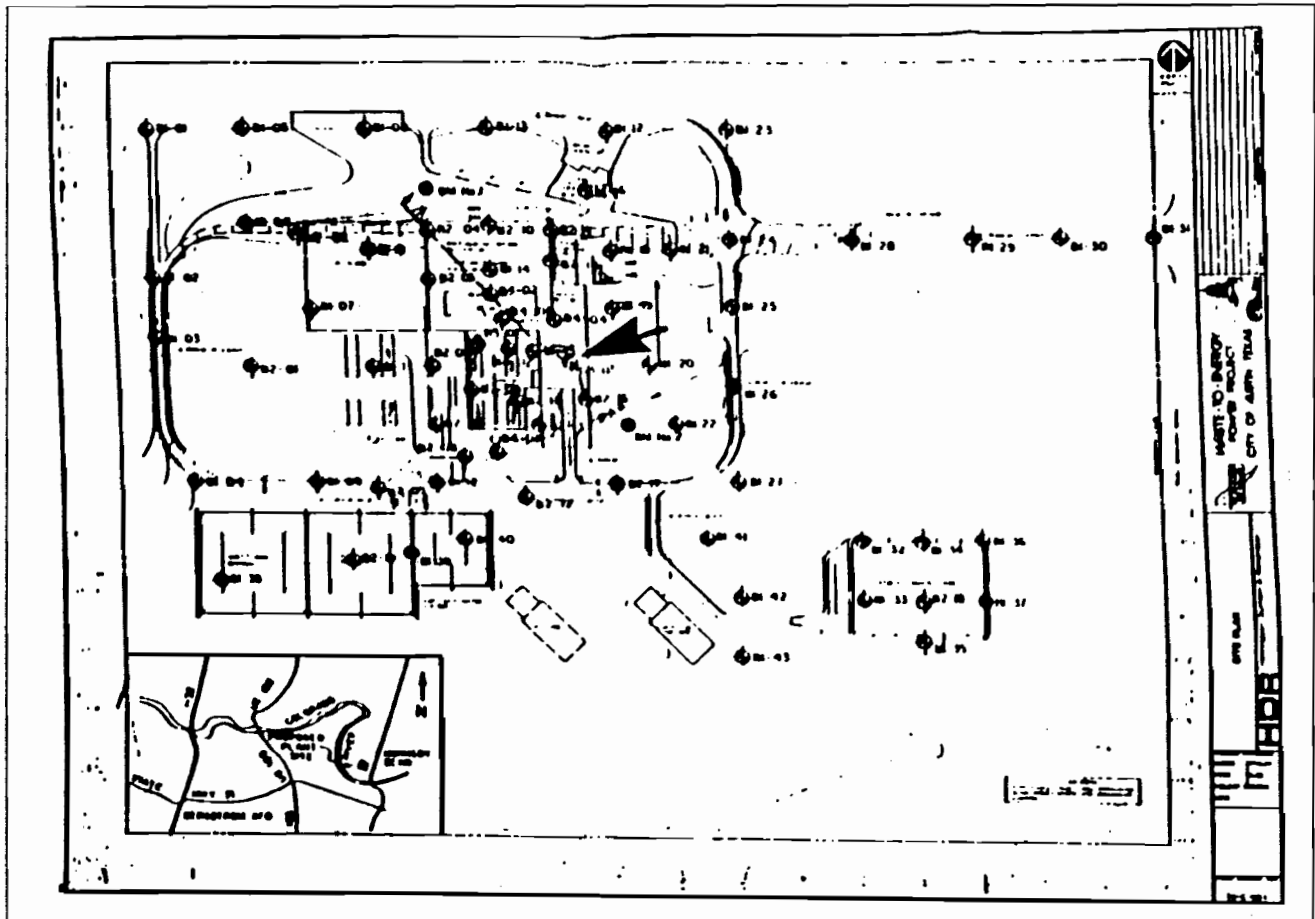


Fig 4.1. Plan view of Hornsby Bend test site (from Southwestern Laboratories).

(2) a hard silty clay layer interbedded with silty fine sand seams from 13.5 to 33.5 ft (4.1 to 10.2 m); (3) a loose to medium dense silty fine sand layer from 33.5 to 45 ft (10.2 to 13.7 m); and (4) a hard gray clay layer extending from 45 ft (13.7 m) to the maximum depth of the boring, 50 ft (15.2 m). The clay layers are part of the Taylor Marl formation. Undrained shear strengths in the upper 20 ft (6.1 m) estimated using a pocket penetrometer are greater than 3.0 kips/ft² (144 kPa). Blow counts from the

standard penetration test vary from 2 to 9 in the range of depths from 23 to 45 ft (7.0 to 13.7 m). These blow counts have not been corrected for overburden pressure.

A cross-sectional view of the test site in the vicinity of the boreholes used for previous crosshole studies and the area used for surface wave studies in this report is shown in Fig 4.3. The same four basic strata which were identified in Boring B3-03 appear to relatively uniform across this portion of the site. However, blow counts

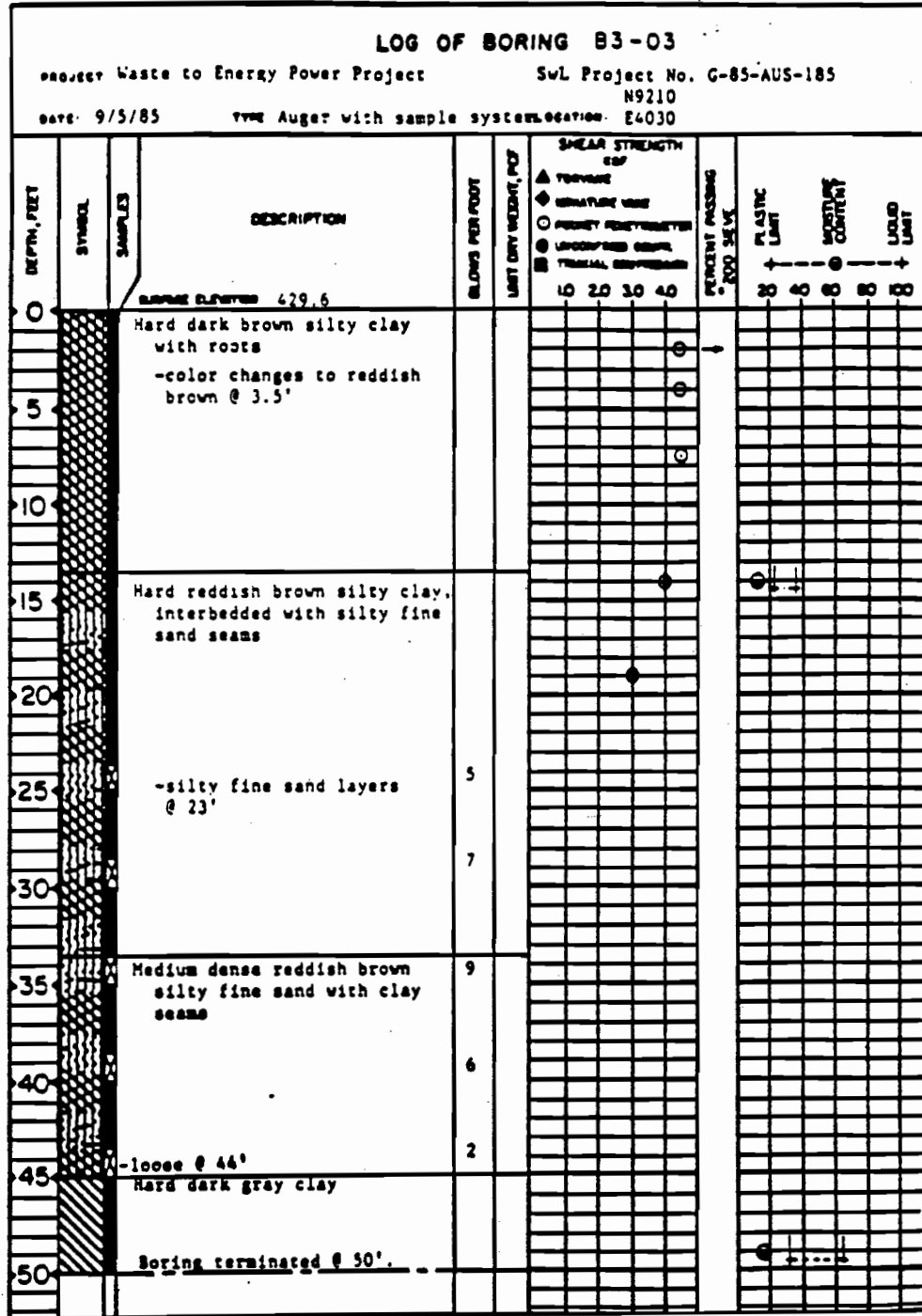


Fig 4.2. Log Boring B3-03 (from Southwestern Laboratories, 1985).

measured in the silty fine sand layer are significantly higher in Boring B4-02, which is located adjacent to Boring B3-03. (Boring B4-02 is located 60 ft (18.3 m) from Boring B3-03.) The groundwater levels encountered immediately after drilling and after 24 hours are also indicated in Fig 4.3. Fortunately, the horizontal stratigraphy at the test site closely approximates the model used for most seismic tests (including the SASW method).

4.3 RESULTS OF PREVIOUS SEISMIC MEASUREMENTS

As mentioned in Section 4.1, the Hornsby Bend test site has been the location of several previous studies using in situ seismic tests. All of these studies have involved the crosshole seismic method to determine the variation of shear wave and compression wave velocity with depth. The values of shear wave velocity and compression wave velocity which were measured during the investigations conducted in September 1985 and September 1986 are presented in Figs 4.4 and 4.5, respectively. Also included in these figures are values of shear and compression wave velocity which were measured at selected depths in May 1988 (Kang *et al*, 1988). With the exception of the relatively large variation in wave velocities measured at about 6 ft (1.8 m), the differences in the

wave velocity values measured over an extended period of time are small. The low value of shear wave velocity observed at the surface (300 ft/sec (91.4 m/sec)) is largely due to a period of wet weather which preceded the crosshole measurements in October 1986. A similar period of wet weather preceded the tests performed for this report. Therefore, this low value of shear wave velocity near the surface is not believed to differ substantially from the velocity which existed during the time the surface wave measurements described in this report were performed.

Since the results of these crosshole tests are used in Chapter 6 to calculate theoretical displacements versus depth at the site, interpreted wave velocity profiles were developed for use in those analyses. The interpreted shear and compression wave profiles are superimposed on the measured values in Figs 4.6 and 4.7, respectively, and are presented in Table 4.1.

4.4 CONCRETE TEST SLAB

A concrete test slab was cast on the silty clay subgrade at the Hornsby Bend site. The test slab was used to perform surface wave tests to examine the influence of the relative stiffness of adjacent layers in the profile and to investigate the effects of different receiver

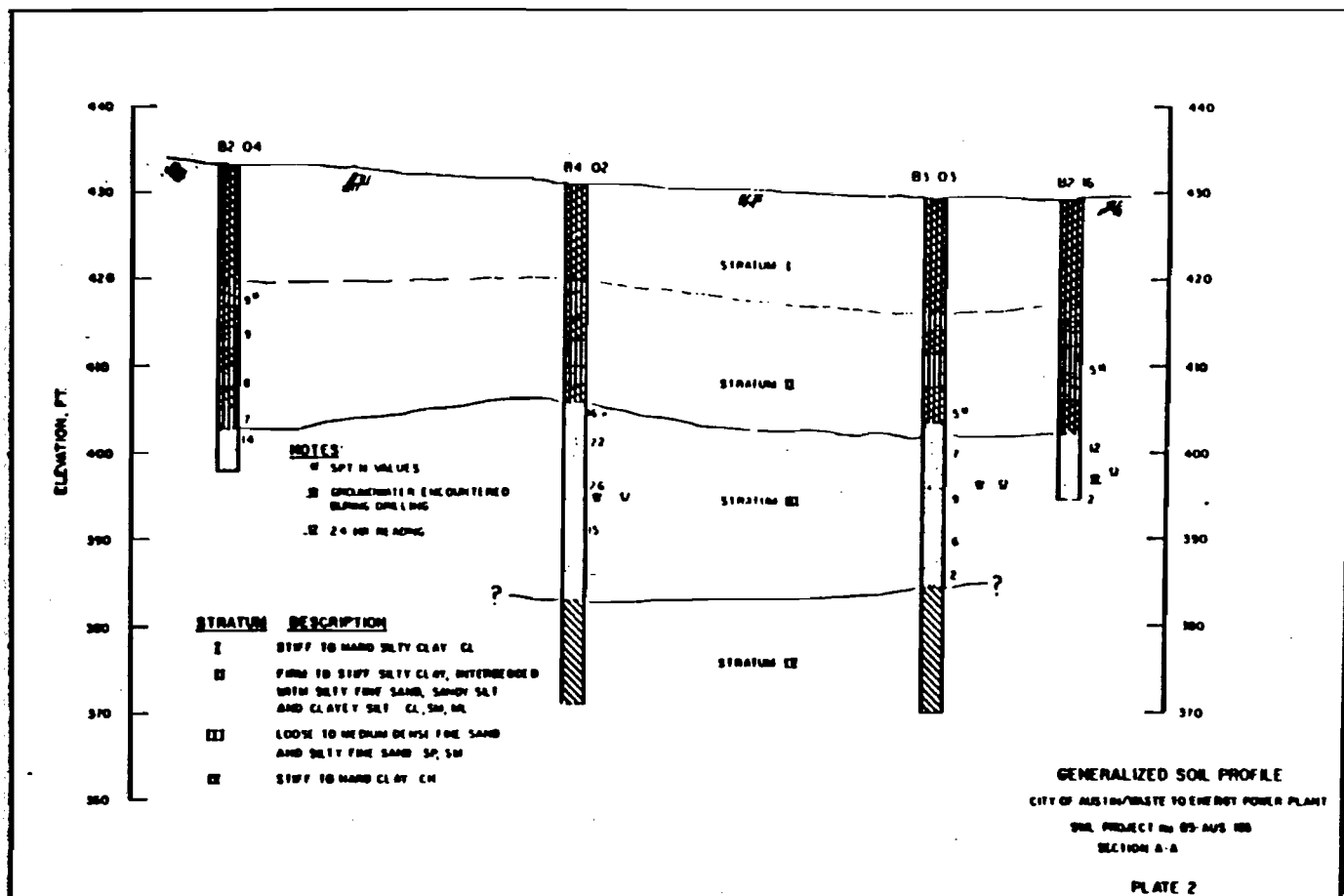


Fig 4.3, Cross-sectional view of Hornsby Bend test site (from Southwestern Laboratories, 1985).

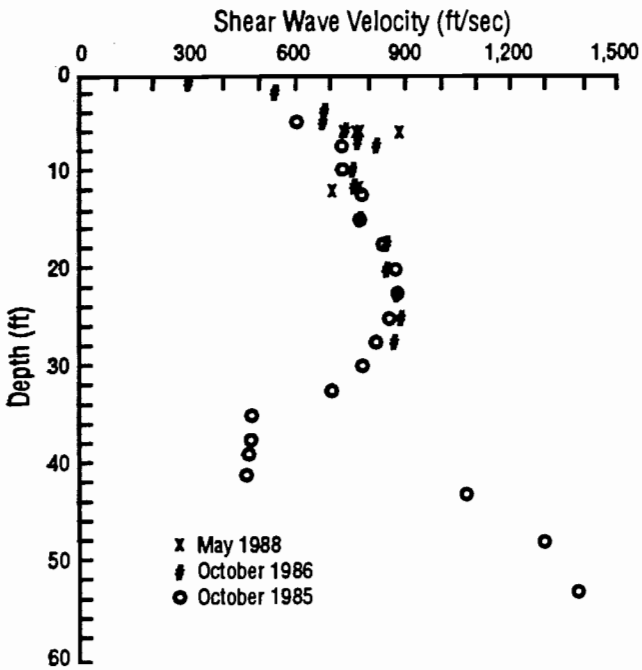


Fig 4.4. Shear wave velocities measured at the Hornsby Bend test site using the crosshole seismic method.

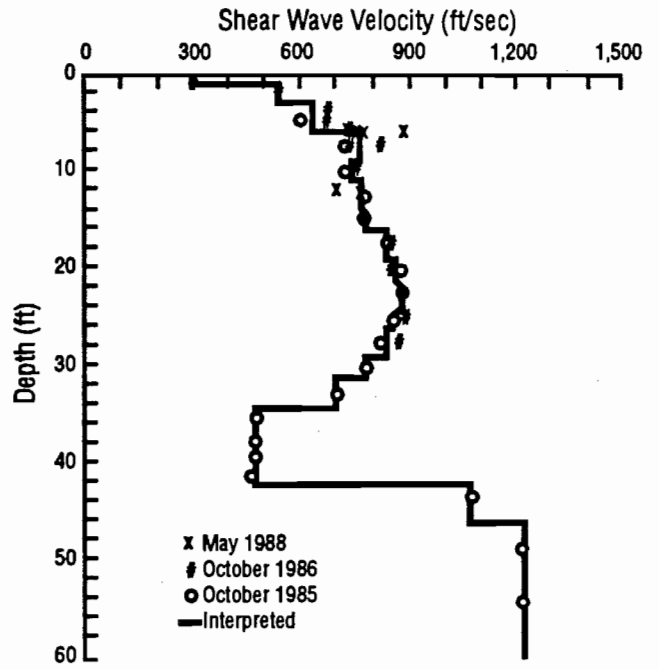


Fig 4.6. Interpreted shear wave velocity profile at the Hornsby Bend test site.

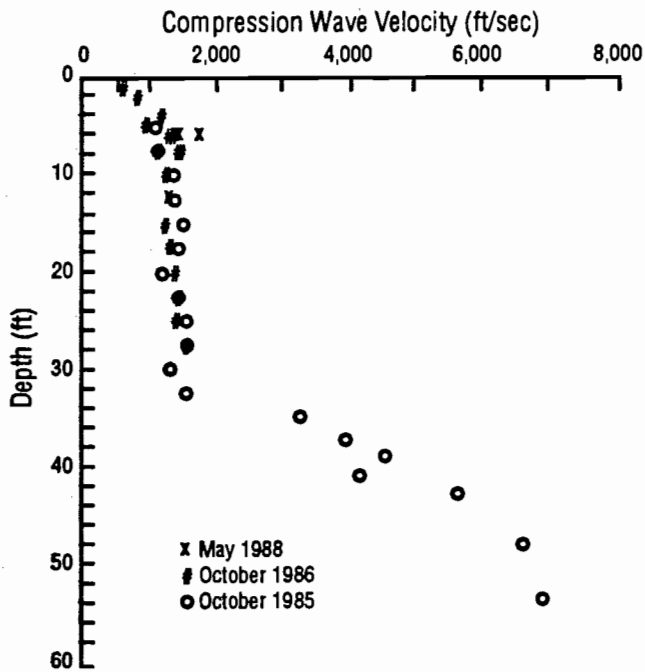


Fig 4.5. Compression wave velocities measured at the Hornsby Bend test site using the crosshole seismic method.

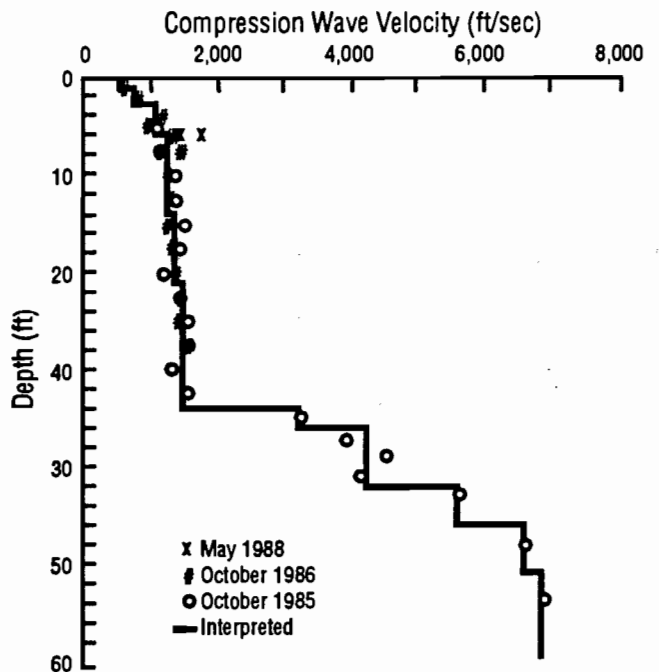


Fig 4.7. Interpreted compression wave velocity profile at the Hornsby Bend test site.

spacings on surface wave dispersion measurements. The results of these tests are discussed in Chapter 7. In this section, a brief description of the design and construction of the slab is presented.

The dimensions of the slab were selected to be 8 by 12 ft (2.4 by 3.7 m) with a nominal depth of 10 in. (25.4 cm). It is believed that this size slab adequately modeled a full-size, unreinforced (or simply reinforced) pavement slab (usually 12 by 20 ft (3.7 by 6.1 m)). No reinforcement was used in the test slab to eliminate potential sources of wave reflections within the concrete. Prior to casting the slab, all vegetation was stripped from the site in order to improve the quality of the contact between the soil and the concrete slab.

Class S concrete with Type I cement was used for the slab. The mix was specified to be 6 sacks/yard³ and 5 gallons/sack with a design 28-day compressive strength of 3600 psi (24.8 MPa). The maximum size of the aggregate was 0.75 in. (1.91 cm). A retarder was also added to the concrete to increase the time available to place and finish the concrete and to install the instrumentation in the slab. (The instrumentation is described in Chapter 7.) Capitol Aggregates, the supplier of the concrete, designates this mix as Design No. 147.

Because of a misunderstanding about the location to which the concrete was to be delivered, the concrete did not arrive on site until 75 minutes after water had been added to the cement-aggregate mixture. The slump of the concrete was immediately checked and was found to be 1.5 in. (3.8 cm). The concrete was then placed, vibrated, screeded, and floated. These operations required approximately one hour. No additional finishing was performed. Twenty-five 6-by-12-in. (15.2-by-30.5-cm) cylinders were cast to perform compressive strength and Young's

modulus tests at 1, 3, 7, and 28 days. Additional 3-by-6-in. (7.6-by-15.2-cm) cylinders were cast for resonant column test specimens. Finally, two samples were cast to be used to determine the initial and final set of the concrete using penetration resistance. The results of these tests are presented and discussed in Chapter 7.

4.5 SUMMARY

The Hornsby Bend test site was selected as the site for much of the experimental work performed as part of this report because of the large number of previous seismic tests conducted at the site as well as the availability of boring logs and other standard geotechnical test results.

Logs of borings made in the vicinity of the test area indicate that there are four distinguishable layers: two hard silty clay layers, a loose to medium dense silty fine sand layer, and a hard gray clay layer which extends to the maximum depth explored. The clay layers belong to the Taylor Marl formations. The stratigraphy in adjacent boreholes is very similar and indicates that no major lateral inhomogeneities are present in the vicinity of the test area (to the extent that boreholes can reveal lateral variability).

The results of crosshole seismic tests performed at the test site within the past several years have been used to develop interpreted shear and compression wave velocity profiles for the site which will be used in analyses in subsequent chapters.

An 8-by-12-ft (2.4-by-3.7-m) unreinforced concrete test slab was cast in place on the silty clay subgrade at the Hornsby Bend test site to be used in the series of surface wave tests described in Chapter 7. The nominal thickness of the test slab was 10 in. (25.4 cm).

TABLE 4.1 INTERPRETED VALUES OF SHEAR AND COMPRESSION WAVE VELOCITY FOR THE HORNSBY BEND TEST SITE

Layer Number	Layer Thickness (ft)	Shear Wave Velocity (ft/sec)	Compression Wave Velocity (ft/sec)	Mass Density (lb-sec ² /ft ⁴)	Poisson's Ratio
1	1.0	300	573	3.4	0.31
2	2.0	553	806	3.4	0.06
3	3.0	645	1,103	3.4	0.24
4	3.0	780	1,294	3.4	0.21
5	2.0	756	1,294	3.4	0.24
6	3.0	772	1,294	3.4	0.22
7	2.0	792	1,401	3.4	0.27
8	3.0	851	1,401	3.4	0.21
9	2.0	875	1,401	3.4	0.18
10	3.0	883	1,507	3.4	0.24
11	2.0	875	1,507	3.4	0.25
12	3.0	851	1,507	3.4	0.27
13	2.0	792	1,507	3.4	0.31
14	3.0	702	1,507	3.4	0.36
15	2.0	481	3,289	3.4	0.49
16	6.0	481	4,286	3.4	0.49
17	4.0	1,082	5,000	3.4	0.49
Half Space		1,225	5,000	3.4	0.49

CHAPTER 5. COMPARISON OF SURFACE WAVE SOURCES AND INPUT MOTIONS

5.1 INTRODUCTION

A persistent problem which has frustrated users of the Spectral-Analysis-of-Surface-Waves (SASW) method has been the unpredictability in the frequency content of impact sources (e.g., simple hammers or dropped weights) from site to site. An impact source which works well at one site (i.e., generates sufficient energy over a wide range of frequencies) may work poorly or not at all at another site because of different soil or pavement conditions. As a result, SASW measurements generally involve trial-and-error testing with various hammers and weights until one is found which generates sufficient energy in the frequency range of interest. This, in turn, increases the time required for performing a surface wave test and, if an adequate source cannot be found, adversely affects the quality of the surface wave measurements.

Different types of input motion are considered in this chapter as alternatives to impact-type sources. Most of these alternate input motions involve the use of an electromechanical vibrator driven by a function generator as a source. This combination gives the user far more control over the range of frequencies input to the subsurface than is available with impact sources. Presumably, this leads to shorter testing times and higher quality results.

In the sections which follow, a description of each type of source and input motion is presented, along with a discussion of the results of surface wave tests performed at the Hornsby Bend test site using each type of source and input motion. Other sources which have been successfully used in the past are also presented and discussed. A brief discussion of the theoretical phase spectra from two solution methods is included. Finally, the use of transfer functions, rather than cross power spectra, to measure dispersion is presented.

5.2 DESCRIPTION OF SOURCES AND INPUT MOTIONS

For the purposes of this chapter, one can consider two types of sources and three types of input motion. The first type of source is an impact source which has been used almost exclusively to date in SASW testing. Examples of impact sources include simple hammers, dropped weights, or instrumented hammers. Evidence of the unpredictability of impact sources is provided by considering the wide variety of hammers and weights used in the past several years in attempts to generate sufficient surface wave energy over the desired frequency ranges. Among these sources have been piezoelectric transducers for very high frequencies, small hammers, sledge hammers, drill bits, Standard Penetration Test

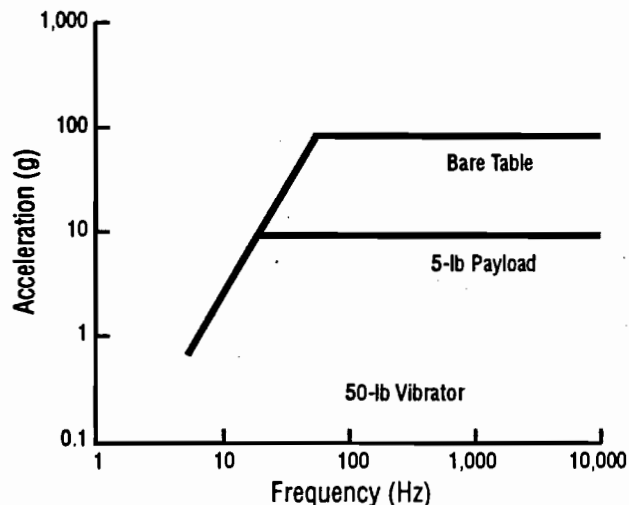


Fig 5.1. Nominal output acceleration spectrum for the 50-lb (223-N) vibrator.

(SPT) hammers, 50- to 200-lb (223- to 890-N) dropped weights, concrete blocks, a car, a 55-gallon (0.21 m³) drum filled with concrete, and a dynamic compaction weight (a 32-ton (285 kN) weight dropped from 100 ft (30 m)).

Despite their unpredictability, impact sources offer several important advantages. The most commonly used of the sources, hammers and 50- to 200-lb (223- to 890-N) dropped weights, are rugged and reasonably portable. Most importantly, impact sources, when they perform well, provide high-quality results rapidly and conveniently.

The second type of source is intended to transmit continuous types of input motion to the ground. The best example of this type of source is an electromechanical vibrator driven by a function generator. Electromechanical vibrators are rated according to the maximum force which they can deliver. Two vibrators were used in this study: a 50-lb (223-N) vibrator and a 250-lb (1.12-kN) vibrator. The nominal output acceleration spectrum for the 50-lb (223-N) vibrator is shown in Fig 5.1. With no mass attached to the table of the vibrator (a "bare" table), at frequencies below 55 Hz, the displacement limit of the table restricts the maximum acceleration (and force) delivered by the vibrator. As payloads of various weights are added to the table, the maximum frequency at which the displacement limit controls the motion decreases. The nominal output acceleration spectrum for the 250-lb (1.12-kN) vibrator is shown in Fig 5.2.

When used as a source for SASW testing, the vibrator is placed directly on the ground surface, and the reaction of the vibrator housing as it opposes the movement

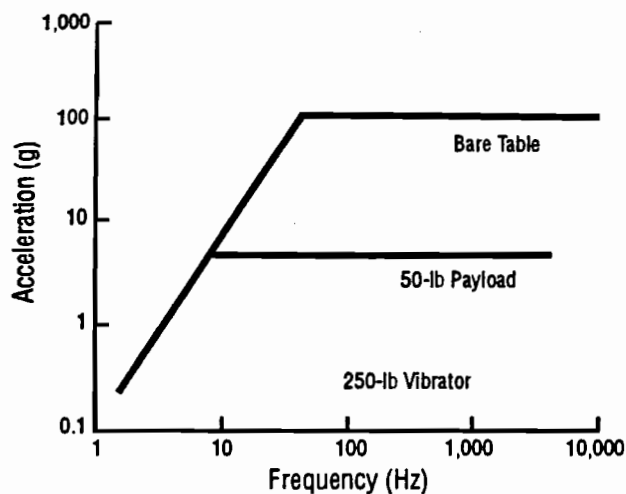


Fig 5.2. Nominal output acceleration spectrum for the 250-lb (1.12-kN) vibrator.

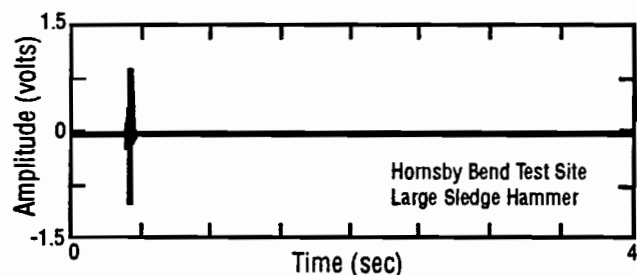


Fig 5.3. Typical transient input motion time record (bandwidth = 200 Hz).

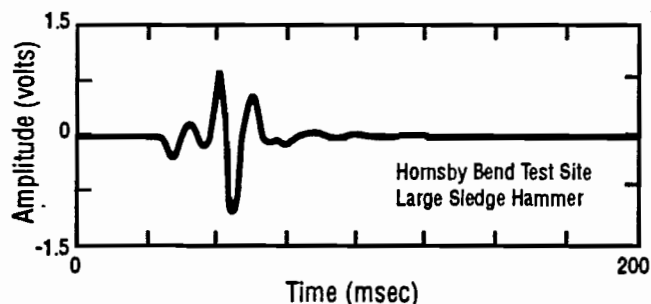


Fig 5.4. Expanded view of transient motion time record shown in Fig 5.3.

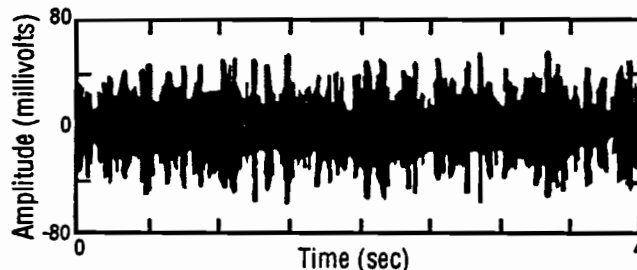


Fig 5.5. Typical random input motion time record (bandwidth = 200 Hz).

of the table of the vibrator is the force which is applied to the soil or pavement. At soil sites, surface vegetation should be removed from the location where the vibrator will be placed. Sand may also be spread on the ground surface before the vibrator is placed to fill voids and to improve the coupling between the base of the vibrator and the ground surface. At pavement sites, vacuum grease or another gel-like material is often used to improve the coupling.

The 50-lb (223-N) vibrator is easily moved from one location to another by one person, but the 250-lb (1.12-kN) vibrator requires the use of a portable floor crane or winch to be safely moved. If large vibrators are incorporated in production-type field testing, more convenient means of moving the vibrator will need to be developed. Another example of a continuous-type source used recently at a number of sites is a piece of heavy equipment (e.g. a bulldozer) which idles or moves back and forth within a short distance and generates a signal which approximates random noise and can provide sufficient energy over a broad range of frequencies. Heavy equipment is often readily available and relatively inexpensive to operate, but it is still not able to provide the controlled input motion of an electromechanical vibrator. The purpose of this investigation is to evaluate whether the relative inconvenience and lack of portability of continuous-type sources can be offset by increased predictability and improved quality of results. The three types of input motion which are considered are transient, random, and sinusoidal motions. Since surface wave dispersion measured using these three types of motion is the focus of this chapter, each is discussed in detail in the sections which follow.

5.2.1 TRANSIENT INPUT MOTION

Transient input motion is associated with impact-type sources. Transient motion is characterized by a pulse of relatively short duration which contains energy over a broad range of frequencies. (Ideally, the transient time signal should equal a delta function, since the delta function contains equal amounts of energy at all frequencies. However, this obviously cannot be achieved in practice.) An example of a transient motion-time history is shown in Fig 5.3. The time history presented in Fig 5.3 was caused by the impact of a sledge hammer on the ground surface and was measured using a velocity transducer (geophone). Time records like that shown in Fig 5.3 are typical of those used almost exclusively in SASW testing since the method's inception in the late 1970's.

The long length of the time window compared with the duration of the pulse in Fig 5.3 is required by the mathematics of the Fast Fourier Transform (FFT). As such, it is often difficult to view many details of the time histories. To aid in understanding the nature of transient time signals, the same time record is plotted on a greatly expanded scale in Fig 5.4. The record is characterized by

an initial quiet period before the arrival of the surface wave. (This quiet period can be seen because a pre-trigger delay has been used to record the time signal.) The particle motion quickly decays after the wave has passed the velocity transducer, and the ground surface returns to its at-rest condition.

One problem which is often faced when using the Fast Fourier Transform on recorded data is *leakage*. Leakage is the "smearing" of energy throughout the frequency domain and is caused by a lack of periodicity of the time signal within the time window. Tapered weighting functions, called *windows*, are often used to reduce the effects of leakage by forcing the signal to be periodic within the time window (Hewlett-Packard, 1980). Since a transient time signal is periodic within the time record, there is no leakage and no window is required.

The range of frequencies which can be generated by impacting the ground surface with an object depends on several factors, including the weight of the object, size of the contact area, impact velocity, and the properties of the ground surface itself. Since the user cannot accurately predict in advance the combination of these factors which will produce the desired frequencies, testing often involves trial-and-error selection of hammers of different weights and contact areas until a suitable combination is found. The end result is that the user has little control over the range of frequencies which are generated.

5.2.2 RANDOM INPUT MOTION

Random input motions are normally used with a continuous-type source such as an electromechanical vibrator. A function generator is used to create a random signal which contains frequencies in a range specified by the operator. In many instances, the function generator may be incorporated into the FFT analyzer used to measure the signals. The random signal is fed to an amplifier which drives the electromechanical vibrator. A typical random signal is shown in Fig 5.5. When random signals are used, a weighting function such as the Hanning window is necessary to reduce leakage, because the random signal is not periodic in the time window.

The most important aspect of random input signals is that the operator has greater control over the amplitude-frequency spectrum than when using transient signals. The operator is able to specify the range of frequencies which are generated by the electromechanical vibrator and to set the output level (within the limits of the vibrator).

5.2.3 SINUSOIDAL INPUT MOTION

Sinusoidal input motion is also implemented using an electromechanical vibrator. There is a fundamental difference, however, between sinusoidal input motion and other types of motion in the manner in which the motion is input to the ground surface. For transient and random input motion, all of the frequencies are input

simultaneously. In sinusoidal testing, the frequencies are introduced one at a time to the ground surface. To measure a range of frequencies, each successive frequency is introduced after measurements have been completed at the previous frequency. This type of testing is referred to as *swept-sine* testing because the function generator "sweeps" through many frequencies. As such, the time record consists of a pure sinusoid at a given frequency. (There are other types of sinusoidal input which sweep through the entire range of frequencies for each time record. They will not be discussed herein.) An example of a time record for swept-sine testing is presented in Fig 5.6. It is important to note that the time record shown in Fig 5.6 is composed of a single-

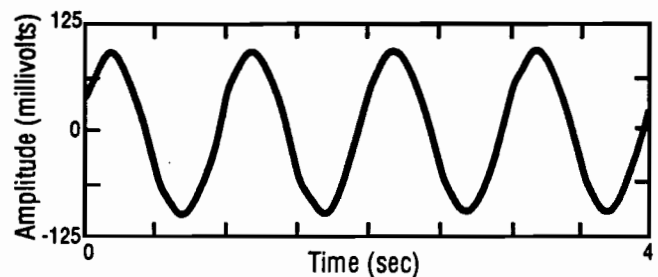


Fig 5.6. Typical sinusoidal input motion time record.

frequency sinusoid. The FFT analyzer automatically adjusts the length of the time record so that no leakage will occur.

The primary advantage of swept-sine testing is that the concentration of energy at individual frequencies results in large signal-to-noise ratios. As in random input motion, the operator has considerable control over the frequencies and amplitudes of motion which are being input to the ground surface. Testing is more time-consuming than it is transient or random input motion because of the time required to sweep through the range of frequencies individually. Depending on the frequency range, swept-sine testing requires several minutes, versus one minute or less for impact or transient testing.

5.2.4 COMPARISON OF TRANSIENT, RANDOM, AND SINUSOIDAL INPUT MOTIONS

Several quantities may be calculated to compare the three different types of input motion. The first of these quantities is the peak amplitude of the time signal. The peak amplitudes of the signals shown in Figs 5.3 through 5.6 are 1.040, 0.056, and 0.095 volts for transient, random, and sinusoidal excitation, respectively. It would appear at first that the transient signal contains more energy than either the random or the sinusoidal signal. It will become apparent, however, that the peak amplitude has very little to do with the energy or power contained in a signal.

A more meaningful comparison of the three types of motion may be obtained by examining the total power contained in the time signal. The total power is calculated using the following expression:

$$\sum_{k=0}^{N-1} x^2(k) \quad (5.1)$$

where

$x(k)$ = the time record, and

N = the number of points in the time record.

For the time records shown in Figs 5.3 through 5.6, the total power contained in each signal is 4.26 volts² for the transient motion, 2.23 volts² for the random motion,

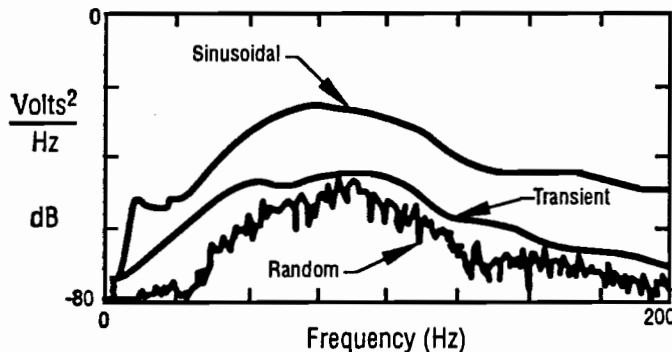


Fig 5.7. Typical auto power spectra for transient, random, and sinusoidal input motion.

and 9.19 volts² for the sinusoidal motion. The total power contained in the sinusoidal record is much greater than the transient record despite the fact that the peak amplitude of the transient record is much larger. The total power contained in the random record is approximately half as large as that of the transient record, whereas the peak amplitude was approximately twenty times smaller.

Furthermore, all of the power contained in the sinusoidal record is concentrated at one frequency. The power contained in either the transient or the random time signal is distributed over the entire range of frequencies (0 to 200 Hz in this case). This important point is the primary reason why the signal-to-noise ratios associated with sinusoidal testing are significantly higher than those of other types of input motion. (High signal-to-noise ratios usually result in coherence values near one. Appendix A contains a discussion of the relationship between noise, the coherence function, and the phase of the cross power spectrum.)

A final point concerning total power is that the power contained in a signal is the same whether the

signal is viewed in the time domain or in the frequency domain. Formally, this is Parseval's theorem and is expressed as (Bracewell, 1978):

$$\sum_{k=0}^{N-1} h^2(k) = N \sum_{m=0}^{N-1} |H(m)|^2 \quad (5.2)$$

where

$h(k)$ = the time record,

$H(m)$ = the linear spectrum of $h(k)$, and

N = the total number of points in the time or frequency domain.

A third means of comparing the three input motions is to examine the autospectral density functions (or auto power spectra) which typically result from each type of motion. The auto power spectrum describes the distribution of power in the frequency domain (Bendat and Piersol, 1980). The auto power spectra for each type of motion are shown in Fig 5.7. The auto power spectrum shown for swept-sine testing in Fig 5.7 represents values for entire range of frequencies used in the test, not just the single frequency shown in Fig 5.6. All three forms of input motion have spectra which contain a broad peak centered at about 40 Hz, but the spectrum for the swept-sine motion is 10 to 20 dB greater than that of the transient motion and approximately 25 dB larger than the spectrum of the random motion. (When considering power, 10 dB is one order of magnitude.)

The final method of comparing the three types of input motion is to calculate the peak-to-rms (root mean square) ratio for each signal. This quantity is the dimensionless ratio of the maximum peak absolute amplitude of the time signal to the rms value of the time signal:

$$\text{Peak-to-rms ratio} = \frac{x(k)_{\text{max}}}{\sqrt{\sum_{k=0}^{N-1} x^2(k)}} \quad (5.3)$$

where

$x(k)$ = the time record, and

N = the number of points in the time record.

Large values of the peak-to-rms ratio indicate that most of the power in a time signal is concentrated in a small fraction of the total time length of the record. Conversely, a relatively low value of the ratio indicates that the power is more evenly distributed over the entire length of the record. For the records shown in Figs 5.3 through 5.6, the peak-to-rms ratios are 22.8 for the transient signal, 2.8 for the random signal, and 1.4 for the sinusoidal signal.

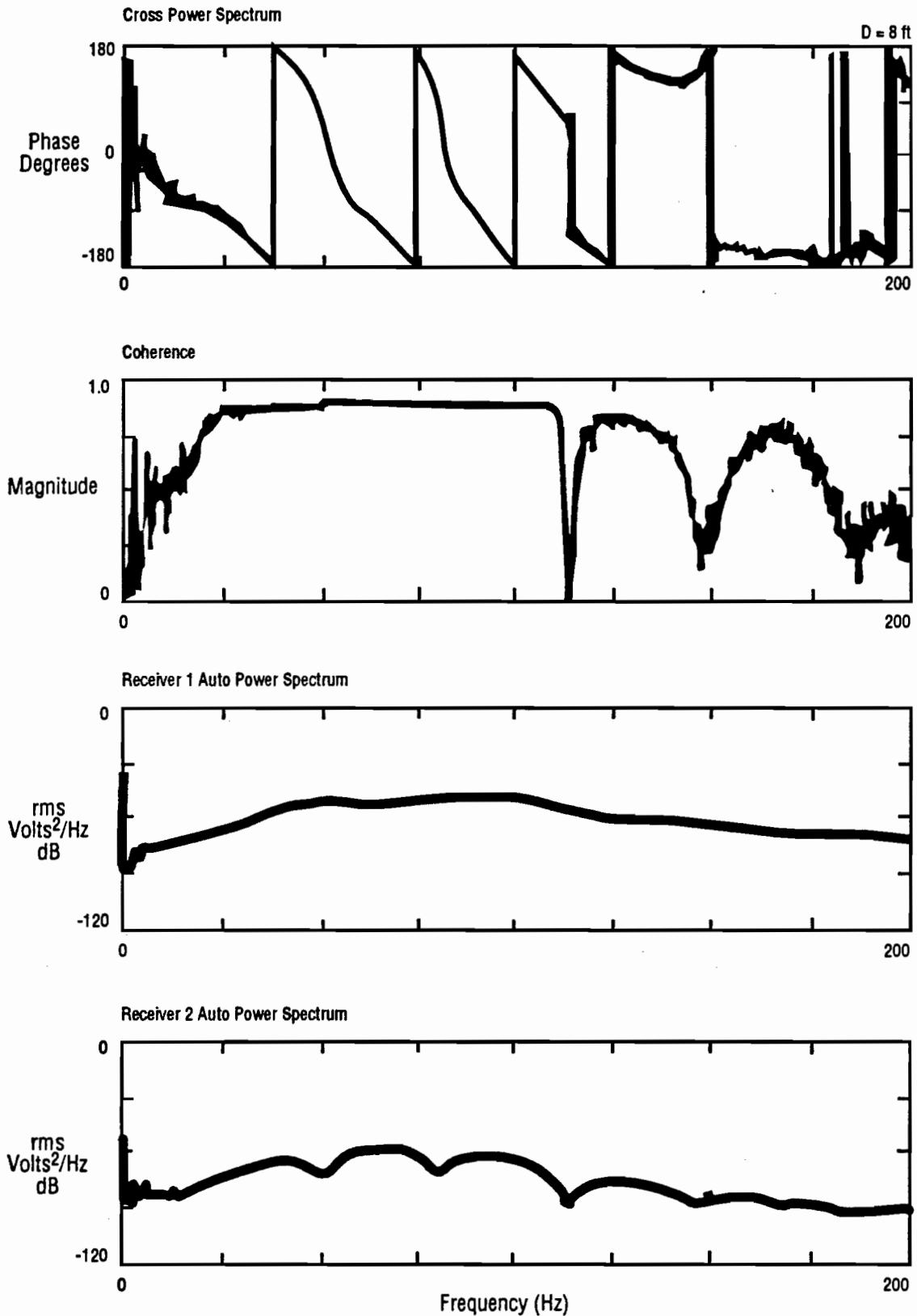


Fig 5.8. Spectral functions obtained using transient input motion for a receiver spacing of 8 ft (2.4 m); sledge hammer source.

The most useful of these four methods of comparing input motions is the auto power spectrum, because the operator can quickly judge the relative power contained in two spectra as well as determine the distribution of the power with frequency. Fortunately, the auto power spectra are readily available as part of the group of frequency domain records which are calculated and saved during the course of an SASW test.

5.3 EXPERIMENTAL RESULTS USING VARIOUS SOURCES AND INPUT MOTIONS

To understand how the results obtained with transient, random, and sinusoidal input motions differ in actual use, tests were performed at the Hornsby Bend test site using the three types of motion. Two receiver spacings were chosen to compare the different input motions. The shortest spacing, 8 ft (2.4 m), was chosen as representative of a relatively close receiver spacing used at most soil sites and a far spacing at most pavement sites. The second spacing, 32 ft (9.8 m), was chosen because it is usually at relatively large distances that impact sources (transient motion) are unable to generate sufficient energy. Therefore, 32 ft (9.8 m) was selected to offer the most potential for demonstrating the difference between the three types of motion. For both receiver spacings, the distance from the source to the first receiver was equal to the distance between receivers ($d_2/d_1 = 2$).

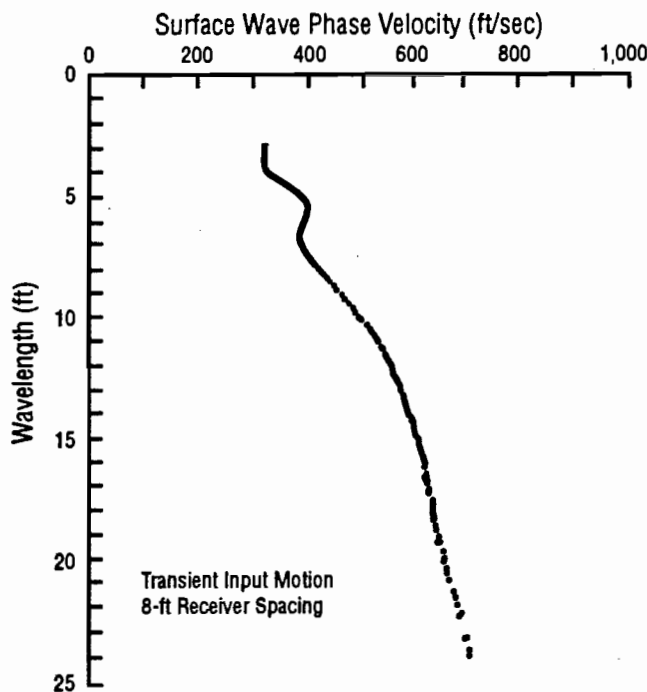


Fig 5.9. Dispersion curve using transient motion for a receiver spacing of 8 ft (2.4 m); phase spectrum shown in Fig 5.8.

Either common hammers or large dropped weights were used as impact sources. Details are provided as each record is discussed individually in the following sections. Both random and sinusoidal motions were implemented using the 50- and 250-lb (223-N and 1.12-kN) electromechanical vibrators discussed previously. The 50-lb (223-N) vibrator was used at the 8-ft (2.4-m) receiver spacing, and the larger vibrator was used for the 32-ft (9.8-m) spacing. For both receiver spacings, Mark Products L-4C geophones with a natural frequency of 1 Hz were used as receivers. A typical calibration curve for a 1-Hz geophone is included in Appendix C.

5.3.1 RESULTS USING TRANSIENT INPUT MOTION

The spectral functions (cross power spectrum, coherence function, and auto power spectra) obtained using a sledge hammer as the source of the 8-ft (2.4-m) receiver spacing are presented in Fig 5.8. The phase and coherence records are typical of those usually measured during an SASW test with impact sources. Below approximately 20 Hz, there is a range of frequencies at which the phase and the coherence are poor. The auto power spectra indicate that the poor phase and coherence are probably due to a the lack of power at these frequencies. Although, in this case, the phase record is not difficult to interpret at low frequencies, it is not uncommon to have a poor-quality phase record at low frequencies, which clouds the interpretation of the number of cycles (i.e., interpretation of the wrapped phase to obtain unwrapped phase, as illustrated in Fig 3.15). At frequencies above 110 Hz, the phase becomes too poor to use; the poor quality in the phase probably reflects insufficient power at frequencies above 110 Hz. The remaining portion of the record from 20 to 110 Hz exhibits good-quality, low-noise data. In this range of frequencies, there is apparently sufficient power to overcome the noise. The peak values observed on the auto power spectra are approximately -44 dB for Receiver 1 and -56 dB for Receiver 2.

The dispersion curve resulting from the phase record in Fig 5.8 is shown in Fig 5.9. Wavelengths longer than 24 ft (7.3 m) have been discarded to eliminate near-field effects, as discussed in Section 3.4.2. The minimum wavelength included in the dispersion curve is 2.9 ft (0.88 m). These maximum and minimum wavelengths correspond to phase differences of 120 and 990°, respectively, in Fig 5.8.

The spectral functions measured at a receiver spacing of 32 ft (9.8 m) using a sledge hammer are shown in Fig 5.10. Data at frequencies less than 20 Hz are not acceptable to use but are still easily interpreted to obtain the number of cycles. High-frequency data above about 55 Hz would also be discarded. The peak values in the auto power spectra are -50 dB for Receiver 1 and -60 dB for Receiver 2.

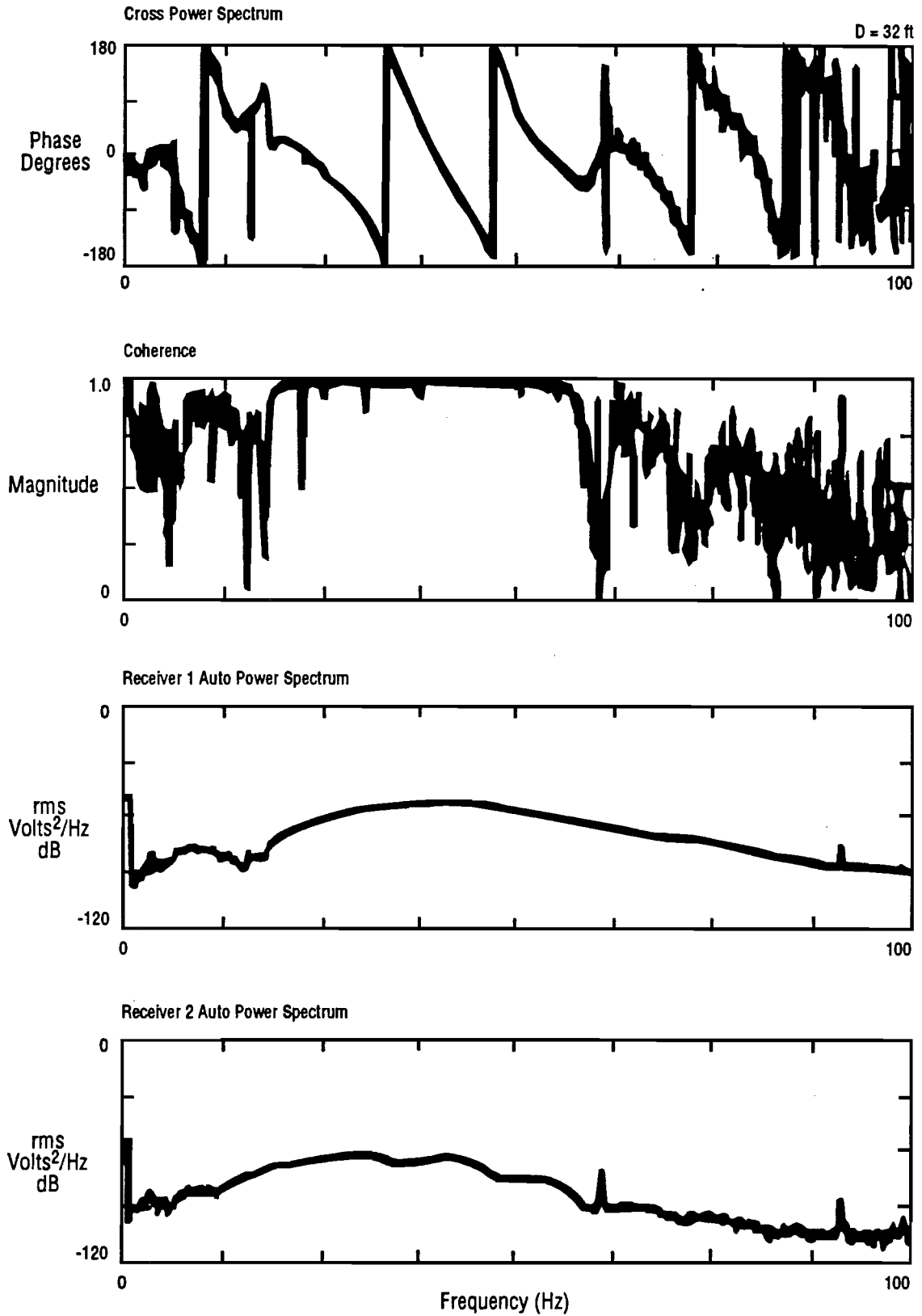


Fig 5.10. Spectral functions obtained using transient input motion for a receiver spacing of 32 ft (9.8 m); sledge hammer source.

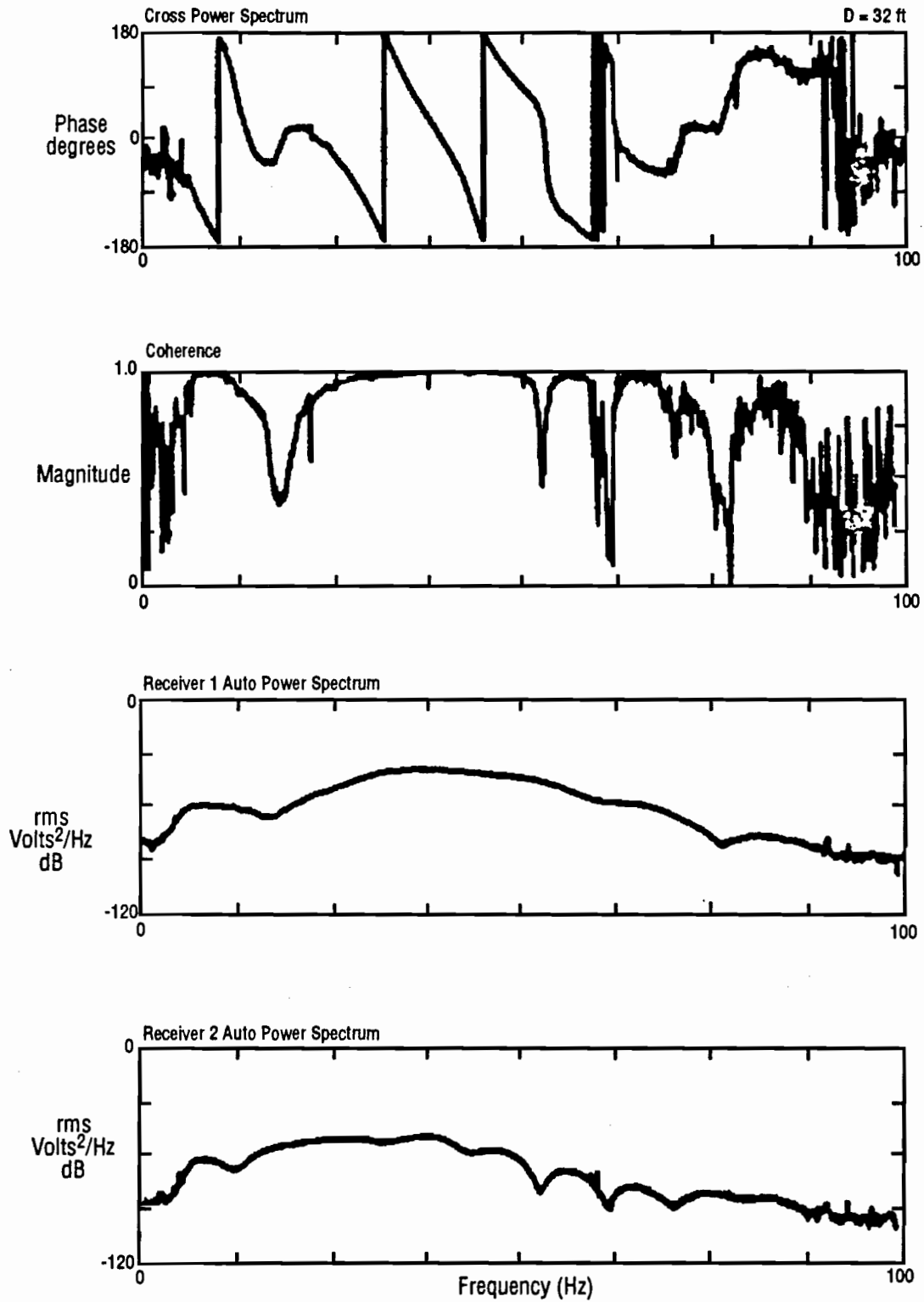


Fig 5.11. Spectral functions obtained using transient input motion for a receiver spacing of 32 ft (9.8 m); dropped weight source.

The test was repeated using a 210-lb (935-N) dropped weight to examine the influence of a larger (heavier) source. The resulting spectral functions are shown in Fig 5.11. A larger source improves the low-frequency portion of the record, as expected, but does not significantly improve the high-frequency data. The peak values of the auto power spectra are -40 dB and -52 dB for Receivers 1 and 2, respectively. The dispersion curve generated using the 210-lb (935-N) dropped weight is shown in Fig 5.12.

The *phase reversal* observed between 15 and 20 Hz might possibly be caused by reflections of waves within the profile. It is not immediately apparent whether the data between 10 and 32 Hz should be interpreted as one or two complete cycles (180 to -180°). One method of resolving this question is to compare the dispersion data from the 32-ft (9.8-m) spacing with the data from the 8-ft (2.4-m) spacing to determine whether the curves coincide in some common range of wavelengths. Both dispersion curves are plotted in Fig 5.13. The dispersion curve shown in Fig 5.13 for the 32-ft (9.8-m) spacing results from interpreting the phase data between 10 and 32 Hz in Fig 5.11 as one complete cycle. This interpretation appears to be correct, since the dispersion data from the 8- and 32-ft (2.4- and 9.8-m) spacings agree well in the range of wavelengths from 10 to 25 ft (3.0 to 7.6 m).

5.3.2 RESULTS USING RANDOM INPUT MOTION

Spectral results measured using random input motion at the 8-ft (2.4-m) receiver spacing are shown in Fig 5.14. Five averages were used to obtain the data shown in Fig 5.14. The phase of the cross power spectrum for frequencies below 30 Hz fluctuates mildly but is not large enough to make interpretation of the phase ambiguous. These fluctuations are most likely due to the poor signal strength in this range of frequencies. The most significant difference between the phase obtained from the transient motion and that from the random motion occurs in the range of frequencies from 110 to 150 Hz. Whereas the transient data become unacceptable at about 110 Hz, the random data are of good quality to 150 Hz. Although the coherence remains reasonably good at frequencies above 150 Hz, the phase data become difficult to interpret. Phase data such as these may be perfectly valid, but at the present time such data are eliminated because they do not match the expected trend (i.e., a sawtooth pattern). Perhaps as surface wave propagation becomes better understood and as more sophisticated models are developed which can accurately predict this type of behavior, phase data like these can be included in analysis of surface wave dispersion.

The "chatter" (variance) observed in the auto power spectra is caused by the random nature of the input motion (Ramsey, 1976). For pure random motion, each record which is included in the average is different from

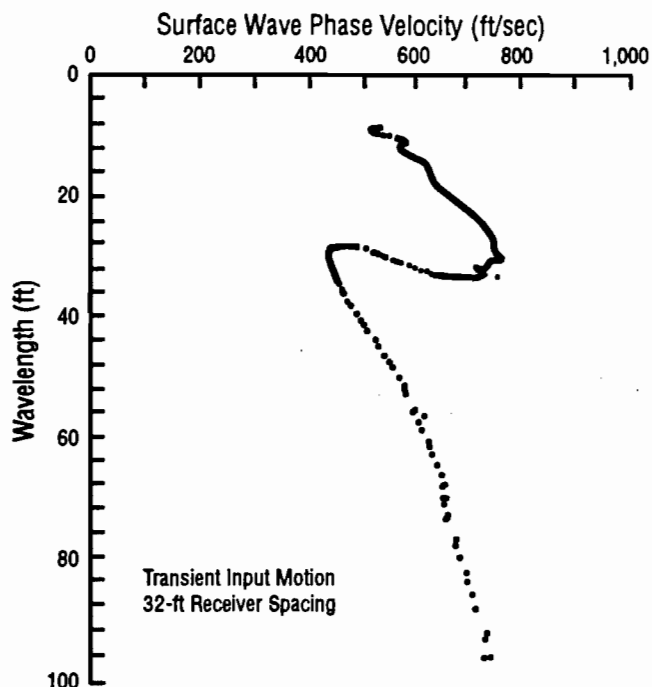


Fig 5.12. Dispersion curve using transient motion for a receiver spacing of 32 ft (9.8 m); phase spectrum shown in Fig 5.11.

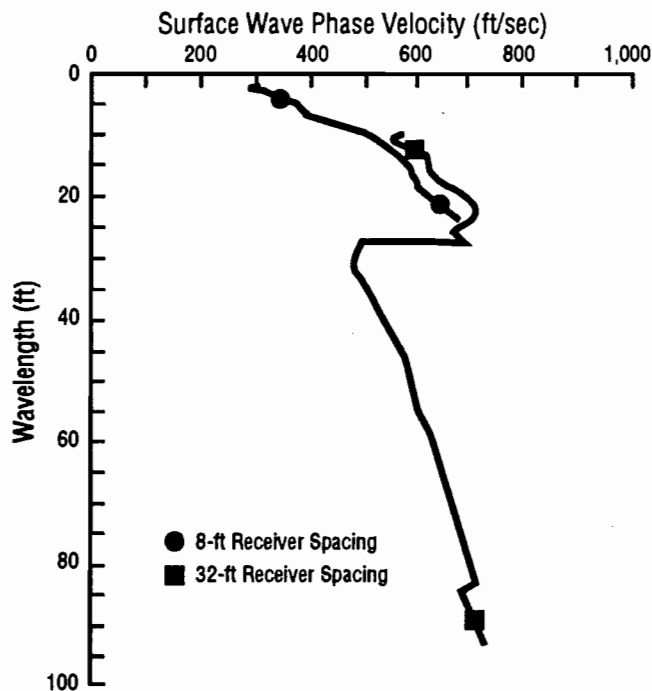


Fig 5.13. Combined dispersion curves using transient motion for receiver spacings of 8 and 32 ft (2.2 and 9.8 m); phase spectra shown in Figs 5.8 and 5.11.

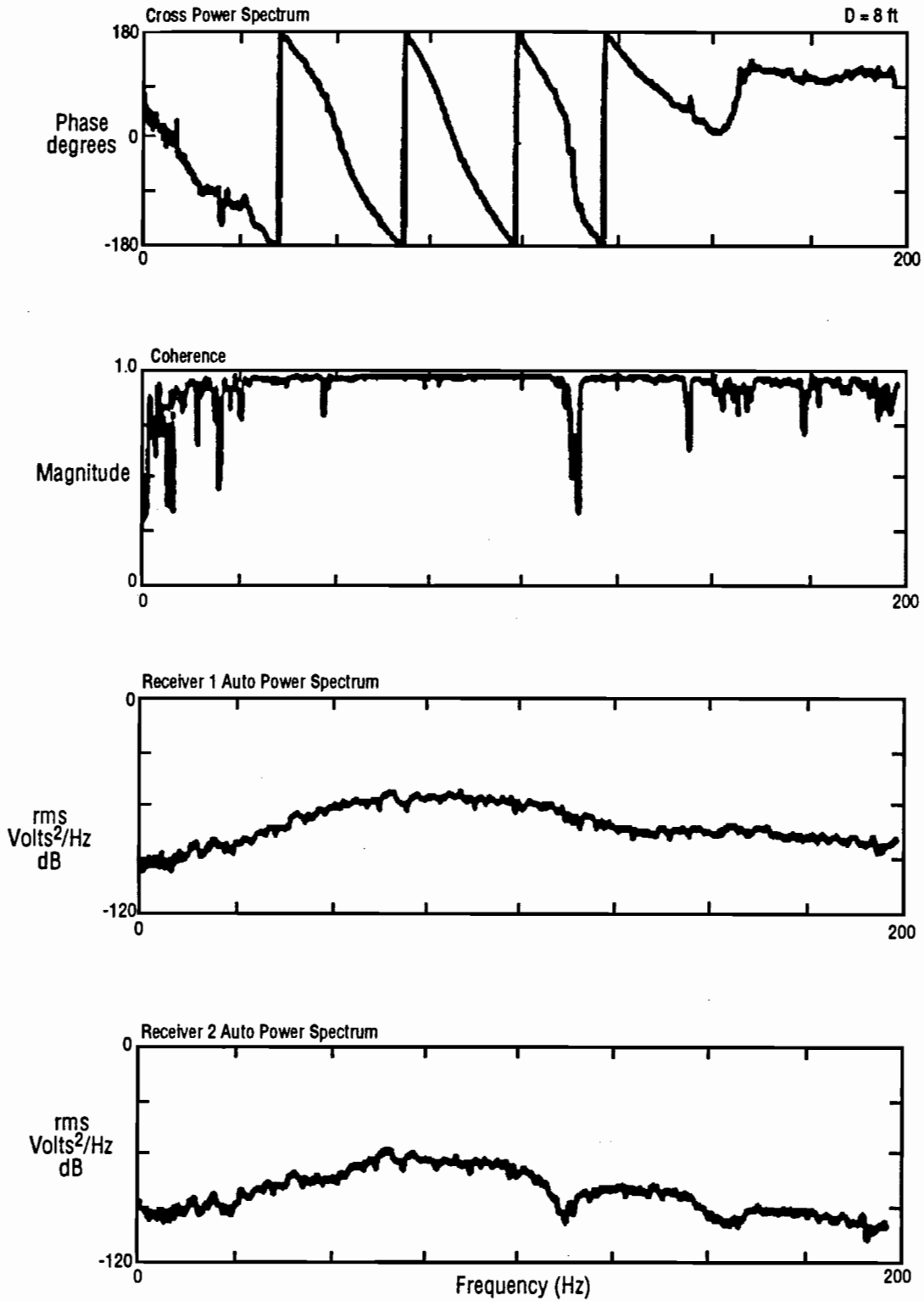


Fig 5.14. Spectral functions obtained using random input motion for a receiver spacing of 8 ft (2.4 m); 5 averages.

the others. This difference gives rise to the variability in the auto power spectra. For transient and swept-sine motions, each record is repeatable. Thus, the auto power spectra for those types of motion do not exhibit the variability that is observed for random motion. The maximum values of power are -46 dB for Receiver 1 and -60 dB for Receiver 2.

The influence of increasing the number of averages is shown in Fig 5.15. Twenty-five averages were used for this series of records. The most noticeable improvement is in the phase at low frequencies. In the remainder of the phase record, the improvement is insignificant. The chatter in the auto power spectra has also been reduced as a result of the increased number of averages.

In an effort to understand how the output level of the source affects the measured results, the test was repeated with the output of the vibrator adjusted down to a very low level. The results are presented in Fig 5.16. The peak values of the auto power spectra are -64 dB and -80 dB for Receivers 1 and 2, respectively, versus -46 dB and -60 dB for the records shown in Fig 5.14. The effect of decreasing the power is clearly seen in the coherence function. Although the phase is essentially unchanged in the central part of the record, both low- and high-frequency data have deteriorated. The reason for the deterioration is that the signal-to-noise ratio of both receivers has decreased because of the decreased signal amplitudes.

The dispersion curve for the 8-ft (2.4-m) receiver spacing using random input motion is shown in Fig 5.17. This dispersion curve corresponds to the set of records with 25 averages.

Spectral functions for the 32-ft (9.8-m) receiver spacing using random input motion are presented in Fig 5.18. The phase and coherence records differ only slightly from the transient motion data except in the vicinity of the phase reversal (15 to 20 Hz). The reversal is much less severe in the case of random motion, and the coherence does not drop as sharply as it does for transient motion. The dispersion curve for the 32-ft (9.8-m) receiver spacing using random input motion is shown in Fig 5.19.

5.3.3 RESULTS USING SINUSOIDAL INPUT MOTION

Spectral functions measured using swept-sine input motion for the 8-ft (2.4-m) receiver spacing are presented in Fig 5.20. The most noticeable difference between this record and those discussed previously is that the coherence is significantly better in the swept-sine record. The good coherence reflects the high signal-to-noise ratios in swept-sine testing. The peak values observed in the auto power spectra are much larger (-35 dB for both Receivers 1 and 2) than those associated with transient or random input motion because of the ability to concentrate large

amounts of energy at individual frequencies. The phase of the cross power spectrum does not differ substantially from the phase measured for random motion, except that there is less variability at very low frequencies. In some instances, this reduced variability may aid in interpreting the phase record to obtain the number of cycles. The dispersion curve for swept-sine input motion at the 8-ft (2.4-m) receiver spacing is shown in Fig 5.21.

The spectral functions determined using swept-sine input motion for the 32-ft (9.8-m) receiver spacing are shown in Fig 5.22. For this spacing, the improvement in the coherence function with respect to the coherence functions of transient or random motions is not as great as it is for the 8-ft (2.4-m) spacing. The improvement in the coherence between 5 and 15 Hz is important, however, in that significantly lower frequencies (longer wavelengths) can now be reliably included in the dispersion curve. The dispersion curve obtained using swept-sine motion for the 32-ft (9.8-m) receiver spacing is shown in Fig 5.23.

5.3.4 COMPARISON OF RESULTS

All three types of input motion resulted in reasonably good-quality records at the Hornsby Bend test site. For this reason the improvement in the quality of the records using random or swept-sine motion with respect to transient motion is not as significant as it might have been. Nevertheless, the modest improvements in this study suggest that in those instances where transient motion fails, random and sinusoidal input motions may provide better-quality results.

5.4 COMPARISON OF OTHER SOURCES AND INPUT MOTIONS

In July 1985, the U. S. Bureau of Reclamation began a four-year effort to strengthen and modify Jackson Lake Dam, located in Teton National Park near Jackson, Wyoming. The Spectral-Analysis-of-Surface-Waves method was used to assess changes in the stiffness of the foundation soils of the dam due to dynamic compaction. This project provided the unique opportunity to compare several different sources at the same site. The first of these sources was a bulldozer. A bulldozer or other piece of heavy equipment which idles in place or moves back and forth within a small area provides a source of seismic surface waves that approximates random input motion. The list of heavy equipment used as sources includes bulldozers, track-mounted backhoes, and rubber-tired front-end loaders. The second type of source used at Jackson Lake Dam was the dynamic compaction weight. The weight consisted of a stack of steel plates weighing 32 tons (285 kN). The weight was lifted and dropped from a height of 100 ft (30 m) by a crane. Results obtained using both of these sources are compared with those from more conventional sources in the following paragraphs.

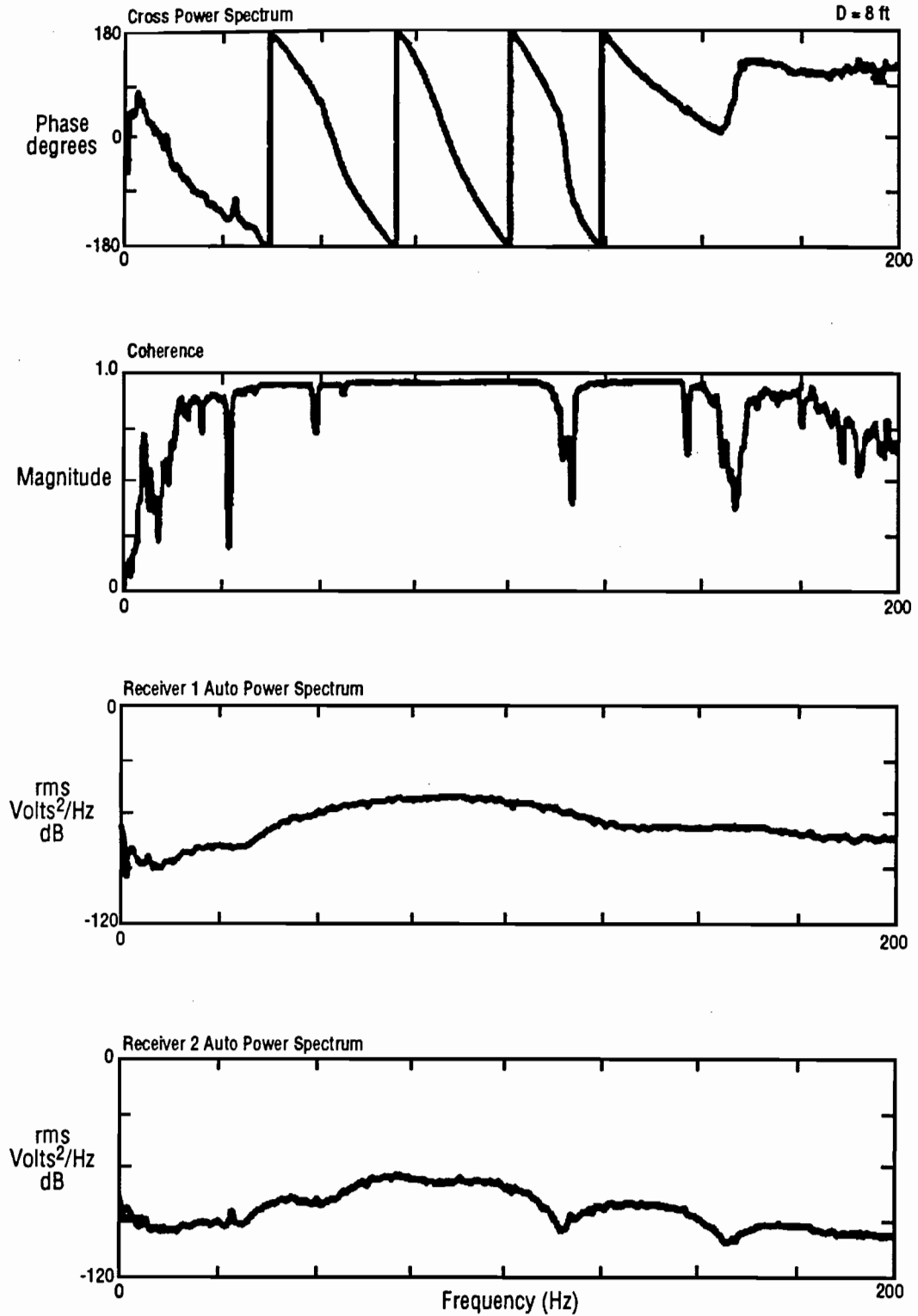


Fig 5.15. Spectral functions obtained using random input motion for a receiver spacing of 8 ft (2.4 m); 25 averages.

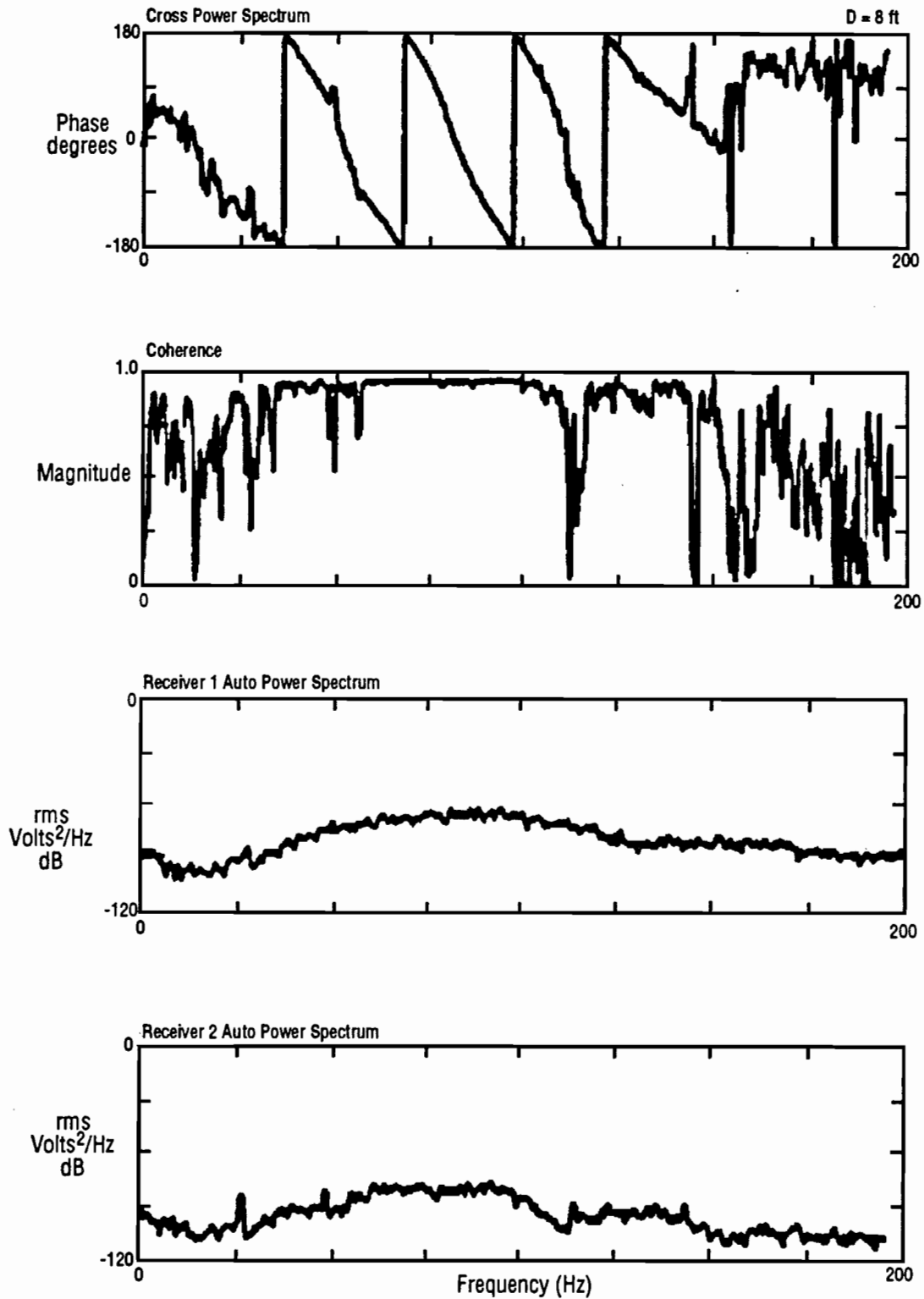


Fig 5.16. Spectral functions obtained using low-amplitude random input motion for a receiver spacing of 8 ft (2.4 m); 5 averages.

A typical set of time records showing the motion of the bulldozer recorded by receivers located 64 ft (19.5 m) apart is shown in Fig 5.24. In this instance, the bulldozer was located 64 ft (19.5 m) from the first receiver (i.e. $d_2/d_1 = 2$). The corresponding phase and coherence records are shown in Fig 5.25. The phase record is quite good and does not require any interpretation. The coherence function, however, is less than one over much of the record. The lower (less than one) value of coherence may have been caused by a number of factors, including (but not limited to) high levels of background noise usually encountered at construction sites or acoustic noise from the bulldozer itself. Another possible source of "noise" is that the bulldozer has two tracks, both of which are sources of seismic waves.

An example of a comparison between data generated using a 210-lb (1.12-kN) dropped weight and a bulldozer is presented in Figs 5.26 and 5.27. Spectral functions resulting from the dropped weight are shown in Fig 5.26 and from the bulldozer in Fig 5.27. Both records were measured using a 32-ft (9.8-m) receiver spacing. The phase record from the dropped weight is extremely poor and cannot be interpreted with any degree of confidence. Despite the fact that the coherence is poor, the phase data from the bulldozer can be interpreted with confidence, and they provide substantially more information than the record obtained with the dropped weight.

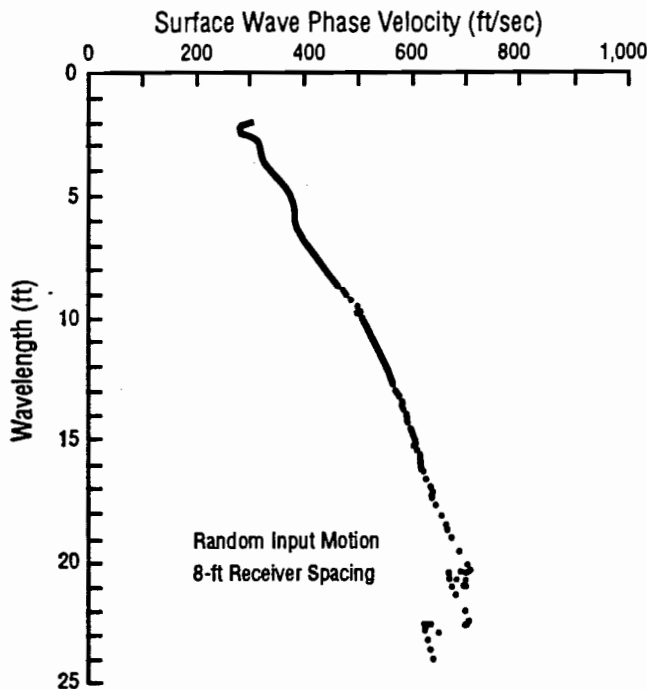


Fig 5.17. Dispersion curve using random motion for a receiver spacing of 8 ft (2.4 m); phase spectrum shown in Fig 5.15.

Another example of the improved results often obtained with a bulldozer is presented in Figs 5.28 and 5.29. Data in Fig 5.28 were collected using the dropped weight source, and data in Fig. 5.29 were obtained using a bulldozer. Both sets of data were recorded with a receiver spacing equal to 32 ft (9.8 m). The phase record from the dropped weight contains usable data only in the ranges of frequencies from 12 to 27 Hz and from 37 to 45 Hz. Again, despite the poor coherence, the phase spectrum from the bulldozer contains usable data over nearly the entire frequency range.

The dynamic compaction weight provided a rare opportunity to measure extremely long wavelengths at the Jackson Lake Dam site. A set of records obtained using the large weight as a source and a receiver spacing of 64 ft (19.5 m) is shown in Fig 5.30. The distance from the point where the weight was dropped was estimated to be 450 ft (140 m). This large distance was a result of safety precautions. The phase record contains usable frequencies as low as 800 mHz and as high as 6.5 Hz. The dispersion curve for this set of records is presented in Fig 5.31. It is remarkable that wavelengths as long as 4,000 ft (1.2 km) have been obtained with this source. This indicates that the surface wave method is an extremely robust test procedure which can be applied on a scale of millimeters, as it is for pavement studies, or on a scale of hundreds of meters, as it has been at the Jackson Lake Dam site.

5.5 COMPARISON OF THEORETICAL PHASE SPECTRA

The Spectral-Analysis-of-Surface-Waves method in its current form assumes that only plane Rayleigh waves are generated and measured during field testing. Sánchez-Salinero (1987) performed an analytical study of the differences between dispersion curves calculated using a solution for wave propagation in a layered half space which accounts only for plane Rayleigh waves and a solution which includes all wave types. In Chapter 6, an experimental means is devised to investigate the validity of the plane wave assumption. Since phase spectra have been used extensively to examine the differences between various sources and input motions in this chapter, it was decided to study the differences between the plane wave solution and the complete (Green's function) solution in terms of phase spectra in this chapter as well. An interesting perspective on the differences between these two solutions can be obtained by examining the phase spectra.

The plane wave solution corresponds to the natural modes of vibration of a layered half space. As such, there is no source per se included in the plane wave solution. In the Green's function solution, a source mechanism is specifically included in the formulation of the

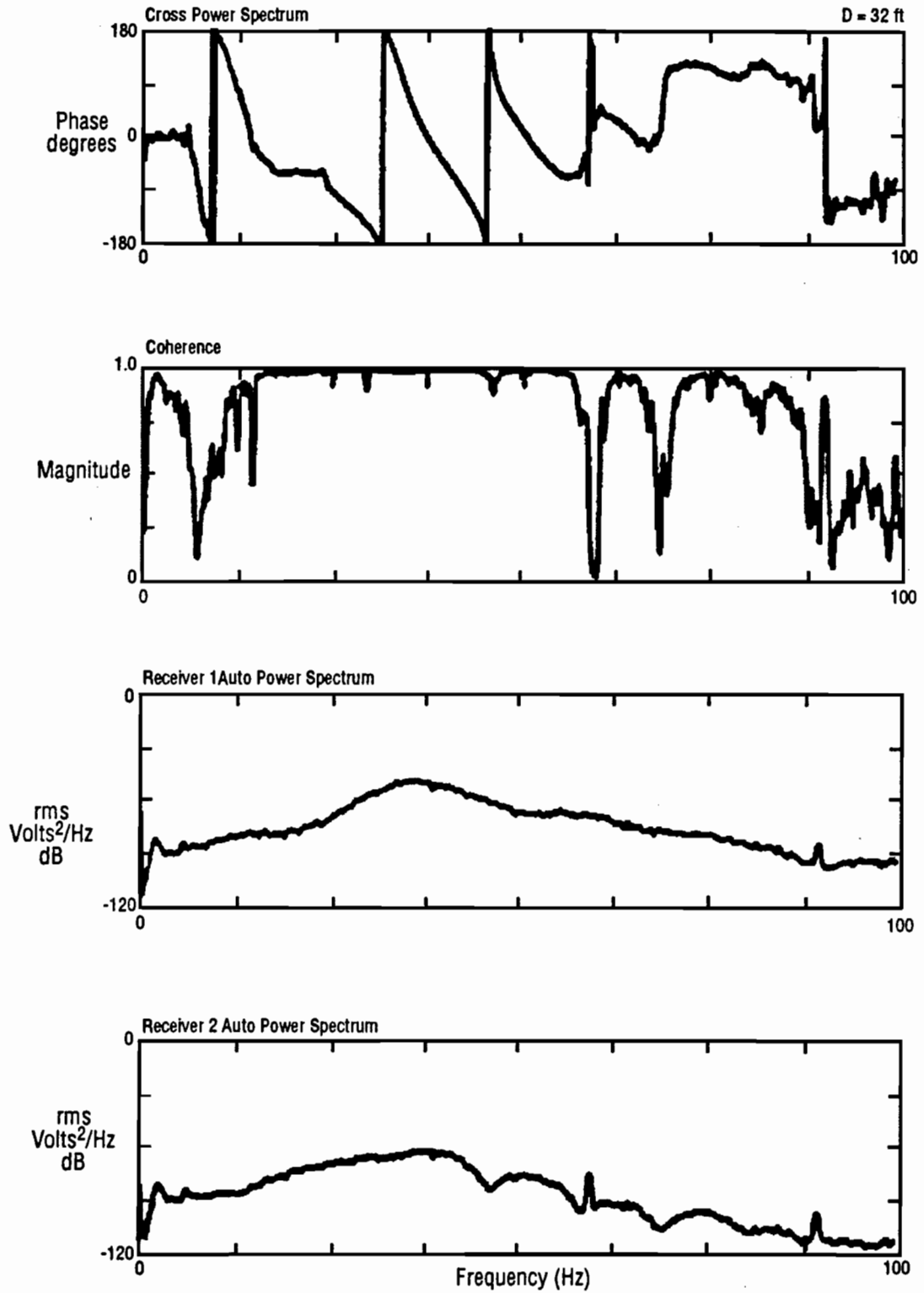


Fig 5.18. Spectral functions obtained using ransom input motion for a receiver spacings of 32 ft (9.8 m); 25 averages.

problem. The Green's function solution, therefore, more closely models the actual field conditions, because it includes all wave types and models the source. More details of each type of solution are included in Chapter 6.

It is possible to compute phase spectra for both of these solutions. The purpose for doing so is to more fully understand what characteristics of phase spectra are caused by the addition of other wave types and more realistic source mechanisms to the solution. The theoretical profile used to calculate the phase spectra for both the plane wave and Green's function solution is the interpreted profile shown in Fig 4.6.

A comparison of the phase spectra corresponding to each solution for a receiver spacing of 8 ft (2.4 m) is shown in Fig 5.32. The two spectra are very similar except from 80 to 120 Hz. In general, the lines which compose the phase spectrum of the plane wave solution tend to be "straighter," whereas the lines which compose the phase spectrum of the Green's function solution exhibit more "curves." The curved behavior coincides more closely with the behavior often observed in experimental data. It is likely that body waves are responsible for this behavior.

A similar comparison between the plane wave and cross power spectrum solution for a 32-ft (9.8-m) receiver spacing is shown in Fig 5.33. At this receiver spacing the two spectra are again very similar except

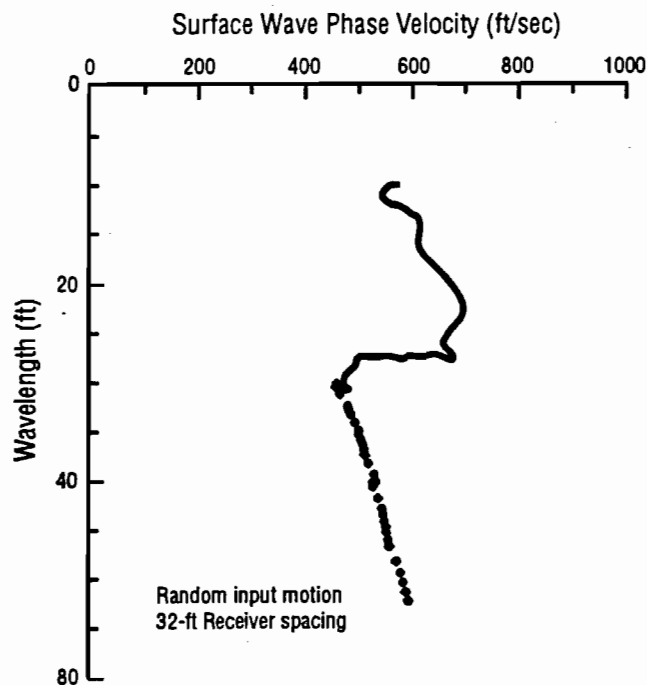


Fig 5.19. Dispersion curve using random input motion for a receiver spacing of 32 ft (9.8 m); phase spectrum shown in Fig 5.18.

between 80 and 100 Hz. In this range of frequencies, the cross power spectrum exhibits behavior which is often associated with reflections of waves within the profile (Sheu, 1987). Trends in phase such as this are usually interpreted to be one cycle, but the plane wave solution suggests that there are actually two cycles present.

It is hoped that by studying the phase calculated using more accurate models such as the Green's function, a better understanding can be gained of behavior like that observed in the phase spectrum in Fig 5.11.

5.6 THE USE OF TRANSFER FUNCTIONS TO MEASURE DISPERSION

It has been suggested (Sánchez-Salineró, 1987) that the transfer function between the source and first receiver be used to calculate dispersion, rather than the cross power spectrum between the first and second receivers. As discussed in Section 3.4.1, the cross power spectrum is the phase difference between two similar types of motion (usually particle velocity or acceleration) measured at each receiver. The transfer function, however, is the phase difference between the *force* applied at the source and motion (either particle velocity or acceleration) at the first receiver. As such, it is an approach to dispersion calculations fundamentally different from the cross power spectrum.

The Green's function solution is well-suited for calculating the theoretical transfer function, because the Green's function describes the displacement (or velocity or acceleration) at one point in the medium in terms of the force applied at another point. Therefore, it is a simple matter to calculate the phase difference between the force and the motion, because this difference is equal to the phase of the Green's function. A comparison of the theoretical phase difference calculated using the transfer function (with particle velocity) and the cross power spectrum for a receiver spacing of 8 ft (2.4 m) is shown in Fig 5.34. The same comparison is presented in Fig 5.35 for a 32-ft (9.8-m) receiver spacing. For both receiver spacings, the two phase spectra differ over portions of the frequency range.

In practice, the measurement of the transfer function between the source and the first receiver is much more difficult. The problem centers around the inability to accurately measure the force which is applied to the ground surface. One possible means of measuring the transfer function experimentally is to use an instrumented hammer (transient input motion) to obtain the force input to the ground surface. An instrumented hammer contains a load cell which senses the force required to stop part of the mass of the hammer when it contacts a surface. Unfortunately, the force required to stop the hammer is different from the force applied to the ground surface (Halvorsen and Brown, 1977). To account for the

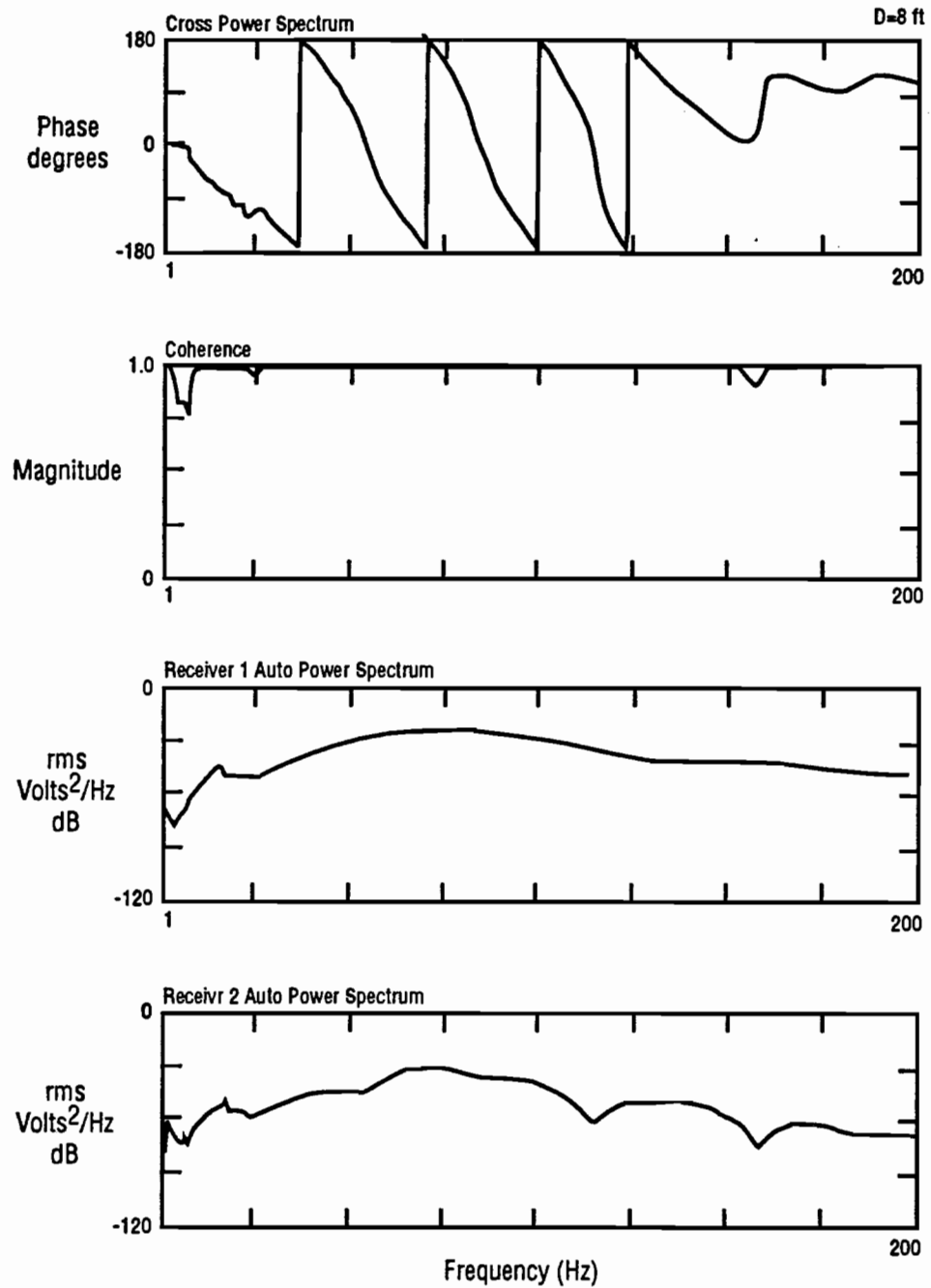


Fig 5.20. Spectral functions obtained using swept-sine input motion for a receiver spacing of 8 ft (2.4 m).

difference, the hammer must be calibrated, but the calibration is very dependent on the surface which the hammer impacts and, to a lesser extent, on how the hammer is swung (Thornhill and Smith, 1980). Therefore, instrumented hammers are difficult to use for surface wave testing, because each hammer needs to be calibrated for each impact surface. Another problem associated with the use of instrumented hammers is that the large peak forces present during the impact may result in nonlinear soil or pavement behavior in the vicinity of the impact.

The use of random input motion or sinusoidal input motion to measure the transfer function is equally difficult. One method of using random or sinusoidal motion is to attach an accelerometer to the base of the electromechanical vibrator to record the acceleration of the base of the vibrator during testing. This system can be modelled using a one-degree-of-freedom model with viscous damping, as shown in Fig 5.36(a), where the mass, m , represents the vibrator and the springs and dashpot represent the soil or pavement. The force vectors acting on the mass are illustrated in Fig 5.36(b). The acceleration measured at the base of the vibrator during testing is proportional to the inertial force, $m\omega^2A$, shown in Fig 5.36(b). The force applied to the soil or pavement is equal and opposite to the resultant of the stiffness and damping force vectors, kA and $c\omega A$, respectively. This resultant force is

illustrated by the dashed line in Fig 5.36(b). Clearly, the inertial force is out of phase with respect to the resultant force applied to the soil or pavement for nonzero values of damping. This fact prevents the use of an accelerometer on the base of the vibrator to measure the force applied to the soil or pavement.

Finally, use of the transfer function to measure surface wave dispersion requires that a Green's function solution be implemented in an inversion algorithm. The plane wave inversion algorithm now in use more closely approximates the characteristics of the cross power spectrum approach rather than the transfer function approach. Unfortunately, the Green's function solution is too time-consuming (expensive) to implement on a production basis (Sánchez-Salineró, 1987).

In short, although the transfer function approach to surface wave dispersion calculations appears attractive from a theoretical viewpoint, there are a number of practical difficulties which must be overcome before the method can be used in practice.

5.7 SUMMARY

The unpredictability of impact-type (transient motion) sources has been a persistent problem encountered when using the Spectral-Analysis-of-Surface-Waves method at soil and pavement sites. Since the inception of the SASW method, many different types of impact sources ranging from simple hammers to large dropped weights have been used, with varying degrees of success, to generate surface seismic waves. Two alternate types of input motion, random and sinusoidal, have been evaluated as alternatives to transient motion. Both of these types of motion utilize an electromechanical vibrator to transmit the motion to the ground surface.

Transient, random, and sinusoidal motions were compared using four criteria: (1) peak value of the time record; (2) total power contained in the signal; (3) the auto power spectrum of each signal; and (4) the peak-to-rms ratio for each type of motion. The auto power spectrum was found to be the most meaningful way to compare the three types of motion. Swept-sine motion was found to contain significantly higher levels of power because of its ability to concentrate power at individual frequencies during the measurement.

The three types of motion were also compared using field measurements of dispersion performed at the Hornsby Bend test site. All three types of motion resulted in phase spectra containing good-quality data. In most instances, the spectra measured using random and sinusoidal motion were slightly improved with respect to the spectra measured with transient motion. At sites where transient motion fails to work well, the improvements as a result of using random or swept-sine motion could make the difference between acceptable and unacceptable data.

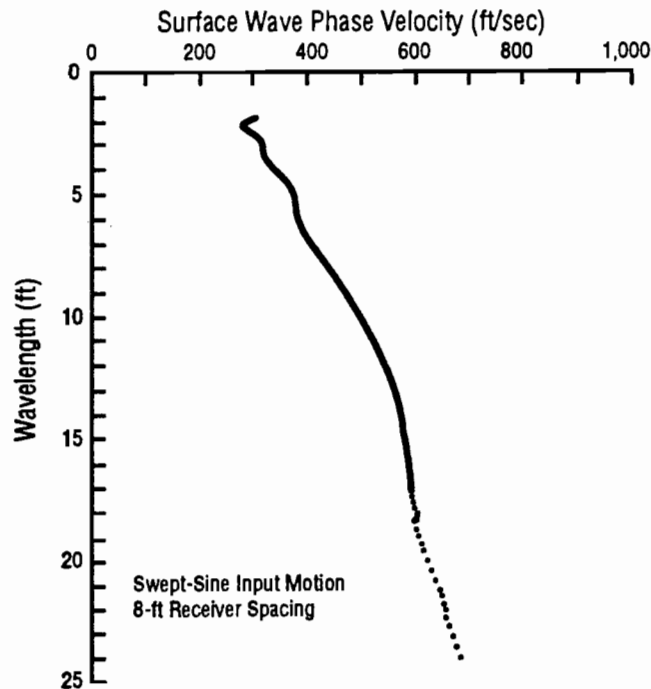


Fig 5.21. Dispersion curve using swept-sine input motion for a receiver spacing of 8 ft (2.4 m); phase spectrum shown in Fig 5.20.

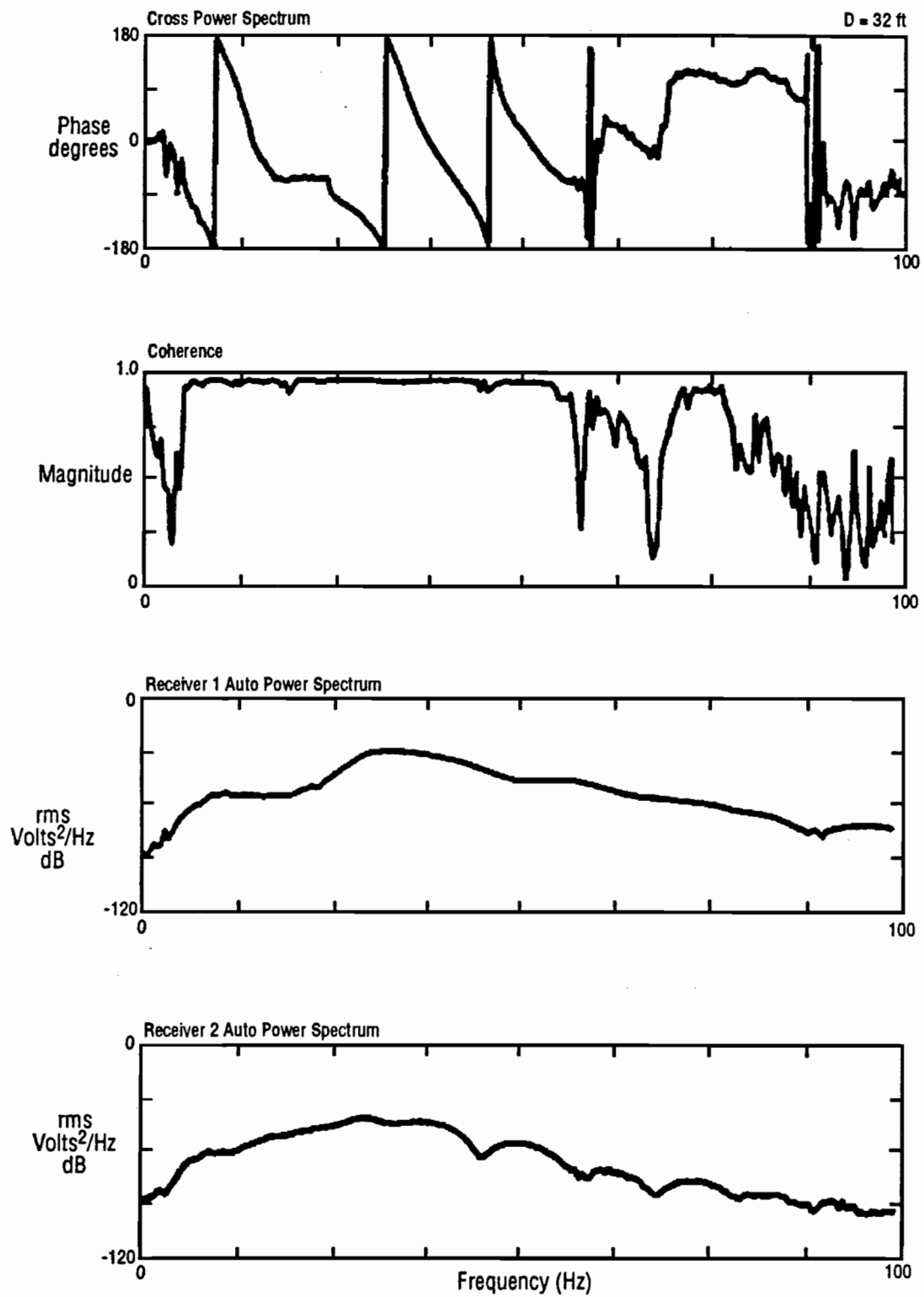


Fig 5.22. Spectral functions obtained using swept-sine input motion for a receiver spacing of 32 ft (9.8 m).

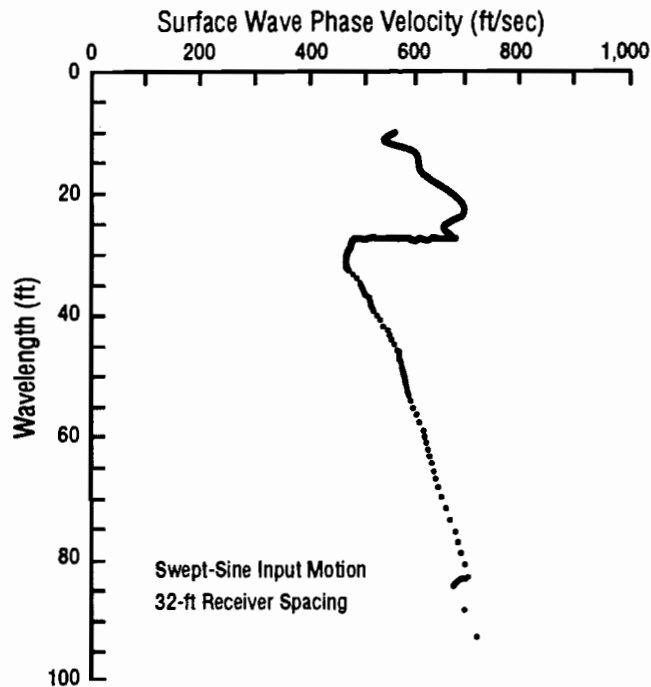


Fig 5.23. Dispersion curve using swept-sine input motion for a receiver spacing of 32 ft (9.8 m); phase spectrum shown in Fig 5.22.

A bulldozer or other heavy equipment which idles in place or moves back and forth within a small area has been used recently as a source of surface waves. The motion from the bulldozer approximates a random input signal. At one site where a bulldozer has been used, Jackson Lake Dam, the increase in the quality of the measured phase spectra with respect to conventional impact sources was substantial. Another source which the Jackson Lake Dam study provided the opportunity to use was a 32-ton (285-kN) dynamic compaction weight dropped from a distance of 100 ft (30 m). The large weight successfully generated frequencies as low as 800 mHz and wavelengths as long as 4,000 ft (1.2 km).

A comparison was made of theoretical phase spectra calculated using a solution which includes only plane surface waves and one which includes all wave types. The comparison indicated that many of the phenomena commonly observed in actual phase spectra such as phase reversals and curved lines likely result from the influence of other wave types.

Finally, one possible alternative to the current way in which SASW testing is performed is to use to transfer function (the phase difference between the force applied to the ground surface by the source and the motion at the first receiver), rather than the cross power spectrum, between the motions at the two receivers. Unfortunately, it is very difficult to make an accurate measurement of the force applied to the ground surface. This fact makes the transfer function method extremely difficult to use in practice.

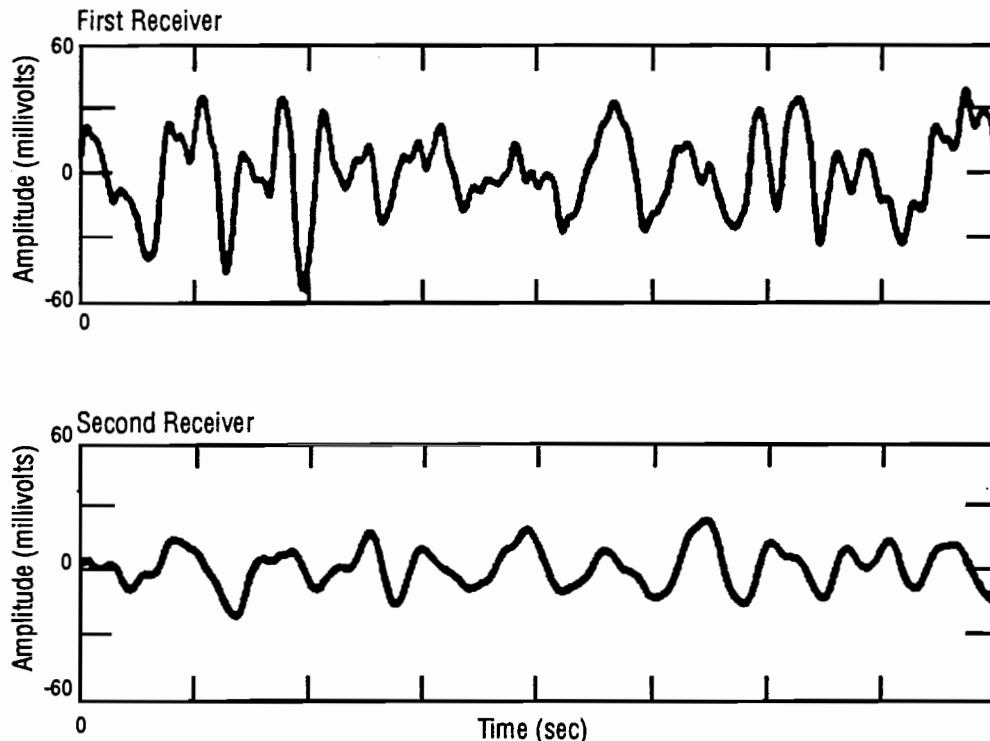


Fig 5.24. Typical time records of motion generated by a bulldozer.

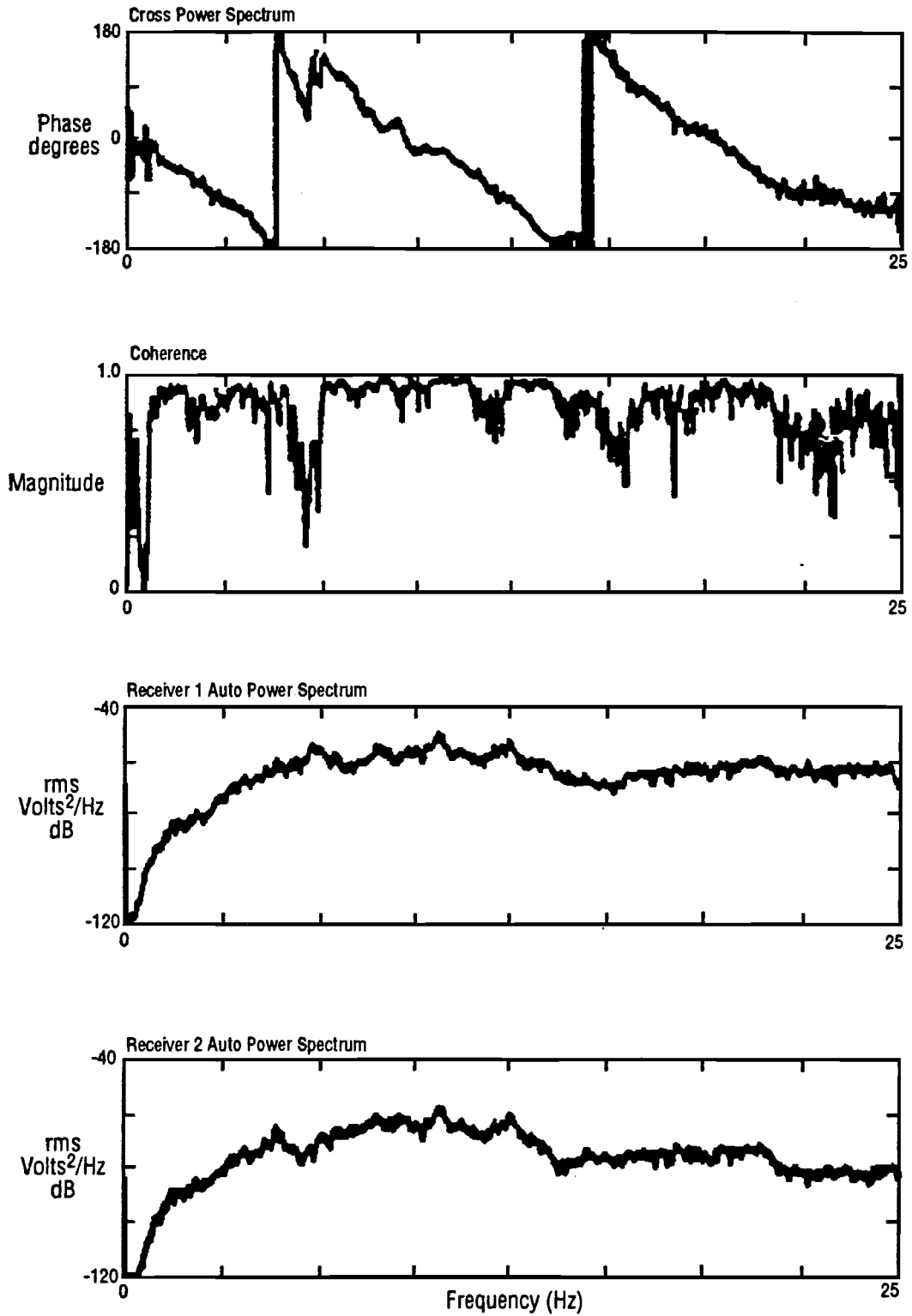


Fig 5.25. Typical phase of the cross power spectrum and coherence function for bulldozer source; time records shown in Fig 5.24.

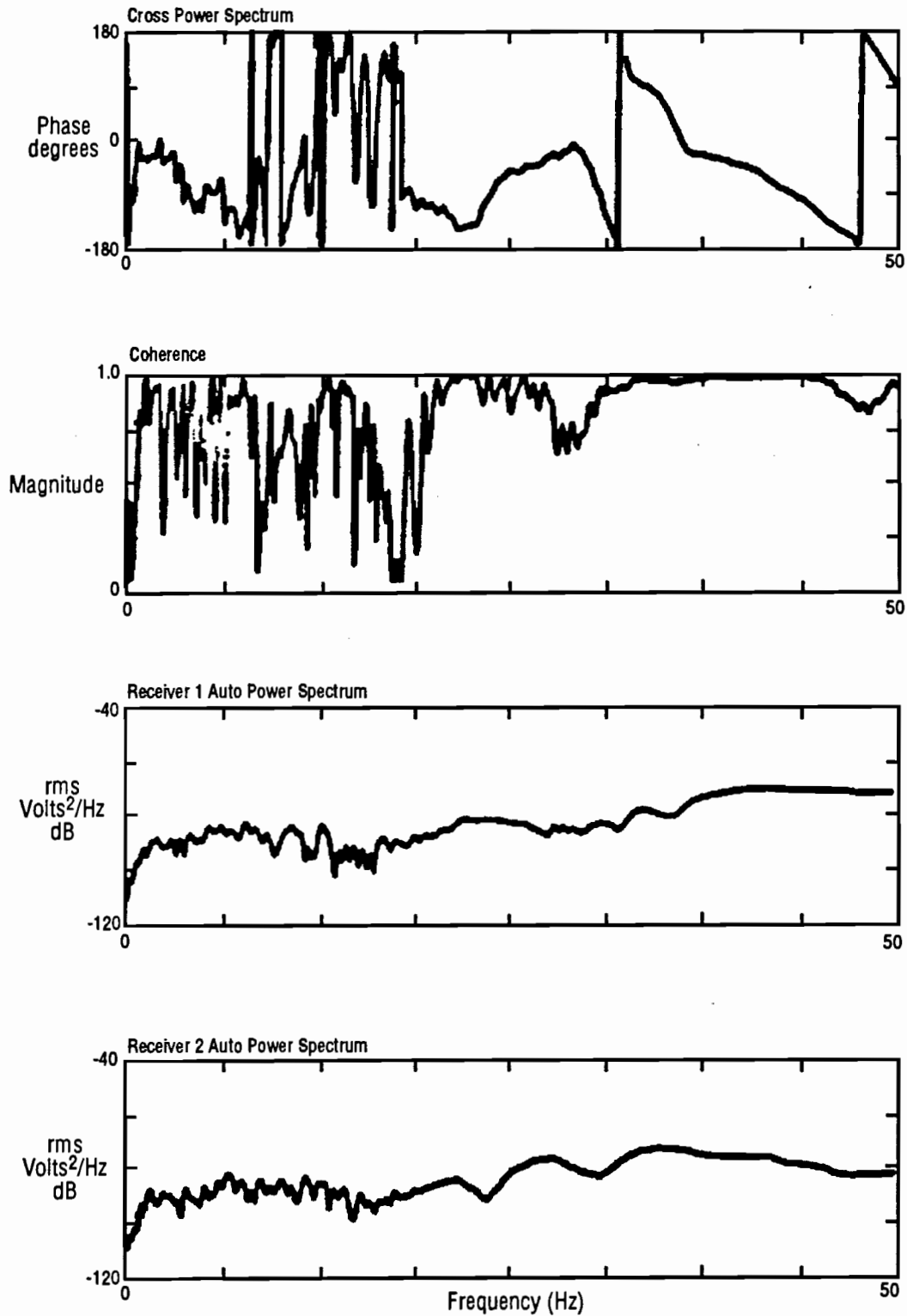


Fig 5.26. Spectral functions measured using conventional 210-lb (935-N) dropped weight source; Example 1.

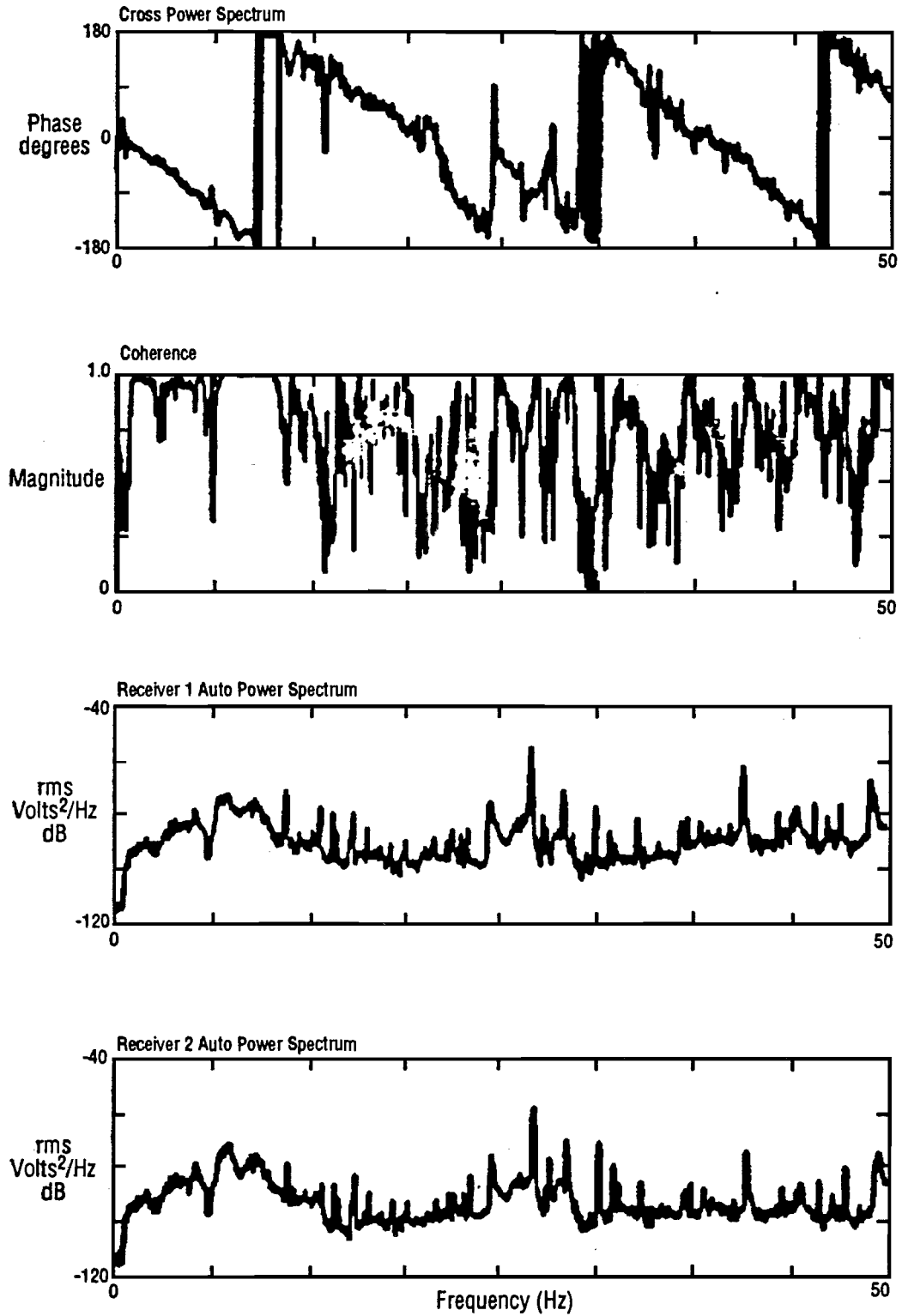


Fig 5.27. Spectral functions measured using bulldozer as a source; Example 1.

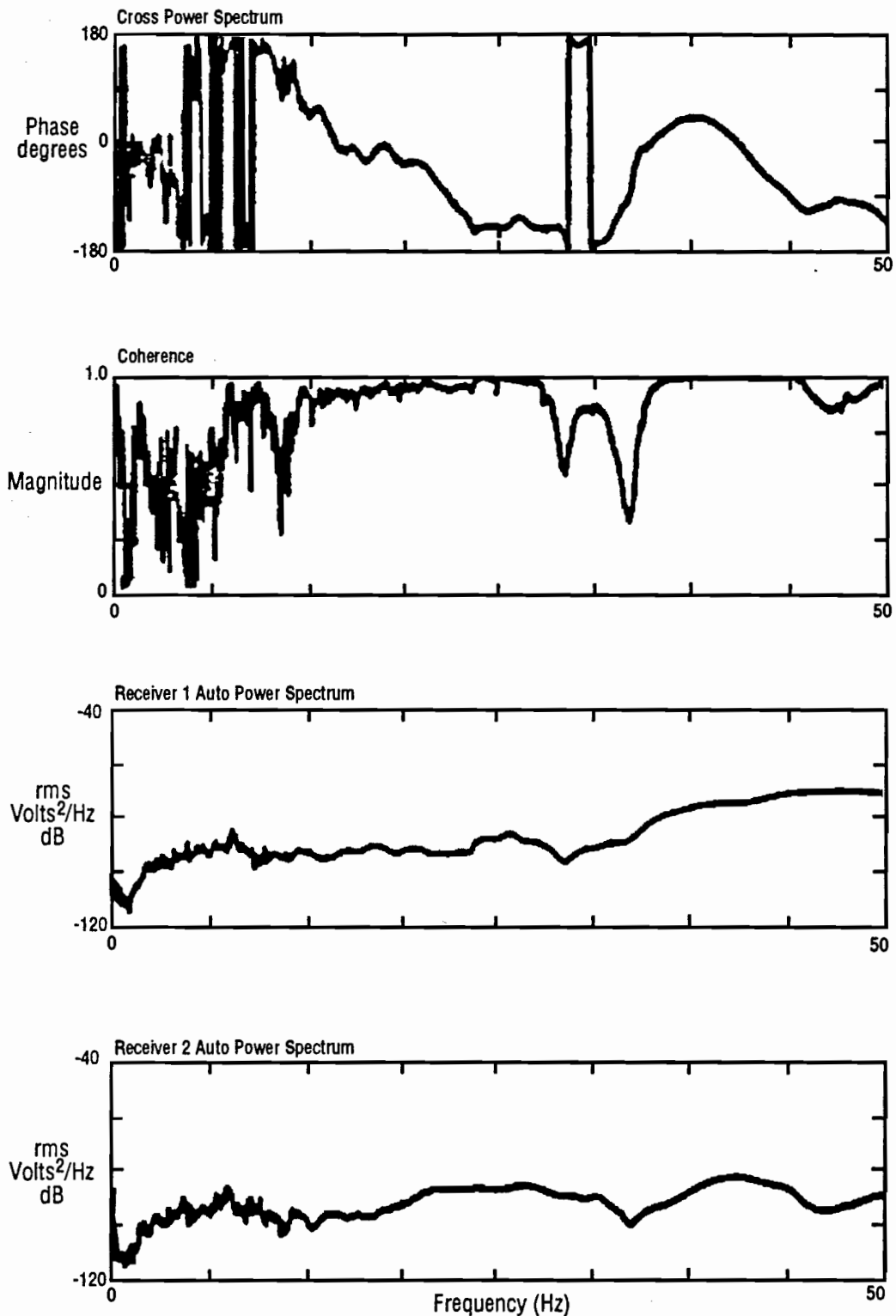


Fig 5.28. Spectral functions measured using conventional 210-lb (935-N) dropped weight source; Example 2.

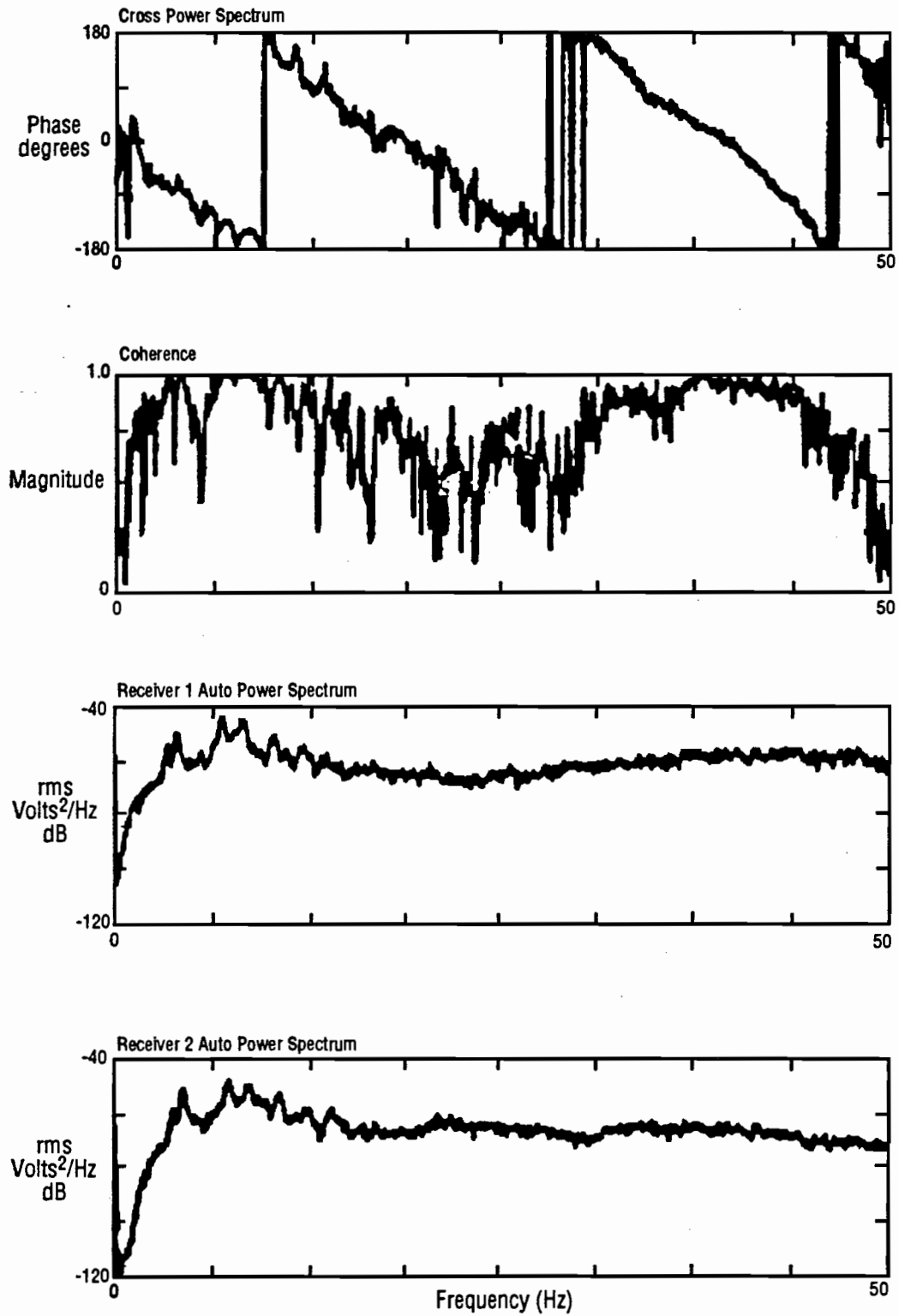


Fig 5.29. Spectral functions measured using bulldozer as a source; Example 2.

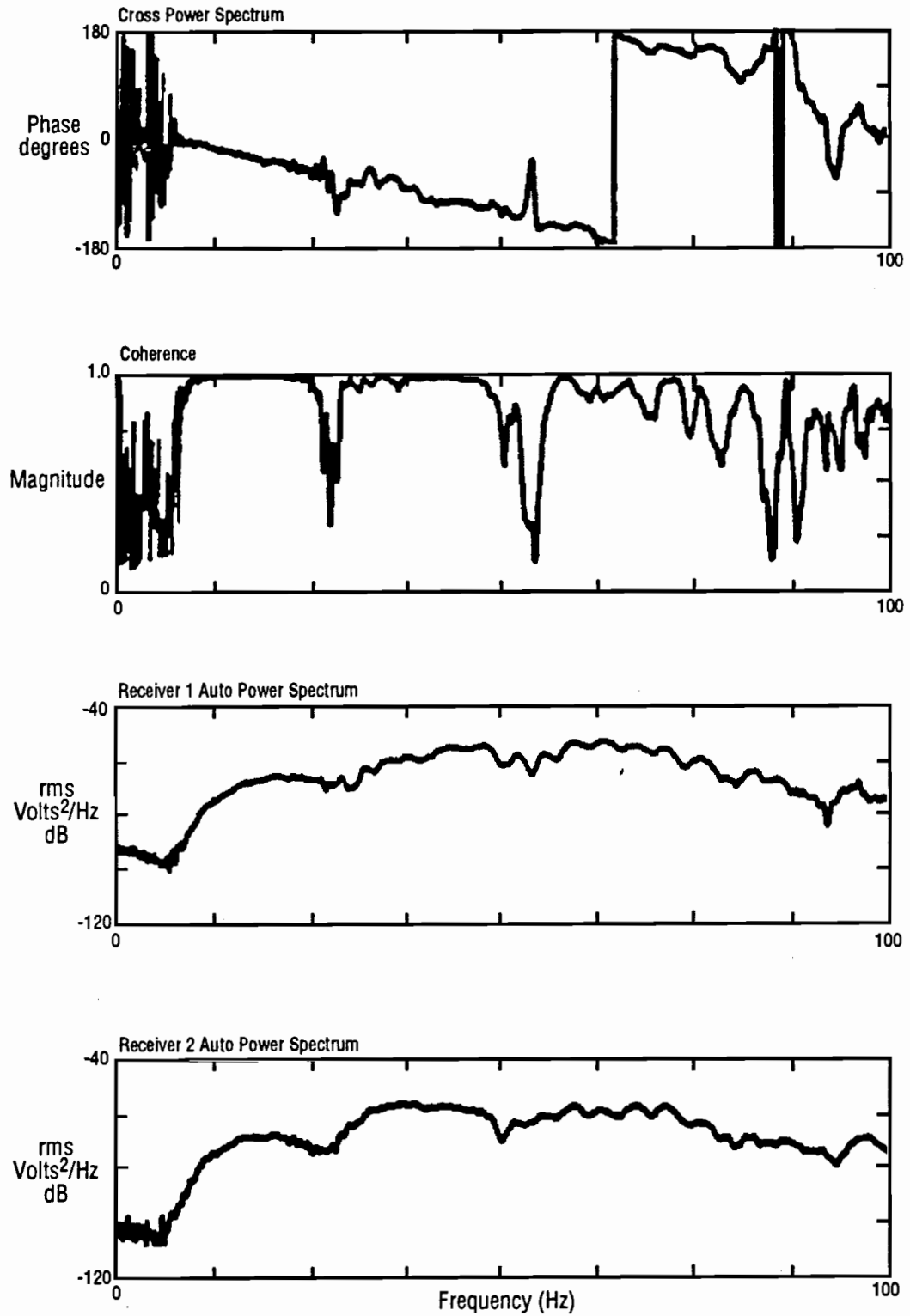


Fig 5.30. Spectral functions obtained using dynamic compaction weight as a source.

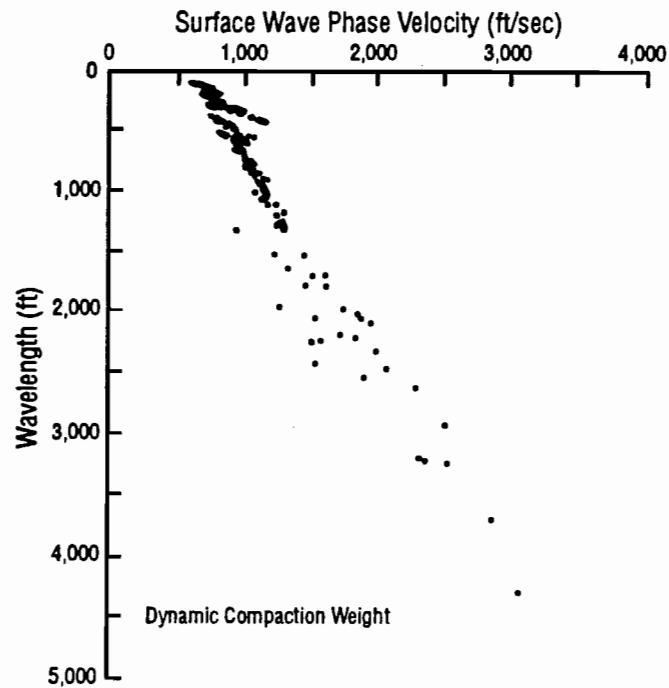


Fig 5.31. Dispersion curve obtained using dynamic compaction weight as a source.

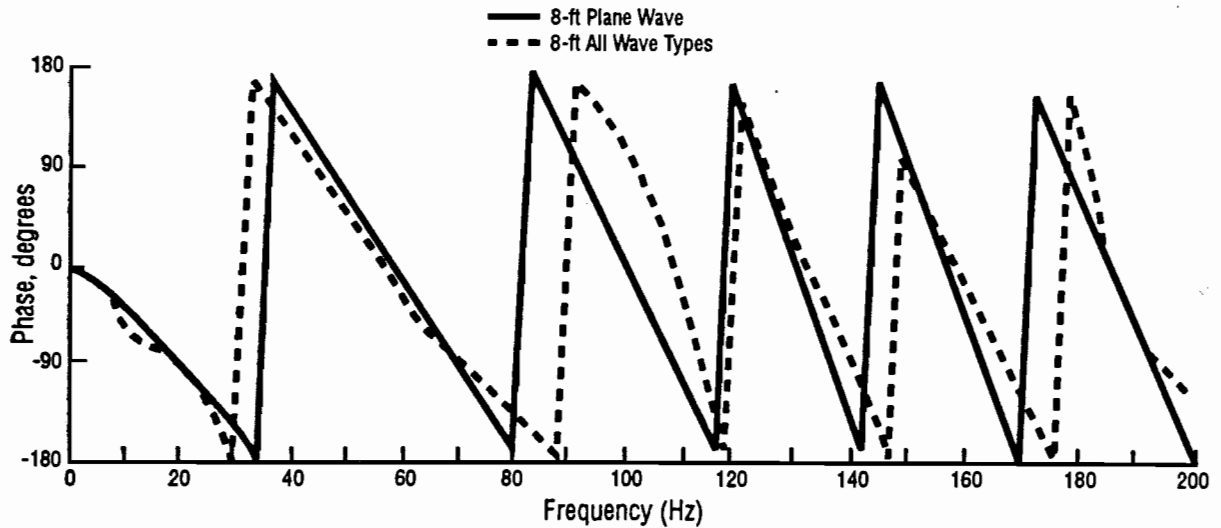


Fig 5.32. Comparison of theoretical phase spectra calculated using the plane wave and Green's function solutions for a receiver spacing of 8 ft (2.4 m).

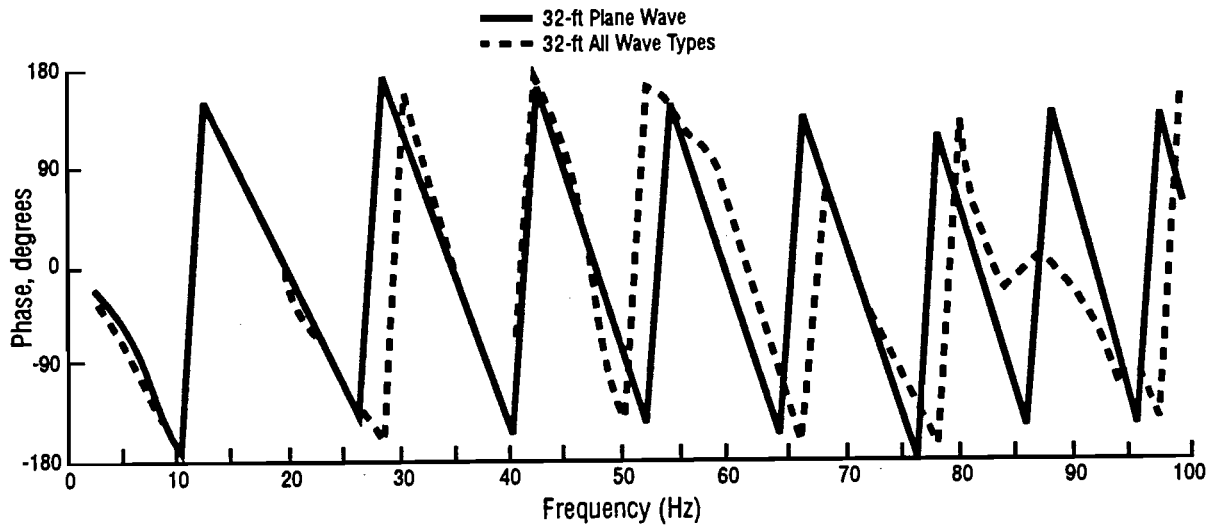


Fig 5.33. Comparison of theoretical phase spectra calculated using the plane wave and Green's function solutions for a receiver spacing of 32 ft (9.8 m).

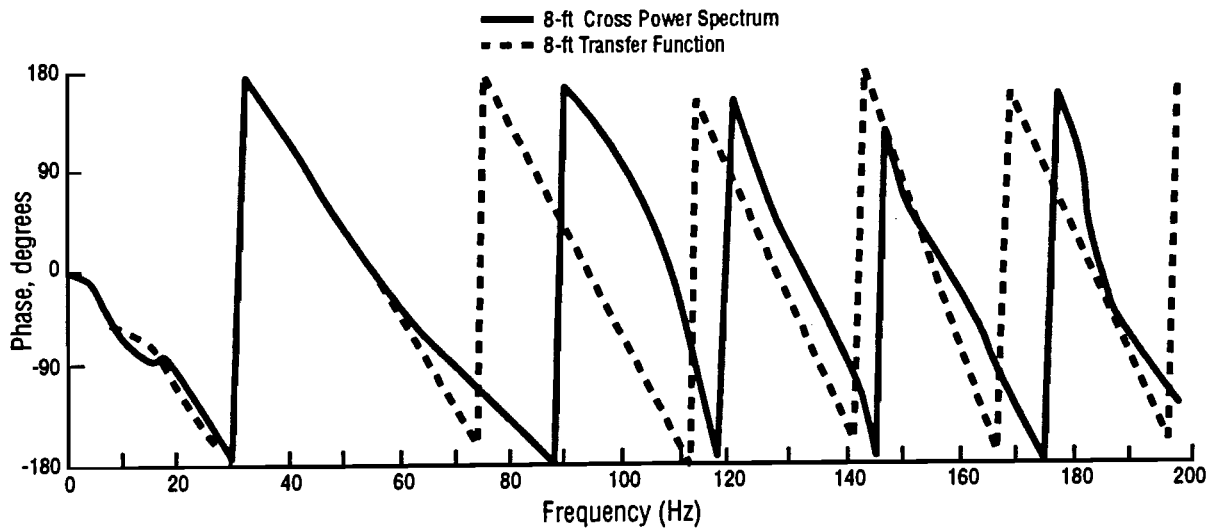


Fig 5.34. Comparison of theoretical phase spectra calculated using the transfer function and the cross power spectrum for a receiver spacing of 8 ft (2.4 m).

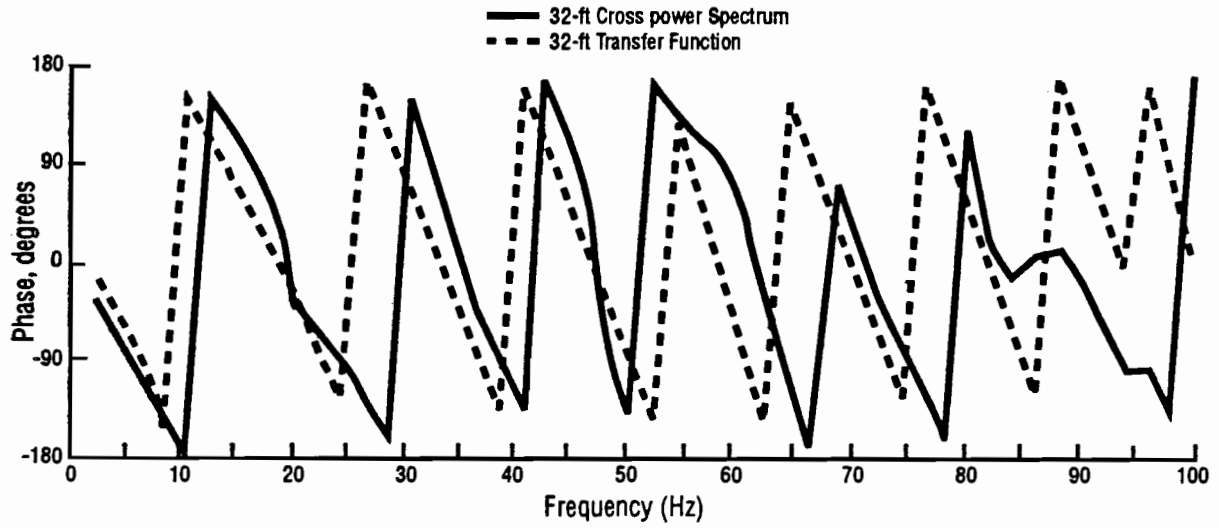


Fig 5.35. Comparison of theoretical phase spectra calculated using the transfer function and the cross power spectrum for a receiver spacing of 32 ft (9.8 m).

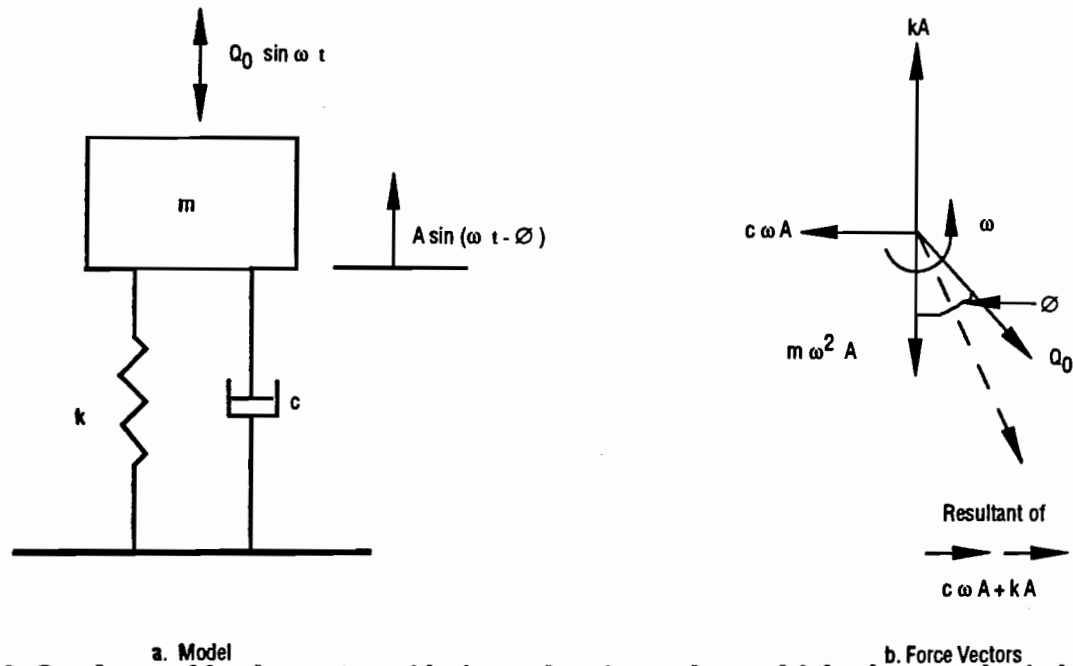


Fig 5.36. One degree of freedom system with viscous damping used to model the electromechanical vibrator (from Richart *et al*, 1970).

CHAPTER 6. COMPARISON OF EXPERIMENTAL AND THEORETICAL WAVE MOTIONS

6.1 INTRODUCTION

As discussed in Chapter Three, there are two basic assumptions which apply to the Spectral-Analysis-of-Surface Waves method in its current form. The first of these assumptions is that only plane surface (Rayleigh) waves are measured during field testing. The effect of body waves on measured dispersion curves is ignored. The second is that only fundamental-mode surface wave motion contributes to the measured dispersion. (Surface wave motion is, in general, a combination of several modes of propagation.) These two assumptions result from the inversion method currently used in surface wave testing. The inversion procedure, which is based upon a

Haskell-Thomson matrix formulation, calculates only the solutions of the equations of motion corresponding to plane surface wave propagation. In using the procedure, the operator usually considers only the fundamental mode when matching the theoretical and experimental dispersion curves as described in Chapter 3. Although algorithms exist which include the effects of body waves and higher modes of surface wave propagation, the algorithms are far too time consuming and expensive to implement in production-type testing (Sánchez-Salineró, 1987). Sánchez-Salineró analytically investigated the implications of using an inversion method based upon the simpler, more economical Haskell-Thomson algorithm and found that it provided acceptable solutions as long as certain criteria regarding relative spacings of source and receivers were observed.

The goal of this chapter is to examine the two assumptions from an experimental viewpoint. This was done by calculating the portion of experimentally-measured displacements resulting from each mode of surface wave propagation to investigate: (1) if surface waves comprise the majority of the measured displacements, and (2) if, furthermore, fundamental-mode surface wave motion dominates. The relative contribution of each mode is calculated using the *mode participation factor*. Finally, a comparison of measured particle motions in cased and uncased boreholes and a comparison of measured and theoretically-predicted particle motions is also presented.

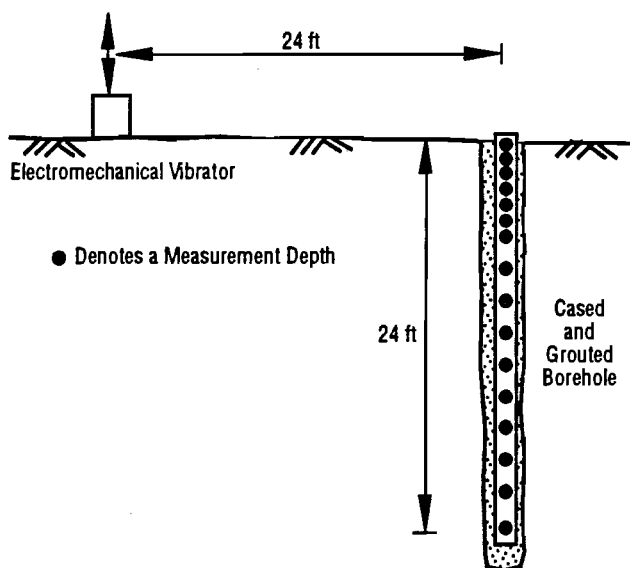


Fig 6.1. Experimental test arrangement used to evaluate the contribution of each surface wave mode.

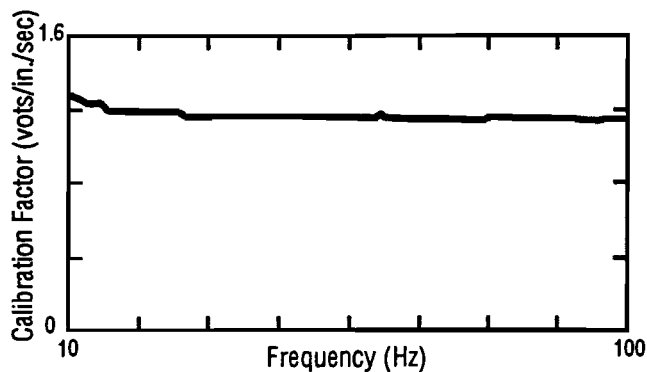


Fig 6.2. Calibration curve of vertical geophone in the 4.5-Hz triaxial geophone package.

6.2 MEASUREMENT OF EXPERIMENTAL PARTICLE MOTIONS

To determine the relative contribution of the various modes of surface wave motion to the overall motion, it was necessary to make measurements of particle motion at various depths within a borehole located at the Hornsby Bend test site. A schematic illustration of the test arrangement used to accomplish this task is presented in Fig 6.1. Sixteen measurement depths were used to define the variation of vertical and horizontal particle motions with depth as accurately as possible. Measurements were performed in 2-ft (0.6-m) increments from the surface to a depth of 24 ft (7.32 m) and also at depths of 1, 3, and 5 ft (0.30, 0.91 and 1.52 m) to provide more detail near the surface. A single, triaxial geophone with a natural frequency of 4.5 Hz was used to measure the vertical, radial and transverse particle velocities in the borehole. Calibration curves for the vertical, radial, and transverse geophones contained within the triaxial geophone package are included in Appendix C. Although it would have been preferable to simultaneously measure

particle velocities at more than one depth, the recording instrument used was limited to two channels. (A Hewlett-Packard Model 3562A Dynamic Signal Analyzer was used to record the signals. A description of the instrument is included in Chapter 3.) An advantage of using only one geophone is that no discrepancies will arise which are caused by the different calibration factors of multiple geophones. At each measurement depth, the geophone was placed and oriented using square aluminum tubing. The geophone was held tightly against the wall of the casing by an inflatable "packer." After the geophone was secured, the orientation tubing was removed to eliminate a potential source of noise. In addition to the triaxial geophone in the borehole, a single vertical geophone with a natural frequency of 2 Hz was placed on the ground surface near the borehole. The 2-Hz geophone acted as a reference so that measurements at each depth could be normalized with respect to the vertical motion at the ground surface if so desired. Normalization reduced the variations in particle motions caused by changes in the output level of the electromechanical source.

The source used in this study was a 50-lb (222-N) electromechanical vibrator located 24 ft (7.32 m) from the borehole as shown in Fig 6.1. The vibrator was programmed to sweep through frequencies ranging from 10 to 100 Hz. The voltage level input to the vibrator was maintained at a constant value so that the output level would be as consistent as possible each time the sweep was repeated for a new measurement depth.

At each depth three pairs of measurements were performed: (1) vertical and radial motion in the borehole, (2) vertical and transverse motion in the borehole, and (3) vertical motion in the borehole and at the ground surface. The power spectrum of each component of motion was recorded using the dynamic signal analyzer. Finally, particle displacement amplitude spectra were calculated from the power spectra by applying the calibration factor of the geophone to the measured voltage and integrating in the frequency domain. Examples of a calibration curve and a particle displacement spectrum are shown in Figs 6.2 and 6.3, respectively. The complete collection of particle displacement spectra are included in Appendix D.

6.3 COMPARISON OF PARTICLE MOTIONS IN A CASED BOREHOLE AND IN THE FREE FIELD

The borehole used to make measurements of particle motion versus depth had 4-in. (10.2-cm) diameter PVC casing which was grouted in place. It was essential, therefore, to determine if the PVC casing and grout influenced the measured particle motions since accurate measurements of the amplitude of motion were critical. Accurate measurements of particle motions in boreholes are

also important in crosshole and downhole testing if values of material damping are to be estimated with either of these methods (Mok, 1987).

To determine to effect of the borehole and casing on particle motions, a second, uncased borehole was drilled approximately three feet (0.91 m) away from the cased borehole. Two triaxial geophones which were identical to the triaxial geophone used in the cased borehole were placed in the uncased borehole at depths of 6 and 12 ft (1.83 and 3.66 m) and the borehole was backfilled with soil. Suddhiprakarn (1984) has determined that the effect of an inclusion such as a geophone on the measured particle motions is very small (less than 3 percent) as long as the ratio of the wavelength to the size of the geophone is greater than four. Since this criterion was satisfied for the entire range of frequencies used in this study (10 to 100 Hz), it was assumed that the two geophones in the backfilled borehole accurately measured the free-field motion. The source was positioned equidistant from both boreholes as shown in Fig 6.4. The geophone in the cased borehole was secured at 6 and then 12 ft (1.83 and

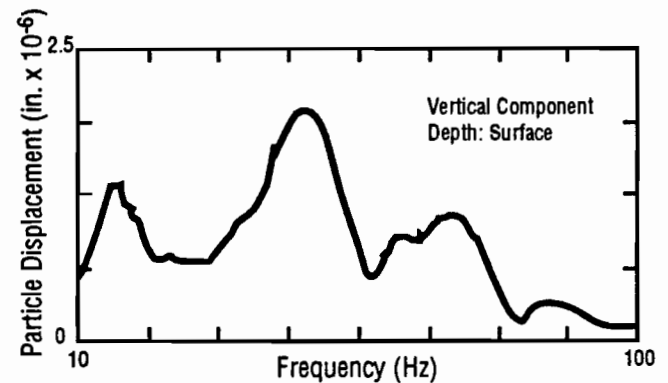


Fig 6.3. Typical particle displacement amplitude spectrum.

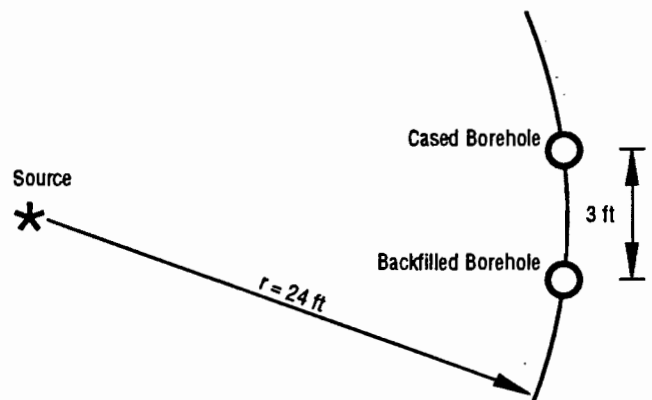


Fig 6.4. Plan view showing the relative locations of the source, cased borehole, and backfilled borehole.

3.66 m) and each component of motion (vertical, transverse and radial) was measured simultaneously with the same component in the backfilled borehole.

A comparison of the measured displacements at depths of 6 and 12 ft (1.83 and 3.66 m) is presented in Figs 6.5 and 6.6, respectively. In each figure, comparisons are presented for vertical, radial, and transverse motion. At a depth of 6 ft (1.83 m), the particle displacements in the vertical and radial directions match within approximately 10 percent, which is considered very good agreement. In the transverse direction, the two motions agree well in the range of frequencies from 25 to 60 Hz but compare poorly from 60 to 90 Hz. It is possible that a resonance in the geophone-PVC casing system may have led to the amplification of the motion at frequencies

centered around 65 Hz. Another contributing factor is that a vertically-acting source on the surface is a poor generator of horizontally-polarized shear waves (SH waves) which the transverse geophone is intended to measure. A more meaningful comparison of transverse motion would be performed using a source which is rich in SH motion. Fortunately, transverse motions were not required to determine the contribution of the various modes of propagation as described in subsequent sections of this chapter.

At the 12-ft (3.66-m) depth (Fig 6.6), the particle displacements in the vertical direction agree very well. In the radial direction, however, the motions compare poorly. The difference between the two motions was traced to a faulty radial geophone in the backfilled

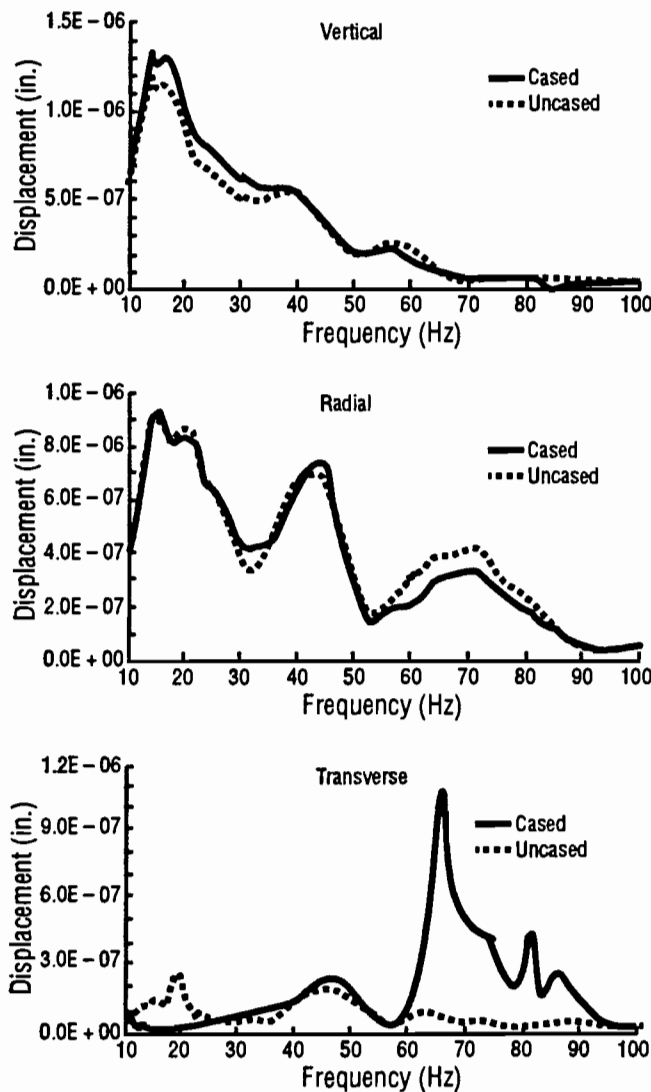


Fig 6.5. Comparison of measured displacements in a cased borehole and free-field displacements at a depth of 6 ft (1.83 m).

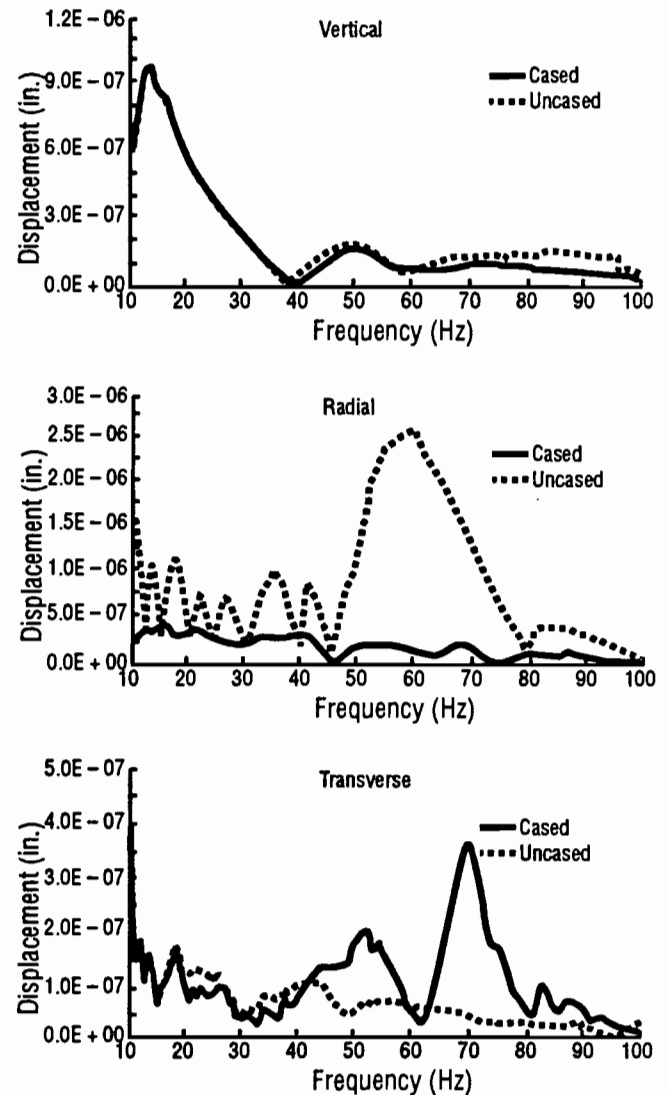


Fig 6.6. Comparison of measured displacements in a cased borehole and free-field displacements at a depth of 12 ft (3.66 m).

borehole. The comparison of displacements in the transverse direction at a depth of 12 ft (3.66 m) indicates the same phenomena which were observed at 6 ft (1.83 m). The motions agree reasonably well from 10 to 30 Hz but rather poorly for the remainder of the record. It is likely that the same factors which contributed to the poor agreement of the transverse motions at a depth of 6 ft (1.83 m) may have also caused the poor agreement at 12 ft (3.66 m).

It was concluded that the measured particle displacements in the cased borehole were not significantly influenced by the presence of the PVC casing and grout. Therefore, particle displacements measured in the cased borehole were assumed to represent free-field motions and were used for the comparisons and calculations presented in the remainder of this chapter. The results also indicate that cased boreholes can successfully be used with the crosshole and downhole seismic methods when accurate amplitudes of motion are required for measurements of material damping.

6.4 COMPARISON OF EXPERIMENTAL AND THEORETICAL MOTIONS

One of the purposes of performing the series of measurements described in this chapter was to see how well experimental displacements could be predicted using theoretical solutions for wave propagation in a layered half-space. In addition, accurate predictions of particle motion are a prerequisite for determining the contribution of different modes of propagation.

In the sections which follow, the results of the experimental measurements of particle displacement versus depth are discussed along with the procedure used to calculate the theoretical displacements. Finally, the experimental and theoretical motions are compared.

6.4.1 EXPERIMENTAL PARTICLE DISPLACEMENTS

The field procedure used to measure the variation of particle displacements with depth is discussed in Section 6.2. A typical particle displacement spectrum resulting from the field measurements is presented in Fig 6.3, and the complete set of measured spectra are included in Appendix D.

Once the experimental displacement spectra had been measured, three frequencies were selected to compare the theoretical and experimental motions versus depth. The lowest frequency (15.96 Hz) was selected to result in a wavelength which was approximately equal to the maximum depth at which displacements were measured (24 ft or 7.32 m). By selecting a low frequency, the number of measurement depths located within one wavelength of the surface was maximized. A high frequency (80.09 Hz) was chosen so that the corresponding wavelength would be short with respect to the distance

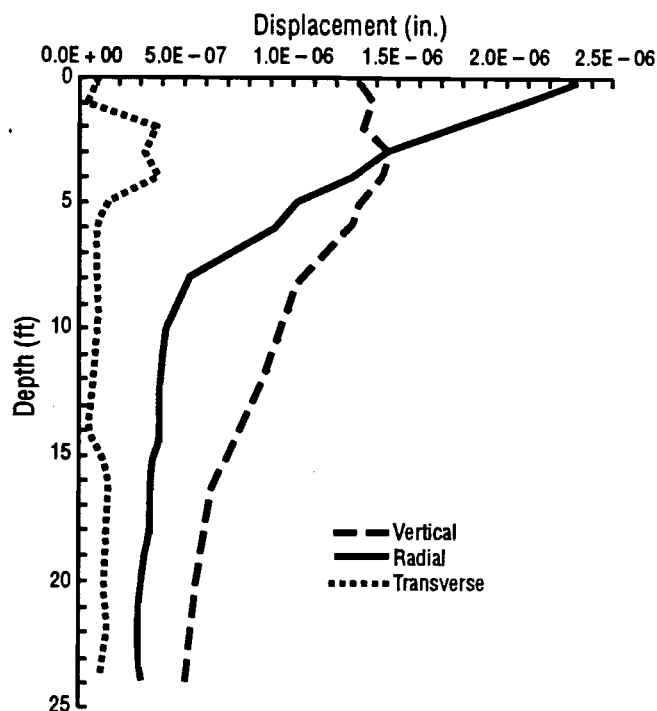


Fig 6.7. Variation of vertical, radial, and transverse particle displacement with depth for a frequency of 15.96 Hz.

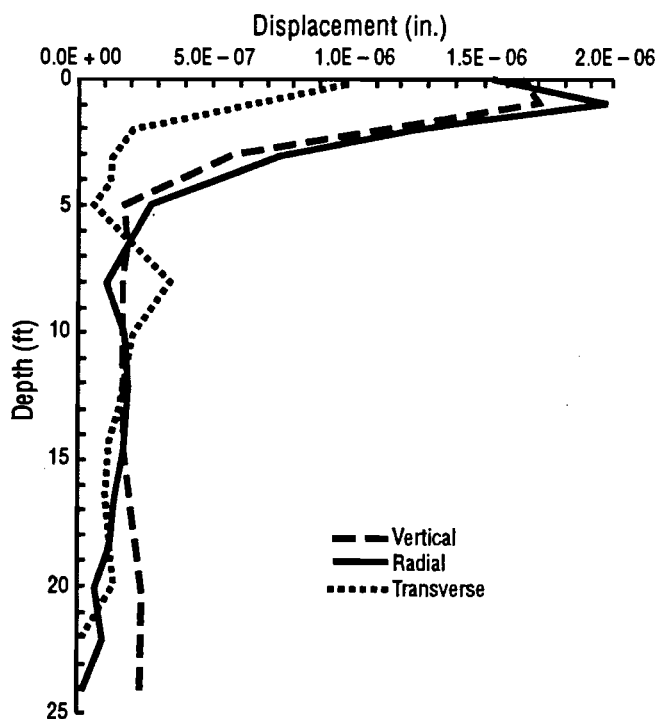


Fig 6.8. Variation of vertical, radial, and transverse particle displacement with depth for a frequency of 50.05 Hz.

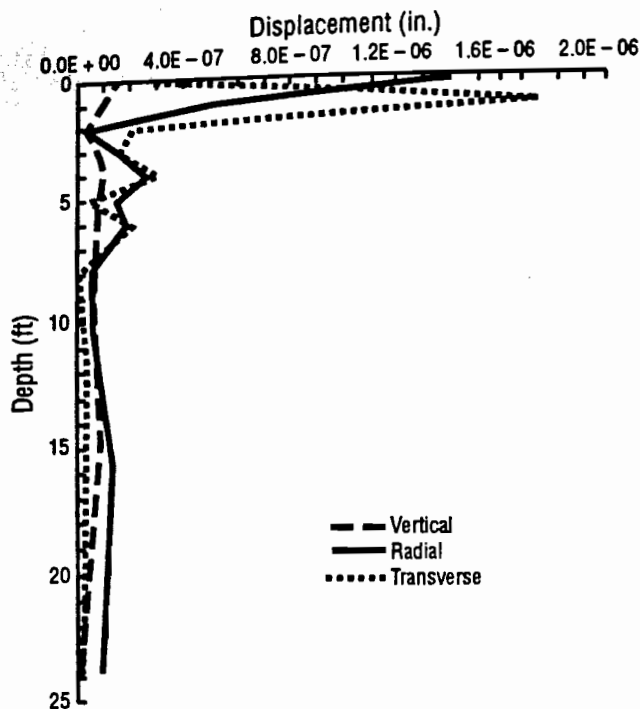


Fig 6.9. Variation of vertical, radial, and transverse particle displacement with depth for a frequency of 80.09 Hz.

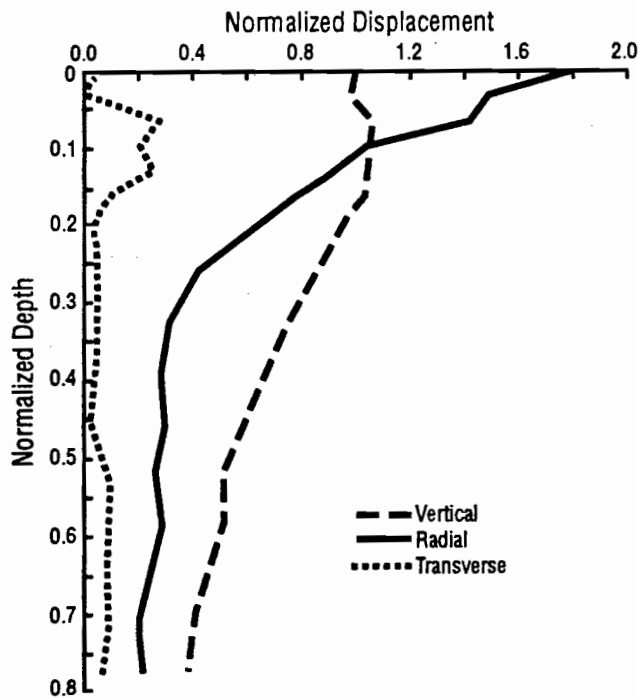


Fig 6.10. Normalized vertical, radial, and transverse displacement versus normalized depth for a frequency of 15.96 Hz.

between the source and the borehole. Although this resulted in relatively few measurement depths within the first wavelength of the surface, the intent of having a large number of wavelengths from the source to the borehole was to reduce the effect of body waves on the measured displacements. Finally, a third frequency, 50.05 Hz, was chosen approximately midway between 15.96 and 80.09 Hz to compromise between the number of measurement depths within the first wavelength of the surface and the number of wavelengths from the source to the borehole. The values of phase velocity corresponding to each frequency are 493, 475, and 376 ft/sec (150, 145, and 115 m/sec) for 15.96, 50.05, and 80.09 Hz, respectively. Values of phase velocity and frequency were used to calculate experimental wavelengths for each frequency. The experimental wavelengths are 30.9, 9.5 and 4.7 ft (9.4, 2.9 and 1.4 m) for frequencies of 15.96, 50.05 and 80.09 Hz, respectively.

For each of these three frequencies, the particle displacements were read from the particle displacement spectra and plotted to examine the variation of displacement with depth. The variation of vertical, radial and transverse motions versus depth are presented in Figs 6.7 through 6.9 for frequencies of 15.96, 50.05 and 80.09 Hz, respectively. The vertical and radial displacements for the lowest frequency (Fig 6.7) decay rapidly with depth as expected for surface wave motion. Furthermore, the vertical displacement amplitudes increased slightly just beneath the surface before rapidly decaying. This distribution of displacements is very similar to the distribution of displacements associated with surface wave motion in a uniform half space (see Fig 3.2). The radial motion differs, however, from that found in a uniform half space because no depth at which the radial displacement is equal to zero (a nodal point) can be easily identified. The transverse displacements are small compared to the vertical and radial motions as expected. For a vertical surface load in a medium in which the material properties vary only with depth and is laterally homogeneous, the theoretical transverse displacements are zero. The relatively large values of transverse displacement observed at depths of 2, 3 and 4 ft (0.61, 0.91 and 1.22 m) may be caused by resonances such as those mentioned in Section 6.3 or by reflections of waves from lateral inhomogeneities.

The distribution of vertical and radial displacements with depth for the middle frequency (Fig 6.8) is very similar to that of the lowest frequency and indicates that the amplitude of displacements decays very rapidly within the first wavelength of the surface. The transverse displacements exhibit more variability than those for the lowest frequency but are still reasonable.

Finally, for the highest frequency (Fig 6.9), the variation of particle displacements is very difficult to interpret. The trends which were present in the low and

middle frequency data are not present in the high frequency data. Part of the reason that this data is difficult to interpret is that there are very few measurement depths available within the first wavelength of the surface to define the variation of displacements accurately. Because the high frequency data is so difficult to interpret, it will not be included in the comparisons and calculations in subsequent sections of this chapter.

To provide a basis for comparing displacement data from different frequencies and to provide a means of correcting the data to account for possible variations in the output level of the source, the displacement data (vertical, radial and transverse components) for the low and middle frequencies were normalized with respect to the vertical displacement at the surface. As described in Section 6.2, a single vertical geophone was placed on the ground surface and was recorded as part of data set at each measurement depth. The output from this geophone was used to normalize the displacements recorded at depth within the borehole. The depths at which measurements were made were also normalized with respect to the experimentally-measured wavelength at each of the frequencies.

Plots of normalized displacement for each component of motion versus normalized depth are shown in Fig 6.10 for the lowest frequency (15.96 Hz) and in Fig 6.11 for the middle frequency (50.05 Hz). In general, data at both frequencies exhibits the same trends as those mentioned previously for the absolute displacements (i.e. rapidly decaying displacements with depth). Plots containing the normalized displacements for both frequencies are shown for vertical motion in Fig 6.12 and for radial motion in Fig 6.13. The comparison of vertical motions indicates that the normalized displacements for each frequency are quite different despite the fact that they both decay rapidly with depth within the first wavelength. The difference is not unexpected since the normalized displacements should be the same only if the measurements were made in a uniform half space. In a heterogeneous, layered half space, the displacements associated with various frequencies will differ because the wave effectively samples different portions of the profile (i.e. dispersion). Although the normalized displacements appear to agree much better for motion in the radial direction (with the exception of displacements in the upper portion of a wavelength), the same reasoning also applies to radial displacements.

6.4.2 THEORETICAL PARTICLE DISPLACEMENTS

A computer program which calculates the Green's function for a layered half space was used to compute the theoretical particle displacements to compare to the experimental displacements. The Green's function for a medium expresses the displacements at one point in the

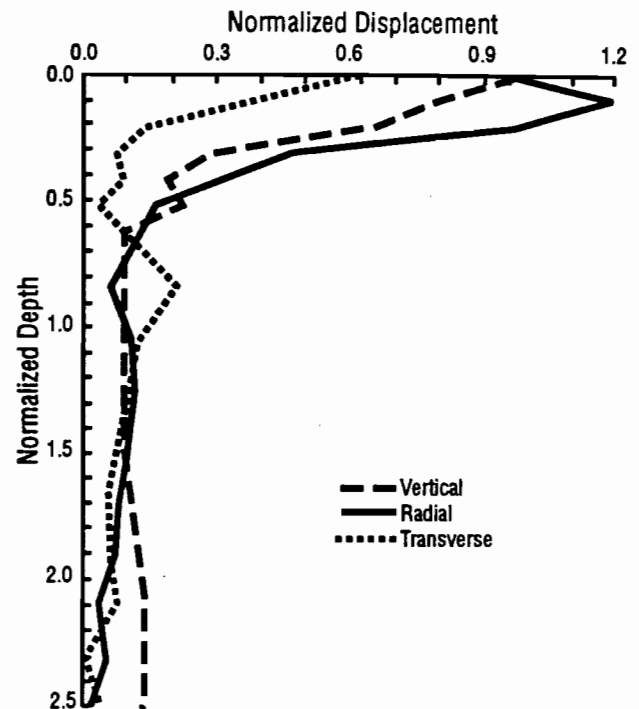


Fig 6.11. Normalized vertical, radial, and transverse displacement versus normalized depth for a frequency of 50.05 Hz.

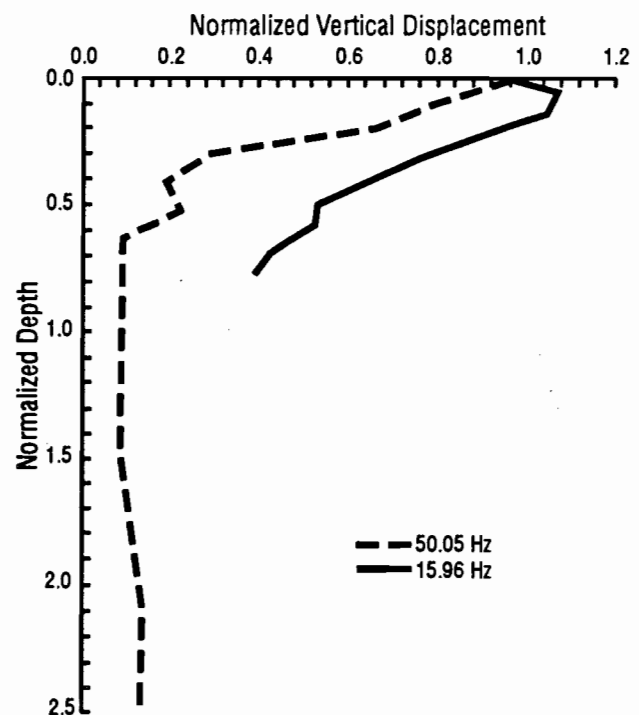


Fig 6.12. Comparison of normalized vertical displacement versus normalized depth.

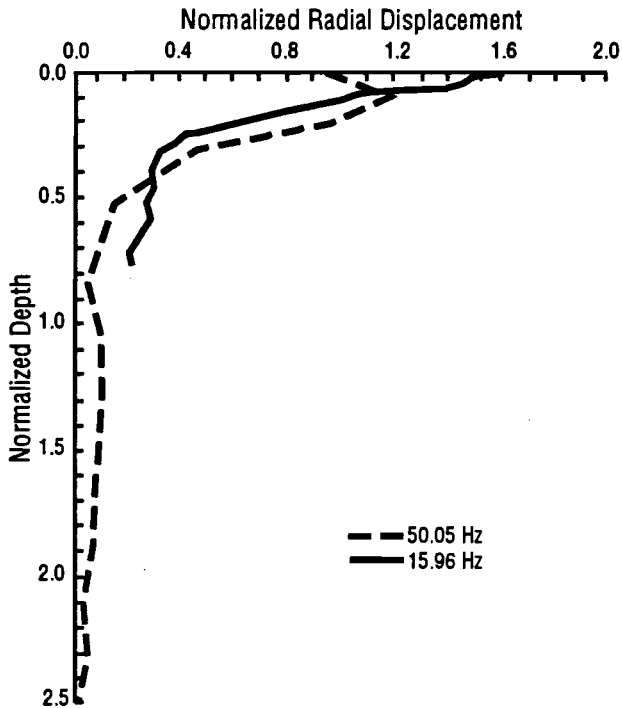


Fig 6.13. Comparison of normalized radial displacement versus normalized depth.

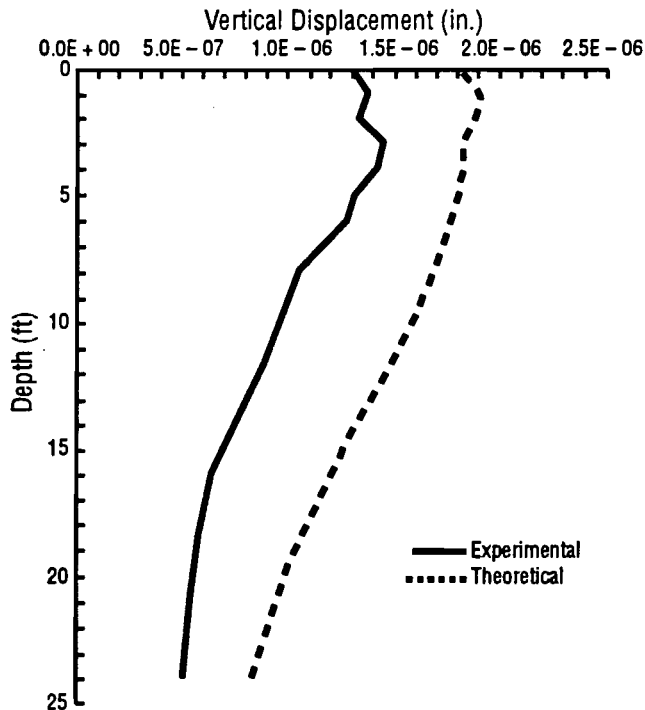


Fig 6.14. Comparison of experimental and theoretical particle displacements in the vertical direction for a frequency of 15.96 Hz.

medium in terms of the applied loads or stresses at another point in the medium. The displacements determined using a Green's function solution include the contributions of all types of waves which propagate in the medium. The computer program used to calculate the theoretical displacements used in this chapter was written by Sánchez-Salinero (1987) and is based upon a formulation of the Green's function developed by Kausel (1981). The version of the program which was used requires the user to manually input the discretized profile. In doing so, the author followed the guidelines recommended by Sánchez-Salinero (1987) to assure that the theoretical displacements were accurate.

The material profile used to calculate the theoretical displacements was the interpreted profile presented in Fig 4.6. The profile was based upon results of several crosshole measurements made in recent years at the Hornsby Bend test site. It was decided to use results from crosshole measurements rather than surface wave measurements to provide an independent means of determining the profile.

6.4.3 COMPARISON OF EXPERIMENTAL AND THEORETICAL PARTICLE DISPLACEMENTS

One method of comparing the experimental and theoretical displacements is to compare the actual values of the measured and predicted motions to see how well they agree. Comparisons between experimental and theoretical displacements for motion in the vertical and radial directions are shown in Figs 6.14 and 6.15, respectively, for the lowest frequency (15.96 Hz). The distribution of vertical particle displacements with depth (Fig 6.12) shows that, although the shape of the two curves is quite similar, the theoretical displacements exceed the measured ones by about 40 percent. The comparison of the radial displacements indicates that the experimental and theoretical displacements have somewhat similar shapes, but that the theoretical displacements again exceed the experimental ones over a significant range of depths. One possible reason that the predicted displacements are greater than the measured ones is that the amplitude of the load used to calculate the predicted displacements is larger than the load which was actually applied in the field. The electromechanical vibrator which was used to generate the motions in the field had a maximum capacity of 50 lb (222 N). The vibrator was operating at frequencies which are in the transition zone between the range of frequencies where the maximum peak-to-peak amplitude of the vibrator limits the available force output and the range of frequencies where the maximum force (50 lb or 222 N) is available. A load of 50 lb (222 N) was used to calculate the theoretical displacements. It is likely that the vibrator was not operating at its maximum capacity and, therefore, the measured displacements are smaller than predicted.

Comparisons between the measured and predicted motions for the middle frequency (50.05 Hz) are presented in Fig 6.16 for vertical motion and in Fig 6.17 for radial motion. The theoretical vertical displacements also exceed the experimental vertical displacements at this frequency, but both measured and predicted displacements have the same general shape. The difference between the two motions is substantially greater than 40 percent (at the surface), however. The experimental and theoretical radial displacements have very different shapes with the theoretical displacements exceeding the experimental displacements over a significant range of depths.

A second means of comparing measured and predicted motions is to normalize the displacements with respect to the vertical motion at the surface. (Experimental and theoretical motions are each normalized by their respective vertical surface motion.) Normalizing the displacements removes differences in motion caused by varying source amplitudes and permits a more meaningful comparison of the differences between measured and predicted displacements. Depths were also normalized with respect to the wavelength corresponding to the frequency of interest.

Normalized experimental and theoretical displacements at the lowest frequency are compared with one another in Fig 6.18 for motion in the vertical direction and in Fig 6.19 for motion in the radial direction. The agreement between the vertical displacements is very good over the entire range of normalized depths. For radial motion, the overall agreement between the experimental and theoretical displacements is reasonable, but the differences between the two curves are more pronounced in this case than in the case of vertical motion.

At the middle frequency, the comparison between the experimental and theoretical displacements is shown in Figs 6.20 and 6.21 for vertical and radial motions, respectively. The vertical motions compare reasonably well; both experimental and theoretical displacements show a very similar decay within the first wavelength of the surface. The radial motions differ substantially near the surface but agree well at depth.

Using the normalized results as the basis of comparison, it may be concluded that the agreement between the experimental and theoretical results is reasonably good, with the exception of radial motions near the surface at the middle frequency. There are two obvious reasons which may account for the discrepancies observed between the measured and predicted motions. The first explanation is that there are either random or systematic errors in the experimental data. The lack of large fluctuations in the experimental displacements at isolated depths seems to indicate that there are relatively few significant random errors in the experimental data. Systematic errors in measuring the experimental displacements

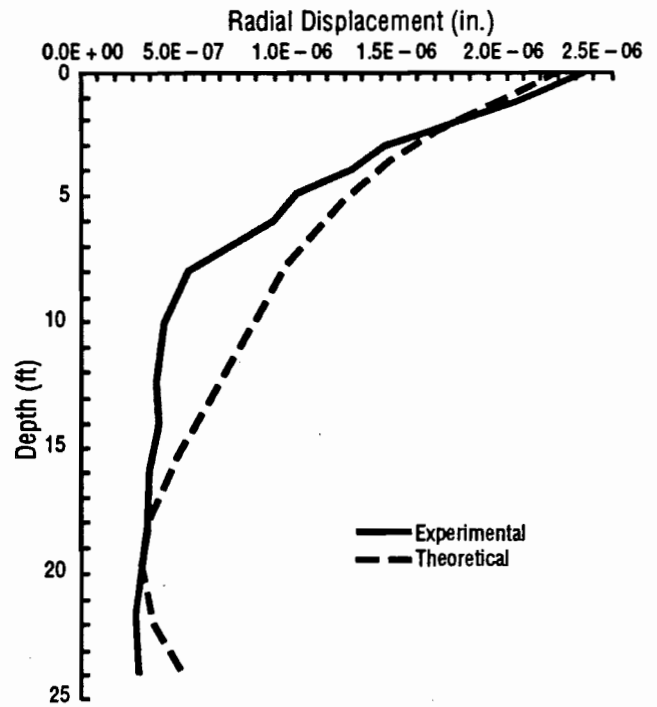


Fig 6.15. Comparison of experimental and theoretical particle displacements in the radial direction for a frequency of 15.96 Hz.

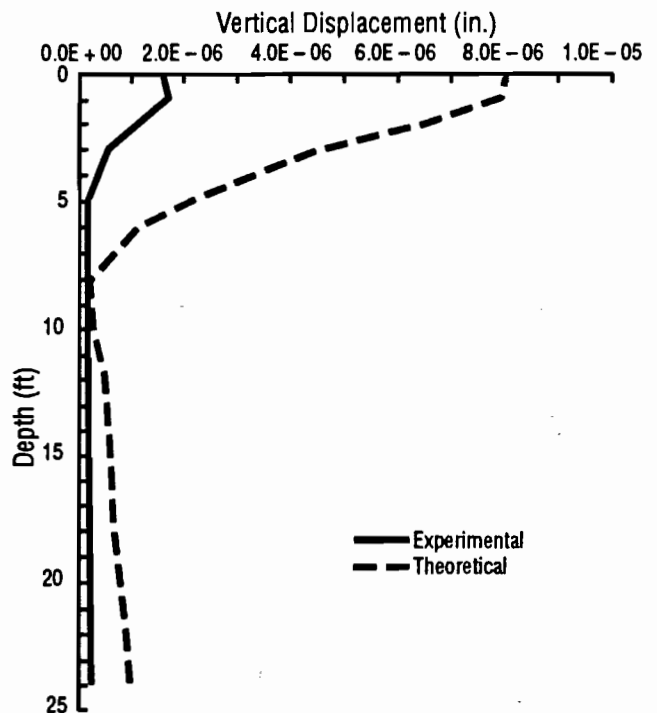


Fig 6.16. Comparison of experimental and theoretical particle displacements in the vertical direction for a frequency of 50.05 Hz.

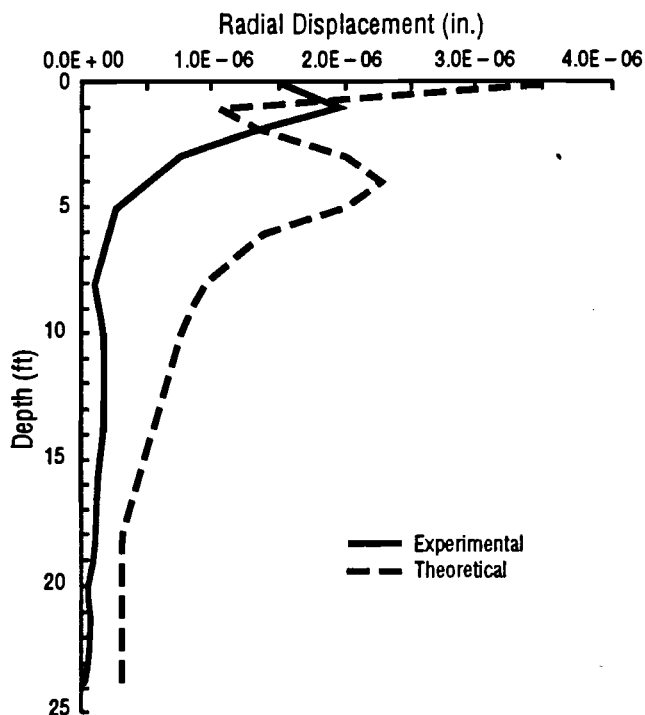


Fig 6.17. Comparison of experimental and theoretical particle displacements in the radial direction for a frequency of 50.05 Hz.

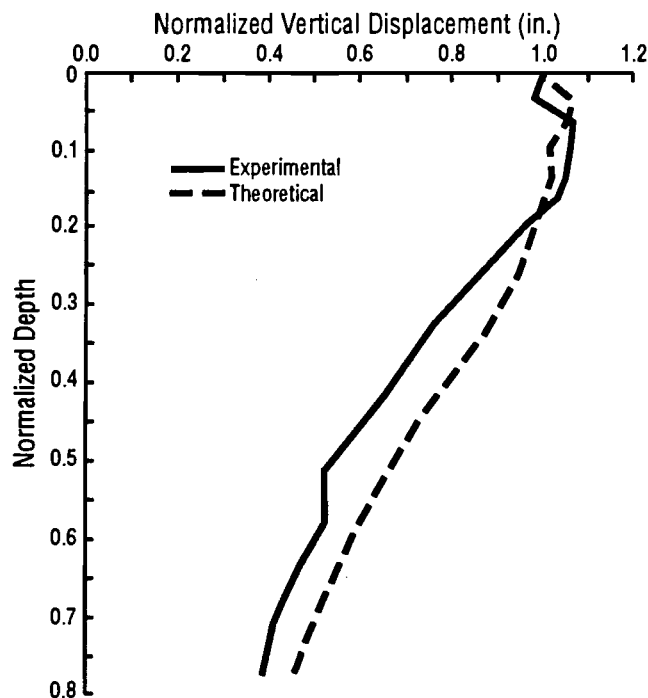


Fig 6.18. Comparison of normalized experimental and theoretical particle displacements in the vertical direction for a frequency of 15.96 Hz.

may be responsible for many of the differences between the measured and predicted motions. Examples of errors of this type which were discussed earlier include resonances in the geophone-PVC casing system, poor coupling between the soil and grout-casing system at shallow depths where the in situ stresses are the smallest (and shrinkage of the grout may occur), and errors caused by differences in the impedance of the soil and casing in the soft soil layers near the surface. The second type of error which may have occurred and led to the observed differences between the experimental and theoretical displacements is an error caused by the inability to model the actual subsurface conditions accurately using a simple "layer cake" model. Obviously, the predicted displacements are only as accurate as the model which was used to calculate them. The presence of lateral inhomogeneities is one example of how the actual subsurface conditions could have differed from those assumed in the model.

6.5 MODE CONTRIBUTION CALCULATIONS

The primary objective of this chapter is to assess the relative contribution of the various modes of surface wave propagation to the overall motion to determine if fundamental-mode surface waves dominate the overall motion. The procedure used to do this consists of three basic steps: (1) calculation and identification of the mode shapes (variation of displacement with depth) for the first few modes of surface wave propagation, (2) determination of the linear combination of these mode shapes which sums to the observed experimental displacements, and (3) calculation of the contribution of each mode using the mode participation factors determined in Step 2. These three steps are explained in detail in the following sections.

This technique has been used by Lysmer and Drake (1972) to determine the portions of incident surface wave energy which were reflected and transmitted by lateral inhomogeneities in a finite element model of the Central Valley of California and the Sierra Nevada.

6.5.1 IDENTIFICATION OF INDIVIDUAL SURFACE WAVE MODES

Two methods were used to identify the displacements associated with the first few modes of surface wave propagation. The first method, which was relied upon to the greatest extent, utilized the same Green's function program described in Section 6.4.2. For each frequency, the displacements corresponding to all modes (surface and body waves) were calculated. In a solution of this type, if there are n layers underlain by a half space, there are $2n + 2$ modes of propagation which must be considered. The subsurface model used for this portion of the study contained 30 layers for the lowest frequency (15.96 Hz) and 37 layers for the middle

frequency (50.05 Hz). (Although only 17 layers are present in the model of the Hornsby Bend site described in Chapter Four, these 17 layers were often subdivided in order to calculate the displacements accurately.) Consequently, there were 62 and 76 modes contained in the solution for the two frequencies of interest. From these many modes, the three or four modes which corresponded to the first few surface wave modes were selected.

The selection process used to identify the modes was often ambiguous because many of the modes have similar characteristics which makes it difficult to choose those modes associated with surface waves. Two criteria were used to make the selection: (1) the characteristics of the wavenumber and (2) the value of phase velocity for each mode. The wavenumber is a complex number defined as the ratio of the circular frequency, ω , to the phase velocity, c . For surface wave modes, the real part of the wavenumber is large compared to the imaginary part (Lysmer and Drake, 1972). This characteristic was used to identify possible surface wave modes. The phase velocity ($c = \omega/k$) of each mode was also calculated and used to further refine the choice of surface wave modes. Using this procedure, it was possible to identify three or four surface wave modes for each frequency. The mode shapes determined for the lowest and middle frequencies are presented later in this section.

The second method used to calculate the modes of propagation associated with surface waves was based upon the solution for the natural modes of propagation which utilizes the continuous stiffness matrix formulation described by Kausel and Roesset (1981). (As a matter of interest, the Green's function solution described in Section 6.4.2 uses the discrete version of the stiffness matrices.) Using this approach it is possible to determine the phase velocities and wavenumbers of the surface wave modes using the methods explained in Kausel and Roesset (1981). Once the phase velocity corresponding to one of the surface wave modes has been calculated, the associated mode shape is found using a technique suggested by Roesset (1988). Unfortunately, the mode shapes determined in this manner are each normalized to a unit vertical displacement at the surface and do not contain information about the actual displacements for each mode or about the relative amplitude of displacements from mode to mode. As such they were used to compare the general mode shapes qualitatively with those determined using the Green's function solution to provide another indication that the proper modes had been selected.

The phase velocities and wavenumbers which were calculated for the first three modes of surface wave propagation at the lowest frequency (15.96 Hz) are summarized in Table 6.1. Only the real parts of the phase velocity and wavenumber are shown in this table because the imaginary parts are nearly zero.

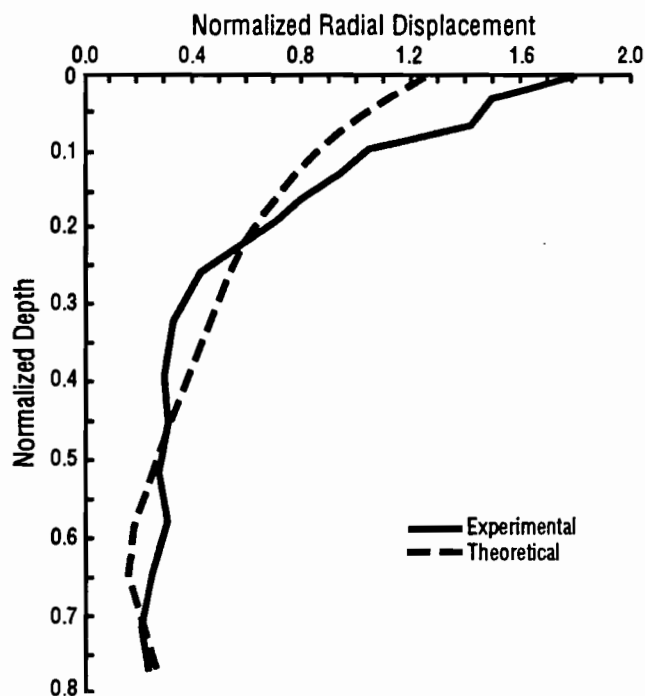


Fig 6.19. Comparison of normalized experimental and theoretical particle displacements in the radial direction for a frequency of 15.96 Hz.

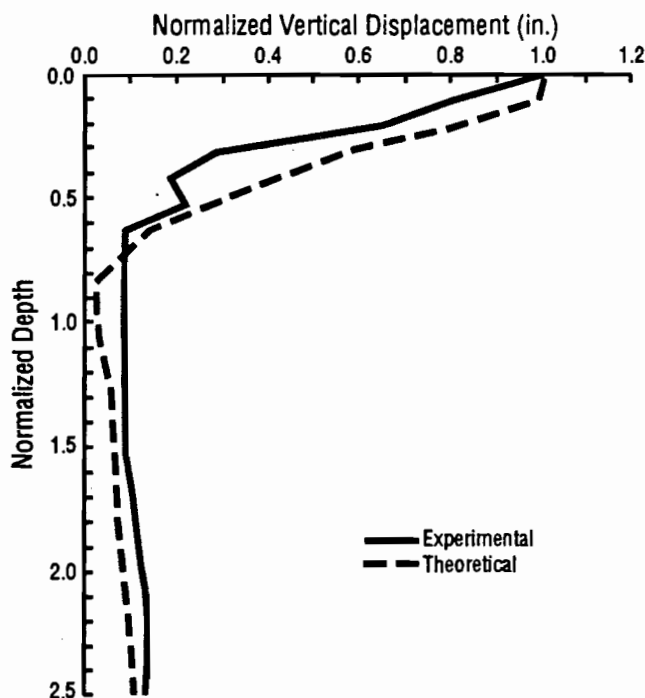


Fig 6.20. Comparison of normalized experimental and theoretical particle displacements in the vertical direction for a frequency of 50.05 Hz.

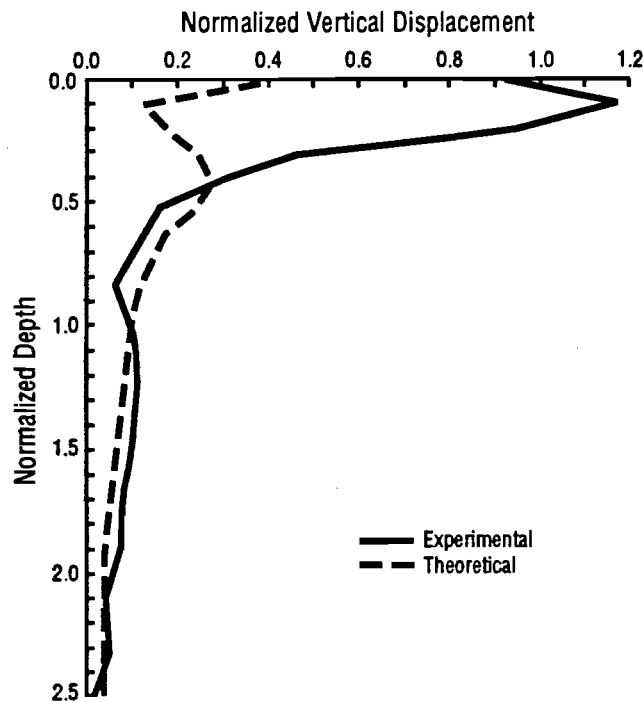


Fig 6.21. Comparison of normalized experimental and theoretical particle displacements in the radial direction for a frequency of 50.05 Hz.

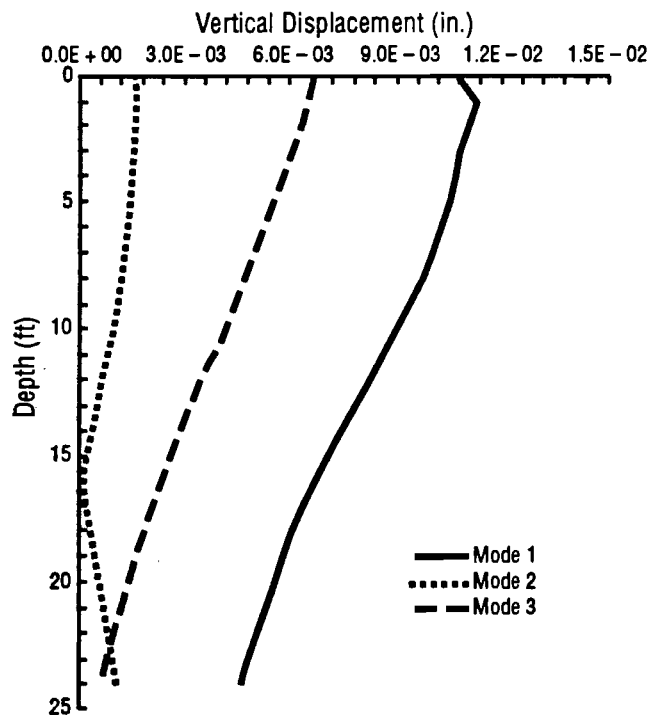


Fig 6.22. Vertical component of displacement for the first three modes of surface wave propagation at a frequency of 15.96 Hz; calculated using the discrete solution.

The values of phase velocity and wavenumber agree very well for the first mode. Values for the second and third modes do not agree as well and serve to emphasize the difficulties encountered when interpreting the modal data.

The variation of the vertical component of displacement with depth for each mode is shown in Fig 6.22 for the discrete solution and in Fig 6.23 for the continuous solution. It is important to remember that the displacements given for the continuous solution are individually normalized for each mode and are not actual displacements, nor is the relative amplitude between the three modes accurate. Nevertheless, it is apparent that the mode shapes are very similar for both the discrete and the continuous solution. This similarity was interpreted as additional evidence that the correct discrete modes had been selected. The horizontal components of the modal displacements are shown in Fig 6.24 for the discrete solution and in Fig 6.25 for the continuous solution. It is important to remember that the horizontal mode shapes calculated using the continuous solution are normalized with respect to a unit vertical displacement for that mode. The shapes of the first and third modes calculated using the two solutions are very similar, but there is a noticeable difference between the second modes. This difference is particularly confusing considering the good agreement between the vertical components of motion for the second mode, and the reasons for the difference are unknown at this time.

TABLE 6.1. SUMMARY OF PHASE VELOCITIES AND WAVENUMBERS ASSOCIATED WITH THE FIRST THREE MODES OF SURFACE WAVE PROPAGATION AT 15.96 HZ

Mode Number	Discrete Solution		Continuous Solution	
	Phase Velocity (ft/sec)	Wave Number	Phase Velocity (ft/sec)	Wave Number
1	661	0.152	658	0.152
2	952	0.073	1,124	0.089
3	2,670	0.037	2,957	0.034

TABLE 6.2. SUMMARY OF PHASE VELOCITIES AND WAVENUMBERS ASSOCIATED WITH THE FIRST FOUR MODES OF SURFACE WAVE PROPAGATION AT 50.05 HZ

Mode Number	Discrete Solution		Continuous Solution	
	Phase Velocity (ft/sec)	Wave Number	Phase Velocity (ft/sec)	Wave Number
1	500	0.628	492	0.639
2	734	0.428	654	0.480
3	843	0.373	822	0.382
4	891	0.353	894	0.351

Phase velocities and wavenumbers for the first four modes for the middle frequency (50.05 Hz) are presented in Table 6.2. As for the low frequency data, only the real parts of the phase velocity and wavenumber are shown in this table. The differences between the phase velocities and wavenumbers calculated using the two alternate approaches again highlight the difficulties encountered in interpreting the data. The vertical components of displacement associated with the first four modes of propagation are shown in Figs 6.26 and 6.27 for the discrete and continuous solutions, respectively. The mode shapes of the first, third, and fourth modes are similar, particularly the first mode. The shapes of the second modes differ significantly. This is reflected in the poor agreement between the phase velocities and wavenumbers of the second mode given in Table 6.2. Unfortunately, no other discrete mode could be identified which agreed more closely with the continuous mode shape. Horizontal components of motion for each mode at 50.05 Hz are shown in Fig 6.28 for the discrete solution and in Fig 6.29 for the continuous solution. The comments which were made about the vertical displacements also apply to the horizontal displacements; the first, third, and fourth modes agree very well but the second mode motion is different for the discrete and the continuous solution.

Despite the differences in some instances between the mode shapes calculated using the two solutions, it was concluded that the discrete mode shapes were sufficiently accurate to determine the mode participation factors as described in the next section.

6.5.2 CALCULATION OF MODE PARTICIPATION FACTORS

The second step of the process used to calculate the mode participation factors was to find the linear combination of the individual modes which sum to the observed displacements (vertical or horizontal). This idea can be expressed in equation form by a system of simultaneous linear equations:

$$\begin{aligned} u_{1,1}\alpha_1 + u_{1,2}\alpha_2 + \dots + u_{1,m-1}\alpha_{m-1} + u_{1,m}\alpha_m &= \delta_1 \\ u_{2,1}\alpha_1 + u_{2,2}\alpha_2 + \dots + u_{2,m-1}\alpha_{m-1} + u_{2,m}\alpha_m &= \delta_2 \\ &\vdots \\ u_{n-1,1}\alpha_1 + u_{n-1,2}\alpha_2 + \dots + u_{n-1,m-1}\alpha_{m-1} + u_{n-1,m}\alpha_m &= \delta_{n-1} \\ u_{n,1}\alpha_1 + u_{n,2}\alpha_2 + \dots + u_{n,m-1}\alpha_{m-1} + u_{n,m}\alpha_m &= \delta_n \end{aligned} \quad (6.1)$$

where

- $u_{a,b}$ = the vertical or horizontal displacement of mode b at depth a ,
- α_c = the mode participation factor of mode c ,
- δ_d = the vertical or horizontal experimental displacement at depth d ,
- m = the number of modes included in the analysis, and

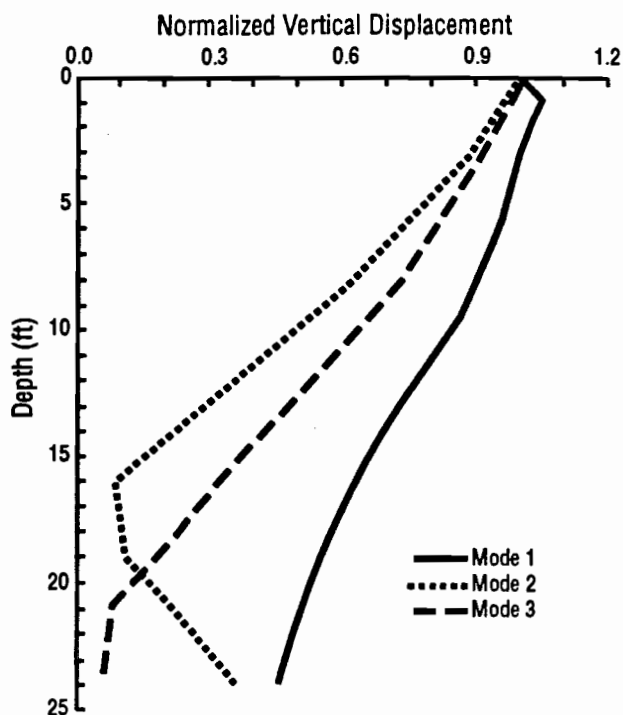


Fig 6.23. Vertical component of displacement for the first three modes of surface wave propagation at a frequency of 15.96 Hz; calculated using the continuous solution.

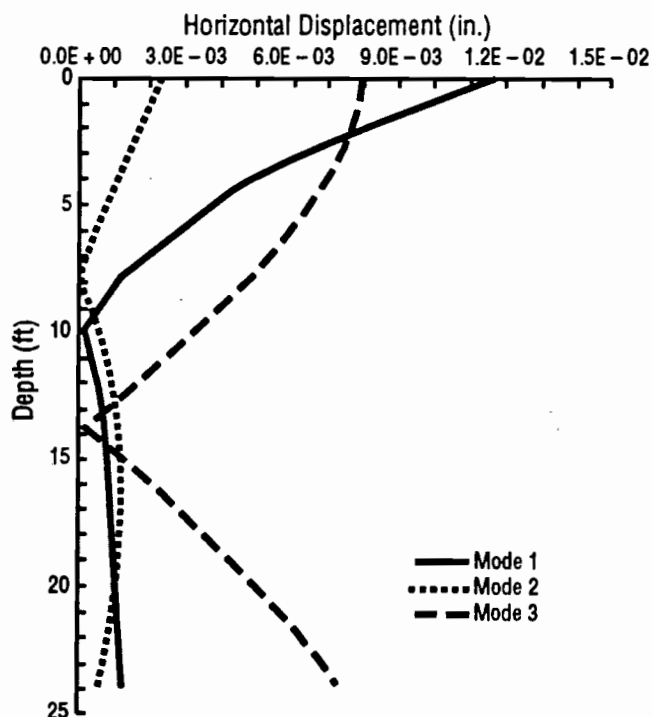


Fig 6.24. Horizontal component of displacement for the first three modes of surface wave propagation at a frequency of 15.96 Hz; calculated using the discrete solution.

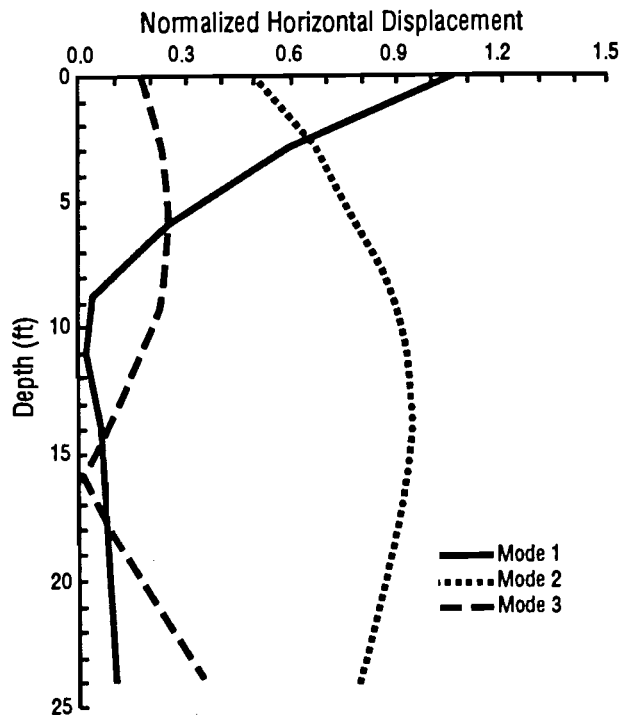


Fig 6.25. Horizontal component of displacement for the first three modes of surface wave propagation at a frequency of 15.96 Hz; calculated using the continuous solution.

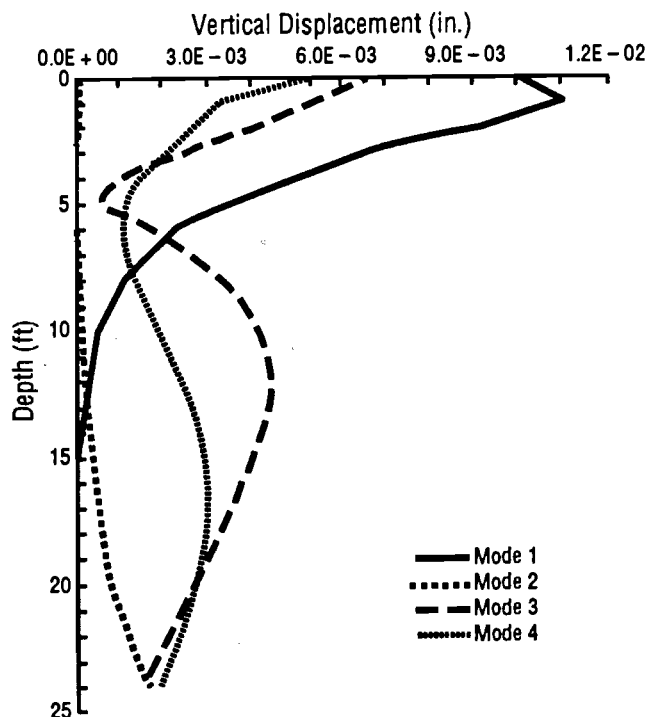


Fig 6.26. Vertical component of displacement for the first four modes of surface wave propagation at a frequency of 50.05 Hz; calculated using the discrete solution.

n = the number of depths included in the analysis.

This set of simultaneous equations can also be expressed in matrix form as follows:

$$\begin{bmatrix} u_{1,1} & u_{1,2} & u_{1,m-1} & u_{1,m} \\ u_{2,1} & u_{2,2} & u_{2,m-1} & u_{2,m} \\ \vdots & \vdots & \vdots & \vdots \\ u_{n-1,1} & u_{n-1,2} & u_{n-1,m-1} & u_{n-1,m} \\ u_{n,1} & u_{n,2} & u_{n,m-1} & u_{n,m} \end{bmatrix} \begin{bmatrix} \alpha_1 \\ \alpha_2 \\ \vdots \\ \alpha_{m-1} \\ \alpha_m \end{bmatrix} = \begin{bmatrix} \delta_1 \\ \delta_2 \\ \vdots \\ \delta_{n-1} \\ \delta_n \end{bmatrix} \quad (6.2)$$

or in shortened notation

$$U \cdot \alpha = \delta \quad (6.3)$$

There were more measurement depths than modes included in the analysis (i.e., more equations than unknowns). The U matrix is, therefore, rectangular and standard methods of solving linear systems of equations cannot be used to solve for α . This overdetermined system of equations must be solved using least squares procedures (Lawson and Hanson, 1974). One method of solving this system of equations is to form the "normal equations" by premultiplying both sides of Eq 6.3 by the Hermitian (complex conjugate) transpose of the U matrix:

$$U^H \cdot U \cdot \alpha = U^H \cdot \delta \quad (6.4)$$

where H denotes the Hermitian transpose of a matrix. The matrix product, $U^H \cdot U$, becomes a square matrix, and the modified system of equations may then be solved using standard methods. Specifically,

$$\alpha = (U^H \cdot U)^{-1} \cdot U^H \cdot \delta \quad (6.5)$$

Using the series of steps outlined in Eqs 6.3 through 6.5, it is possible to calculate the mode participation factors from a set of experimental displacements and the individual mode shapes which correspond to the same type of motion (vertical or horizontal) at the same frequency.

6.5.3 CALCULATION OF THE CONTRIBUTION OF INDIVIDUAL MODES

The final step is to calculate the relative contribution of individual modes to the overall motion. To accomplish this, the rate of energy transmission is determined for each mode using an expression given by Lysmer and Drake (1972):

$$E_s = \pm 0.5\omega k_s |\alpha_s|^2 \quad (6.6)$$

where

E_s = the rate of energy transmission associated with the s^{th} mode,

- ω = the circular frequency (rad/sec),
 k_s = the wavenumber associated with the s^{th} mode,
 α_s = the mode participation factor of the s^{th} mode, and
 $||$ denotes the magnitude of a complex number.

The negative sign in Eq 6.6 corresponds to a situation which occurs infrequently and the rate of energy transmission is usually a positive quantity (Lysmer and Drake, 1972). Equation 6.6 is applicable to only *real* modes (i.e., those modes for which the imaginary part of the wavenumber is equal to zero). Real modes correspond to Rayleigh wave propagation in an undamped medium. Since material damping was included in this study, the wavenumbers associated with Rayleigh wave propagation had a small imaginary component. Despite this discrepancy, Eq 6.6 was used to calculate the rate of energy transmission of each mode. The rate of energy transmission for each mode can be divided by the sum for all of the modes considered to determine the fraction of the total energy contained in any one mode or combination of modes. This fraction also reflects the relative contribution of that mode to the overall motion.

6.5.4 RESULTS

Using the procedures outlined in the previous sections, rates of energy transmission were calculated for both vertical and radial motion at each frequency (15.96 and 50.05 Hz). Two types of displacements were considered in each case: (1) *actual* experimental and modal displacements and (2) *normalized* experimental and modal displacements.

The results obtained using vertical displacements at the lowest frequency are presented in Table 6.3.

The results obtained using the normalized displacements appear to be more reasonable than those calculated using the actual displacements. Based upon a qualitative comparison of the shape of the first mode (Fig 6.22) to the experimental displacements (Fig 6.7), one would expect the first mode to be the dominant mode as it is when normalized displacements are used. The unusual results obtained using the actual displacements are probably reflective of the poor agreement between the actual values of experimental and the theoretical displacements (Fig 6.14). The reasonable results obtained using the normalized displacements are due in large part to the very good agreement between the normalized experimental and theoretical results (Fig 6.18).

For radial motion at the lowest frequency, the relative contributions of the individual modes are given in Table 6.4.

The results are very similar for both types of displacement in this case. Unfortunately, the modal contributions determined using radial motions differ

TABLE 6.3. SUMMARY OF THE RELATIVE CONTRIBUTION OF EACH OF THE FIRST THREE MODES FOR VERTICAL MOTION AT A FREQUENCY OF 15.96 HZ

Mode Number	Percent Contribution	
	Using Actual Displacements	Using Normalized Displacements
1	20.4	74.8
2	38.0	9.0
3	41.6	16.1

TABLE 6.4. SUMMARY OF THE RELATIVE CONTRIBUTION OF EACH OF THE FIRST THREE MODES FOR RADIAL MOTION AT A FREQUENCY OF 15.96 HZ

Mode Number	Percent Contribution	
	Using Actual Displacements	Using Normalized Displacements
1	27.7	25.8
2	72.3	74.1
3	0.0	0.0

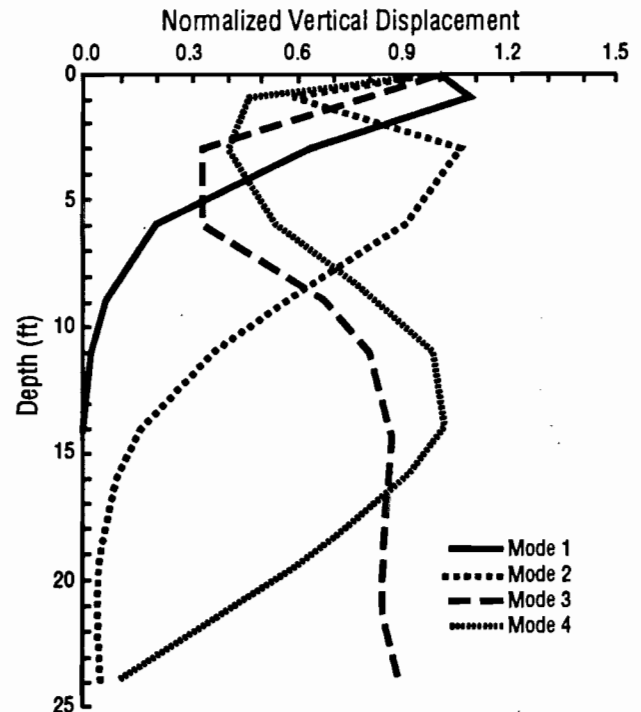


Fig 6.27. Vertical component of displacement for the first four modes of surface wave propagation at a frequency of 50.05 Hz; calculated using the continuous solution.

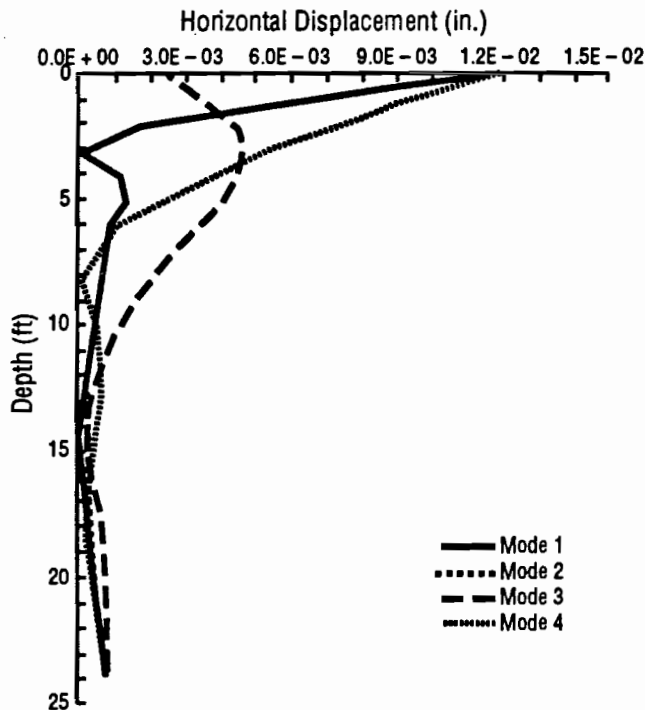


Fig 6.28. Horizontal component of displacement for the first four modes of surface wave propagation at a frequency of 50.05 Hz; calculated using the discrete solution.

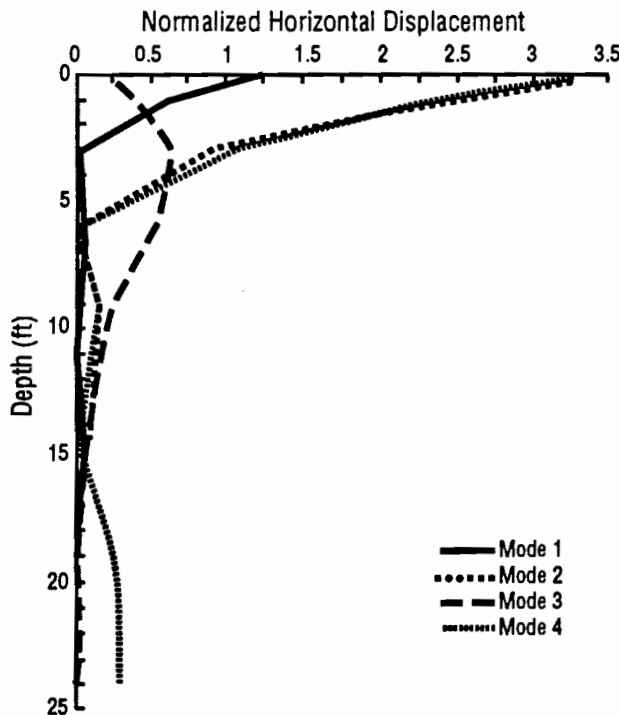


Fig 6.29. Horizontal component of displacement for the first four modes of surface wave propagation at a frequency of 50.05 Hz; calculated using the continuous solution.

substantially from those determined using vertical motions when, in fact, they should be the same. The difference is probably caused by discrepancies between the experimental and theoretical displacements (Figs 6.15 and 6.19).

Similar variations are present in the data calculated for the middle frequency. The relative contributions of each of the first four modes are given in Table 6.5 for vertical motion and in Table 6.6 for radial motion.

To provide a basis for analyzing these results, the theoretical mode participation factors (calculated as part of the Green's function solution) were used to determine the partition of energy between the modes for the theoretical solution. The results are summarized in Table 6.7. These values of modal contribution apply to both vertical and radial motion.

There is a reasonably good agreement between the theoretical values for each mode at 15.96 Hz and the values given in Table 6.3 for normalized displacements. This reflects the good agreement between the normalized experimental and theoretical displacements as discussed previously. Unfortunately, there is poor agreement between the values in Table 6.7 and the remainder of the experimental values.

In general, two related factors are responsible for the variability in the results. One factor which has already been mentioned is the poor agreement between the experimental and theoretical results. Although the trends in the experimental and theoretical data are similar, the differences are still substantial enough to cause significant variations in the mode contribution data. A second, related factor involves the manner in which the mode participation factors are calculated as described in Section 6.5.2. The matrix product, $U^H \cdot U$, in Eq 6.4 is ill-conditioned. An ill-conditioned matrix means that small errors in the right-hand vector, δ , are "magnified" in the solution vector, α (Golub and Van Loan, 1983). Therefore, errors in the experimental displacements influence the calculated mode participation factors to a large extent. Similarly, if differences between the experimental and theoretical displacements are considered to be "errors" in the experimental values, the mode participation factors will probably not be accurate. The ill-conditioned matrix probably results from the similarities between the individual mode shapes for a given direction of particle motion (vertical or horizontal) and frequency.

6.6 SUMMARY

Two assumptions which play an important role in the Spectral-Analysis-of-Surface-Waves (SASW) method in its current form are: (1) the effects of body waves on the measured dispersion curve are ignored and (2) the experimental dispersion curve is assumed to include only fundamental-mode surface wave motion. The purpose of this chapter is to investigate these two assumptions

experimentally by determining the portion of the total motion which is composed of fundamental mode surface wave energy. Measurements of particle displacement were made in a cased borehole at depths ranging from the surface to 24 ft (7.3 m) so that the relative contributions of the various modes of surface wave propagation could be determined. The source was an electromagnetic vibrator placed on the surface and located 24 ft (7.3 m) from the borehole. Also included in this chapter are a comparison of measured particle displacements in a cased borehole and in the free field and a comparison between experimentally-measured displacements and those predicted using a Green's function algorithm.

Comparisons of motions in a cased borehole and in the free field indicate that the grout and PVC casing had little impact on the measured displacements in the vertical and radial directions at depths of 6 and 12 ft (1.83 and 3.66 m). In addition, the ratio of the wavelength to the size of the geophone was large enough to prevent the geophone itself from influencing the motion. This result has important implications for the use of cased boreholes for measuring material damping with borehole seismic methods such as the crosshole and downhole methods. Experimental and theoretical particle displacements were compared to determine how well algorithms such as the Green's function solution can predict measured displacements. Although the actual experimental and theoretical displacements do not agree well (probably due to uncertainties in the output level of the electromagnetic vibrator), the normalized displacements agree reasonably well in most instances. Possible reasons for the discrepancies between the experimental and theoretical solutions include errors in the experimental measurements, errors caused by the inability of the simple model used in the theoretical calculations to accurately model the actual subsurface conditions, and errors in the parameters (i.e. wave velocities) of the model.

There is a significant variability in the values calculated for the relative contribution of each of the modes of surface wave propagation. This variability can be traced to two factors: (1) differences between the experimental and theoretical displacements and (2) errors in the mode contribution values caused by the poorly conditioned system of equations used to determine the mode participation factors. Theoretical solutions indicate that the fundamental-mode surface wave composes between 72 and 86 percent of the total motion.

Finally, there are several aspects of the measurements and calculations performed in this study which could be improved in future studies. The most significant improvement in the measurement of particle displacements in the field would be to simultaneously measure

particle motions at as many depths as possible. This improvement would reduce the variability in the experimental displacements caused by measuring each depth individually which would, in turn, increase the accuracy of the mode contribution results. Another improvement would be to use a more sophisticated algorithm (such as singular value decomposition) to solve the rectangular system of equations for the mode contribution calculations. It is also possible to use the vertical and radial particle motions *simultaneously* to calculate the mode contribution factors.

TABLE 6.5. SUMMARY OF THE RELATIVE CONTRIBUTION OF EACH OF THE FIRST FOUR MODES FOR VERTICAL MOTION AT A FREQUENCY OF 50.05 HZ

Mode Number	Percent Contribution	
	Using Actual Displacements	Using Normalized Displacements
1	29.4	17.6
2	5.6	3.7
3	7.2	8.8
4	57.9	70.0

TABLE 6.6. SUMMARY OF THE RELATIVE CONTRIBUTION OF EACH OF THE FIRST FOUR MODES FOR RADIAL MOTION AT A FREQUENCY OF 50.05 HZ

Mode Number	Percent Contribution	
	Using Actual Displacements	Using Normalized Displacements
1	2.8	0.9
2	68.7	39.6
3	4.6	2.6
4	23.8	56.9

TABLE 6.7. SUMMARY OF THE RELATIVE CONTRIBUTION OF EACH MODES FOR THE THEORETICAL SOLUTION

Mode Number	Percent Contribution	
	15.96 Hz	50.05 Hz
1	72.1	86.0
2	26.0	0.0
3	1.8	8.9
4		5.1

CHAPTER 7. INFLUENCE OF SOURCE-RECEIVER SPACING AND RELATIVE LAYER STIFFNESS ON SURFACE WAVE TESTS

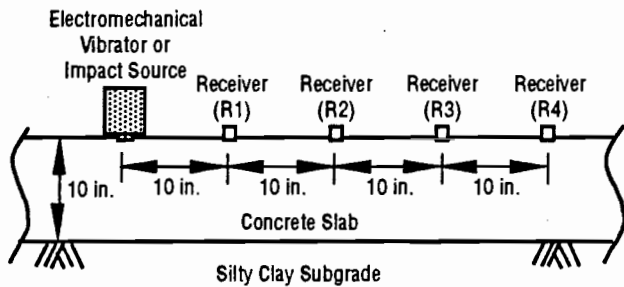
7.1 INTRODUCTION

Two factors which influence surface wave testing are the relative spacing of the source and receivers and the relative stiffness of adjacent layers within the profile. Surface waves tests were performed on the concrete test slab described in Chapter 4 to investigate the influence of these two factors. Testing was performed on the slab while the concrete was curing. The stiffening of the concrete during curing provided a simple means of varying the stiffness of the top layer in the profile to create profiles with different stiffness ratios between adjacent layers. In this manner, the influence of the

relative stiffness of the top layer and the underlying material on surface wave dispersion could be determined. For each series of measurements, six combinations of source-receiver spacings were used to investigate the effect of the relative distances between the source and receivers on the measured dispersion.

Several other tests were performed either on the curing concrete of the test slab or on concrete test specimens so that comparisons could be made with the results of surface wave tests on the slab. One such comparison is between the values of shear wave velocity determined using surface waves and those measured in the laboratory using the resonant column technique. Direct measurements of the compression wave velocity of the curing concrete were also made so that the Poisson's ratio of the concrete could be determined. Penetration tests of fresh concrete are used to determine the times to initial and final set of the concrete. Values of shear wave velocity are compared with values of penetration resistance to evaluate the use of shear wave velocity as a means of determining the set of concrete. Finally, Young's moduli from seismic measurements are compared to Young's moduli from cylinder compression tests to examine the differences between seismic (low-strain) moduli and higher-strain moduli.

An important point to remember is that all curing times mentioned in this chapter are elapsed times between the time when water was added to the portland cement-aggregate mixture at the batch plant and the time at which the test was performed.



Note: 1. All measurements are nominal
2. Plan dimensions of slab are 8 ft by 12 ft

Fig 7.1. Test configuration used for surface wave tests on the concrete slab during curing.

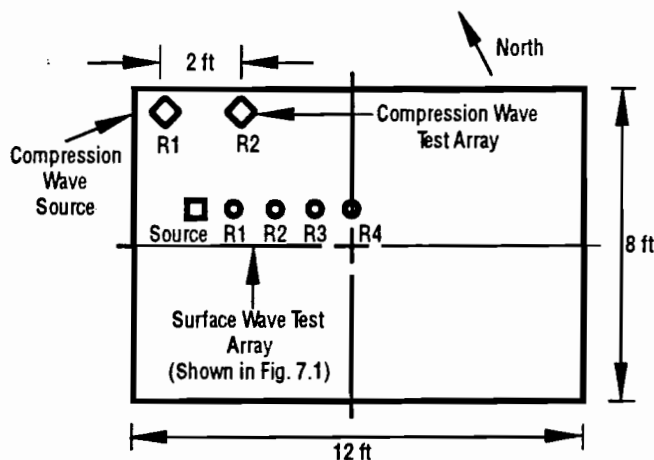


Fig 7.2. Plan view of concrete slab showing locations of seismic arrays used in surface wave and compression wave testing.

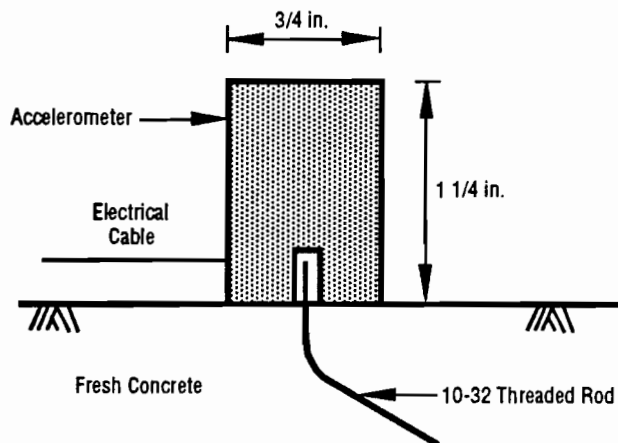


Fig 7.3. Technique used to couple accelerometers to fresh concrete.

7.2 TEST PROCEDURES

In the following sections, the equipment and test procedures used to perform the surface wave, compression wave, and other tests which were employed to determine the properties of the concrete during the time it was curing are discussed.

7.2.1 SURFACE WAVE TESTS

The test configuration used to perform the surface wave tests is shown in Fig 7.1. Four receivers were used so that any two could be combined to yield different relative spacings between the source and receivers. The nominal spacing between adjacent receivers was 10 in. (25.4 cm). (The actual distance between any two adjacent receivers varied from 9.375 to 10.5 in. (23.8 to 26.7 cm).) A plan view showing the location of the source and four receivers relative to the boundaries of the slab is presented in Fig 7.2.

PCB Model 308B02 accelerometers were used as receivers for the surface wave tests. The nominal calibration factor of these accelerometers is 1 volt/g. The accelerometers were coupled to the fresh concrete using short (2-in. (5.1-cm)-long) pieces of 10-32 threaded rod embedded into the concrete as illustrated in Fig 7.3. Two sources were used to perform the surface wave tests. A 50-lb (223-N) electromechanical vibrator was used during the early stages of testing when the concrete surface was too soft to allow impact sources to be used. The vibrator was supported by a wooden frame which prevented the vibrator from penetrating the uncured concrete and kept the vibrator upright. The frame was supported by the ground surface surrounding the slab and was constructed in such a way that the 2.5-in. (6.35-cm) diameter base plate of the vibrator was the only surface in contact with the concrete. Once the concrete had cured sufficiently, the frame was no longer required and was removed. Swept-sine input motion was used with the vibrator over frequencies ranging from 20 Hz to 20 kHz. A small, 4-oz. ballpeen hammer was also used as a source once the concrete had cured enough to permit impact testing. The hammer was successfully used to generate frequencies as high as 40 kHz.

A Hewlett-Packard Model 3562A Dynamic Signal Analyzer was used to record and process data. A complete description of this piece of equipment is included in Chapter 3. Unfortunately the HP 3562A is a two-channel device which made it necessary to repeat the frequency sweep for each pair of receivers which were measured (6 pairs in all).

7.2.2 COMPRESSION WAVE TESTS

Compression wave tests were performed to provide an independent means of measuring the compression wave velocity of the concrete as it cured. Two PCB Model 303A12 accelerometers were embedded

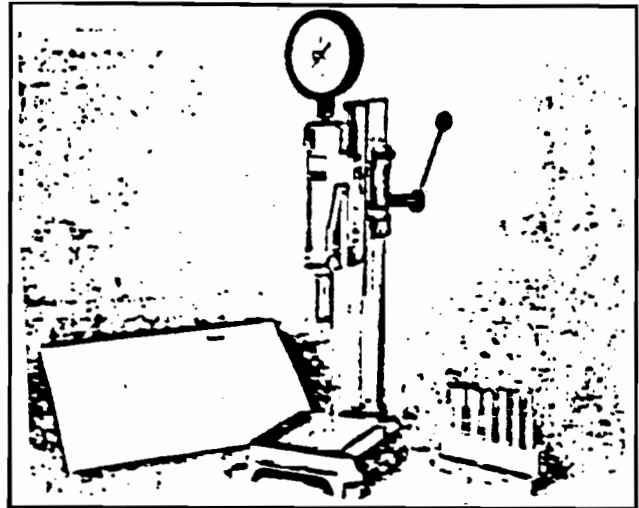


Fig 7.4. Concrete penetrometer used to determine times of initial and final sets.

horizontally at the mid-depth of the slab (approximately 5 in. (12.7 cm) below the surface) at the locations indicated in Fig 7.2. The distance separating the two accelerometers was 2 ft (0.61m). The 4-oz. (113-g) ballpeen hammer was used to strike the edge of the slab at the location shown by the arrow in Fig 7.2 and generate compression waves. Time records at each receiver were captured using the HP 3562A, and the time difference between the first arrivals at each accelerometer was used to calculate the compression wave velocity. Compression wave tests were performed to accompany each set of surface wave measurements.

7.2.3 SUPPLEMENTAL TESTS

In addition to the in situ seismic tests which were performed on the test slab, three other types of tests were conducted to compare with these tests. Standard compression tests performed on 6-by-12-in. (15.2-by-30.5-cm) cylindrical specimens (ASTM, 1988a). Compression tests were performed 1, 3, 7, and 28 days after the slab was poured. Young's modulus of the cylinders was also determined as part of the cylinder testing program so that seismic moduli could be compared with cylinder moduli.

Tests were also conducted to determine the times to initial and final set of the concrete. These tests involve a sample of concrete which has been passed through a No. 4 sieve to remove the large aggregate. A penetrometer is forced into the sample of concrete, and the load necessary to cause 1 in. (2.54 cm) of penetration is recorded. A photograph of the type of penetrometer used in this study is shown in Fig 7.4. The load is divided by the cross-sectional area of the penetrometer to calculate the penetration resistance. Initial set is defined as the time at which the penetration resistance is equal to 500 psi (3.45 MPa). Final set is the time at which the penetration resistance is

equal to 4,000 psi (27.6 MPa). A complete description of the test procedure is given in ASTM (1988b).

Finally, torsional resonant column tests were performed on 3-by-6-in. (7.6-by-15.2-cm) cylindrical samples of concrete to compare laboratory values of shear wave velocity to those obtained in situ using surface wave measurements. Resonant column tests were performed using the procedure described by Ni (1987).

7.3 RESULTS OF SURFACE WAVE TESTS

For each set of surface wave measurements, six source-receiver combinations were used to investigate the influence of the relative spacing between the source and receivers on the measured dispersion. Two parameters can be used to describe the relative spacing of the source

and receivers. These parameters are d_1 and d_2/d_1 where d_1 and d_2 are the distances from the source to the first and second receivers, respectively. Values of these two parameters for each of the six combinations of receivers are given in Table 7.1. Also shown in Table 7.1 is the ratio of d_1 to the thickness of the slab, H . This ratio is often used as a parameter in theoretical studies of source-receiver combinations and is included here for completeness. A value of d_2/d_1 equal to two is normally used for testing with the SASW method. In all of the dispersion curves presented in this chapter, wavelengths longer than three times the distance from the source to the first receiver ($l_R > 3d_1$) have been removed from the dispersion curve to eliminate any significant near-field effects as discussed in Section 3.4.2. Finally, phase spectra, coherence functions, and auto power spectra for each of the test series described in this chapter are included in Appendix E.

TABLE 7.1. VALUES OF d_1 AND d_2/d_1 FOR EACH OF THE SIX RECEIVER COMBINATIONS USED IN THE SLAB TESTS

Receiver Combination	d_1 (ft)	d_2/d_1	d_1/H
R2-R4	1.66	2.0	2.00
R1-R2	0.78	2.1	0.94
R3-R4	2.50	1.3	3.00
R1-R3	0.78	3.2	0.94
R2-R3	1.66	1.5	2.00
R1-R4	0.78	4.2	0.94

7.3.1 ON SUBGRADE

A series of tests was performed on the subgrade prior to casting the slab. Four receiver combinations were used for this series of tests. (Receiver combinations R1-R4 and R2-R3 were inadvertently omitted from the test series.) The dispersion curves for the four receiver combinations are shown in Fig 7.5. Dispersion curves for the two receiver spacings with a d_2/d_1 ratio equal to two are shown in Fig 7.5a. These receiver spacings are designated as *standard* spacings because a ratio of d_2/d_1 equal to two is usually used in production testing. The

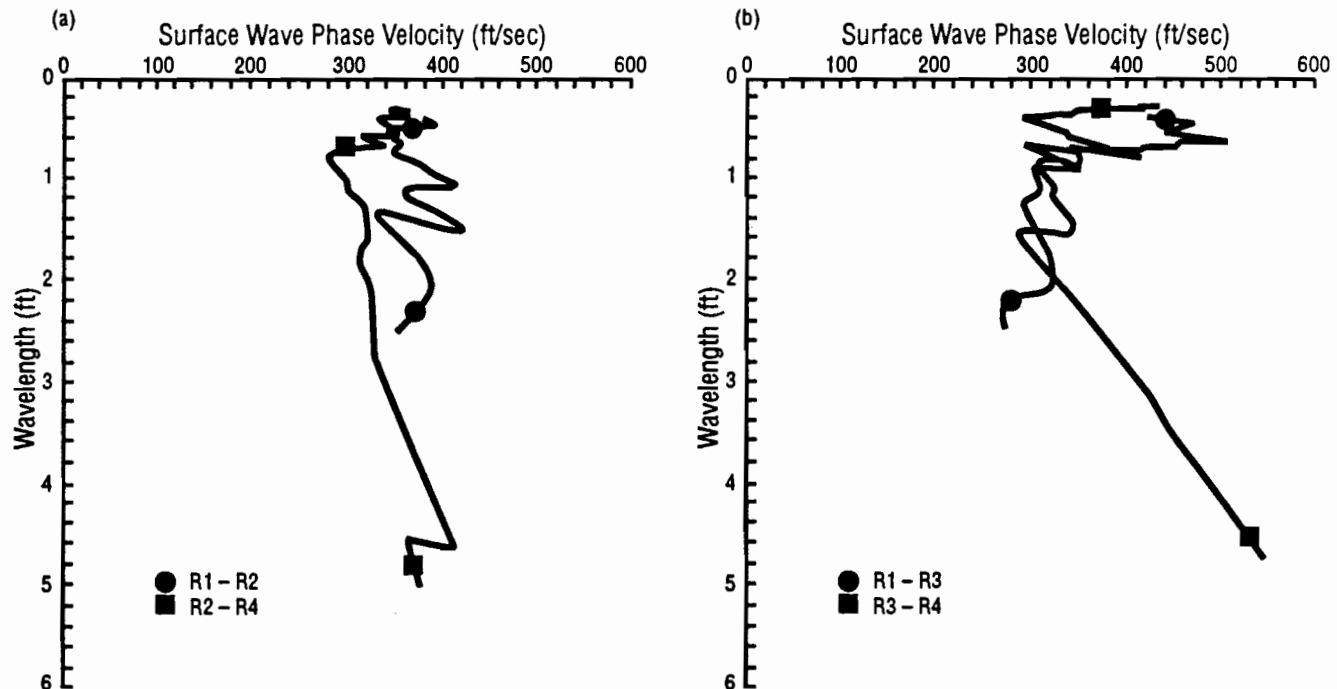


Fig 7.5. Dispersion curves for measurements performed on subgrade prior to casting the concrete slab; (a) standard spacings and (b) additional spacings.

dispersion curves shown in Fig 7.5b are called *additional spacings* because they are not normally used in production SASW testing. There is significant scatter among the four curves, but it is still possible to identify an average value within the top 2 feet (0.61 m) of wavelength which is approximately equal to 340 ft/sec (103.7 m/sec). Fluctuations in each of the dispersion curves are believed to be caused by reflections of waves from layer interfaces in the profile. The longer wavelengths which are included in the R2-R4 and R3-R4 dispersion curves are a result of the larger values of d_1 for these spacings. A larger distance between the source and first receiver permits longer wavelengths to be considered without including potentially harmful near-field effects using the criterion discussed in Section 3.4.2.

Several observations can be made about the differences between the dispersion curves from the standard and the additional receiver spacings. Within the first foot (0.30 m) of wavelength, the dispersion curves from the standard spacings fall in a narrower band (300 to 400 ft/sec (90 to 120 m/sec)) than do the curves determined from the additional spacings (300 to 520 ft/sec (90 to 160 m/sec)). This behavior is reversed between one and two feet (0.30 and 0.61 m) of wavelength where the dispersion curves from the additional spacings lie within a narrower band than do those from the standard receiver spacings. The reasons for this behavior are unknown at the present time and deserve additional study. For wavelengths longer than 2.5 ft (0.76 m), the R2-R4 dispersion curve lies significantly to the left of the R3-R4 receiver spacing. This is discussed further in the following paragraphs.

When dispersion data like that shown in Fig 7.5 is inverted to determine the shear wave velocity profile, it is usually only possible to obtain a theoretical dispersion curve which matches the overall trend in the experimental dispersion curve. To illustrate this point, consider the dispersion curve shown in Fig 7.6. The composite dispersion curve in Fig 7.6 is composed of the two standard receiver spacings and the dispersion curve from the 8-ft (2.4-m) receiver spacing discussed in Section 5.3.3. (Note that the dispersion data from the 8-ft (2.4-m) receiver spacing more closely matches the R2-R4 dispersion curve than the R3-R4 dispersion curve shown in Fig 7.5b. For this reason, the R2-R4 curve is believed to be the more correct dispersion curve.) The composite dispersion curve shown in Fig 7.6 was inverted to demonstrate how a "smoothed" theoretical dispersion curve is usually fit to experimental dispersion data that contain fluctuations. The match between the theoretical and experimental dispersion curves for this case is presented in Fig 7.7. The theoretical curve agrees very well with the trend of the experimental dispersion curves. Until more sophisticated models of wave propagation are incorporated into inversion algorithms, it will not be possible to

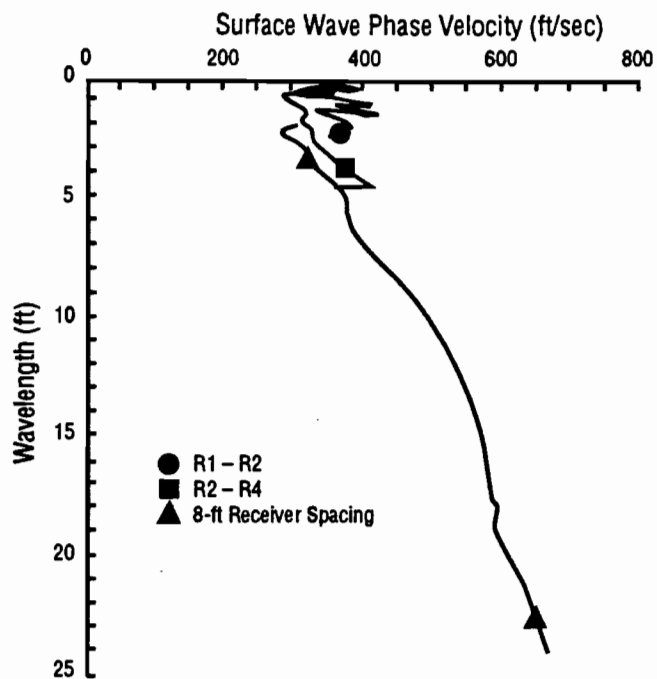


Fig 7.6. Composite dispersion curve using standard receiver spacings.

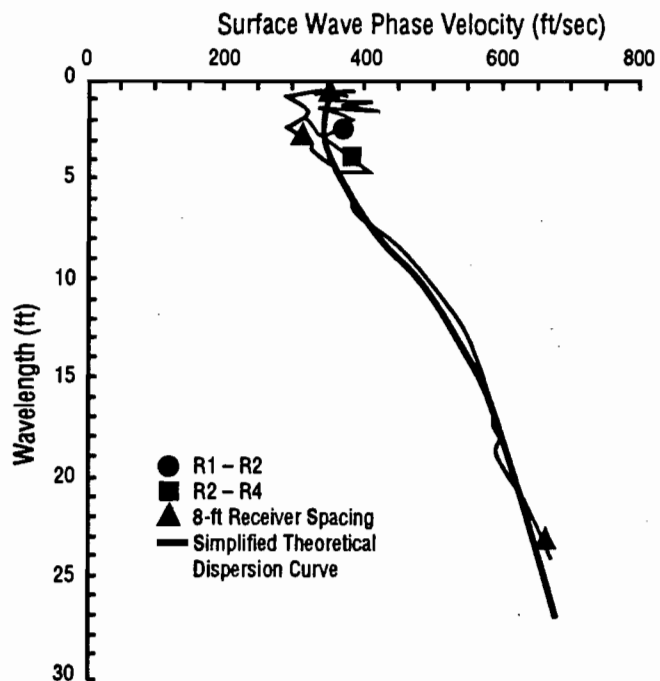
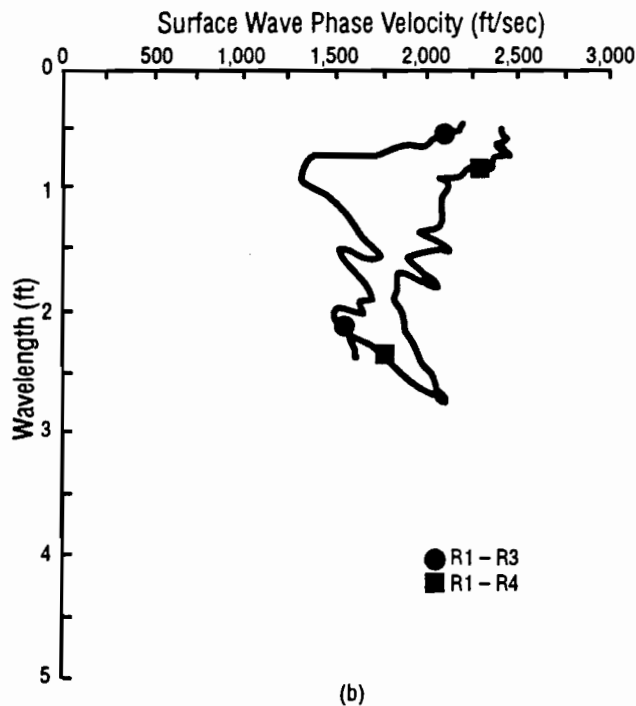
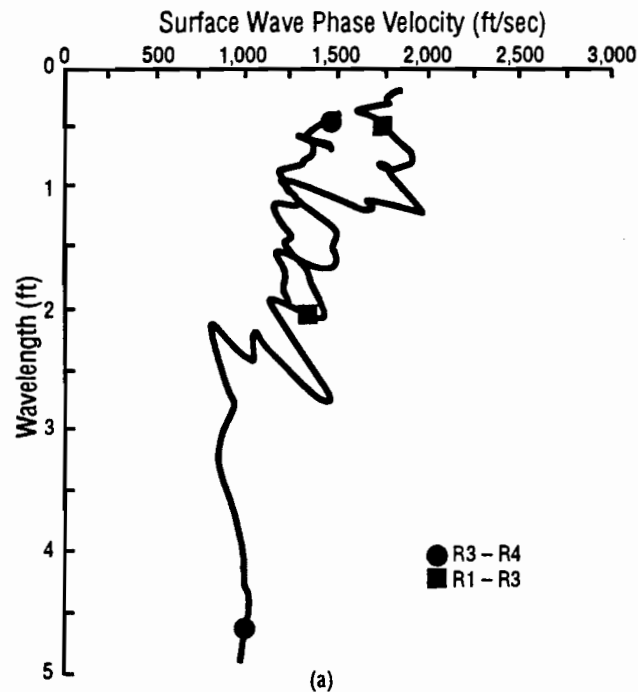


Fig 7.7. Comparison of theoretical and experimental dispersion curves.

match the theoretical and experimental curves more exactly to account for reflections. The material profile resulting from inversion of the experimental dispersion curves is presented in Table 7.2.



7.3.2 ON CURING SLAB

The first series of surface wave tests which was performed following the placement of the slab was initiated 207 minutes after water was added to the cement-aggregate mixture at the concrete batch plant. The dispersion curves for this series of tests are presented in Figs 7.8a, b, and c. Dispersion curves for the standard receiver spacings are shown in Fig 7.8a; spacings with d_2/d_1 greater than two are presented in Fig 7.8b; and receiver spacings with d_2/d_1 less than two are presented in Fig 7.8c. The dispersion curves shown in Figs 7.8a and b for receiver spacings with values of d_2/d_1 equal to or greater than two exhibit fluctuations caused by reflections of waves within the profile and from the lateral boundaries of the slab (Sheu, 1987) but are, nonetheless, reasonable dispersion curves. The dispersion curves shown in Fig 7.8c for receiver spacings with d_2/d_1 less than two are significantly poorer in quality (i.e., incorrect trend as in the case of R3-R4 or lack of wavelengths longer than 0.5 ft (0.15 m) in the case of R2-R3). The difference in behavior between receiver spacings with d_2/d_1 equal to or greater than two and those spacings with d_2/d_1 less than two is similar to behavior observed by Sánchez-Salineró (1987) in an analytical study.

An interesting phenomenon is revealed by this test series. Although the test sequence was initiated 207 minutes after the addition of water, testing required 30 minutes to complete for the six receiver combinations.

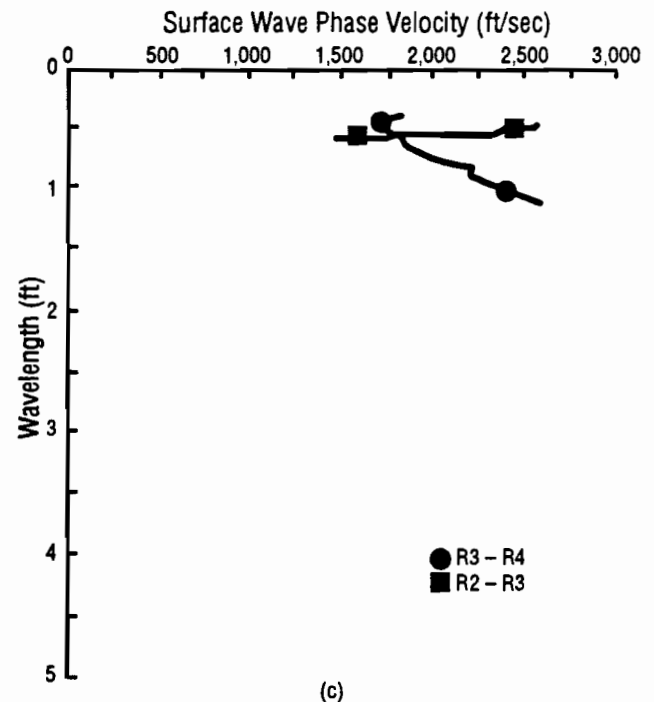


Fig 7.8. Dispersion curves for measurements on curing slab initiated 207 minutes after the addition of water to the cement-aggregate mixture; (a) standard spacings, (b) additional spacings with $d_2/d_1 > 2$, and (c) additional spacings with $d_2/d_1 < 2$.

During this time, the stiffness of the concrete was increasing due to the curing process. This increase in stiffness is reflected in the dispersion curves shown in Fig 7.8a and b. The dispersion curves gradually shift to the right (increasing phase velocity) for each successive receiver combination. The elapsed times between the

addition of water and the time of testing are noted in Fig 7.8.

A second series of surface wave tests was initiated 287 minutes after the addition of water. The dispersion curves for this series of tests are presented in Fig 7.9 (The dotted lines in Fig 7.9 correspond to ranges of dis-

TABLE 7.2. VALUES OF SHEAR AND COMPRESSION WAVE VELOCITY RESULTING FROM A SIMPLIFIED DISPERSION CURVE FIT TO THE EXPERIMENTAL DISPERSION DATA FROM STANDARD RECEIVER SPACINGS

Layer Number	Layer Thickness (ft)	Shear Wave Velocity (ft/sec)	Compression		Poisson's Ratio
			Wave Velocity (ft/sec)	Mass Density (lb-sec ² /ft ⁴)	
1	1.0	376	717	3.4	0.31
2	1.0	339	645	3.4	0.31
3	1.0	421	750	3.4	0.27
4	1.0	559	996	3.4	0.27
5	1.0	952	1,629	3.4	0.24
6	1.0	943	1,613	3.4	0.24
7	1.0	942	1,613	3.4	0.24
8	1.0	817	1,345	3.4	0.21
9	1.0	817	1,345	3.4	0.21
10	1.0	860	1,416	3.4	0.21
11	1.0	823	1,407	3.4	0.24
12	1.0	905	1,548	3.4	0.24
Half Space		1,018	1,740	3.4	0.24

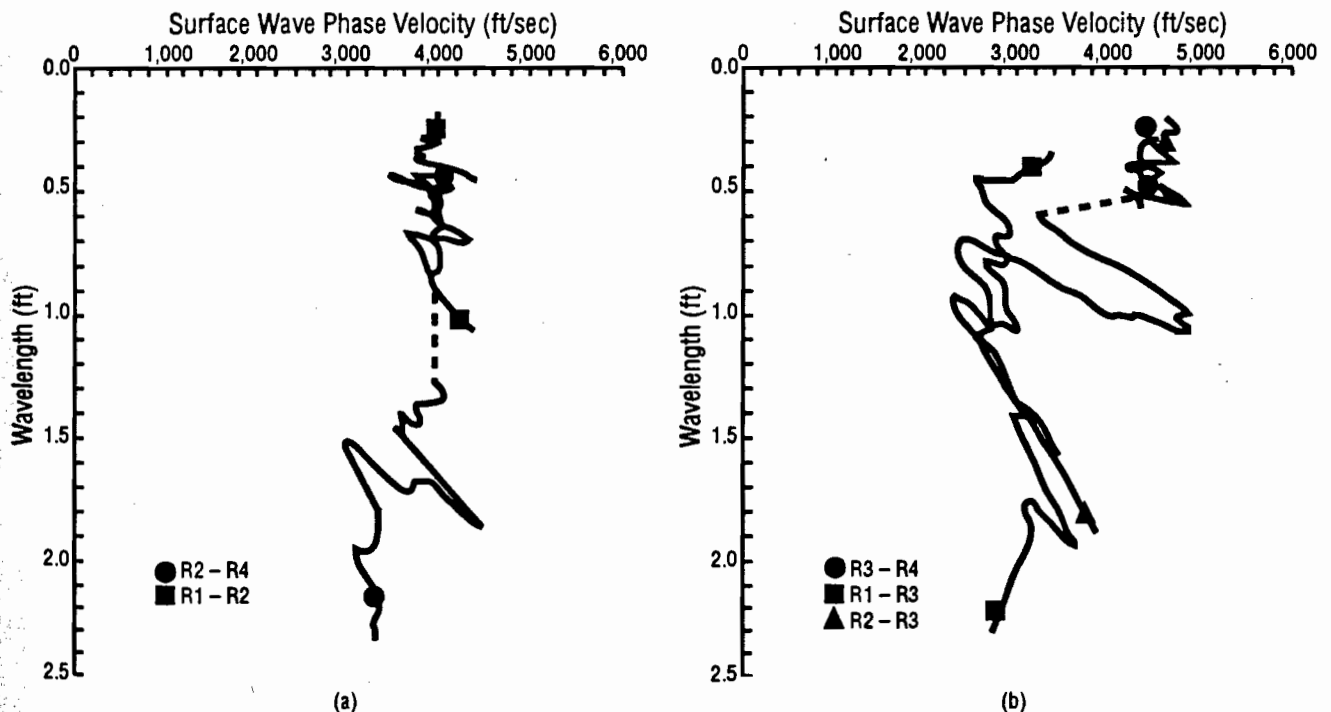


Fig 7.9. Dispersion curves for measurements on curing slab initiated 287 minutes after the addition of water to the cement-aggregate mixture; (a) standard spacings, (b) additional spacings.

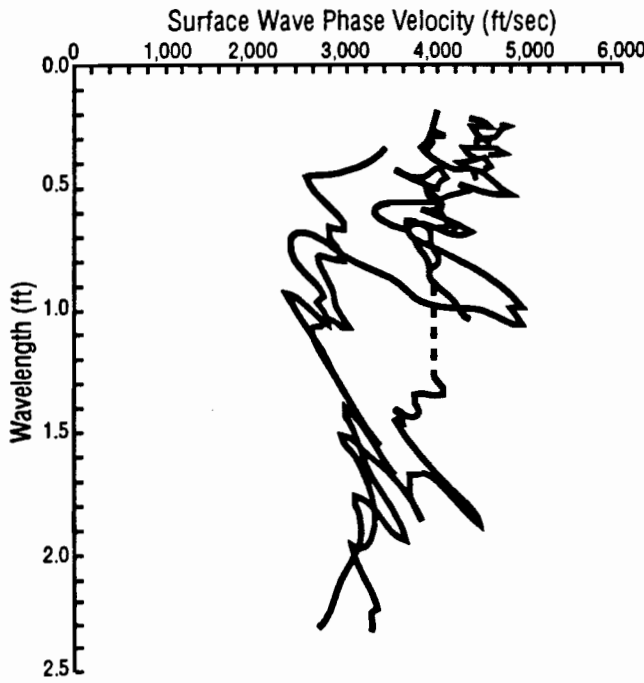


Fig 7.10. Combined dispersion curves for measurements on curing slab initiated 287 minutes after the addition of water to the cement-aggregate mixture.

person data which are missing because the phase spectra was poor in that range of frequencies.) The dispersion curve corresponding to the R1-R4 receiver spacing has been omitted because of a blunder. It is likely that the blunder results from an error made in connecting the accelerometer inputs to the dynamic signal analyzer during the test at this spacing.

It is more difficult to assess the differences between receiver spacings corresponding to different ratios of d_2/d_1 for this test series. The dispersion data for the standard receiver spacings (Fig 7.9a) agree very well for wavelengths less than one foot (0.30 m). The dispersion data for the additional receiver spacings do not agree as well for wavelengths less than one foot (0.30 m), particularly in the case of the R1-R3 receiver spacing. The contrast in stiffness between the concrete and the underlying soil appears to have affected the R2-R3 receiver spacing to the greatest extent because of the large fluctuation present in the R2-R3 dispersion curve for wavelengths between 0.6 and 1.0 ft (0.18 and 0.30 m).

All five dispersion curves have been plotted together in Fig 7.10 to compare the overall trends in the dispersion data more easily. The values of surface wave phase velocity agree reasonably well for wavelengths less than 0.6 ft (0.2 m) (with the exception of the R1-R3 spacing) and for wavelengths greater than 1.5 ft (0.5 m). The range of

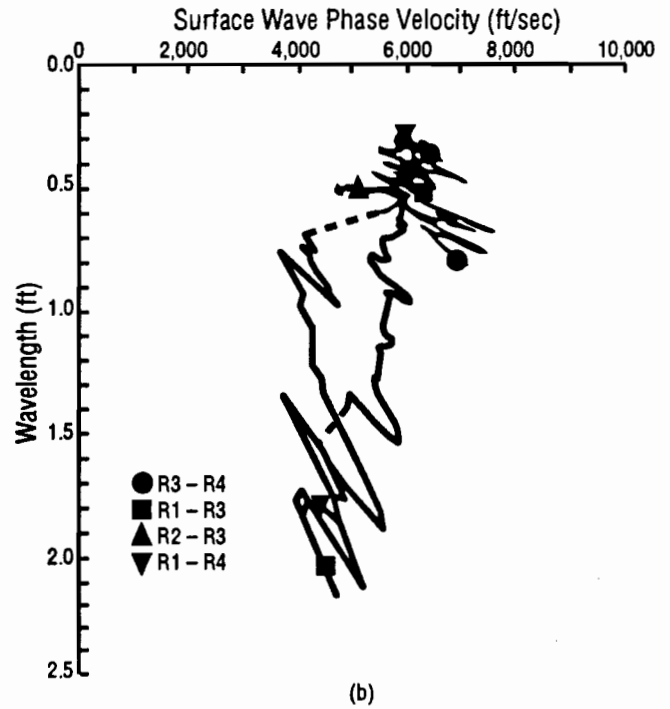
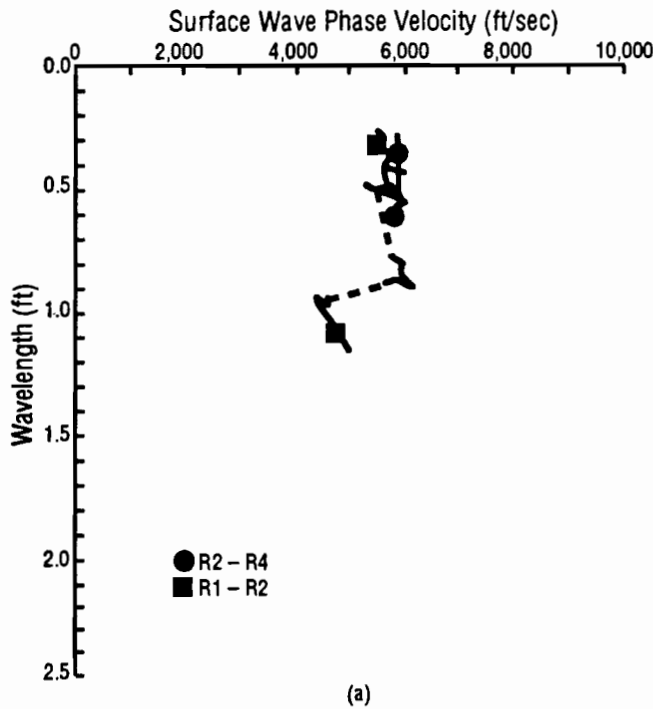


Fig 7.11. Dispersion curves for measurements on curing slab initiated 377 minutes after the addition of water to the cement-aggregate mixture; (a) standard spacings, and (b) additional spacings.

wavelengths from 0.6 to 1.5 ft (0.2 to 0.5 m) is where the curves differ the most. Perhaps not surprisingly, this range of wavelengths corresponds to ratios of the wavelength to the thickness of the slab (10 in. (25.4 cm)) ranging from 0.72 to 1.8. Sánchez-Salinero (1987) and Sheu (1987) have observed similar phenomena in both theoretical and experimental data. This phenomena suggests that wavelengths which are not very different from the thickness of the slab may be the wavelengths (frequencies) which are most affected by body wave reflections from the abrupt change in stiffnesses between the concrete and the underlying soil. An effect which was not considered in this study is the influence of the ratio of d_1 to the thickness of the slab.

Similar comments apply to dispersion curves measured during subsequent test series on the concrete slab. These dispersion curves are shown in Figs 7.11 through 7.14 for test series initiated 377 minutes and 517 minutes after the addition of water. Tests were also performed one day (1,337 minutes) and four days (6,037 minutes) after the slab was poured. Dispersion curves for these two test series are presented in Figs 7.15 through 7.18. For these four sets of dispersion curves, values of phase velocity for all of the receiver combinations agree very well for wavelengths less than 0.6 ft (0.18 m). This range of wavelengths represents waves which are not

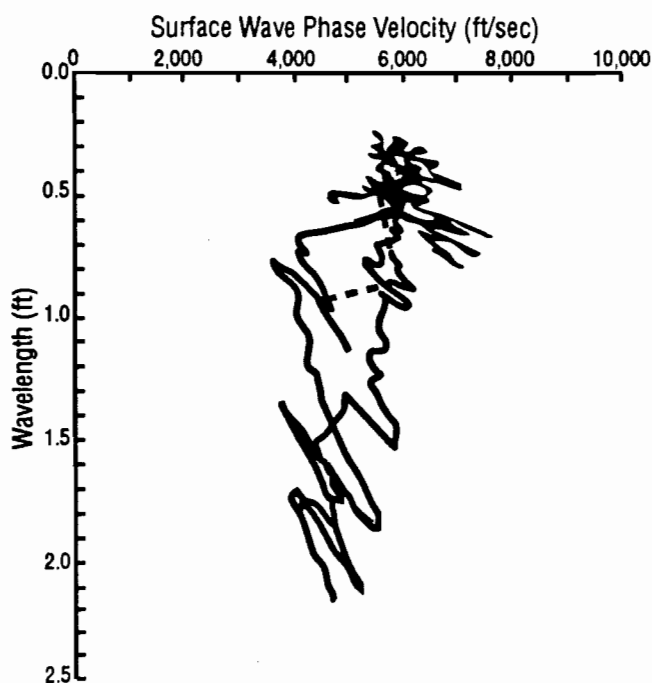


Fig 7.12. Combined dispersion curves for measurements on curing slab initiated 377 minutes after the addition of water to the cement-aggregate mixture.

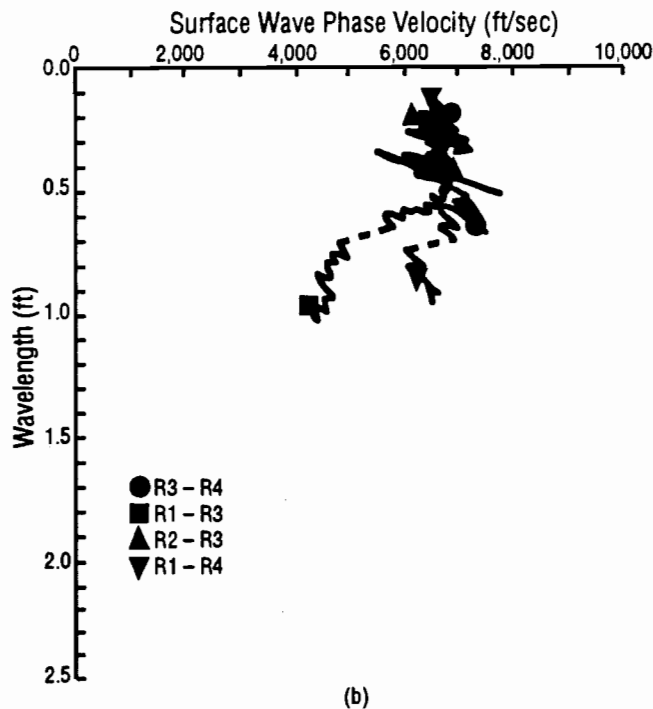
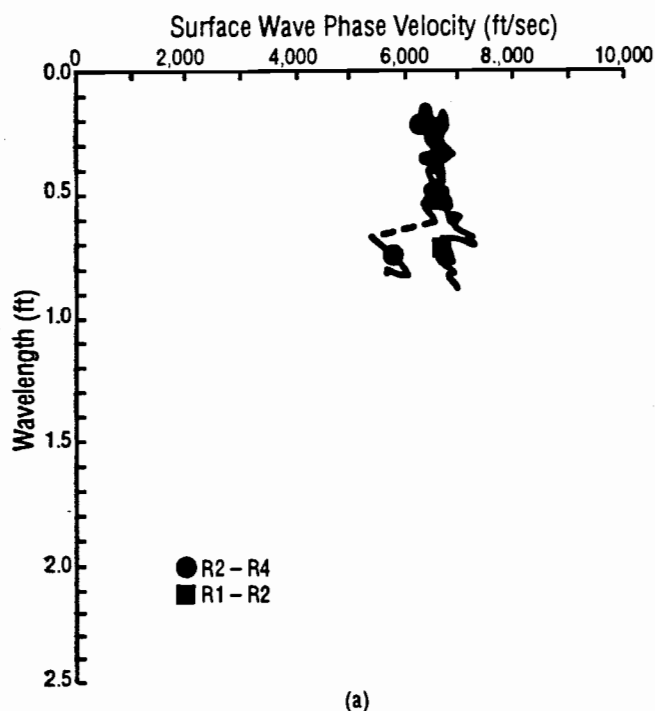


Fig 7.13. Dispersion curves for measurements on curing slab initiated 517 minutes after the addition of water to the cement-aggregate mixture; (a) standard spacings, and (b) additional spacings.

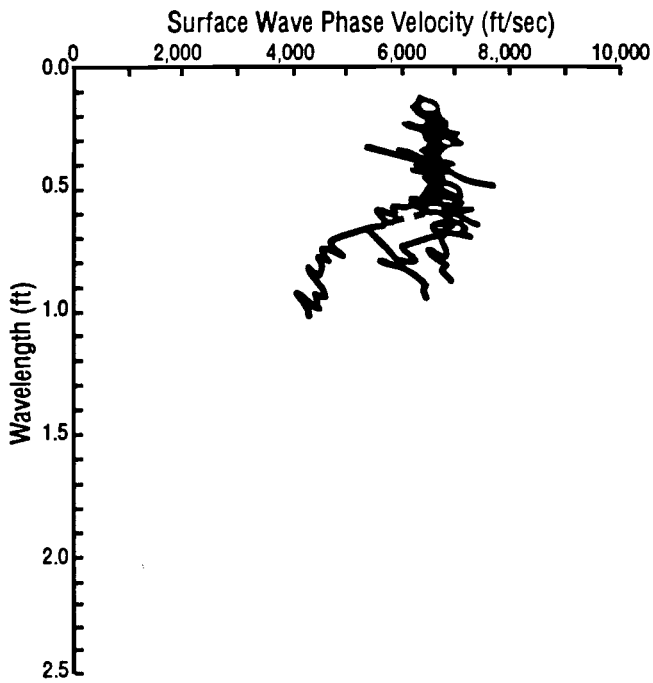


Fig 7.14. Combined dispersion curves for measurements on curing slab initiated 517 minutes after the addition of water to the cement-aggregate mixture.

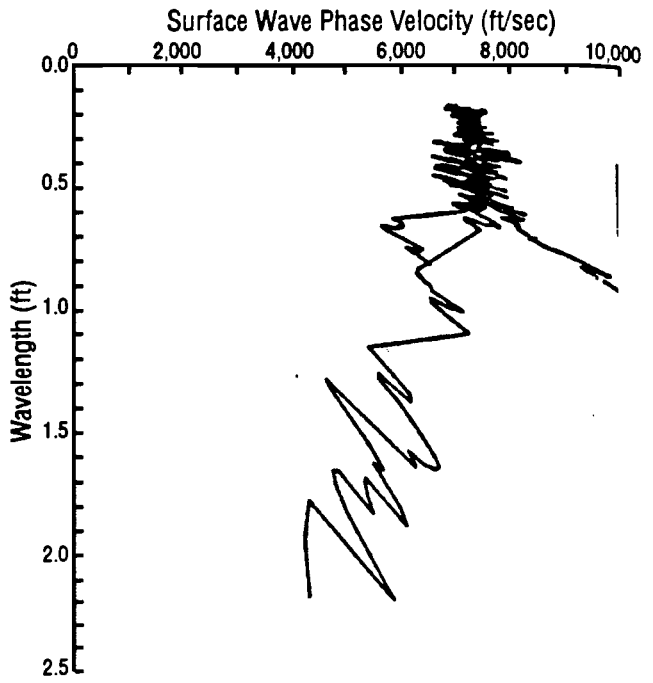


Fig 7.16. Combined dispersion curves for measurements on curing slab initiated 1 day (517 minutes) after the addition of water to the cement-aggregate mixture.

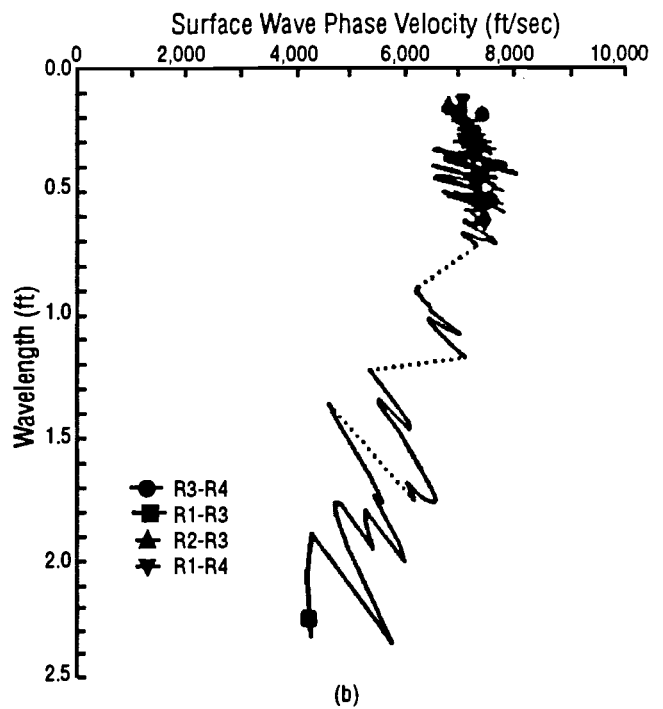
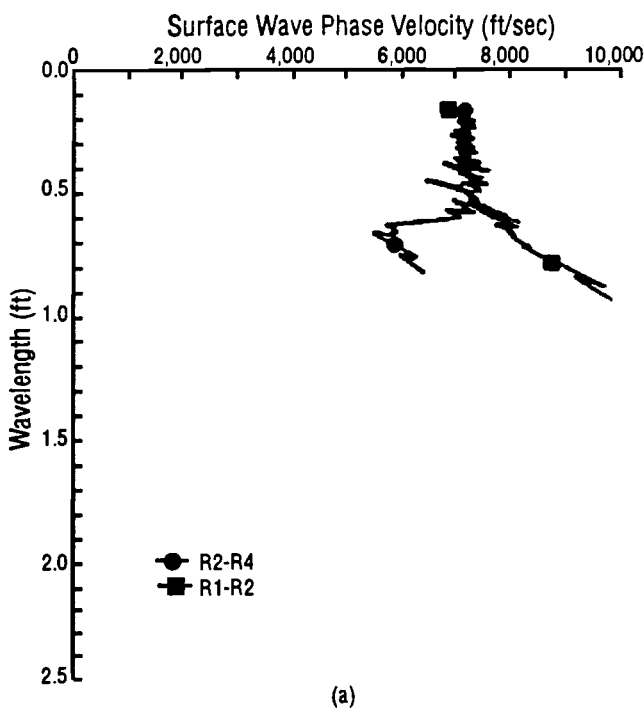


Fig 7.15. Dispersion curves for measurements on curing slab initiated 1 day (1,337 minutes) after the addition of water to the cement-aggregate mixture; (a) standard spacings, and (b) additional spacings.

sufficiently long enough to be influenced by the stiffness contrast between the soil and the pavement.

It is apparent that the large stiffness contrast between the concrete and the underlying soil is an important factor which influences the measured dispersion curves. For wavelengths which are nearly equal to the thickness of the slab, the effect of reflected body waves causes large fluctuations in the measured dispersion curves. Since the effect of body waves cannot be taken into account in the plane wave solution which is currently the basis for inversion, these fluctuations cannot be modeled during inversion. Fortunately, Sánchez-Salineró (1987) has demonstrated that dispersion curves based upon plane waves often follow the trend of the fluctuations quite well and that inversion methods based upon plane wave solutions should not, therefore, result in serious errors. This was illustrated in Section 7.3.1 for measurements prior to the placement of the slab.

It is more difficult to definitively assess the difference between the different receiver combinations used to measure dispersion. For the first series of surface wave tests on the concrete slab, the differences between receiver spacings with values of d_2/d_1 equal to or greater than two and those with d_2/d_1 ratios less than two are apparent. One of the reasons that the influence of different receiver spacings is difficult to assess is that there exists no "true" dispersion curve to use as a basis of

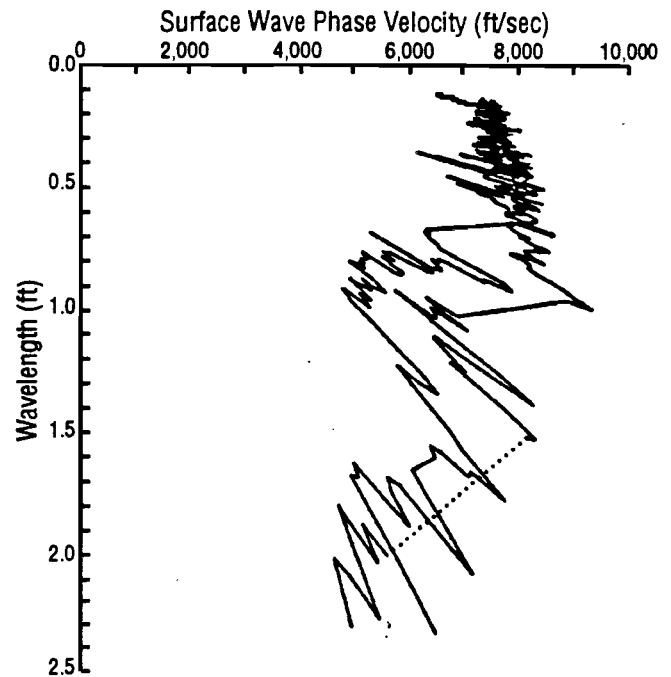


Fig 7.18. Combined dispersion curves for measurements on curing slab initiated 4 days (6,037 minutes) after the addition of water to the cement-aggregate mixture.

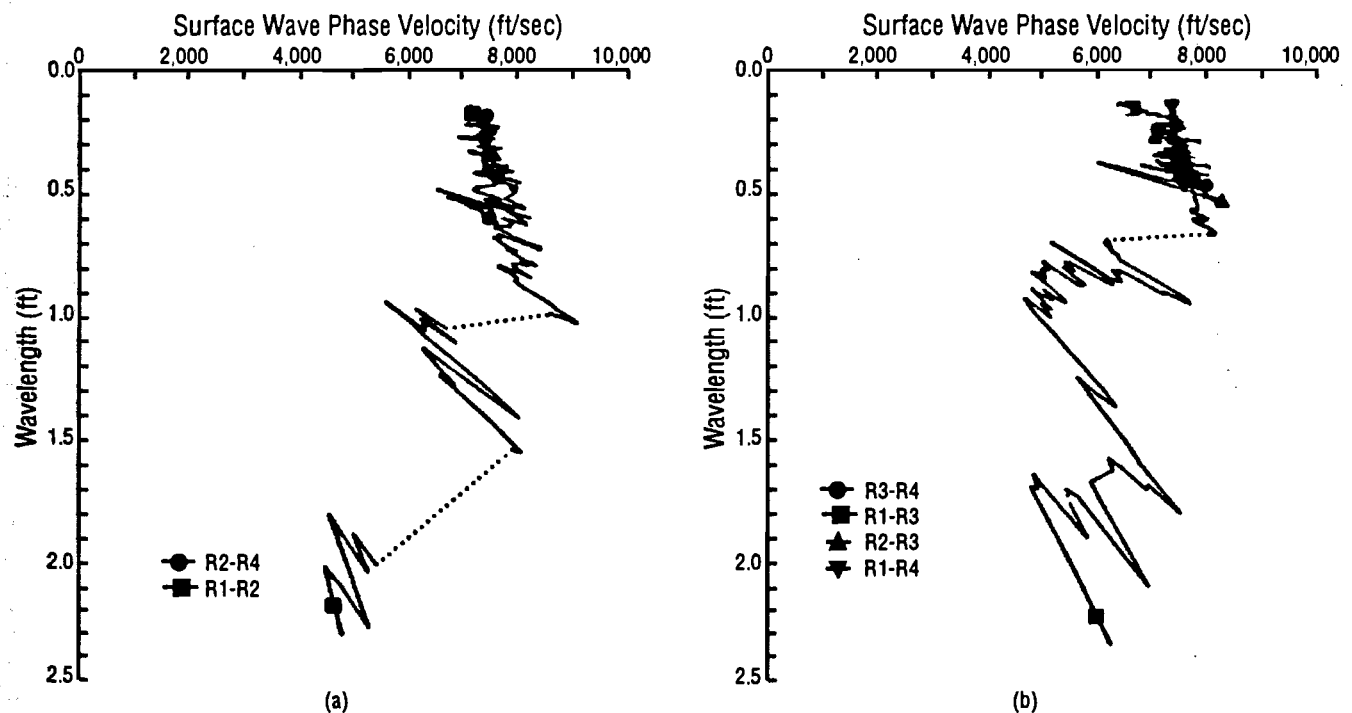


Fig 7.17. Dispersion curves for measurements on curing slab initiated 4 days (6,037 minutes) after the addition of water to the cement-aggregate mixture; (a) standard spacings, and (b) additional spacings.

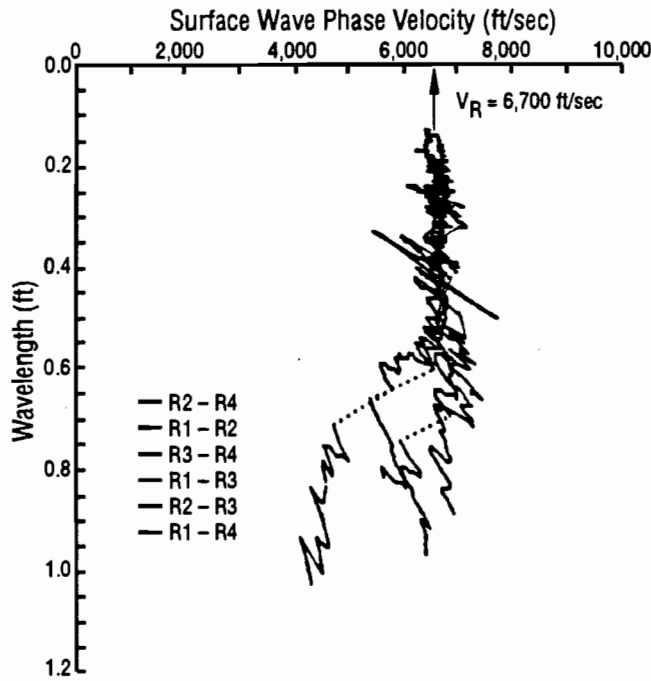


Fig 7.19. Short-wavelength portion of dispersion curve showing constant value of phase velocity for wavelengths which are small compared to the thickness of the slab.

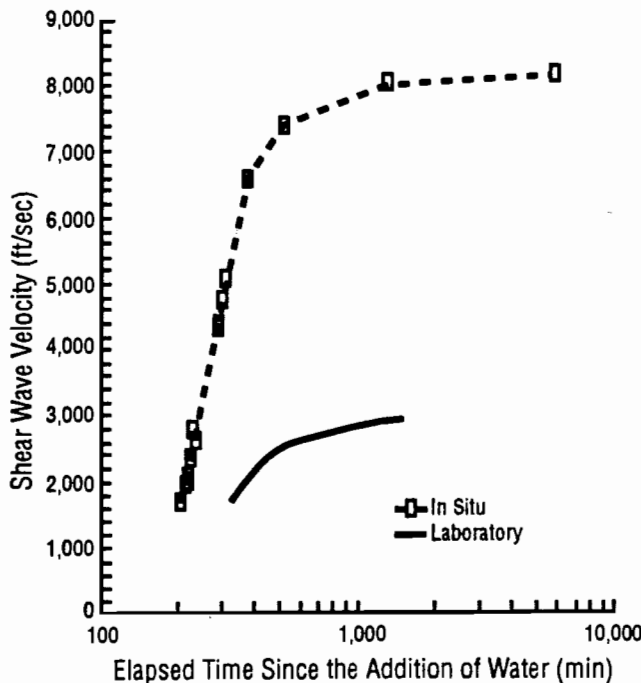


Fig 7.20. Comparison of laboratory and in situ values of shear wave velocity.

comparison. Furthermore, the influence of other factors which were not studied, such as the ratio of d_1/H , can also make interpreting the results difficult. It appears that all of the receiver combinations correctly measure dispersion for values of wavelength which are not influenced by reflections (less than 0.6 ft (0.18 m) in this case).

7.4 COMPARISON OF SURFACE WAVE TEST RESULTS WITH OTHER TEST METHODS

In the sections which follow, the values of shear wave velocity and moduli determined using surface wave tests are compared with the results of other tests including laboratory values of shear wave velocity, in situ compression wave velocity, penetration resistances, and values of Young's modulus from concrete cylinder tests.

For several of the comparisons, it is first necessary to determine the shear wave velocity of the concrete from the measured phase velocity values (i.e., the dispersion curve). This is done using a greatly simplified form of "inversion" which is applicable *only* to the surface layer. The simplified inversion is similar to the crude method of inversion described in Section 3.3. The basis of the simplified form of inversion is that, for wavelengths which are very short compared to the thickness of the slab, the slab will appear to be a uniform half space. This point is illustrated in Fig 7.19 where the phase velocity attains a constant value of approximately 6,700 ft/sec (2,040 m/sec) for wavelengths less than 0.6 ft (0.18 m). (The data in Fig 7.19 are from tests performed 517 minutes after the addition of water to the cement-aggregate mixture. All six receiver spacings are shown.) Using Eq. 3.3, it is possible to calculate the shear wave velocity of the concrete from this value of phase velocity (i.e., $1.1 \cdot 6,700$ ft/sec = 7,370 ft/sec or 2,247 m/sec). It must be emphasized that this simple method of determining the shear wave velocity is only applicable to the surface layer. As discussed in Section 3.3, a crude inversion method such as this can lead to large errors when it is used to determine the shear wave velocities of layers other than the surface layer. To determine the shear wave velocities of other layers accurately, it is necessary to use a theoretically-based inversion algorithm like that discussed in Section 3.4.3.

7.4.1 COMPARISON OF LABORATORY AND IN SITU VALUES OF SHEAR WAVE VELOCITY

Torsional resonant column tests were performed on 3- by 6-in. (7.6- by 15.2-cm) cylindrical specimens of concrete cast at the time the slab was poured to permit a comparison of shear wave velocities measured in situ and in the laboratory. This comparison is shown in Fig 7.20. The laboratory values of shear wave velocity differ in two respects from the in situ values: (1) the initial portion

of the laboratory curve is shifted to the right of the in situ curve by about 100 minutes, and (2) the laboratory curve never attains the large values of shear wave velocity measured in situ. A likely reason that the initial portion of the curve is shifted to the right is that the cylinders were not cast until well after the concrete in the slab had been placed and finished. Because of the large number of test cylinders made for compression tests, the specimens for the resonant column tests were not cast until approximately one hour after the slab had been poured. At the time the specimens were cast, the concrete was rodded which may have resulted in the delayed hardening of the concrete. The reason that the laboratory specimens never attain the large values observed in the field can be explained by considering the assumptions involved in the resonant column test method. The specimen in the resonant column test is assumed to be fixed (i.e., no rotation) at one end and free at the other (Ni, 1987). The torsional excitation is applied at the free end of the specimen. For soil samples, the stiffness of the base pedestal (the fixed end) is more than one order of magnitude larger than the stiffness of the soil sample which means that the end of the specimen in contact with the pedestal is essentially fixed. For a concrete sample, however, the stiffness of

the pedestal is only several times larger than the stiffness of the concrete. This implies that the effective length of the specimen increases which lowers the resonant frequency of the specimen and decreases the observed shear wave velocity.

Unfortunately, it is not possible to draw any meaningful comparisons between the laboratory and in situ values of shear wave velocity for these reasons. Future tests of this type should be performed only after the appropriate modifications have been made to the resonant column device.

7.4.2 COMPARISON OF IN SITU VALUES OF SHEAR AND COMPRESSION WAVE VELOCITY

Direct measurements of compression wave velocity were made using the procedure described in Section 7.2.2 to provide an independent means of determining the compression wave velocity of the concrete as it cured. A compression wave test was performed to accompany each series of surface wave tests. Typical time histories showing the arrival of the waves at each receiver are presented in Fig 7.21. The increase in compression and shear wave velocities with time is shown in Fig 7.22. Both types of waves exhibit very similar patterns of

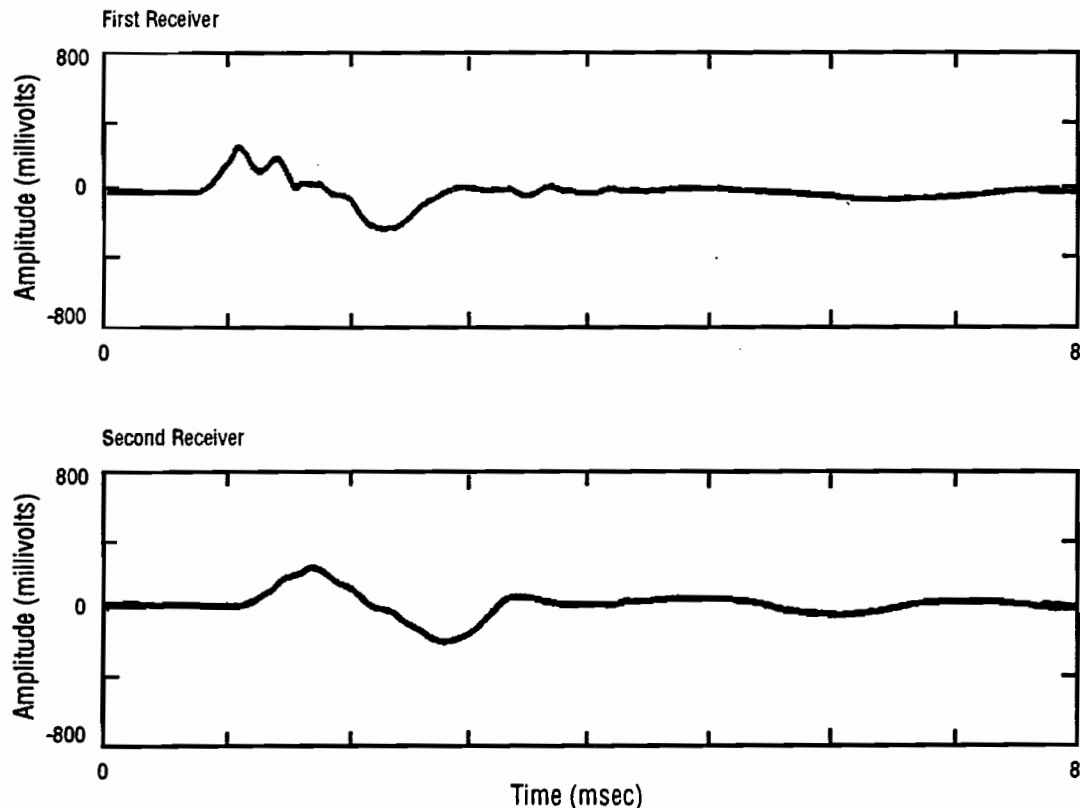


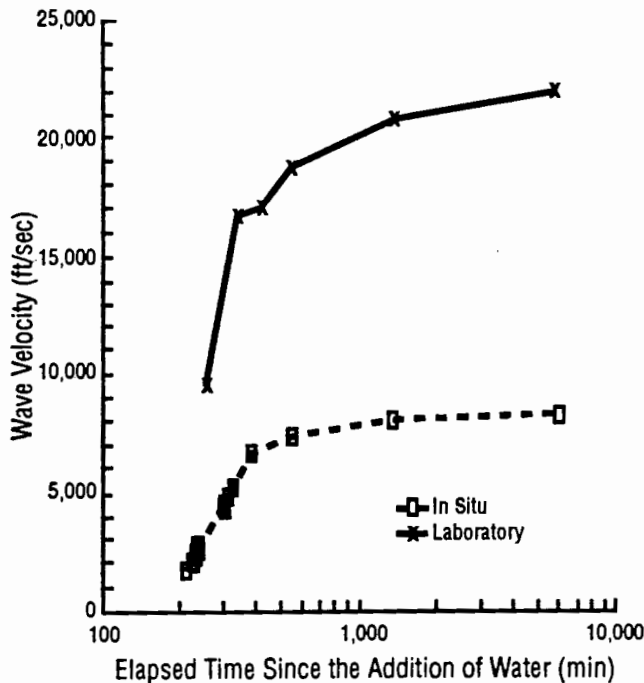
Fig 7.21. Typical compression wave time histories recorded during curing of the concrete slab; measurement performed 207 minutes after the addition of water to the cement-aggregate mixture.

TABLE 7.3. COMPRESSION AND SHEAR WAVE VELOCITIES VERSUS TIME

Elapsed Time (min)	Shear Wave Velocity (ft/sec)	Compression	
		Wave Velocity (ft/sec)	Poisson's Ratio
242	2,618	6,321	0.40
317	5,093	11,129	0.37
392	6,600	11,376	0.25
522	7,370	12,484	0.23
1,347	8,030	13,841	0.25
6,037	8,140	14,630	0.28

TABLE 7.4. AVERAGE VALUES OF COMPRESSIVE STRENGTH AT 1, 3, 7, AND 28 DAYS

Elapsed Time (days)	Number of Tests	Average	
		Range in Compressive Strengths (ksi)	Compressive Strength (ksi)
1	2	4.89 - 4.93	4.91
3	3	5.20 - 5.74	5.44
7	2	5.69 - 5.74	5.71
28	4	6.30 - 6.69	6.47

**Fig 7.22. Increase in compression and shear wave velocities with time for curing concrete.**

increase. The values of shear and compression wave velocity versus time are summarized in Table 7.3 Also presented in Table 7.3 are values of Poisson's ratio for each pair of wave velocity measurements. These values agree quite well with values which are typically assumed for concrete.

7.4.3 COMPARISON OF SHEAR WAVE VELOCITY AND PENETRATION RESISTANCE

Values of shear wave velocity were compared to values of penetration resistance to evaluate if shear wave velocity can be used in a manner similar to penetration resistance to determine the degree of "set" of fresh concrete. The comparison between these two measurements is presented in Fig 7.23. (Following the penetration reading of 3,600 psi (24.8 MPa) at 252 minutes after the addition of water, the subsequent test could not penetrate the sample.) Initial set occurred 200 minutes (3 hours and 20 minutes) after the addition of water, and final set occurred 256 minutes (4 hours and 16 minutes) after water was added. The time of final set was extrapolated from the final two readings.

Both shear wave velocity and penetration resistance exhibit very similar rates of increase suggesting that shear wave velocity is potentially useful as a tool to assess the set of concrete. Additional studies are needed to investigate the use of shear wave velocity for this purpose.

7.4.4 COMPARISON OF IN SITU SEISMIC MODULI AND MODULI DERIVED FROM CYLINDER TESTS

Young's modulus tests were performed on 6-by-12-in. (15.2-by-30.5-cm) concrete test specimens so that the moduli determined at larger levels of strain could be compared with moduli determined using seismic methods (i.e., strains less than 0.01×10^{-3} in./in.). Young's modulus tests accompanied tests of the compressive strength of the cylinders performed at 1, 3, 7, and 28 days after the slab was cast. The procedure used is as follows: (1) several compression tests were conducted to determine the average compressive strength of the cylinders and (2) Young's modulus tests were performed on other cylinders using the compressive strength to choose the proper stress at which to calculate Young's modulus. The average compressive strengths of the concrete cylinders are summarized in Table 7.4. (Note that these values are substantially greater than the specified compressive strength, 3.6 ksi.)

Values of Young's modulus were calculated at 40 percent of the compressive strength. The measured stress-strain curves used to calculate Young's modulus are presented in Figs 7.24 through 7.27 for tests performed at 1, 3, 7, and 28 days, respectively. For each test the strain corresponding to a stress equal to 40 percent of the compressive strength was determined, and these two values

were used to calculate the secant value of Young's modulus from the origin. Young's moduli determined in this fashion along with the corresponding strains are summarized in Table 7.5.

Seismic moduli were calculated using the shear wave velocities measured in situ using surface waves and values of Poisson's ratio calculated in Section 7.4.2. The expression used to calculate the moduli is:

$$E = 2\rho V_s^2 \cdot (1 + \nu) \quad (7.1)$$

where

- E = Young's modulus,
- ρ = mass density,
- V_s = shear wave velocity, and
- ν = Poisson's ratio.

An assumed unit weight of 145 lb/ft³ (2,323 kg/m³) was used to calculate the modulus. Since surface wave tests were not performed at 7 and 28 days, it is only possible to compare moduli values at 1 and 3 days. (Seismic tests performed at four days are used to compare to cylinder moduli at three days.) A comparison of the two moduli are presented in Table 7.6. As one would expect, the seismic moduli (initial tangent moduli) are greater than the moduli from cylinder tests (secant moduli). The seismic moduli are 6 percent greater than the cylinder moduli for testing performed at one day and 14 percent greater for testing at three days. It is also interesting to compare the strain levels at which the two moduli have been measured. Whereas the strains utilized in seismic tests are

TABLE 7.5. VALUES OF YOUNG'S MODULUS DETERMINED USING CYLINDER TESTS

Elapsed Time (days)	Number of Tests	Average Young's Modulus (ksi)	Average Value of Strain (in./in. x 10 ⁻³)
1	3	4.75	0.38
3	3	4.63	0.47
7	2	4.79	0.48
28	3	4.86	0.54

TABLE 7.6. COMPARISON OF SEISMIC MODULI AND MODULI DETERMINED USING CYLINDERS

Elapsed Time (days)	Modulus from Seismic Tests (ksi)	Modulus from Cylinder Tests (ksi)
1	5.04	4.75
3	5.30	4.63

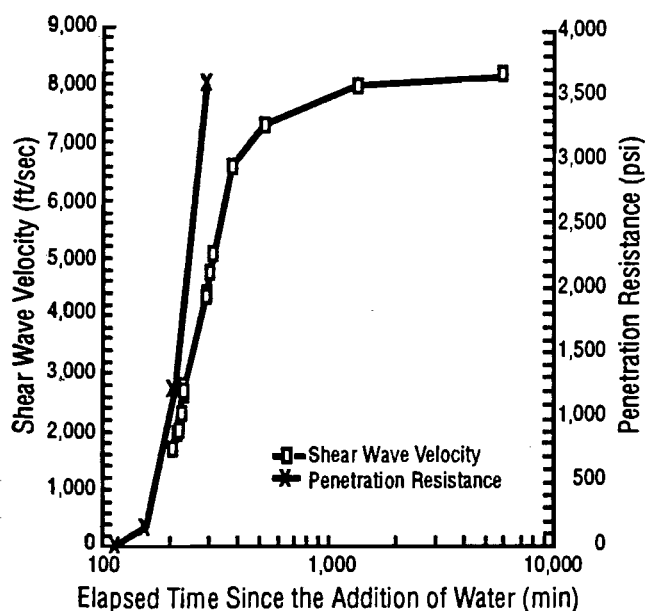


Fig 7.23. Comparison of shear wave velocity and penetration resistance measured during curing of the concrete slab.

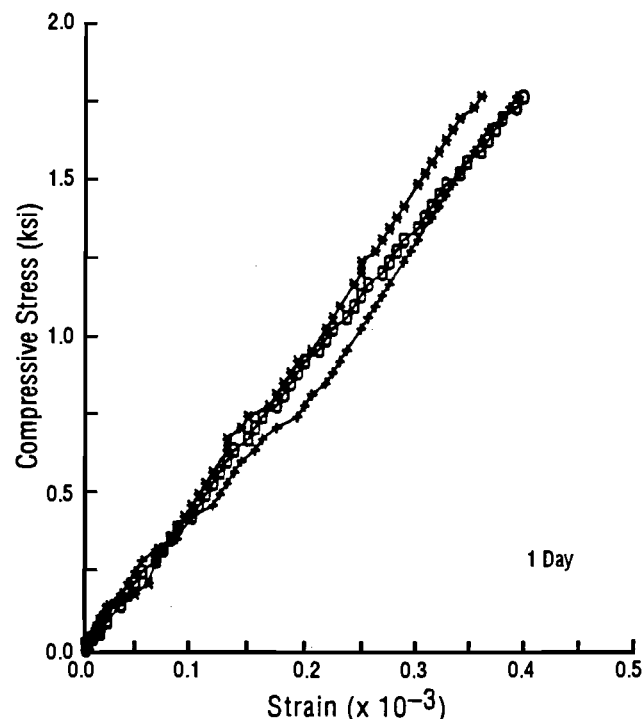


Fig 7.24. Stress-strain curves for Young's moduli tests performed 1 day after casting of the slab.

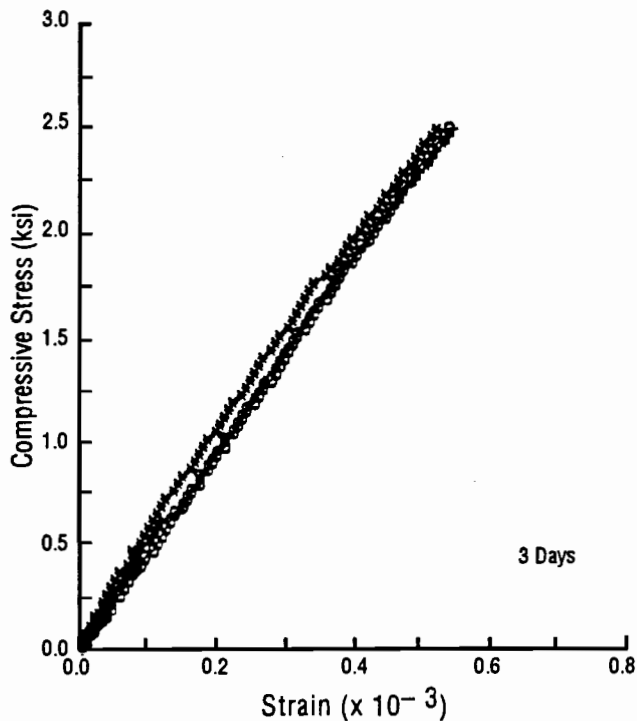


Fig 7.25. Stress-strain curves for Young's moduli tests performed 3 days after casting of the slab.

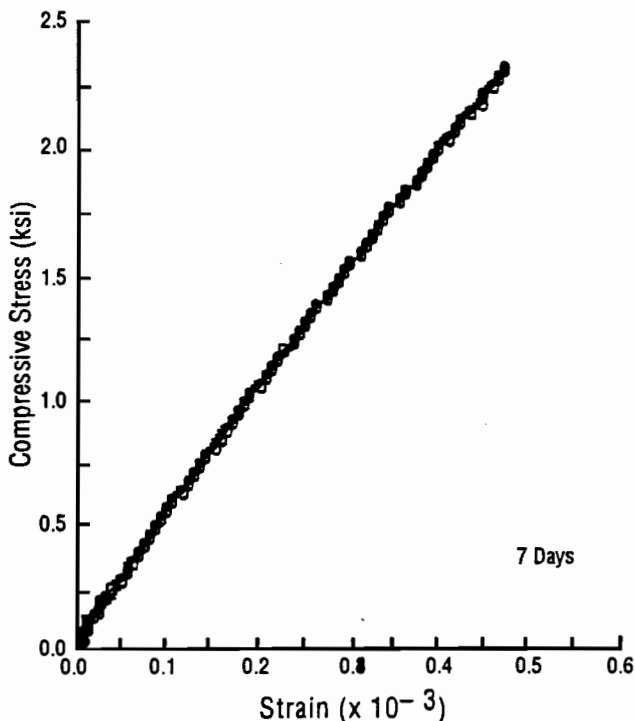


Fig 7.26. Stress-strain curves for Young's moduli tests performed 7 days after casting of the slab.

less than 0.01×10^{-3} in./in., the moduli from cylinder tests have been calculated at strains ranging from 0.38×10^{-3} to 0.54×10^{-3} in./in.

7.5 SUMMARY

Several series of surface wave tests were performed on the concrete slab at the Hornsby Bend test site. Tests were conducted throughout the time the concrete was curing so that the concrete-soil system would appear to be many different systems, each with a different ratio of stiffness between the concrete and the underlying soil. For each series of tests, six source-receiver spacing combinations were used to determine the influence of the ratio of d_2/d_1 on the measured dispersion. The test results were also used to examine the influence of the relative stiffness of the concrete and the soil on dispersion.

The influence of the relative stiffness of the concrete and the soil was apparent for several of the test series. For values of wavelength which were small compared to the thickness of the slab, the values of phase velocity all fell within a very narrow band for all receiver combinations. Similarly, at long wavelengths (ratios of wavelength to thickness greater than 1.8), the dispersion curves also tended to fall within a narrow range, although the agreement was not as pronounced as at short wavelengths. For wavelengths between 0.7 and 1.8 times the thickness of the slab, reflected body waves resulted in large fluctuations in the dispersion curves. Other researchers (Sánchez-Salineró, 1987; and Sheu, 1987) have observed similar behavior in both analytical and experimental studies of wave propagation.

The influence of the receiver spacing is more difficult to assess because there exists no "true" dispersion curve with which to compare the results. Based upon selected records (those from tests started 207 minutes after water was added), values of d_2/d_1 equal to or greater than 2.0 appear to yield improved results. These results agree well with those of an analytical study by Sánchez-Salineró (1987) which found that d_2/d_1 ratios greater than two provided better results.

Comparisons of laboratory and in situ values of shear wave velocity of the concrete revealed a problem concerning the manner in which the laboratory specimens were cast and a limitation of the resonant column test method. Initial values of shear wave velocity were different because the laboratory specimens were not cast (and rodded) until well after the slab had been placed and finished. It is likely that the disturbance associated with casting the specimen delayed the increase in the shear wave velocity with time. The second problem caused inaccurate values of shear wave velocity to be measured in the resonant column cell because the assumption of a fixed-free system was violated. The ratio of the stiffness of the base pedestal to that of the concrete specimen effectively increased the length of the specimen and re-

sulted in values of shear wave velocity which were erroneously low.

Compression wave velocities were determined directly to accompany each series of surface wave tests. Values of shear wave velocity and compression wave velocity were then used to calculate Poisson's ratio. The resulting values of Poisson's ratio ranged from 0.40 during the early stages of curing to 0.25 when the concrete had more fully cured. These values agree very well with values that are typically assumed for concrete.

Shear wave velocities were compared with values of penetration resistance to evaluate if shear wave velocity might be used in a manner similar to penetration resistance to measure the set of concrete. Both shear wave velocity and penetration resistance exhibit the same rate of increase with time which indicates that seismic measurements may have the potential to be used as test methods to assess the curing of concrete. Additional studies are needed on this topic.

Finally, Young's moduli calculated using the results of seismic tests were compared with moduli determined using cylinder tests. The seismic moduli were found to be 6 percent greater than the cylinder moduli for testing performed one day after the slab was cast and 14 percent greater for tests performed three days after the slab was cast. Seismic moduli are initial tangent moduli measured at strains less than 0.01×10^{-3} in./in. In contrast, moduli from cylinder tests are secant moduli measured at strain between 0.38×10^{-3} and 0.54×10^{-3} in./in. The difference in the moduli from the two test methods is most likely due to the differences in the strain levels used in the two tests. However, the difference in moduli is surprisingly small and demonstrates the nearly linear behavior of concrete in these strain ranges.

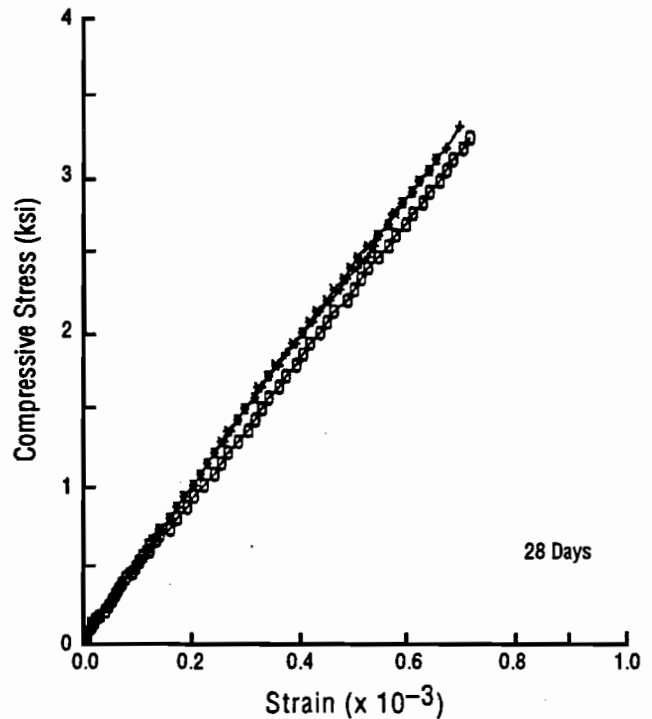


Fig 7.27. Stress-strain curves for Young's moduli tests performed 28 days after casting of the slab.

CHAPTER 8. CONCLUSIONS AND RECOMMENDATIONS

8.1 SUMMARY

Engineering seismic methods are used to assess the properties of geotechnical materials at small strain levels (less than 0.001 percent). At small strain levels, soils and pavement materials behave as linear, elastic materials. The property which is most often determined using seismic methods is the propagation velocity of either compression or shear waves. These propagation velocities may be used to calculate small-strain values of constrained and shear moduli using relationships from the theory of elasticity (Eqs 1.1 and 1.2). Propagation velocities and small-strain moduli are used directly in the analyses of dynamically-loaded foundations or in site amplification studies. Frequently, however, propagation velocities and small-strain moduli are used to infer other material parameters such as density or effective stress state using relationships like those in Eqs 1.3 and 1.4 (e.g., Stokoe *et al*, 1988).

The seismic methods described in this report are in situ methods. In situ testing eliminates (or significantly reduces) sampling disturbance and permits tests to be conducted at the in situ stress state. Furthermore, the strain levels associated with in situ seismic methods more closely approximate the strain levels encountered in the field under working loads than do the strain levels associated with other in situ methods such as the cone penetrometer. It is also usually possible to sample more representative volumes of soil using in situ seismic methods than with other in situ methods.

In situ seismic methods can generally be divided into two categories: (1) those which use body waves (shear and compression) waves and (2) those which use surface waves. The most commonly used body wave methods are the refraction method and the crosshole method. The refraction method suffers from a significant limitation in that it cannot be used at sites which contain a low velocity layer under a high velocity layer. The method will provide erroneous results in this case. This limitation effectively eliminates the refraction method for use on pavement structures and for many important soil investigations (e.g., liquefaction potential studies). The crosshole method is a fundamentally sound technique which provides reliable results in nearly all situations. At some sites, however, the need for boreholes may make the crosshole method impractical or expensive to use.

Methods based upon surface waves offer several advantages with respect to body wave methods. Surface waves are the predominant type of wave generated by a source on the surface, and surface waves attenuate less compared with body waves. These two important points along with the fact that no boreholes are needed combine

to make surface wave methods an attractive alternative to body wave methods. Furthermore, surface wave methods, unlike refraction methods, permit low velocity layers to be accurately measured.

The Spectral-Analysis-of-Surface-Waves (SASW) method is one surface wave method which offers a great deal of promise. The method is based upon the dispersive property of surface waves in a layered half space. The SASW method improves upon its predecessor, the steady-state Rayleigh wave method, in two areas: (1) the use of spectral analysis techniques allows information to be gathered at many more frequencies in less time, and (2) theoretically-based inversion of surface wave dispersion data permits more accurate shear wave velocity profiles to be determined.

The subject of this report is an experimental study of factors which affect the results obtained with the SASW method. The experimental work described herein was performed at the Hornsby Bend test site. The Hornsby Bend site has been the location of numerous other in situ seismic tests in addition to standard geotechnical tests which provided independent data for this study. A summary of the study is presented in the following sections.

8.2 ALTERNATIVE SOURCES AND INPUT MOTIONS

Transient input motion resulting from impact-type sources such as hammers or dropped weights has been used almost exclusively in SASW testing for the past several years. At most sites, transient input motion provides very good results (i.e., easily interpretable, low noise measurements), but at several sites transient motion has failed to provide acceptable results. These unacceptable results are due in large part to a lack of control over the frequencies which are input to the ground when using impact sources. The frequencies which are generated are a function of the weight of the source, the contact area, the velocity of impact, and the characteristics of the ground surface itself. Since trial and error testing of various sources is usually necessary to find the one which generates the proper frequencies, the time required to perform a surface wave test often increases significantly.

Random and sinusoidal input motions were evaluated as alternatives to transient motion to investigate if either could provide more predictable results. Both random and sinusoidal motions were implemented using electromechanical vibrators with 50- or 250-lb (223-N or 1.12-kN) capacities. Transient, random, and sinusoidal motions were compared using four criteria: (1) peak value of the time record, (2) total power contained in the signal, (3) the auto power spectrum of each signal, and

(4) the peak-to-rms ratio of each type of signal. The auto power spectra were found to provide the most meaningful comparison. Sinusoidal motion contained the highest level of power because of the ability to concentrate power at individual frequencies during the measurement.

The three types of input motion were also compared in actual use using field measurements of phase and coherence spectra and dispersion curves at the Hornsby Bend test site. Although all three type of motion resulted in good quality data at this site, there were modest improvements in the data obtained using random and sinusoidal motions. Sinusoidal motion appears to have the most potential to improve the quality of the data at sites where transient motion does not work well.

An idling bulldozer has been used as a source of surface waves recently at a number of sites. The motion from the bulldozer approximates random input motion. At one site where the bulldozer has been used, the increase in the quality of the data with respect to conventional impact sources made the difference between acceptable and unacceptable results. Another field investigation provided the rare opportunity to use a 32-ton (285-kN) dynamic compaction weight as a source of surface waves. The weight successfully generated surface waves with frequencies as low as 800 mHz and wavelengths as long as 4,000 ft (1.2 km).

A comparison of phase spectra resulting from a theoretical solution which includes only fundamental-mode, plane surface waves and a solution which includes all wave types indicates that many of the phenomena which are often observed in experimental phase spectra such as "curved lines" and "phase reversals" can be attributed to wave types other than fundamental-mode surface waves.

Finally, it has been suggested that the phase difference between the force applied at the source and the first receiver (the transfer function) can be used instead of the phase difference between receivers (the cross power spectrum) to calculate surface wave dispersion. There are three problems which complicate the use of the transfer function instead of the cross power spectrum in practice: (1) the force applied at the source is extremely difficult to measure accurately whether an instrumented hammer is used or whether the source is an electromechanical vibrator, (2) nonlinear soil or pavement behavior may exist in the vicinity of the source, and (3) use of the transfer function requires a more sophisticated inversion algorithm than is presently used in the SASW method.

8.3 COMPARISON OF EXPERIMENTAL AND THEORETICAL WAVE MOTIONS

Two assumptions which are important in the SASW method in its current form are (1) the effects of body waves on the experimental dispersion curve are not taken into account, and (2) the experimental dispersion curve is

assumed to be comprised only of fundamental-mode surface wave motion. To investigate the validity of these assumptions, particle motions were measured at various depths within a borehole and used to calculate the relative contribution of the first several modes of surface wave propagation. The objective was to determine what portion of the total motion was attributable to surface wave motion. As a preliminary step in these calculations, free-field particle motions were compared with particle motions in a cased and grouted borehole to investigate the influence of the casing and grout on the measured particle motions. This comparison was performed to assure that the measured particle motions in a cased borehole, which were used to determine the relative contribution of each surface wave mode, were not adversely affected by the presence of the casing and grout. The accuracy of measured particle motions in a cased borehole also has important implications when the motions are used to estimate material damping with the crosshole method. A comparison of the measured particle displacements and the theoretical displacements calculated using a Green's function solution for a layered half space was also conducted.

Vertical and radial free-field particle motions agreed with those in the cased and grouted borehole within approximately 10 percent for measurements made at depths of 6 and 12 ft (1.83 and 3.66 m) for frequencies between 10 and 100 Hz. The agreement is considered quite good for this type of measurement. Experimental and theoretical particle displacements did not agree very well probably due to uncertainties in the output level of the electromechanical vibrator used to generate seismic waves in the field. When the particle motions were normalized with respect to the vertical motion at the surface, the comparison between experimental and theoretical particle displacements was much more favorable in most cases. Several factors probably contributed to the observed differences between the experimental and theoretical motions including (1) errors in the experimental measurements, (2) errors caused by the inability of the simple "layer cake" model used to calculate the theoretical solution to model the actual site conditions accurately, and (3) errors in the parameters (i.e., shear wave velocity and thickness of each layer) of the simple model.

There was significant variability in the results of the calculations to determine the relative contribution of the first several modes of surface wave propagation. The variability was likely caused by two factors: (1) discrepancies between the experimental and theoretical displacements described in the previous paragraph, and (2) the poorly conditioned system of equations used to calculate the mode contribution values amplified small errors in the experimental data. When theoretical solutions were used to determine the contribution of each mode, it was

found that fundamental-mode surface waves comprised between 72 and 86 percent of the total motion.

8.4 INFLUENCE OF SOURCE-RECEIVER SPACING AND RELATIVE LAYER STIFFNESS ON SURFACE WAVE RESULTS

Two factors which can influence the results of surface wave tests because of their effect on measured dispersion curves are (1) the relative spacing of the source and receivers used to perform the test, and (2) the relative stiffness of adjacent layers within the profile. These two factors were experimentally investigated using a concrete test slab at the Hornsby Bend test site. Surface wave measurements were made throughout the time the fresh concrete was curing so that the ratio of the stiffness of the concrete to the underlying soil was changing. In this manner, the influence of the relative stiffness of the concrete and soil on measured dispersion curves could be determined. Six different source-receiver combinations were also used to examine the effect of various ratios of distances between the source and receivers on surface wave dispersion. Finally, surface wave test results were compared with several other test methods including compression wave measurements, resonant column tests, compressive strength tests, and penetration resistance tests.

The influence of the relative stiffness of the concrete and the underlying soil was most apparent for wavelengths between 0.7 and 1.8 times the thickness of the concrete slab (10 in. (25.4 cm)). Dispersion data for wavelengths in this range exhibited the fluctuations that are typically caused by reflections of body and surface waves from the concrete-soil interface and have been observed in other experimental and theoretical studies. For wavelengths shorter than 0.7 times the thickness of the slab, the surface wave phase velocities usually fell within a narrow band. For these short wavelengths, the thickness of the slab is large enough with respect to the wavelength that the wave is not yet influenced by the underlying soil.

The effect of various source-receiver combinations on dispersion data was more difficult to assess. Based upon selected records, source-receiver spacings with values of d_2/d_1 greater than two appeared to yield dispersion curves which were less affected by body waves and reflections within the profile.

Independently measured values of compression wave velocities in the curing concrete were used along with shear wave velocity values from surface wave testing to calculate values of Poisson's ratio for the concrete. Values of Poisson's ratio varied from 0.40 when the concrete was still relatively new (242 minutes after the addition of water at the batch plant) to consistent values

of approximately 0.25 once the concrete had more fully cured. These values agree very well with values which are typically assumed for concrete.

Penetration resistance tests are used to determine the times to initial and final set of fresh concrete. Measured values of shear wave velocity and penetration resistance values showed similar rates of increase during the period of time in which the concrete was curing. The promising results indicated that shear wave velocity may possibly be used as a means of determining the times of initial and final set of fresh concrete.

Young's moduli calculated using the results of compression tests on concrete cylinders were compared to moduli determined by in situ seismic tests. The seismic moduli were found to be 6 percent greater than the cylinder moduli for tests performed one day after the slab had been cast and 14 percent greater for tests performed four days after casting. Seismic moduli are generally measured at strains less than 0.01×10^{-3} in./in. whereas the cylinder moduli were measured at strains ranging from 0.38×10^{-3} to 0.54×10^{-3} in./in.

Finally, a comparison of shear wave velocities measured in situ and those measured in the laboratory using the resonant column test was inconclusive because of difficulties encountered when using the resonant column device to determine the shear wave velocity of very stiff materials.

8.5 RECOMMENDATIONS FOR FUTURE RESEARCH

There are several areas where the author believes that important research remains to be done on the development of surface wave testing for engineering purposes. These areas are briefly described in the following paragraphs.

One area where more work is needed is in experimental investigations of surface wave methods under carefully controlled conditions. The work described in this report was an initial attempt at this type of study. Although the test site chosen for many of the tests described herein had been thoroughly investigated in the past, it was, nonetheless, a very complex site comprised of many different layers. It would be desirable to (1) use a much simpler site consisting of a very few layers, (2) construct a full-size test facility using engineered fills, or (3) construct a model facility which can be easily changed to represent different types of profiles. The third option is similar to the use of calibration chambers which have been so successful in studying in situ devices such as the cone penetrometer, flat plate dilatometer, and pressuremeter. A preliminary study of the third option by the author revealed that urethane elastomers are an ideal material to use in the construction of such a model facility.

Alternative sources and input motions should be used at as many sites as possible to learn more about how they can be used to improve surface wave test results. The acquisition of a truck-mounted, hydraulically-operated source such as those used in geophysical exploration by The University of Texas will be a major step in this direction.

More sophisticated inversion algorithms should be developed which not only automate the inversion process, but also model the subsurface more accurately and take the effects of other types of waves into account. Although the geophysical literature contains a great deal of information about algorithms of this type, a challenge to engineers will be to develop or implement techniques

which are appropriate for use in *engineering* seismic investigations.

Finally, the part of surface wave testing which may prove the most difficult to automate is the interpretation of phase spectra (i.e., the process of converting from wrapped phase to unwrapped phase). The coherence function and auto power spectra will probably play important roles in developing rules for use in expert system shells or other means of automating the interpretation. Hopefully, the information summarized in Appendix A will provide a first step to understanding the influence of noise on the relationship between phase spectra, coherence functions, and auto power spectra. A great deal more work is needed in this area.

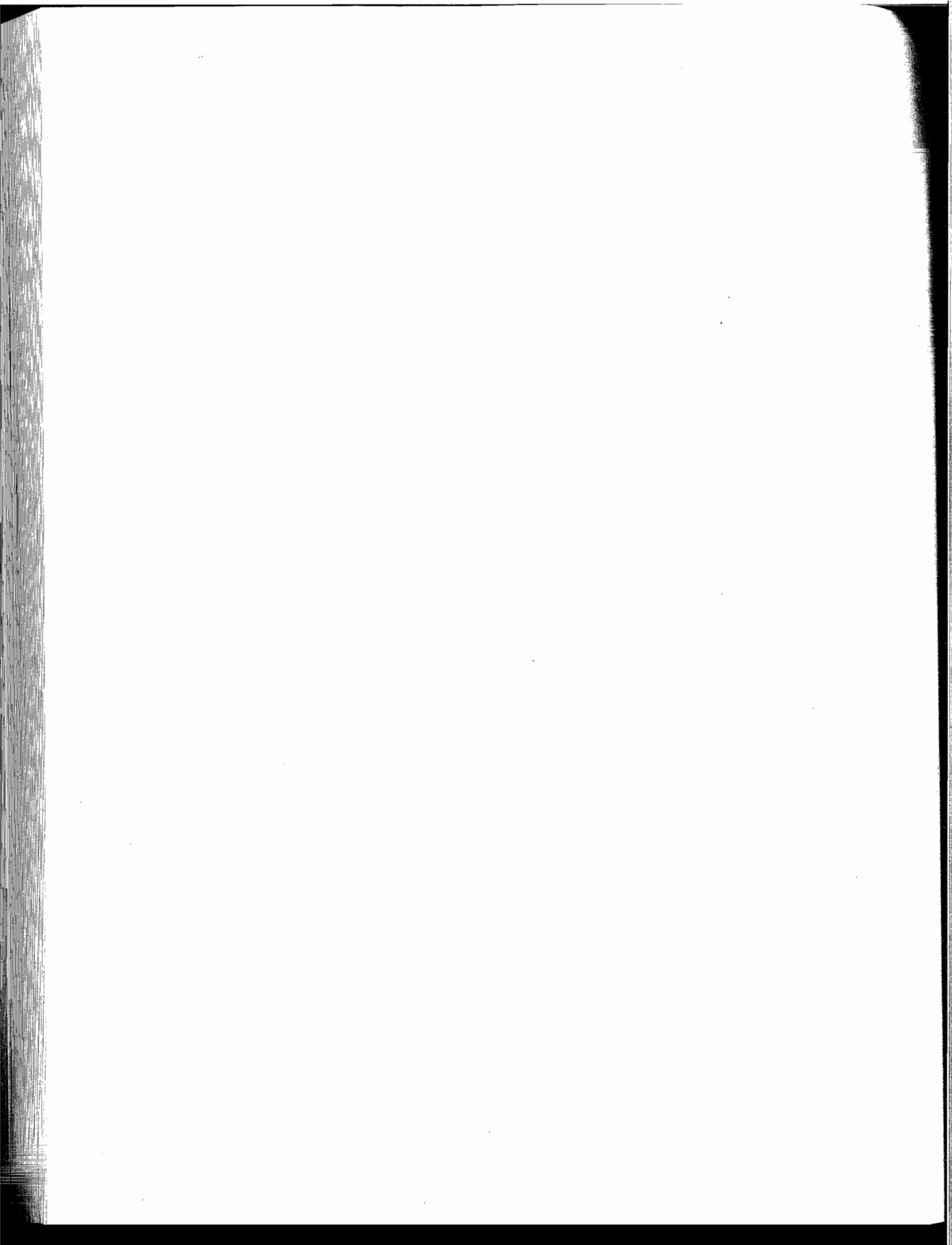
REFERENCES

- Aki, K. and P. G. Richards, (1980) *Quantitative Seismology: Theory and Methods*, W.H. Freeman and Company, New York, 932 pp.
- Allen, N. F., F. E. Richart, Jr., and R. D. Woods, (1980), "Fluid Wave Propagation in Saturated and Nearly Saturated Sand," *Journal of the Geotechnical Engineering Division*, ASCE, Vol. 106, No. GT3, pp. 235-254.
- American Society for Testing and Materials, (1988a), "Test for Compressive Strength of Cylindrical Concrete Specimens," C39, *Annual Book of ASTM Standards*, ASTM, Philadelphia.
- American Society for Testing and Materials, (1988b), "Time of Setting of Concrete Mixtures by Penetration Resistance," C403, *Annual Book of ASTM Standards*, ASTM, Philadelphia.
- American Society for Testing and Materials, (1988c), "Standard Test Methods for Crosshole Seismic Testing," D4428 M-84, *Annual Book of ASTM Standards*, ASTM, Philadelphia, 14 pp.
- American Society of Civil Engineers, (1979), *Analyses of Soil-Structure Interactions Effects for Nuclear Power Plants*, ASCE, New York, 155 pp.
- Baldi, G., D. Bruzzi, S. Superbo, M. Battaglio, and M. Jamiolkowski, (1988) "Seismic Cone in Po River Sand," in *Penetration Testing 1988, ISOPT-1*, J. DeRuiter, Ed., Balkema, Rotterdam, pp. 643-650.
- Baligh, M. M., (1985), "Strain Path Method," *Journal of the Geotechnical Engineering Division*, ASCE, Vol. 111, No. GT9, pp. 1108-1136.
- Ballard, R. F., Jr., (1964), "Determination of Soil Shear Moduli at Depth by In Situ Vibratory Techniques," Waterways Experiment Station, Miscellaneous Paper No. 4-691, December.
- Ballard, R. F., Jr., and D. R. Casagrande, (1967), "Dynamic Foundation Investigation, TAA-2A Radar Site, Cape Kennedy, Florida," Waterways Experiment Station, Miscellaneous Paper No. 4-878, February.
- Bendat, J. S., and A. G. Piersol, (1980), *Engineering Applications of Correlation and Spectral Analysis*, John Wiley & Sons, Inc., New York, 302 pp.
- Biot, M. A., (1956), "Theory of Propagation of Elastic Waves in a Fluid-Saturated Porous Solid," *J. Acoustical Society of America*, Vol. 28, March, pp. 168-191.
- Bracewell, R. N., (1978), *The Fourier Transform and Its Applications*, 2nd Edition, McGraw-Hill, New York, 444 pp.
- Camp, W. M., III, (1988), "Seismic Evaluation of Rock Quality Around Large Excavations," Thesis submitted in partial fulfillment of the Master of Science Degree, The University of Texas at Austin, in progress.
- Department of the Army, (1979), *Geophysical Exploration*, Engineering Manual 1110-1-1802, Corps of Engineers.
- Dines, K. A., and R. J. Lytle, (1979), "Computerized Geophysical Tomography," *Proceedings of the IEEE*, Vol. 67, No. 7, pp. 1065-1073.
- Dobrin, M. B., (1976), *Introduction to Geophysical Prospecting*, 3rd Edition, McGraw-Hill, New York, 630 pp.
- Dobry, R., K. H. Stokoe, II, R. S. Ladd, and T. L. Youd, (1981), "Liquefaction Susceptibility From S-Wave Velocity," *In Situ Testing to Evaluate Liquefaction Susceptibility*, Preprint of Session No. 24 at the ASCE National Convention, St. Louis, Missouri.
- Ewing, W. M., W.S. Jardetzky, and F. Press, (1957), *Elastic Waves in Layered Media*, McGraw-Hill Book Co. Inc., New York, 380 pp.
- Fry, Z. B., (1963), "Development and Evaluation of Soil Bearing Capacity, Foundations of Structures," Waterways Experiment Station, Technical Report No. 3-632, Report No. 1, July.
- Fry, Z. B., (1965), "Dynamic Soils Investigations Project Buggy, Buckboard Mesa Nevada Test Site, Mercury, Nevada," Waterways Experiment Station, Miscellaneous Paper No. 4-666, January.
- Fung, Y. C., (1965), *Foundations of Solid Mechanics*, Prentice-Hall, Inc., Englewood Cliffs, New Jersey, 525 pp.
- Gazetas, G., (1983), "Analysis of Machine Foundation Vibrations: State of the Art," *Soil Dynamics and Earthquake Engineering*, Vol. 2, No. 1, pp. 2-42.
- Gazetas, G., and M. K. Yegian, (1979), "Shear and Rayleigh Waves in Soil Dynamics," *Journal of the Geotechnical Engineering Division*, ASCE, Vol. 105, No. GT12, pp. 1455-1470.
- Golub, G. H., and C. F. Van Loan, (1983) *Matrix Computations*, Johns Hopkins University Press, Baltimore, Maryland, 476 pp.

- Haas, R., and W. R. Hudson, (1978) *Pavement Management Systems*, Robert E. Krieger Publishing Co., Inc., Florida, 457 pp.
- Halvorsen, W. G., and D. L. Brown, (1977) "Impulse Technique for Structural Frequency Response Testing," *Sound and Vibration*, November, pp. 8-21.
- Hardin, B. O., (1978), "The Nature of Stress-Strain Behavior for Soils," Proceedings, Earthquake Engineering and Soil Dynamics, ASCE Specialty Conference, Pasadena, California, pp 3-90.
- Hardin, B. O., and V. P. Drnevich, (1972), "Shear Modulus and Damping in Soils: Design Equations and Curves," *Journal of the Soil Mechanics and Foundations Division*, ASCE, Vol. 98, No. SM7, pp 667-692.
- Haskell, N. A., (1953), "The Dispersion of Surface Waves in Multilayered Media," *Bulletin of the Seismological Society of America*, Vol. 43, pp 17-34.
- Heukelom, W., and C. R. Foster, (1960), "Dynamic Testing of Pavements," *Journal of the Soil Mechanics and Foundations Division*, ASCE, Vol. 86, No. SM1, pp 1-28.
- Hewlett-Packard, (1982), *The Fundamentals of Signal Analysis*, Application Note 243, 57 pp.
- Hoar, R. J., (1982), "Field Measurement of Seismic Wave Velocity and Attenuation," Dissertation submitted in partial fulfillment of the Doctor of Philosophy Degree, The University of Texas at Austin.
- Hoar, R. J., and K. H. Stokoe, II, (1978), "Generation and Measurement of Shear Waves In Situ," *Dynamic Geotechnical Testing*, ASTM STP 654, American Society for Testing and Materials, pp 3-29.
- Hunter, J. A., S. E. Pullan, R. A. Burns, R. M. Gagné, and R. L. Good, (1984), "Shallow Seismic Reflection Mapping of the Overburden-Bedrock Interface with the Engineering Seismograph - Some Simple Techniques," *Geophysics*, Vol. 49, pp 1381-1385.
- Jones, R., (1958), "In Situ Measurement of the Dynamic Properties of Soil by Vibration Methods," *Geotechnique*, Vol. 8, No. 1, March.
- Jones, R., (1962), "Surface Wave Technique for Measuring the Elastic Properties and Thickness of Roads: Theoretical Development," *British Journal of Applied Physics*, Vol. 13, pp 21-29.
- Kang, Y. V., J. M. Roesset, W. M. Camp, III, and K. H. Stokoe, II, (1988), "Tunnel Detection Using Body Waves with an Emphasis on SH-Waves," Geotechnical Engineering Center Report No. GR88-2, The University of Texas at Austin, 103 pp.
- Kausel, E., (1981), "An Explicit Solution for the Green Functions for Dynamic Loads in Layered Media," Research Report R81-13, Department of Civil Engineering, Massachusetts Institute of Technology.
- Kausel, E., and J. M. Roesset, (1981) "Stiffness Matrices for Layered Soils," *Bulletin of the Seismological Society of America*, Vol. 71, No. 6, pp 1743-1761.
- Lacasse, S., and T. Lunne, (1988), "Calibration of Dilatometer Correlations," in *Penetration Testing 1988, ISOPT-1*, J. DeRuiter, Ed., Balkema, Rotterdam, pp 539-548.
- Lawson, C. L., and R. J. Hanson, (1974), *Solving Least Squares Problems*, Prentice-Hall, Inc., Englewood Cliffs, New Jersey, 340 pp.
- Lee, S. H. H., and K. H. Stokoe, II, (1986), "Investigation of Low-Amplitude Shear Wave Velocity in Anisotropic Material," Geotechnical Engineering Center Report No. GR86-6, The University of Texas at Austin, 343 pp.
- Liu, H. P., R. E. Warrick, R. E. Westerlund, J. B. Fletcher, and G.L. Maxwell, (1988) "An Air-Powered Impulsive Shear-Wave Source with Repeatable Signals," *Bulletin of the Seismological Society of America*, Vol. 78, No. 1, pp 355-369.
- Lysmer, J., and L. A. Drake, (1972), "A Finite Element Method for Seismology," in *Methods in Computational Physics*, Vol. 11, B.A. Bolt, Ed., Academic Press, New York, pp 181-216.
- Miller, G. F., and H. Pursey, (1955), "On the Partition of Energy Between Elastic Waves in a Semi-Infinite Solid," *Proc. Royal Society, London, A*, Vol. 233, pp 55-69.
- Miller, R. D., S. E. Pullan, J. S. Waldner, and F. P. Haeni, (1986), "Field Comparison of Shallow Seismic Sources," *Geophysics*, Vol. 51, pp 2067-2092.
- Mok, Y. J., (1987), "Analytical and Experimental Studies of Borehole Seismic Methods," Dissertation submitted in partial fulfillment of the Doctor of Philosophy Degree, The University of Texas at Austin, 272 pp.
- Nazarian, S., (1984) "In Situ Determination of Elastic Moduli of Soil Deposits and Pavement Systems by Spectral-Analysis-of-Surface-Waves Method," Dissertation submitted in partial fulfillment of the Doctor of Philosophy Degree, The University of Texas at Austin.

- Nazarian, S., K. H. Stokoe, II, and W. R. Hudson, (1983), "Use of Spectral Analysis of Surface Waves Method for Determination of Moduli and Thicknesses of Pavement Systems," *Transportation Research Record No. 930*, Washington, D. C., pp 38-45.
- Ni, S. H., (1987), "Dynamic Properties of Sand Under True Triaxial States of Stress from Resonant Column/Torsional Shear Tests," Dissertation submitted in partial fulfillment of the Doctor of Philosophy Degree, The University of Texas at Austin, 421 pp.
- Patel, N. S., (1981) "Generation and Attenuation of Seismic Waves in Downhole Testing," Thesis submitted in partial fulfillment of the Master of Science Degree, The University of Texas at Austin.
- Peck, R. B., W. E. Hanson, and T. H. Thornburn, (1974), *Foundation Engineering*, John Wiley & Sons, Inc., 514 pp.
- Piersol, A. G., (1978), "Use of Coherence and Phase Data Between Two Receivers in Evaluation of Noise Environments," *Journal of Sound and Vibration*, Vol. 56, No. 2, pp 215-228.
- Powers, M. H., (1984), "Velocity Imaging Between Boreholes Using Seismic First Arrivals - A Practical Field System Approach," *Second Technical Symposium on Tunnel Detection*, Colorado School of Mines/U. S. Army, Golden, Colorado, pp 26-28.
- Ramsey, K. A., (1976), "Effective Measurements for Structural Dynamics Testing - Part II," *Sound and Vibration*, Vol. 10, No. 4, pp 18-31.
- Richart, F. E., Jr., J. R. Hall, Jr., and R. D. Woods, (1970), *Vibrations of Soils and Foundations*, Prentice-Hall, Inc., Englewood Cliffs, New Jersey, 414 pp.
- Robertson, P. K., R. G. Campanella, D. Gillespie, and A. Rice, (1985), "Seismic CPT to Measure In Situ Shear Wave Velocity," *Measurement and Use of Shear Wave Velocity for Evaluating Dynamic Soil Properties*, R. D. Woods, Ed., ASCE, New York, 78 pp.
- Roble, C. J., (1988), "Application of Seismic Tomography to Geotechnical Site Investigations," Dissertation submitted in partial fulfillment of the Doctor of Philosophy Degree, The University of Texas at Austin, in progress.
- Roesset, J. M., (1988), Private communication.
- Sánchez-Salinero, I., (1987), "Analytical Investigation of Seismic Methods Used For Engineering Applications," Dissertation submitted in partial fulfillment of the Doctor of Philosophy Degree, The University of Texas at Austin, 401pp.
- Sánchez-Salinero, I., D. W. Chen, K. H. Stokoe, II, and J. M. Roesset, (1988) "Analytical Investigation of Surface Wave Dispersion," Geotechnical Engineering Center Report, The University of Texas at Austin, in progress.
- Seed, H. B., and I. M. Idriss, (1970), "Soil Moduli and Damping Factors for Dynamic Response Analyses," Report No. EERC 70-10, Earthquake Engineering Research Center, The University of California, Berkeley.
- Seed, H. B., R. T. Wong, I. M. Idriss, and K. Tokimatsu, (1986), "Moduli and Damping Factors for Dynamic Analyses of Cohesionless Soils," *Journal of the Geotechnical Engineering Division*, ASCE, Vol. 112, No. GT11, 17 pp.
- Sheu, J. C., (1987), "Applications and Limitations of the Spectral-Analysis-of-Surface-Waves Method," Dissertation submitted in partial fulfillment of the Doctor of Philosophy Degree, The University of Texas at Austin.
- Southwestern Laboratories, Inc., (1985), "Geotechnical Investigation, City of Austin, Waste-to-Energy Project, C.I.P. Project No. 127554," report prepared for HDR Techserve, Inc.
- Steeple, D. W., (1984), "High-Resolution Seismic Reflections at 200 Hz," *Oil and Gas Journal*, Dec. 3, Vol. 49, pp 86-92.
- Stokoe, K.H., II, and G.J. Rix, (1988), "Use of the Spectral-Analysis-of-Surface-Waves Method to Determine In Situ Shear Wave Velocities at Fucino, Italy," Geotechnical Engineering Center Report GR88-5, The University of Texas at Austin.
- Stokoe, K.H.,II, S. Nazarian, G.J. Rix, I. Sánchez-Salinero, J.C. Sheu, and Y.J. Mok, (1988), "In Situ Seismic Testing of Hard-To-Sample Soils by Surface Wave Method," *Proceedings, Earthquake Engineering and Soil Dynamics II - Recent Advances in Ground Motion Evaluation*, J.L. Von Thun, Ed., ASCE Specialty Conference, Park City, Utah, pp. 264-278.
- Suddhiprakarn, C., (1984), "Wave Propagation in Heterogeneous Media," Geotechnical Engineering Center Report No. GR84-6, The University of Texas at Austin, 182 pp.
- Talbot, C.R.S., (1975), "Coherence Function Effects on Phase Difference Determination," *Journal of Sound and Vibration*, Vol. 39, No. 3, pp. 345-358.

- Thomson, W.T., (1950), "Transmission of Elastic Waves Through a Stratified Solid," *Journal of Applied Physics*, Vol. 21, pp. 89-93.
- Thornhill, R.J., and C.C. Smith, (1980) "Fourier and Spectral Analysis - A Short Course," Course Notes Used for ME 397 at the University of Texas.
- Waters, K.H., (1981), *Reflection Seismology*, 2nd Edition, John Wiley & Sons, Inc., New York, 453 pp.
- Woods, R.D., (1986) "In Situ Tests for Foundation Vibrations," in *Use of In Situ Tests in Geotechnical Engineering*, S.P. Clemence, Ed., ASCE, New York, pp. 336-375.



Appendix A
The Influence of Noise on Phase Spectra
and Coherence Functions

A.1 Introduction

Interpreting the phase of the cross power spectrum to determine the total difference in phase between the receivers (i.e. unwrapping the phase as discussed in Section 3.4.2) can be difficult in many instances. The operator usually relies upon the coherence function, the auto power spectra, comparisons with other phase spectra measured at the site, and his/her *a priori* knowledge of the site to aid in the interpretation.

There are many factors which adversely influence the measured phase spectrum including the failure of the source to generate sufficient wave energy over a broad range of frequencies, reflections from interfaces and boundaries within the profile, and measurement noise. The intent of this appendix is to examine the influence of one of these factors, measurement noise, on phase spectra and coherence functions. The purpose of doing so is to understand better the influence of noise so that the phase spectra and coherence functions can be interpreted more intelligently.

In the following sections, simple relationships which express the influence of noise on phase spectra and coherence functions are presented. The effect of uncorrelated and correlated noise on idealized measurements of phase spectra and coherence functions is discussed to illustrate these simple relationships and to provide several examples of the effect of noise on phase and coherence.

A.2 Effect of Noise on Phase and Coherence: Simple Relationships

The model of the SASW method used to study the effect of noise on phase and coherence is shown in Fig. A1. In this model, $H_1(f)$ and $H_2(f)$ are linear systems and represent the soil profile or pavement system in the SASW method. These two linear systems are closely related; the differences result from the different rates of attenuation (gain) or propagation distance (phase) for different receiver spacings in SASW testing. The source in SASW testing is represented by $x(t)$. The *true* outputs at the receivers are represented by $v_1(t)$ and $v_2(t)$. At each receiver, an

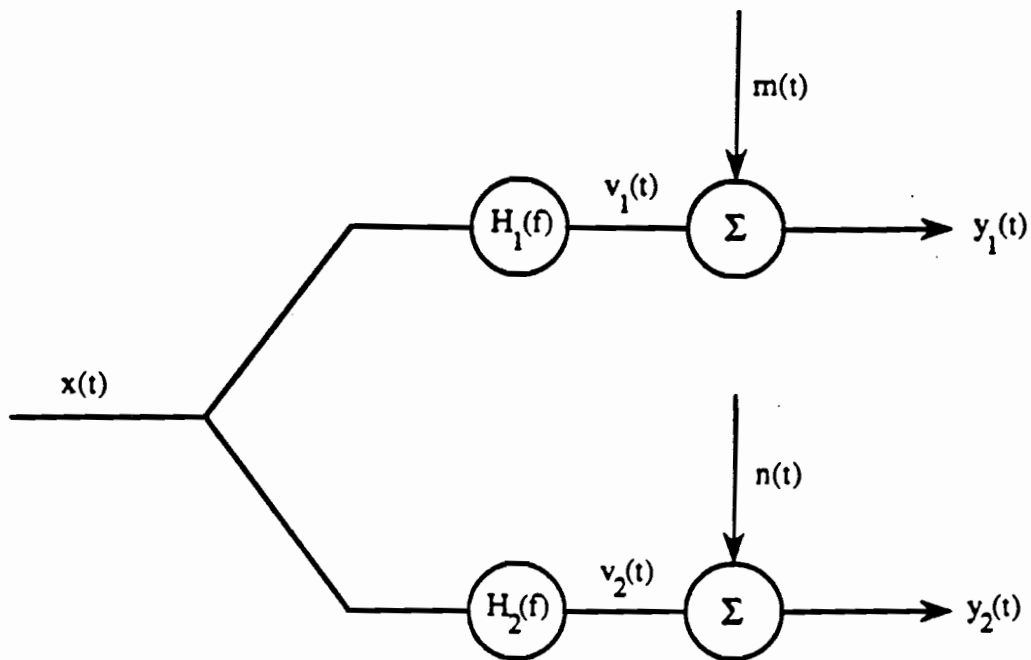


Fig. A1 Model of Linear System Including Additive Noise

additive noise term is combined with the true signal which results in the *measured* outputs, $y_1(t)$ and $y_2(t)$. The noise at each receiver is represented by $m(t)$ and $n(t)$ as shown in the figure. It is important to note that $m(t)$ and $n(t)$ do not represent noise which has passed through the linear systems; that is, $m(t)$ and $n(t)$ are not caused by extraneous seismic waves propagating through the soil or pavement. The terms represent air-borne noise which has been measured by the receivers or electrical noise present in the receivers and cables.

Define the ratio of noise to signal at each receiver by the following expressions:

$$\alpha(f) = \frac{G_{mm}(f)}{G_{v_1v_1}(f)}, \text{ and} \quad (\text{A.1})$$

$$\beta(f) = \frac{G_{nn}(f)}{G_{v_2v_2}(f)} \quad (\text{A.2})$$

where

$G_{mn}(f)$ = the auto power spectrum of the noise at the first receiver,
 $G_{nn}(f)$ = the auto power spectrum of the noise at the second receiver,
 $G_{v_1v_1}(f)$ = the auto power spectrum of the true signal at the first receiver,
 and
 $G_{v_2v_2}(f)$ = the auto power spectrum of the true signal at the second receiver.

Furthermore, assume that the *true* coherence function, $\gamma_{v_1v_2}^2$, is equal to one.

Consider the case of correlated noise defined by the following expression:

$$0 \leq \gamma_{mn}^2 \leq 1 \quad (\text{A.3})$$

Note that the noise terms are correlated only with one another; the noise terms are not correlated with the signal terms, $v_1(t)$ and $v_2(t)$. The *measured* coherence function, $\gamma_{y_1y_2}^2$, is given by the following expression:

$$\gamma_{y_1y_2}^2 = \frac{1 - \gamma_{mn}^2 \cdot \alpha(f) \cdot \beta(f)}{[1 + \alpha(f)] \cdot [1 + \beta(f)]} \quad (\text{A.4})$$

The expression for uncorrelated noise is a special case of Eq. A.4 with γ_{mn}^2 equal to zero. The change in the phase of the cross power spectrum, $\Delta\Theta_{y_2y_1}$, is given by:

$$\Delta\Theta_{y_2y_1} = \sin^{-1} [|\gamma_{mn}| \cdot \alpha(f)^{0.5} \cdot \beta(f)^{0.5}] \quad (\text{A.5})$$

Notice that the change in the phase of the cross power spectrum is equal to zero if the noise terms are uncorrelated (i.e. $\gamma_{mn}^2 = 0$). Equation A.5 represents the maximum change in phase and was developed using the assumption of Talbot (1975) which concerns the relationship between the cross power spectrum of the noise, G_{mn} , and the cross power spectrum of the true signals, $G_{v_1v_2}$.

Finally, it is possible to include the effects of *random* errors (as opposed to the *bias* errors represented by Eqs. A.4 and A.5) on phase and coherence. The normalized random error (also called coefficient of variation) of the coherence function, $\epsilon(\gamma_{y_1y_2}^2)$, is given by the expression:

$$\varepsilon(\gamma_{y_1 y_2}^2) \cong \frac{\sqrt{2}(1 - \gamma_{y_1 y_2}^2)}{|\gamma_{y_1 y_2}| \sqrt{n_d}} \quad (\text{A.6})$$

where

$\gamma_{y_1 y_2}^2$ = the measured coherence function, and
 n_d = the number of ensemble averages.

The standard deviation of the phase of the cross power spectrum is expressed by:

$$\text{s.d.}(\Theta_{y_2 y_1}) \cong \sin^{-1} \left[\frac{(1 - \gamma_{y_1 y_2}^2)^{0.5}}{|\gamma_{y_1 y_2}| \sqrt{2n_d}} \right] \quad (\text{A.7})$$

Equations A.4 through A.7 can be used to calculate the measured phase and coherence for those situations where it is desired to include the effects of noise and random errors on a measurement. In-depth discussions of the influence of noise on spectral functions are included in Talbot (1975), Piersol (1978), and Bendat and Piersol (1980).

A.3 Effect of Noise on Phase and Coherence: Idealized Measurements

Phase and coherence measurements were made on an idealized linear system to provide several examples of the influence of noise on actual measurements. To isolate the effect of noise on phase spectra and coherence functions, idealized measurements were made using a *linear system simulator* (Hewlett Packard Model 05423-60002). This simulator is a small device which imitates a mechanical linear system. As such, the device creates a phase difference between the input and output to the device which can be used to study the influence of noise.

The noise-free phase spectrum and coherence function of the linear system simulator are shown in Fig. A2. These spectra were generated using 2-volt random input motion. To study the influence of noise on these spectral functions, three

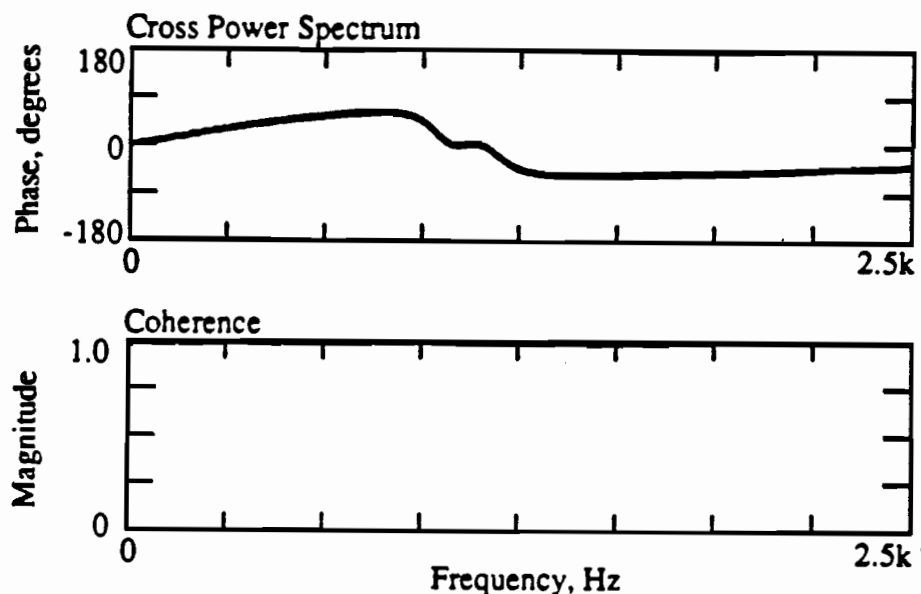


Fig. A2 Noise-Free Phase Spectrum and Coherence Function of the Linear System Simulator

quantities were varied: (1) uncorrelated vs. correlated noise, (2) ratio of noise to signal, and (3) number of averages.

The influence of uncorrelated noise on the spectra is shown in Fig. A3. These spectra were generated using 20-millivolt noise signals and 10 averages. Increasing the number of averages from 10 to 100 dramatically reduces the variability in the phase spectrum and coherence function as shown in Fig. A4. The effect of increasing the noise-to-signal ratio is illustrated in Fig. A5. For this record the noise level was increased to 200 millivolts and 10 averages were used. In addition to added variability, the coherence function has decreased significantly over much of the record. The results obtained using 100 averages are shown in Fig. A6. With the exception of the central portion of the phase record (900 to 1300 Hz), increasing the number of averages does not improve the records to the extent that the records become usable for this higher noise level.

Similar comparisons are now performed for correlated noise. Because of the manner in which the correlated noise was introduced to the system in the

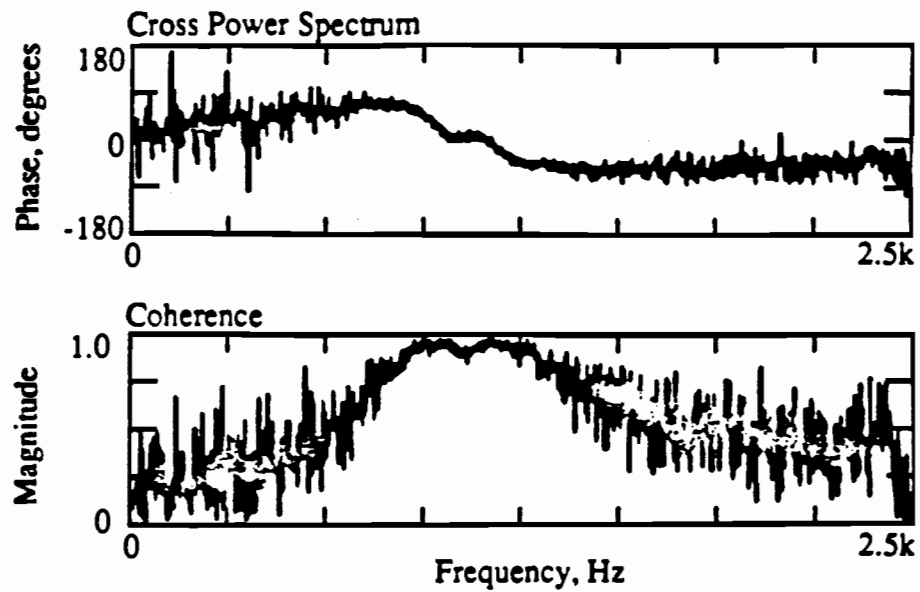


Fig. A3

Influence of Uncorrelated Noise on Phase and Coherence; 2-volt Signal Level; 20-millivolt Noise Level; 10 Averages

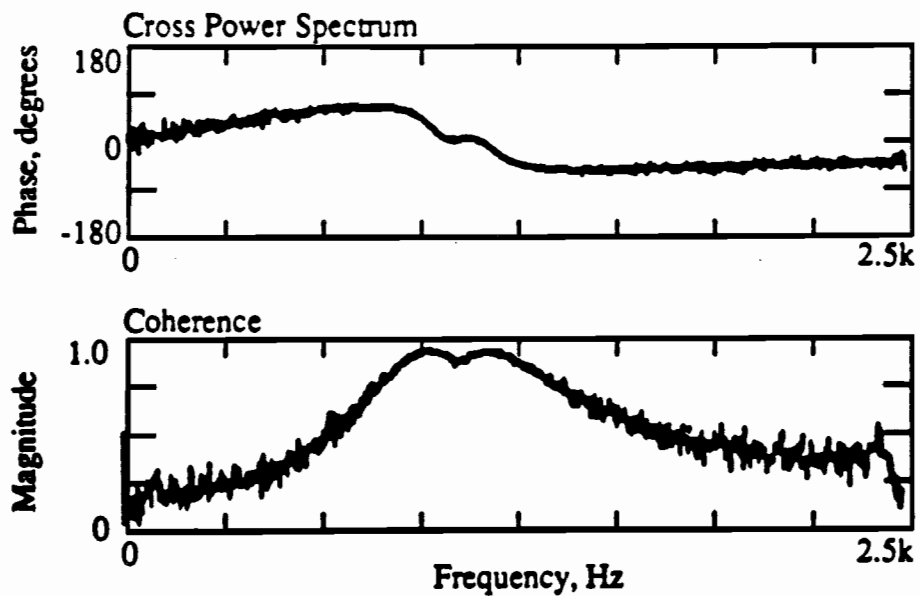


Fig. A4

Influence of Uncorrelated Noise on Phase and Coherence; 2-volt Signal Level; 20-millivolt Noise Level; 100 Averages

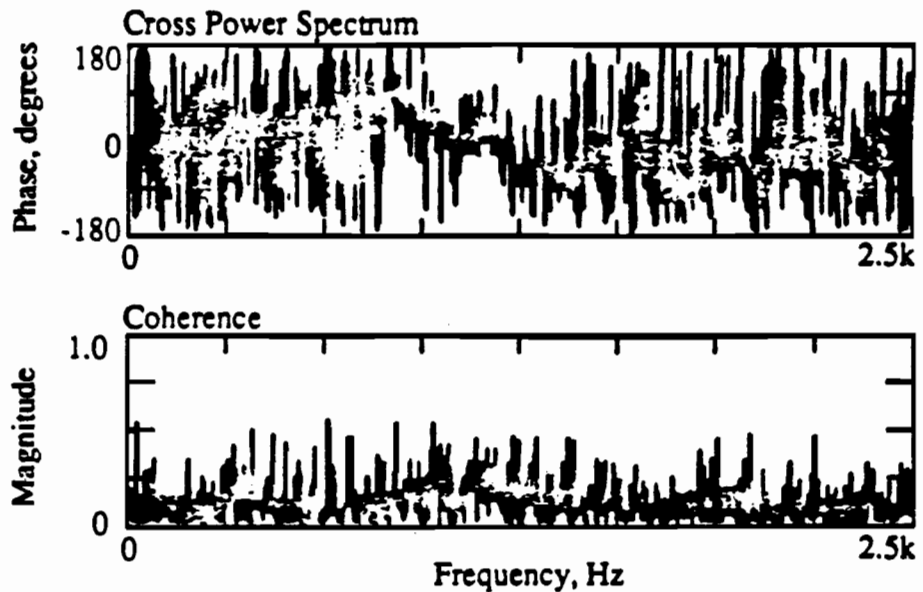


Fig. A5 Influence of Uncorrelated Noise on Phase and Coherence; 2-volt Signal Level; 200-millivolt Noise Level; 10 Averages

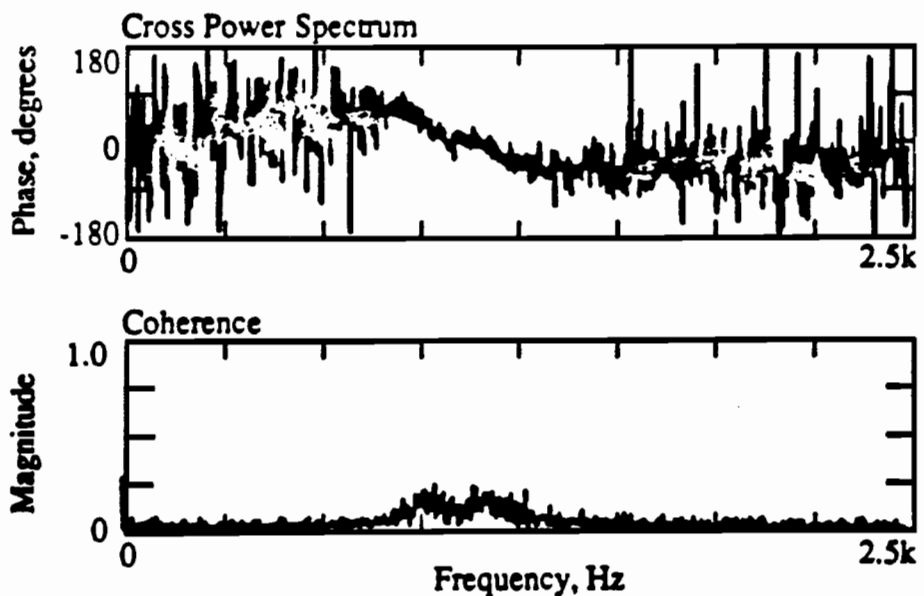


Fig. A6 Influence of Uncorrelated Noise on Phase and Coherence; 2-volt Signal Level; 200-millivolt Noise Level; 100 Averages

experimental arrangement, it is not possible to specify the noise level used in each measurement. The noise-to-signal ratio was varied by changing the input signal level rather than the noise level. Phase and coherence spectra are shown in Fig. A7 for a "low" noise-to-signal ratio. The effect of increasing the number of averages from 10 to 100 is illustrated in Fig. A8. For this low noise level, increasing the number of averages significantly reduces the variability in the phase and coherence spectra. Increasing the noise-to-signal ratio (by decreasing the signal amplitude in this case) introduces large variations into the phase and coherence spectra and greatly reduces the value of the coherence function in the range of frequencies from 750 to 1500 Hz. This is demonstrated in Fig. A9 Spectra which result after increasing the number of averages to 100 are shown in Fig. A10. Unlike uncorrelated noise, increasing the number of averages significantly reduces the variability in the phase record.

A.4 Summary

An understanding of the effect of noise on phase and coherence spectra can be helpful when interpreting the phase of the cross power spectrum to calculate a dispersion curve. In this appendix, simple relationships which express the influence of noise-to-signal ratios, noise correlation, and number of averages on phase and coherence have been presented. These relationships can be used to generate synthetic phase and coherence records to illustrate the effect of each of these factors.

Measurements were performed using an idealized linear system to demonstrate these effects on actual measured data. The noise-to-signal ratio and number of averages exerted the largest influence on phase and coherence records. The differences between correlated and uncorrelated noise are too small to be apparent in the presence of these other factors.

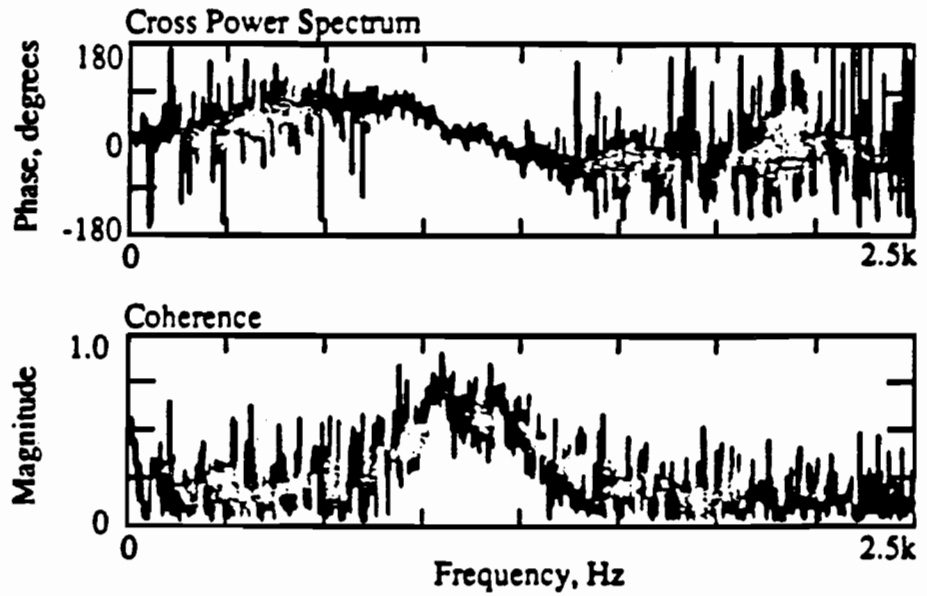


Fig. A7 Influence of Correlated Noise on Phase and Coherence; 2-volt Signal Level; Low Noise Level; 10 Averages

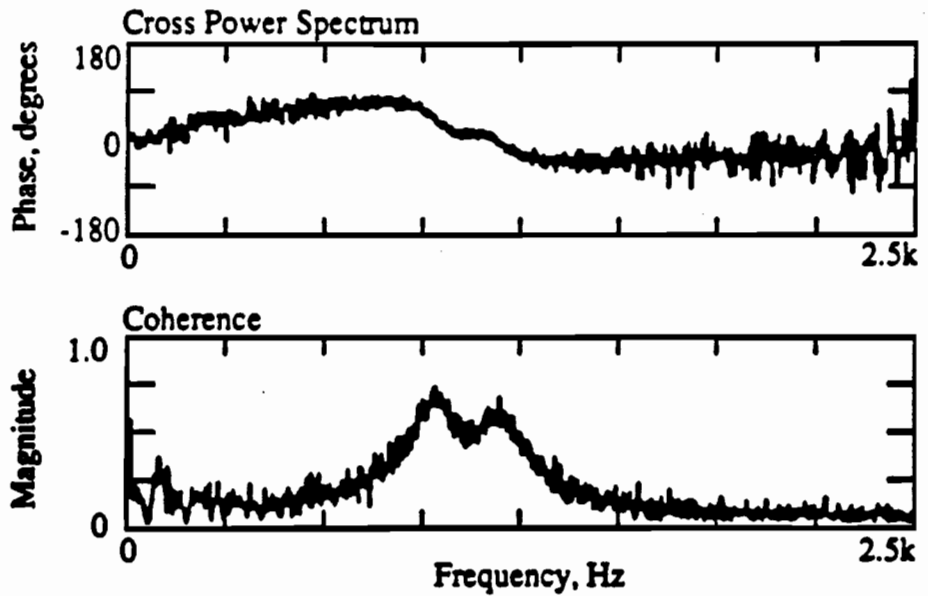


Fig. A8 Influence of Correlated Noise on Phase and Coherence; 2-volt Signal Level; Low Noise Level; 100 Averages

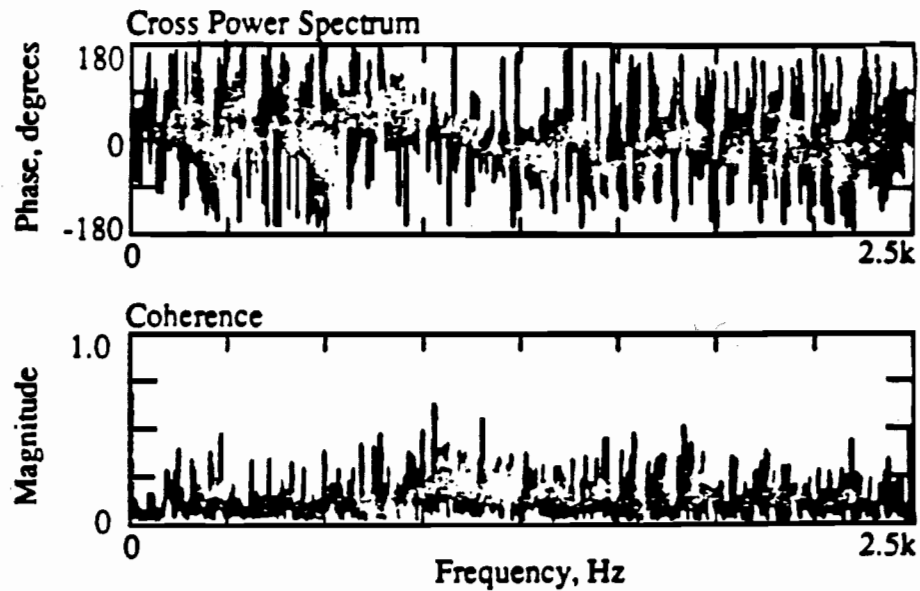


Fig. A9 Influence of Correlated Noise on Phase and Coherence; 0.5-volt Signal Level; High Noise Level; 10 Averages

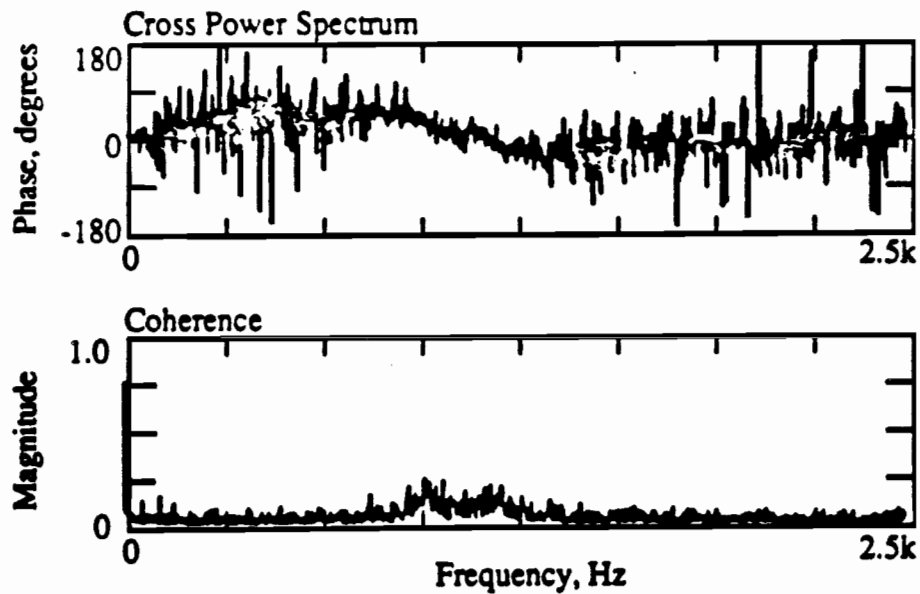


Fig. A10 Influence of Correlated Noise on Phase and Coherence; 0.5-volt Signal Level; High Noise Level; 100 Averages

Appendix B Tabulated Dispersion Curve

The dispersion curve presented in this appendix is an abbreviated version of the complete composite dispersion curve. When the dispersion data from several receiver spacings are combined to form the composite dispersion curve for a site, the total number of points is often very high. It can be difficult to manipulate files containing such a large number of data points. To make the composite dispersion curve more manageable in size, the number of points is reduced. The objective is to select a reduced number of points which still are representative of the complete dispersion curve and to prevent information from being "lost" when fewer points are used.

A simple algorithm is used to select the desired number of points from the complete dispersion curve such that the resulting data points are approximately evenly distributed between the minimum and maximum wavelengths contained in the complete dispersion curve. All of the original points within one of these wavelength increments are averaged together to calculate one point which is representative of that increment. Other methods of selecting a reduce number of data points are, of course, possible.

The dispersion curve presented in this appendix contains 371 points which were selected from a complete dispersion curve containing 7796 points.

<i>Frequency</i> Hz	<i>Phase</i> <i>Velocity</i> ft/sec	<i>Wavelength</i> ft	<i>Frequency</i> Hz	<i>Phase</i> <i>Velocity</i> ft/sec	<i>Wavelength</i> ft
1.325	704.22	531.36	1.875	498.56	266.01
1.337	678.30	507.42	1.880	478.88	254.86
1.350	647.47	479.54	1.887	490.36	259.78
1.362	632.06	464.12	1.900	471.34	247.97
1.375	624.18	453.95	1.912	455.26	238.13
1.387	619.59	446.74	1.920	459.86	239.44
1.400	615.98	439.85	1.925	445.10	231.24
1.412	620.90	439.85	1.938	445.42	229.93
1.425	630.74	442.80	1.950	448.05	229.60
1.437	652.06	453.95	1.962	448.70	228.62
1.450	672.07	463.46	1.975	463.14	234.52
1.462	675.68	462.15	1.980	428.37	216.48
1.475	674.04	456.90	1.987	468.06	235.50
1.487	650.42	437.22	2.000	450.02	225.01
1.500	629.76	419.84	2.012	449.36	223.37
1.512	605.82	400.49	2.020	424.76	210.25
1.525	590.40	387.04	2.025	435.58	215.17
1.537	580.56	377.86	2.038	423.45	207.62
1.550	582.53	375.56	2.051	413.94	202.05
1.562	587.12	375.89	2.060	423.45	205.66
1.575	585.48	371.62	2.062	410.33	199.10
1.587	582.53	367.03	2.074	409.34	197.46
1.600	566.78	354.24	2.080	421.81	202.70
1.612	554.65	344.07	2.087	410.00	196.47
1.625	541.53	333.25	2.101	411.64	196.14
1.637	532.34	325.05	2.112	409.02	193.85
1.650	525.78	318.49	2.124	408.36	192.21
1.662	517.26	311.27	2.136	407.05	190.57
1.675	496.26	296.18	2.140	402.46	187.94
1.687	477.57	283.06	2.150	405.08	188.27
1.700	463.14	272.24	2.159	394.58	182.70
1.712	464.78	271.58	2.162	399.50	184.66
1.725	475.27	275.52	2.176	392.29	180.40
1.737	501.51	288.64	2.187	383.10	175.15
1.750	493.97	282.41	2.200	377.20	171.54
1.762	479.86	272.24	2.211	366.05	165.64
1.775	459.86	259.12	2.220	377.53	170.23
1.787	432.63	242.06	2.224	364.08	163.67
1.800	411.64	228.94	2.237	367.36	164.33
1.812	409.67	226.32	2.240	360.80	161.05
1.820	509.06	279.78	2.249	374.25	166.30
1.825	421.15	230.91	2.261	369.66	163.34
1.837	444.11	241.74	2.274	387.70	170.56
1.840	504.46	274.21	2.280	359.82	157.77
1.850	470.35	254.20	2.287	392.94	171.87
1.862	492.00	264.37	2.300	378.51	164.66

<i>Frequency Hz</i>	<i>Phase Velocity ft/sec</i>	<i>Wavelength ft</i>	<i>Frequency Hz</i>	<i>Phase Velocity ft/sec</i>	<i>Wavelength ft</i>
2.312	399.83	172.86	2.824	325.05	115.13
2.323	378.18	162.69	2.838	326.03	114.80
2.338	371.95	159.08	2.846	324.06	113.82
2.350	380.48	162.03	2.861	323.74	113.16
2.360	364.08	154.16	2.876	324.06	112.83
2.375	378.84	159.41	2.886	322.75	111.85
2.380	345.06	144.98	2.899	320.78	110.86
2.387	383.43	160.72	2.911	316.52	108.57
2.400	365.72	152.52	2.924	317.50	108.57
2.411	392.94	163.02	2.937	312.91	106.60
2.422	369.00	152.52	2.945	315.86	107.26
2.438	369.33	151.54	2.962	314.55	106.27
2.449	396.22	161.70	2.974	309.96	104.30
2.461	365.06	148.26	2.984	313.24	104.96
2.477	356.21	143.66	3.000	312.91	104.30
2.487	345.71	139.07	3.012	308.98	102.66
2.500	339.48	135.79	3.024	312.26	103.32
2.512	329.31	131.20	3.038	310.94	102.34
2.523	337.18	133.82	3.055	309.96	101.35
2.538	331.28	130.54	3.062	306.02	100.04
2.540	342.10	134.81	3.081	306.68	99.38
2.549	340.46	133.50	3.100	306.68	99.06
2.561	340.14	132.84	3.112	304.06	97.74
2.575	339.81	131.86	3.123	306.35	98.07
2.579	337.18	130.54	3.138	306.68	97.74
2.588	338.17	130.54	3.154	306.68	97.09
2.601	336.20	129.23	3.168	306.02	96.43
2.612	333.90	127.92	3.184	306.02	96.10
2.622	333.90	127.26	3.200	304.38	95.12
2.637	328.66	124.64	3.216	302.74	94.14
2.640	339.48	128.58	3.231	299.46	92.82
2.649	327.34	123.66	3.246	298.15	91.84
2.662	331.28	124.64	3.261	296.51	90.86
2.678	331.28	123.66	3.277	295.20	90.20
2.687	328.98	122.34	3.296	294.22	89.22
2.700	331.61	122.67	3.312	293.23	88.56
2.711	332.26	122.34	3.322	293.89	88.56
2.721	329.31	121.03	3.342	293.56	87.90
2.725	332.26	122.02	3.361	293.23	87.25
2.738	329.64	120.38	3.377	292.58	86.59
2.749	329.97	120.05	3.396	290.61	85.61
2.761	326.36	118.08	3.414	286.34	83.97
2.776	323.41	116.44	3.432	284.38	82.98
2.787	322.42	115.78	3.446	290.94	84.30
2.801	323.08	115.46	3.462	288.64	83.31
2.811	325.70	115.78	3.481	296.18	84.95

<i>Frequency Hz</i>	<i>Phase Velocity ft/sec</i>	<i>Wavelength ft</i>	<i>Frequency Hz</i>	<i>Phase Velocity ft/sec</i>	<i>Wavelength ft</i>
3.501	293.89	83.97	4.612	271.91	59.04
3.519	298.15	84.62	4.647	269.29	58.06
3.537	292.25	82.66	4.677	271.26	58.06
3.558	290.94	81.67	4.713	269.62	57.07
3.577	292.58	81.67	4.747	268.30	56.42
3.595	289.95	80.69	4.776	270.93	56.74
3.615	291.92	80.69	4.812	268.30	55.76
3.634	289.62	79.70	4.849	267.65	55.10
3.657	287.66	78.72	4.886	266.66	54.45
3.676	287.98	78.39	4.923	266.66	54.12
3.694	286.02	77.41	4.955	263.38	53.14
3.718	285.36	76.75	4.989	264.04	52.81
3.738	286.02	76.42	5.027	263.06	52.48
3.756	284.38	75.77	5.068	263.06	51.82
3.780	282.41	74.78	5.110	261.74	51.17
3.800	282.08	74.13	5.151	260.43	50.51
3.817	283.06	74.13	5.187	259.45	50.18
3.842	282.74	73.47	5.224	258.79	49.53
3.868	282.74	73.14	5.269	258.79	49.20
3.884	283.39	72.82	5.312	256.50	48.22
3.907	282.74	72.49	5.350	256.17	47.89
3.935	281.10	71.50	5.393	256.50	47.56
3.961	279.78	70.52	5.439	254.86	46.90
3.980	280.44	70.52	5.483	256.17	46.58
4.003	279.46	69.86	5.531	255.18	46.25
4.031	281.10	69.86	5.575	255.18	45.92
4.058	278.14	68.55	5.619	253.87	45.26
4.081	278.80	68.22	5.669	254.20	44.94
4.101	276.18	67.24	5.719	252.56	44.28
4.130	276.83	66.91	5.768	252.23	43.62
4.158	273.88	65.93	5.817	250.59	42.97
4.182	272.90	65.27	5.867	251.25	42.64
4.210	273.22	64.94	5.920	250.92	42.31
4.234	272.57	64.29	5.977	252.23	42.31
4.255	270.60	63.63	6.031	253.22	41.98
4.288	269.94	62.98	6.081	253.54	41.66
4.317	269.94	62.65	6.138	253.54	41.33
4.343	270.27	62.32	6.196	252.89	40.67
4.371	271.26	61.99	6.255	252.56	40.34
4.400	275.19	62.65	6.312	253.54	40.02
4.431	272.57	61.66	6.374	256.17	40.34
4.459	273.55	61.34	6.434	255.84	39.69
4.489	272.24	60.68	6.498	256.17	39.36
4.521	272.90	60.35	6.561	256.17	39.03
4.551	272.24	59.70	6.622	254.86	38.38
4.584	272.90	59.70	6.695	255.84	38.05

<i>Frequency Hz</i>	<i>Phase Velocity ft/sec</i>	<i>Wavelength ft</i>	<i>Frequency Hz</i>	<i>Phase Velocity ft/sec</i>	<i>Wavelength ft</i>
6.761	255.84	37.72	12.648	233.21	18.37
6.829	256.82	37.72	12.894	232.55	18.04
6.899	256.17	37.06	13.147	232.22	17.71
6.968	255.51	36.74	13.412	231.90	17.38
7.045	256.17	36.41	13.687	232.55	17.06
7.120	254.53	35.75	13.971	232.88	16.73
7.194	254.86	35.42	14.260	233.21	16.40
7.272	253.22	34.77	14.577	232.88	16.07
7.353	253.54	34.44	14.904	232.55	15.74
7.433	251.90	33.78	15.246	232.22	15.09
7.522	251.58	33.46	15.597	231.24	14.76
7.610	251.90	33.13	15.933	232.22	14.43
7.694	250.59	32.47	16.355	232.55	14.10
7.786	250.26	32.14	16.768	232.55	13.78
7.874	249.28	31.82	17.194	233.54	13.45
7.971	248.62	31.16	17.661	232.55	13.12
8.064	247.97	30.83	18.160	231.90	12.79
8.163	247.64	30.18	18.645	232.55	12.46
8.264	248.95	30.18	19.175	232.55	12.14
8.370	248.95	29.85	19.745	232.22	11.81
8.477	249.28	29.52	20.359	232.22	11.48
8.583	248.30	28.86	20.995	231.90	11.15
8.697	246.33	28.21	21.653	229.27	10.50
8.811	246.00	27.88	22.416	225.34	10.17
8.930	245.34	27.55	23.182	225.01	9.84
9.049	245.34	27.22	23.998	227.63	9.51
9.169	245.02	26.57	24.890	226.65	9.18
9.301	244.69	26.24	25.841	224.35	8.53
9.428	244.03	25.91	26.900	223.04	8.20
9.560	243.38	25.58	28.000	222.71	7.87
9.700	242.72	24.93	29.263	222.38	7.54
9.849	241.41	24.60	30.600	224.35	7.22
9.987	239.44	23.94	32.042	228.94	7.22
10.154	237.80	23.29	33.689	233.86	6.89
10.310	236.16	22.96	35.476	242.39	6.89
10.466	235.83	22.63	37.489	247.64	6.56
10.628	235.18	21.98	39.715	250.59	6.23
10.797	234.19	21.65	42.161	251.58	5.90
10.980	234.19	21.32	45.027	251.58	5.58
11.166	235.50	20.99	48.320	247.31	5.25
11.356	235.18	20.66	52.090	244.36	4.59
11.551	235.50	20.34	56.256	250.92	4.59
11.747	235.50	20.01	61.499	250.26	3.94
11.963	235.18	19.68	68.011	246.33	3.61
12.182	234.52	19.35	75.600	245.67	3.28
12.415	233.86	18.70	85.685	250.26	2.95

<i>Frequency</i> <i>Hz</i>	<i>Phase</i> <i>Velocity</i> <i>ft/sec</i>	<i>Wavelength</i> <i>ft</i>
96.718	253.54	2.62
115.133	260.10	2.30
138.311	311.27	2.30

Appendix C Geophone Calibration Curves

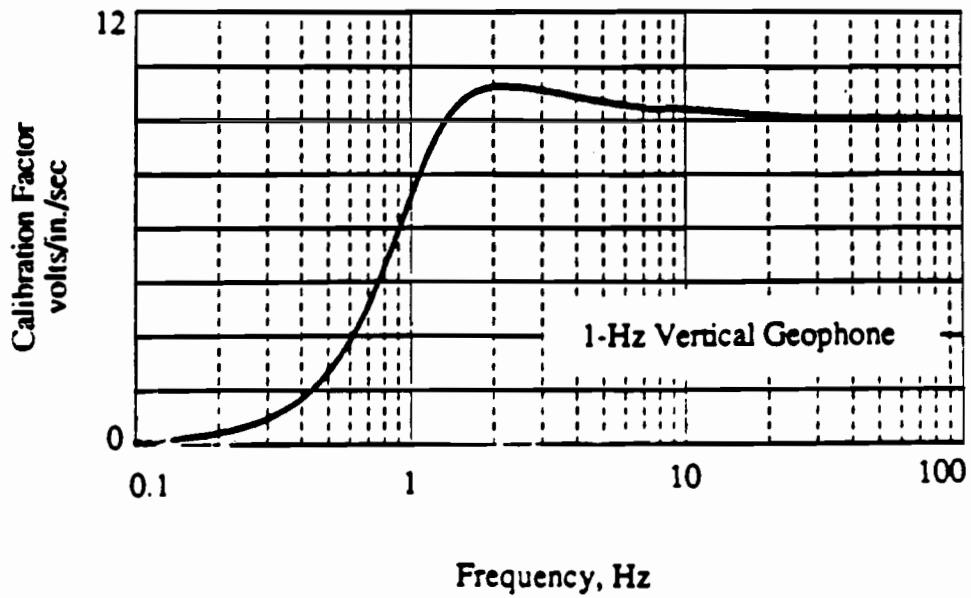


Fig. C1 Calibration Curve for a 1-Hz Natural Frequency Geophone

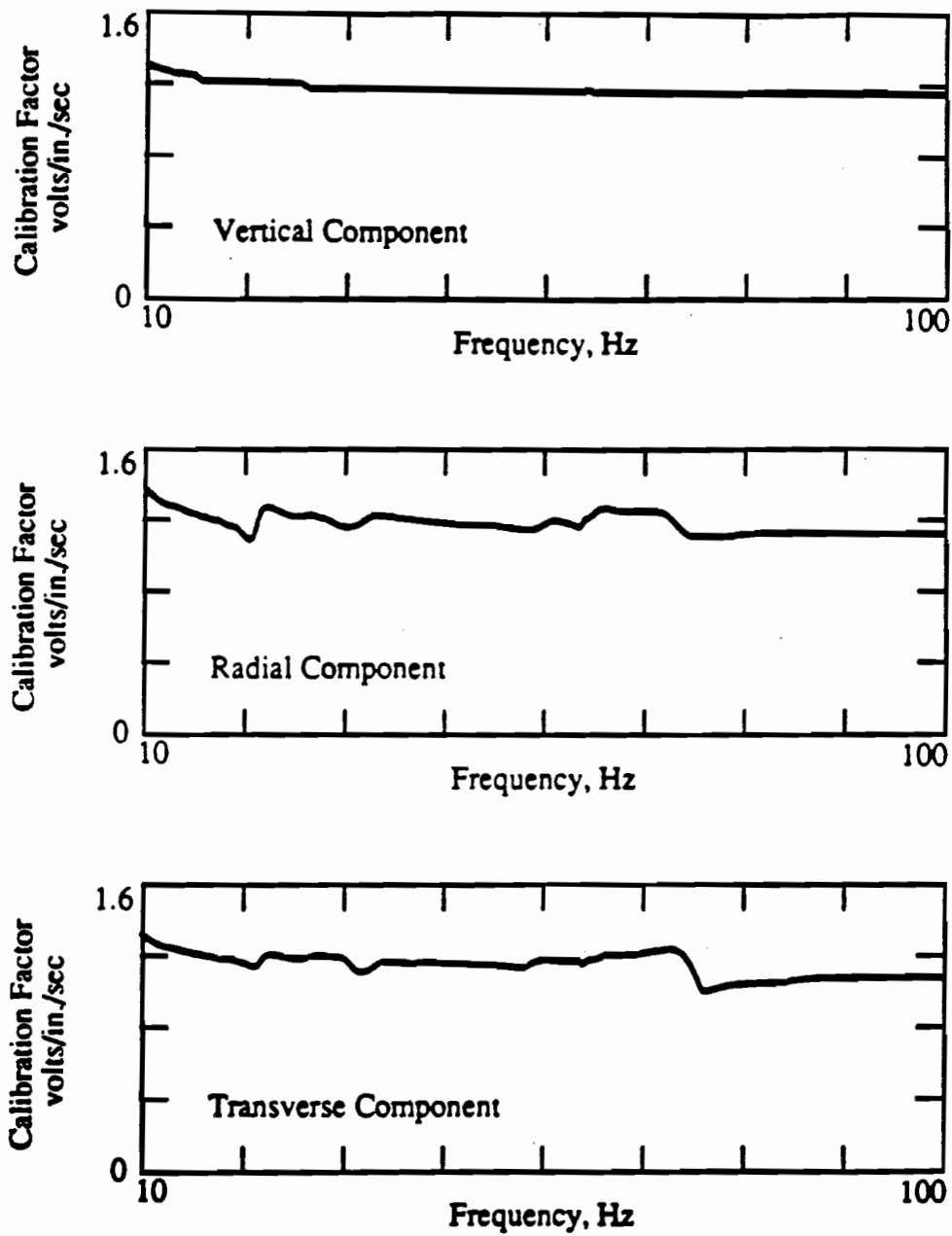


Fig. C2

Calibration Curves for the Vertical, Radial, and Transverse Components of a 4.5-Hz Natural Frequency Triaxial Geophone

Appendix D
Particle Displacement Spectra

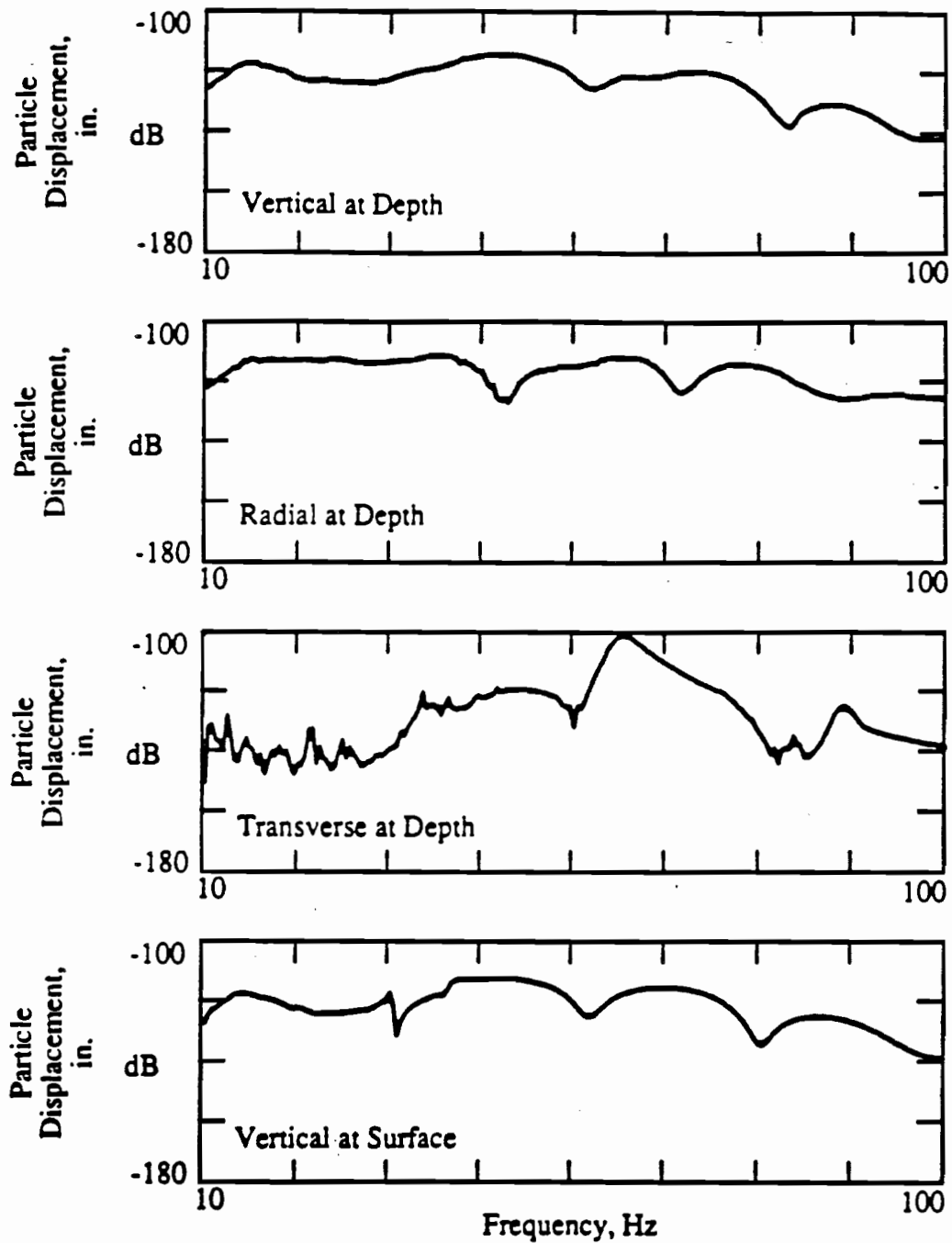


Fig. D1 Particle Displacement Spectra for Measurements at the Surface; (a) Vertical Component, (b) Radial Component, (c) Transverse Component, and (d) Vertical Component at the Surface

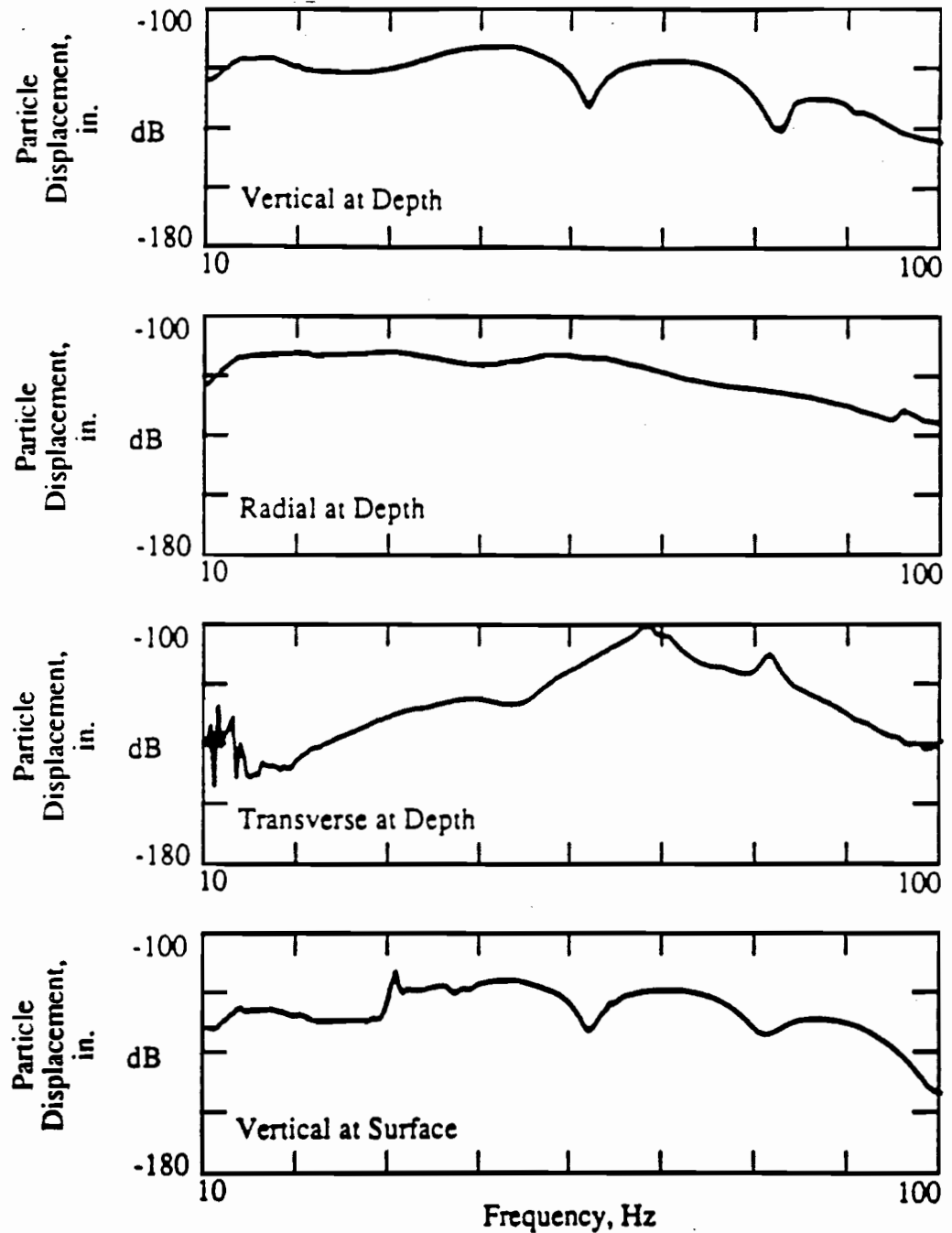


Fig. D2

Particle Displacement Spectra for Measurements at a Depth of 1 ft; (a) Vertical Component, (b) Radial Component, (c) Transverse Component, and (d) Vertical Component at the Surface

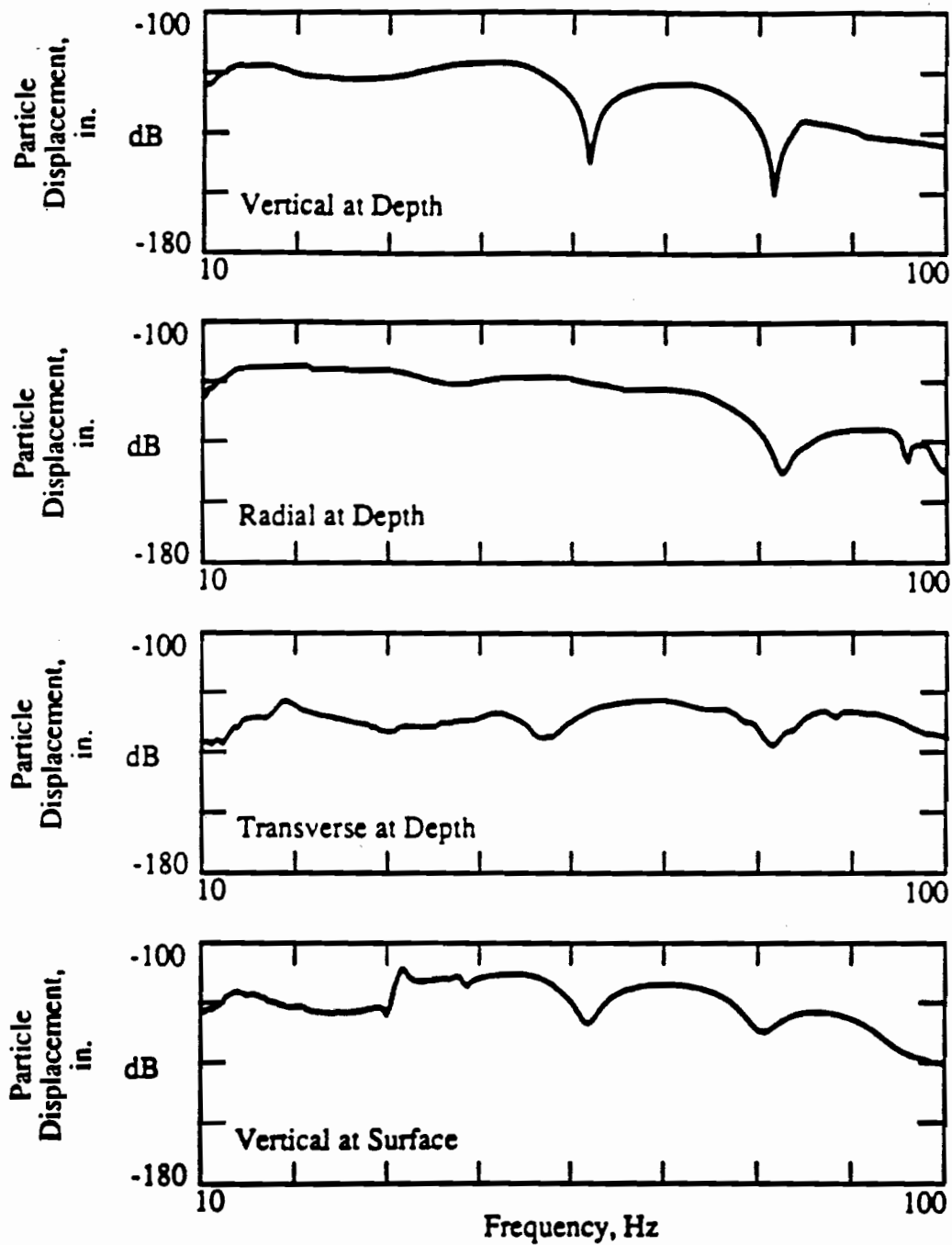


Fig. D3

Particle Displacement Spectra for Measurements at a Depth of 2 ft; (a) Vertical Component, (b) Radial Component, (c) Transverse Component, and (d) Vertical Component at the Surface

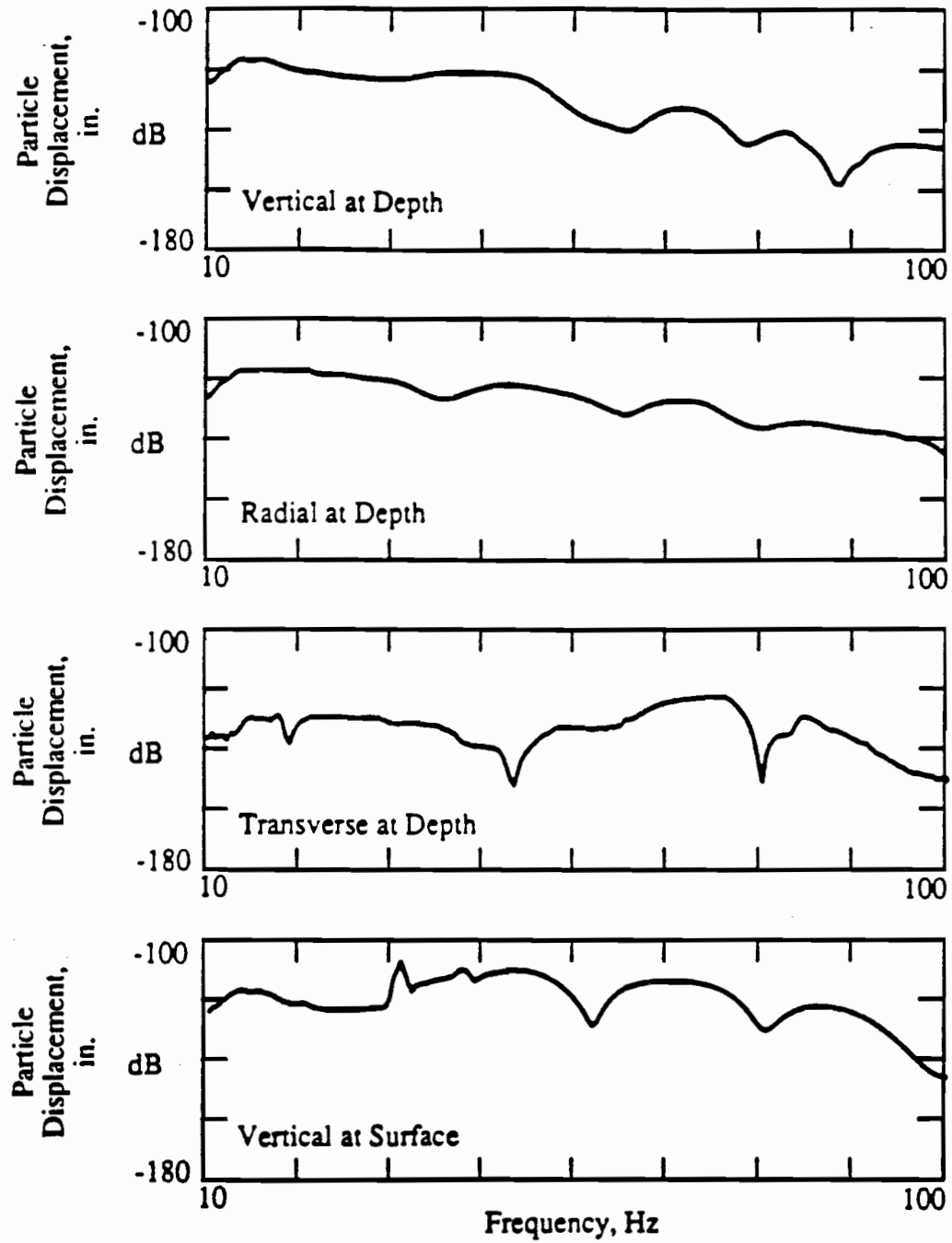


Fig. D4

Particle Displacement Spectra for Measurements at a Depth of 3 ft; (a) Vertical Component, (b) Radial Component, (c) Transverse Component, and (d) Vertical Component at the Surface

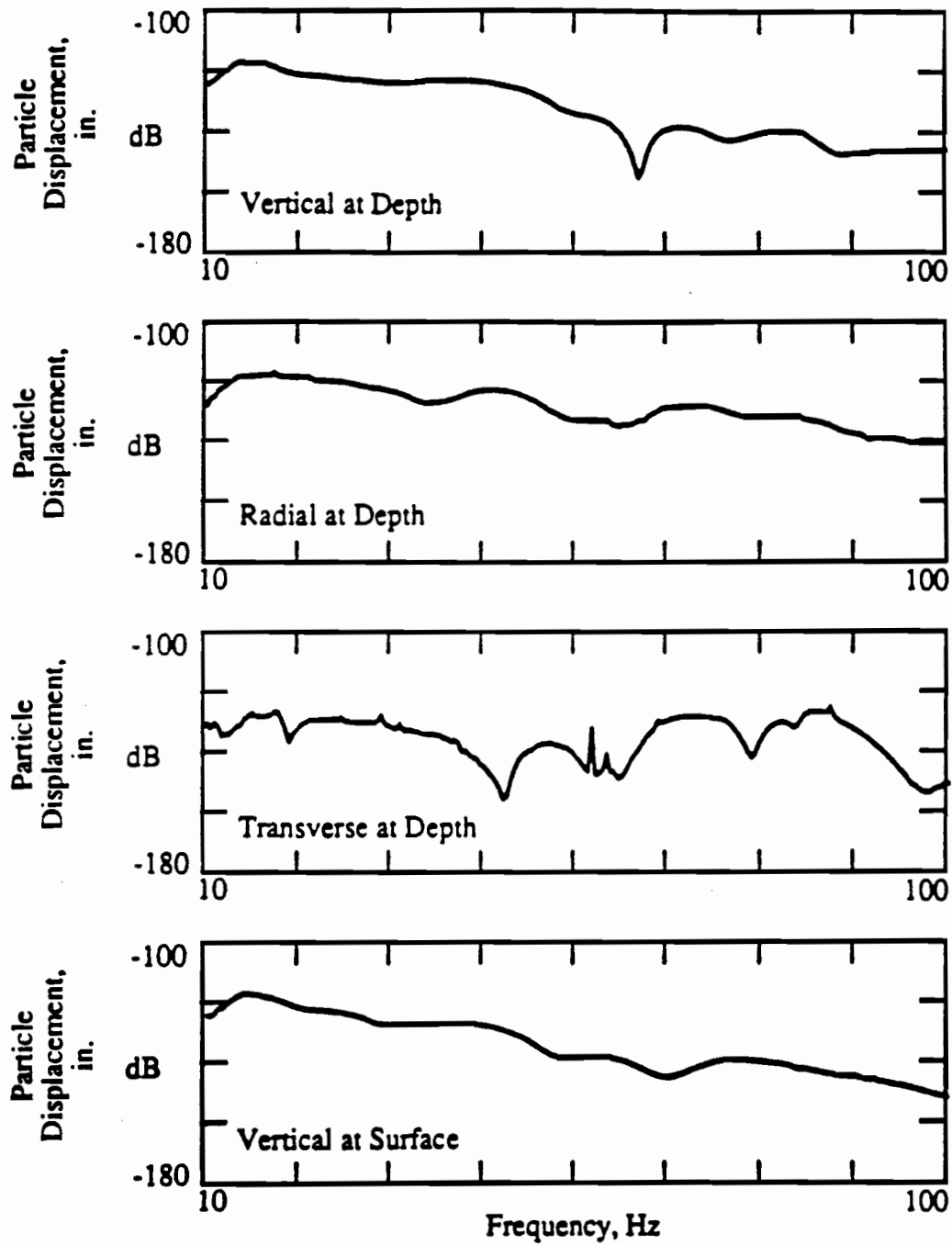


Fig. D5

Particle Displacement Spectra for Measurements at a Depth of 4 ft; (a) Vertical Component, (b) Radial Component, (c) Transverse Component, and (d) Vertical Component at the Surface

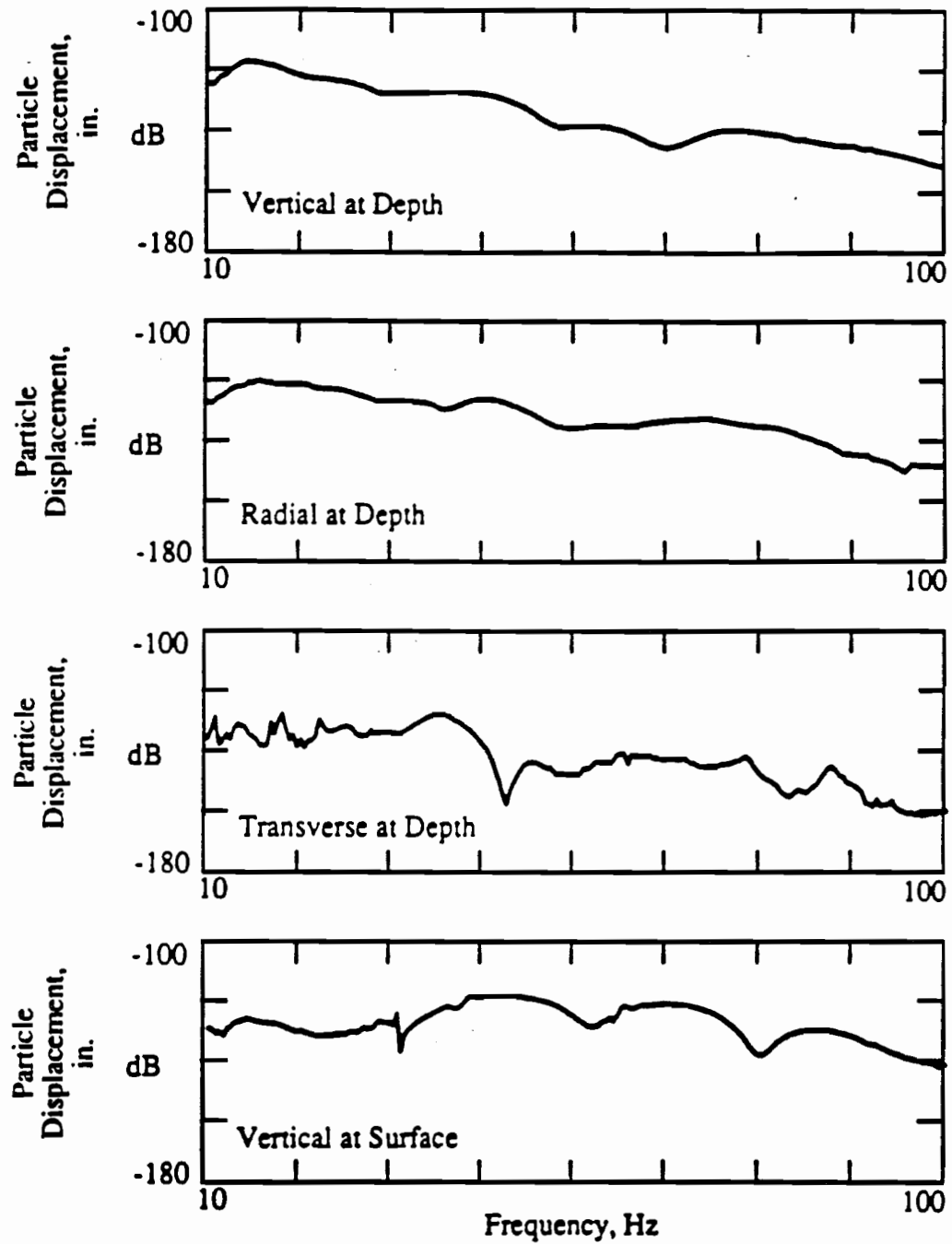


Fig. D6

Particle Displacement Spectra for Measurements at a Depth of 5 ft; (a) Vertical Component, (b) Radial Component, (c) Transverse Component, and (d) Vertical Component at the Surface

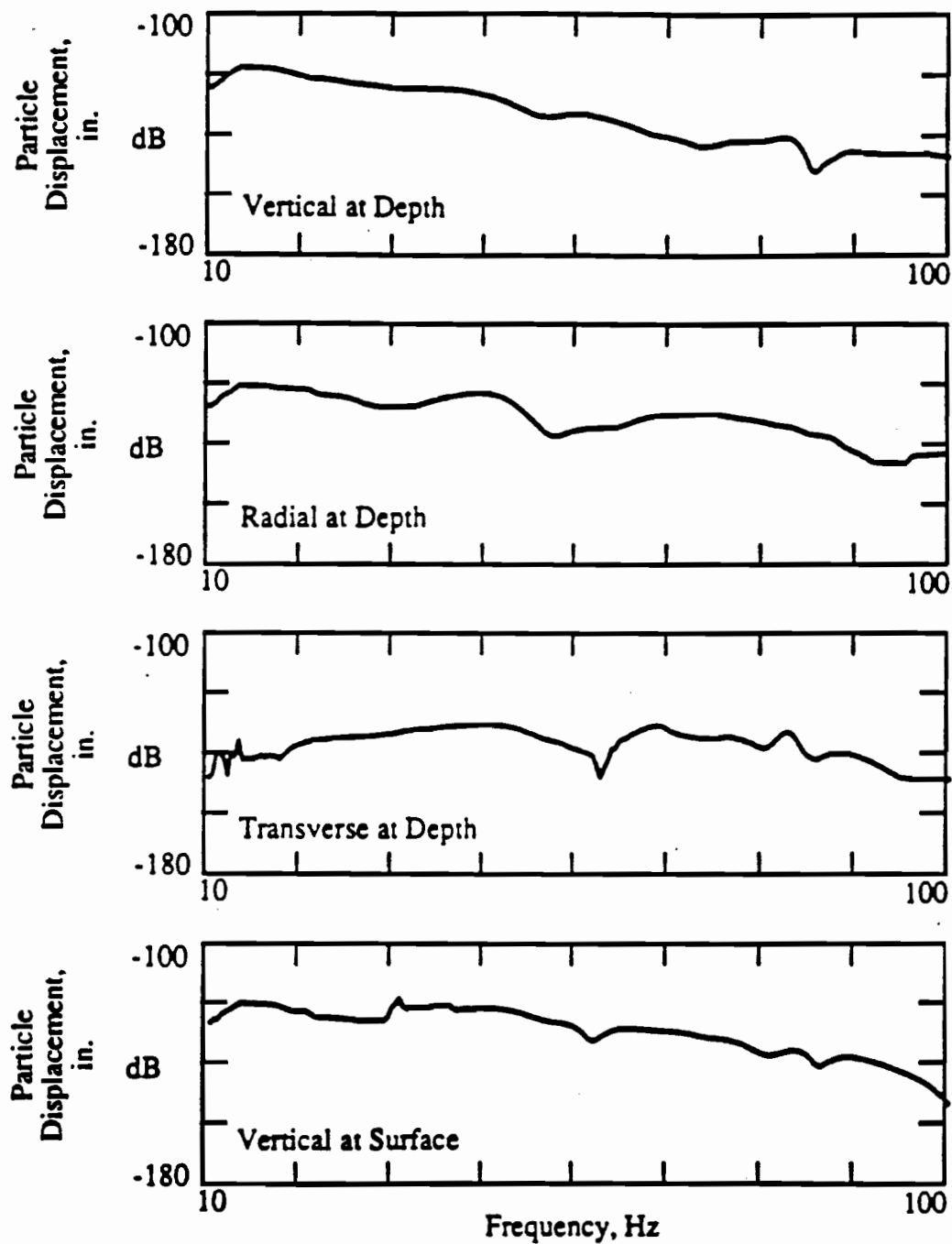


Fig. D7

Particle Displacement Spectra for Measurements at a Depth of 6 ft; (a) Vertical Component, (b) Radial Component, (c) Transverse Component, and (d) Vertical Component at the Surface

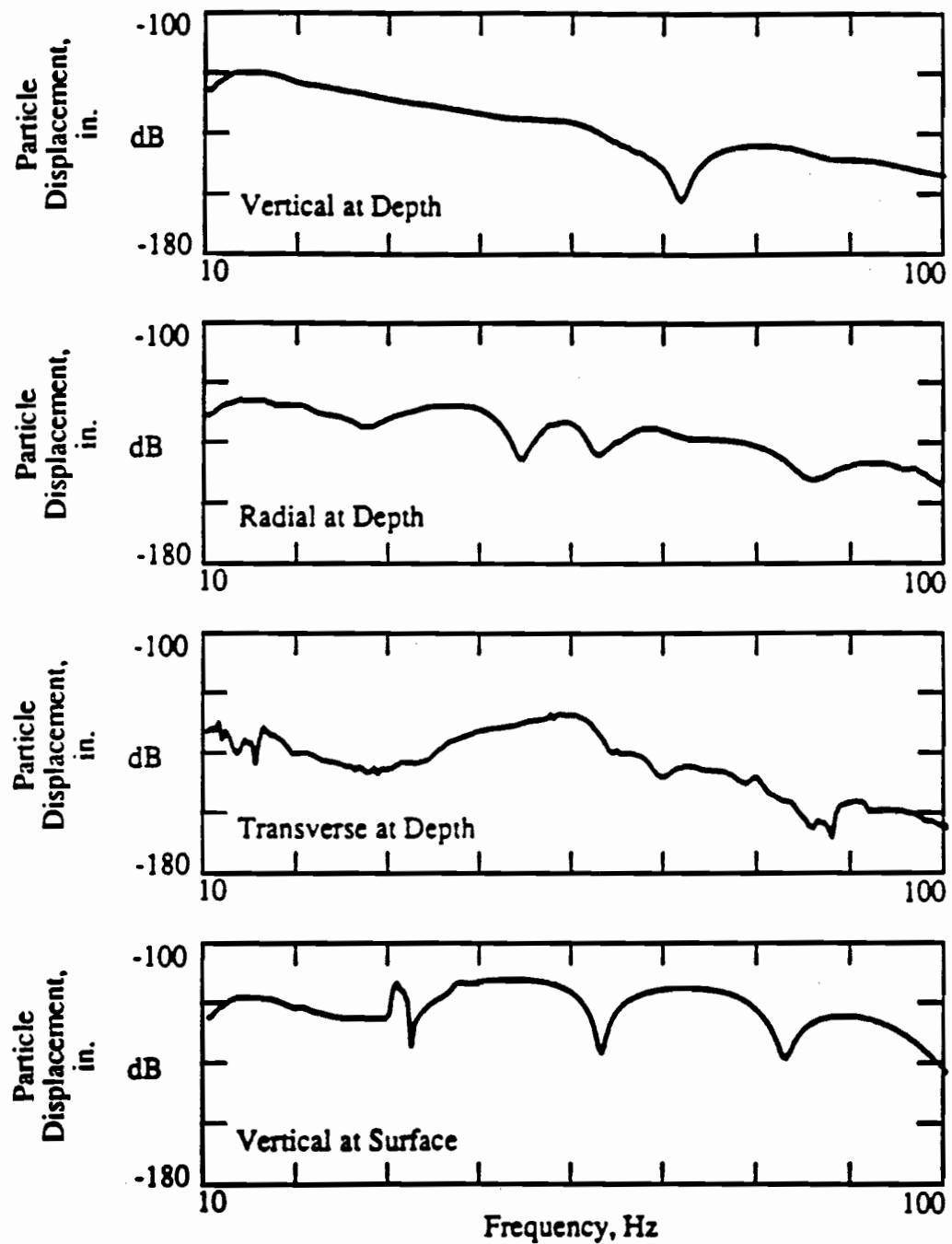


Fig. D8

Particle Displacement Spectra for Measurements at a Depth of 8 ft; (a) Vertical Component, (b) Radial Component, (c) Transverse Component, and (d) Vertical Component at the Surface

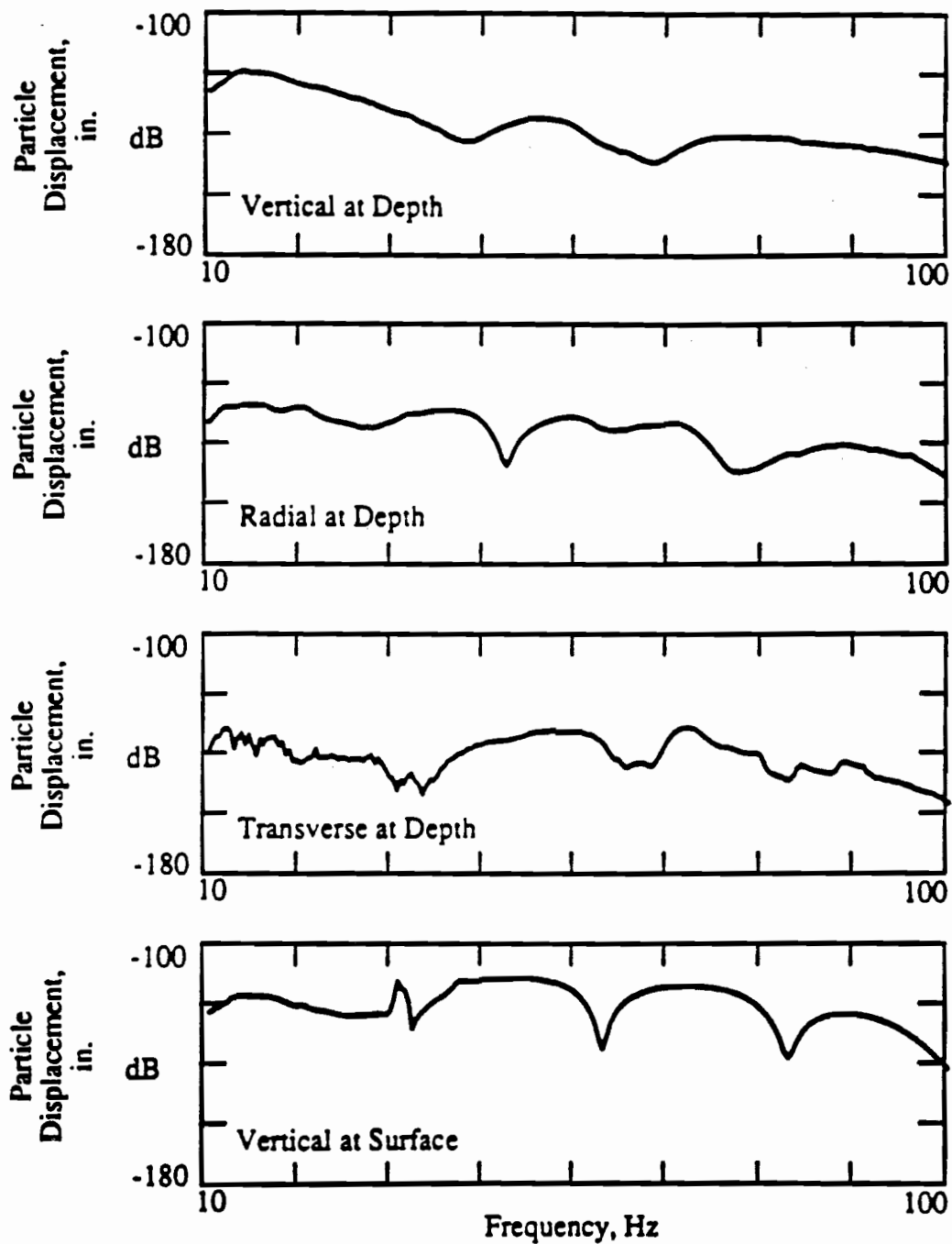


Fig. D9

Particle Displacement Spectra for Measurements at a Depth of 10 ft; (a) Vertical Component, (b) Radial Component, (c) Transverse Component, and (d) Vertical Component at the Surface

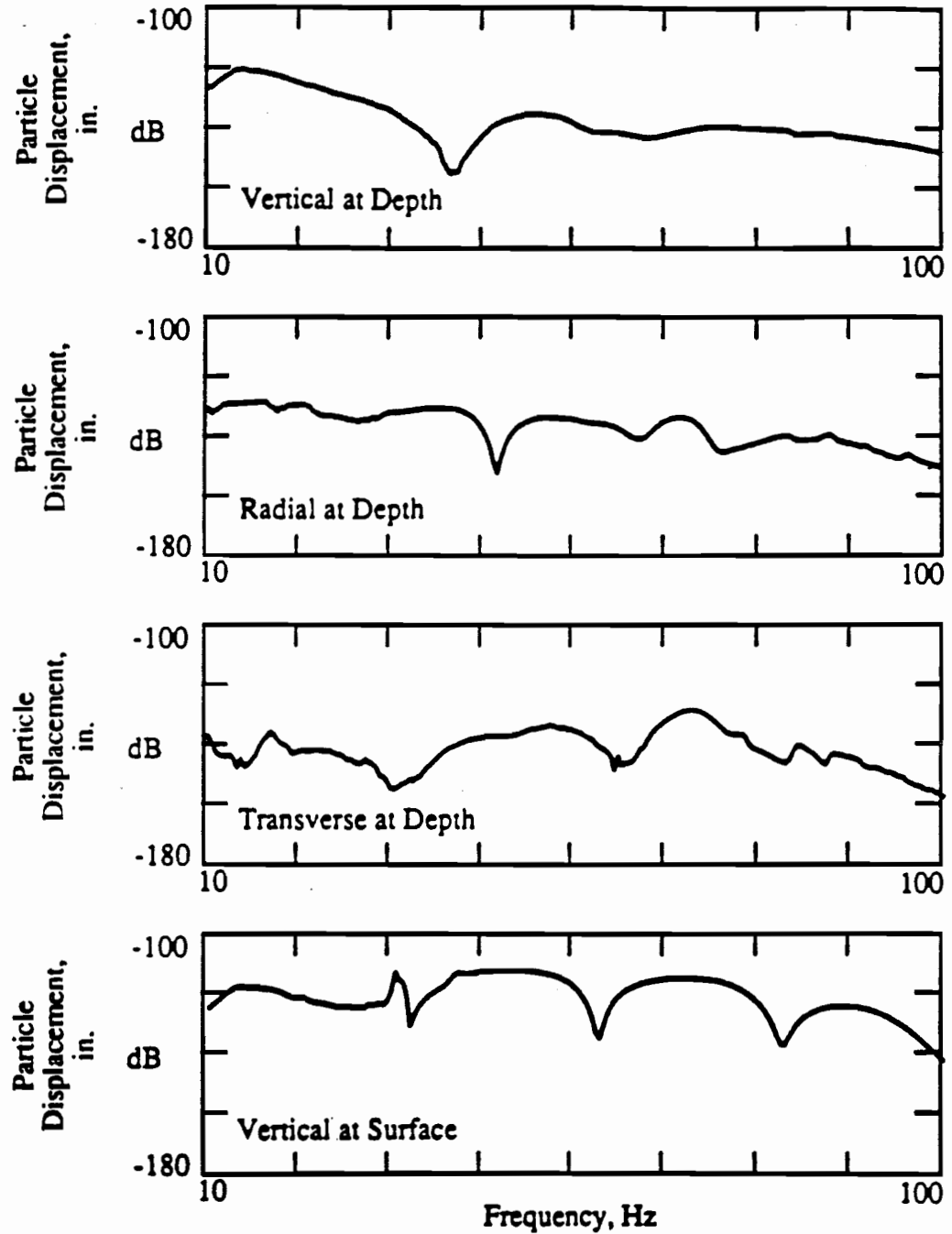


Fig. D10

Particle Displacement Spectra for Measurements at a Depth of 12 ft; (a) Vertical Component, (b) Radial Component, (c) Transverse Component, and (d) Vertical Component at the Surface

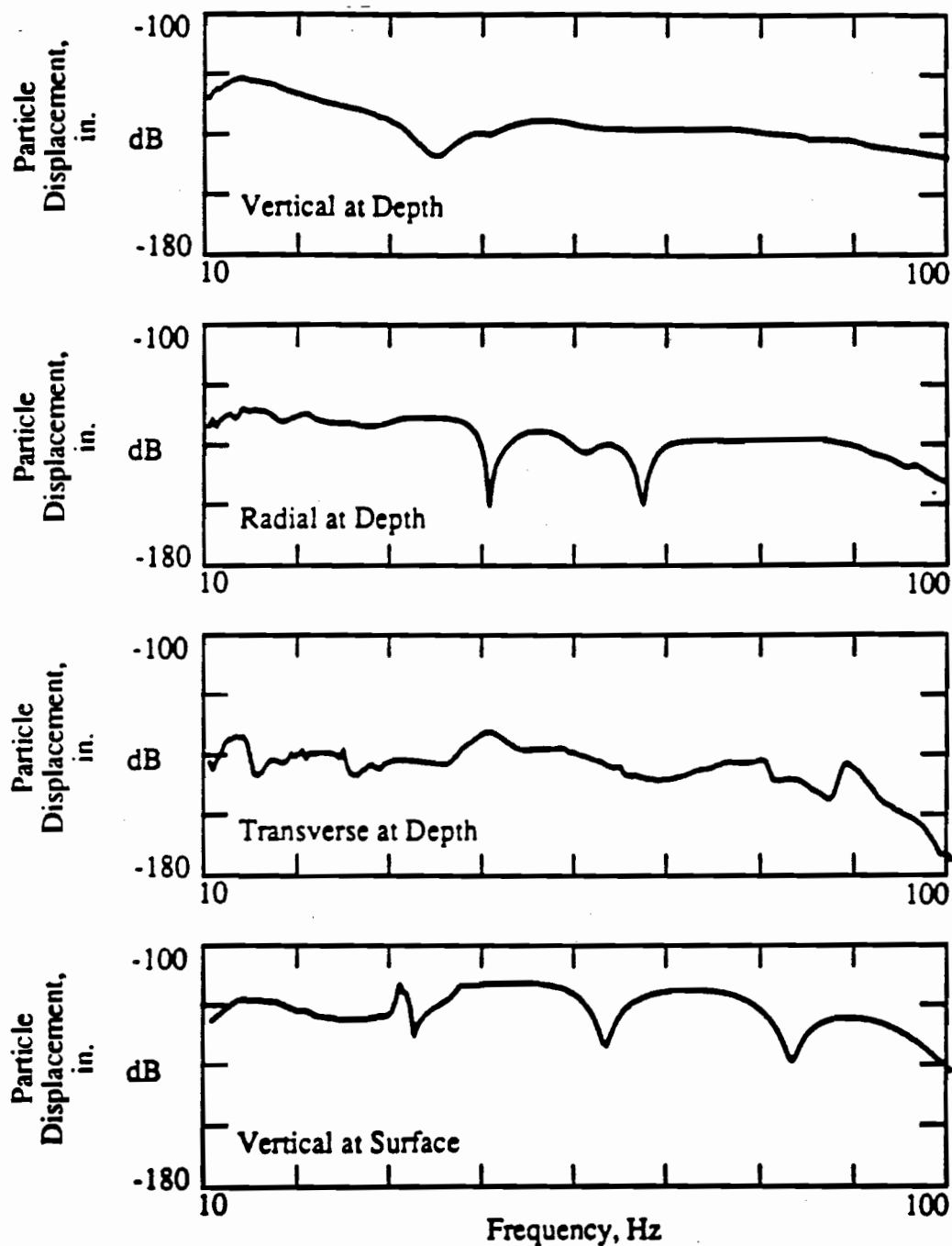


Fig. D11 Particle Displacement Spectra for Measurements at a Depth of 14 ft; (a) Vertical Component, (b) Radial Component, (c) Transverse Component, and (d) Vertical Component at the Surface

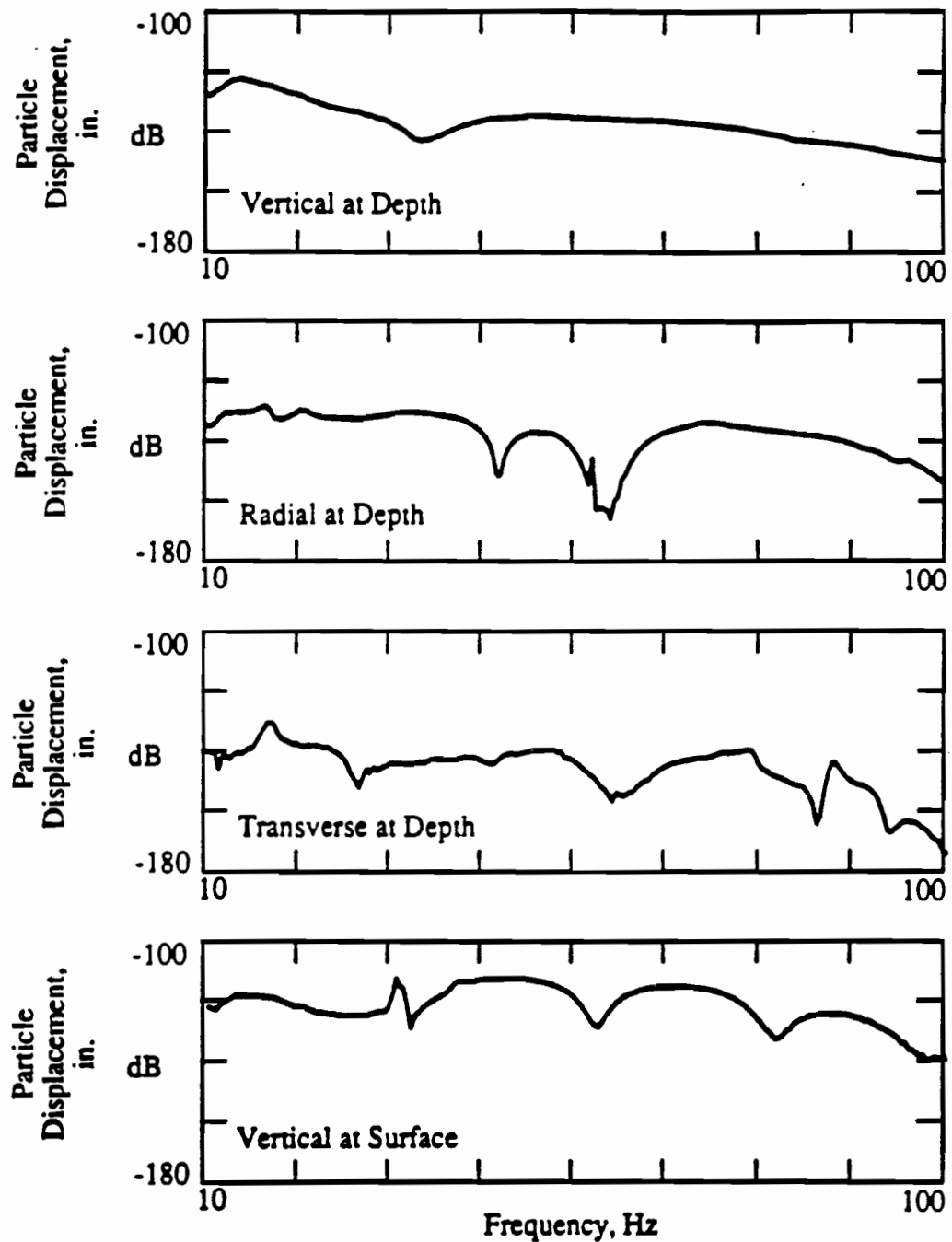


Fig. D12

Particle Displacement Spectra for Measurements at a Depth of 16 ft; (a) Vertical Component, (b) Radial Component, (c) Transverse Component, and (d) Vertical Component at the Surface

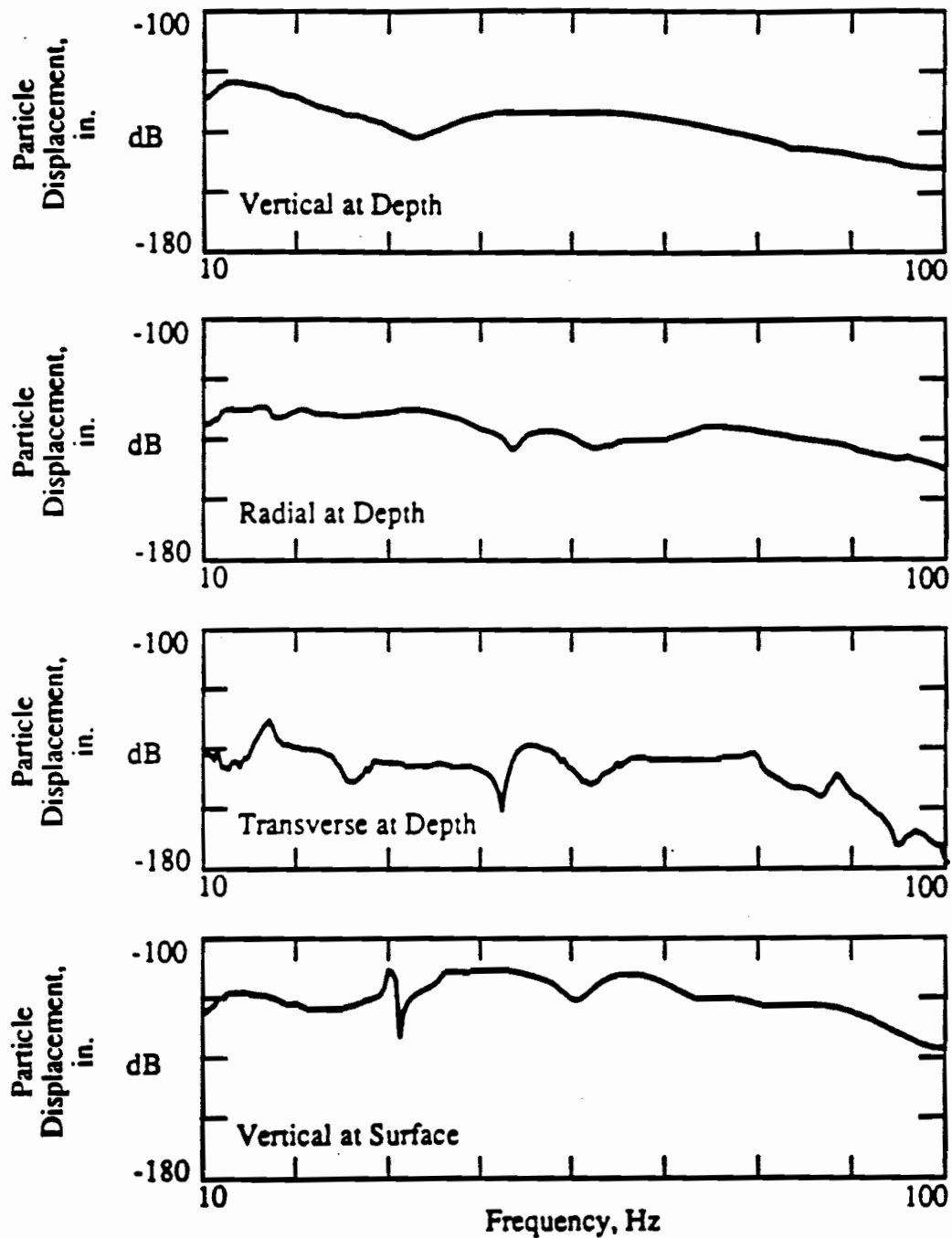


Fig. D13

Particle Displacement Spectra for Measurements at a Depth of 18 ft; (a) Vertical Component, (b) Radial Component, (c) Transverse Component, and (d) Vertical Component at the Surface

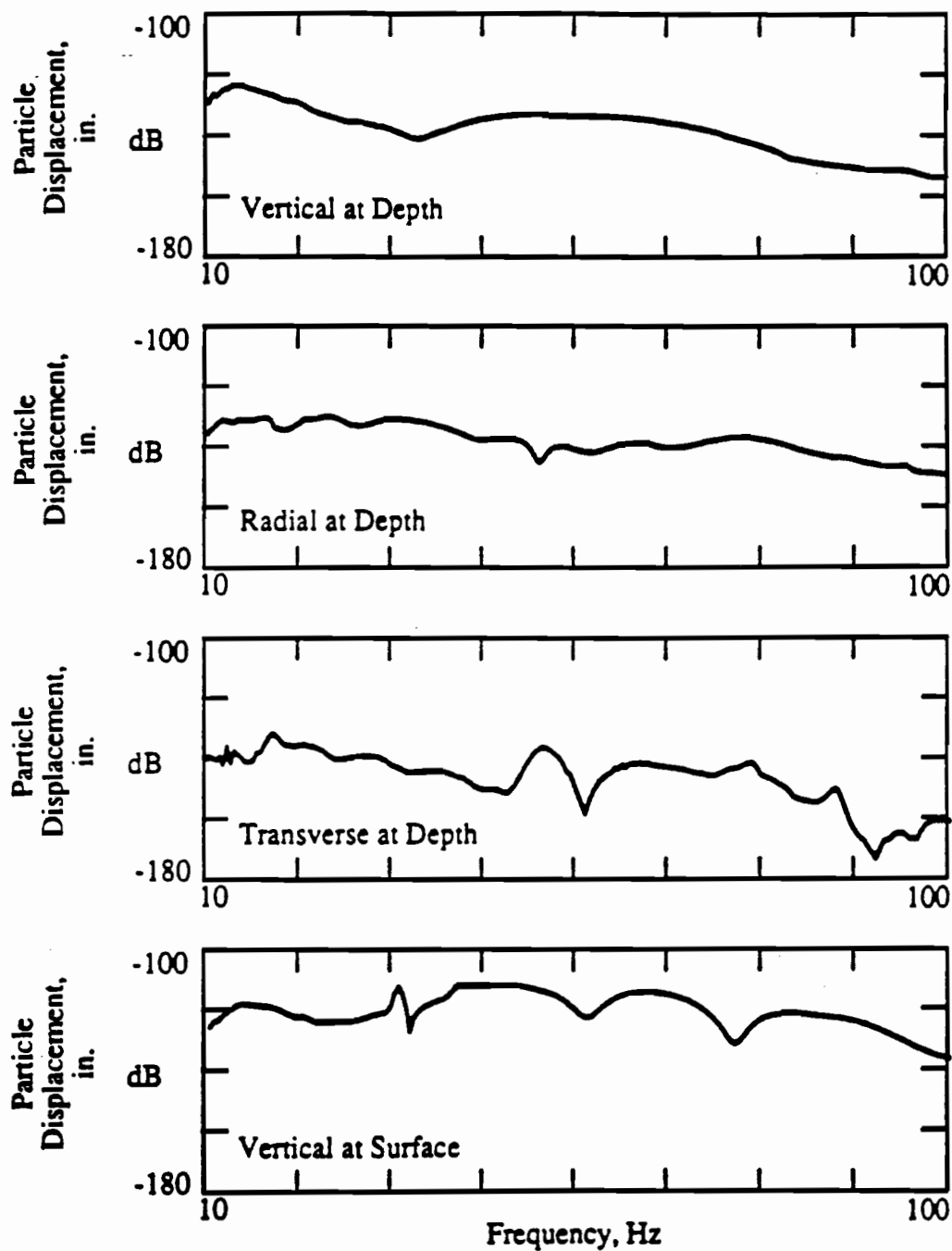


Fig. D14

Particle Displacement Spectra for Measurements at a Depth of 20 ft; (a) Vertical Component, (b) Radial Component, (c) Transverse Component, and (d) Vertical Component at the Surface

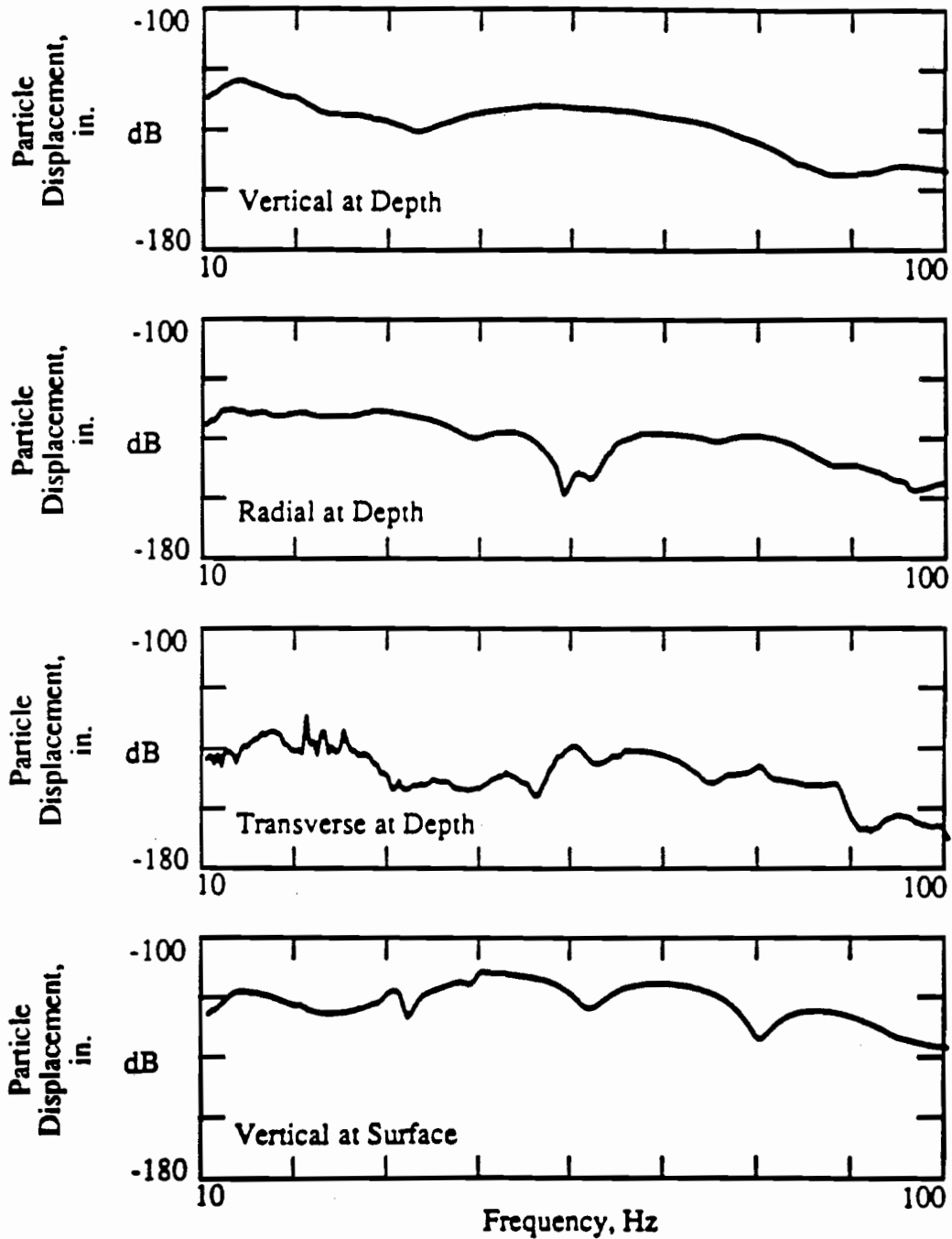


Fig. D15

Particle Displacement Spectra for Measurements at a Depth of 22 ft; (a) Vertical Component, (b) Radial Component, (c) Transverse Component, and (d) Vertical Component at the Surface

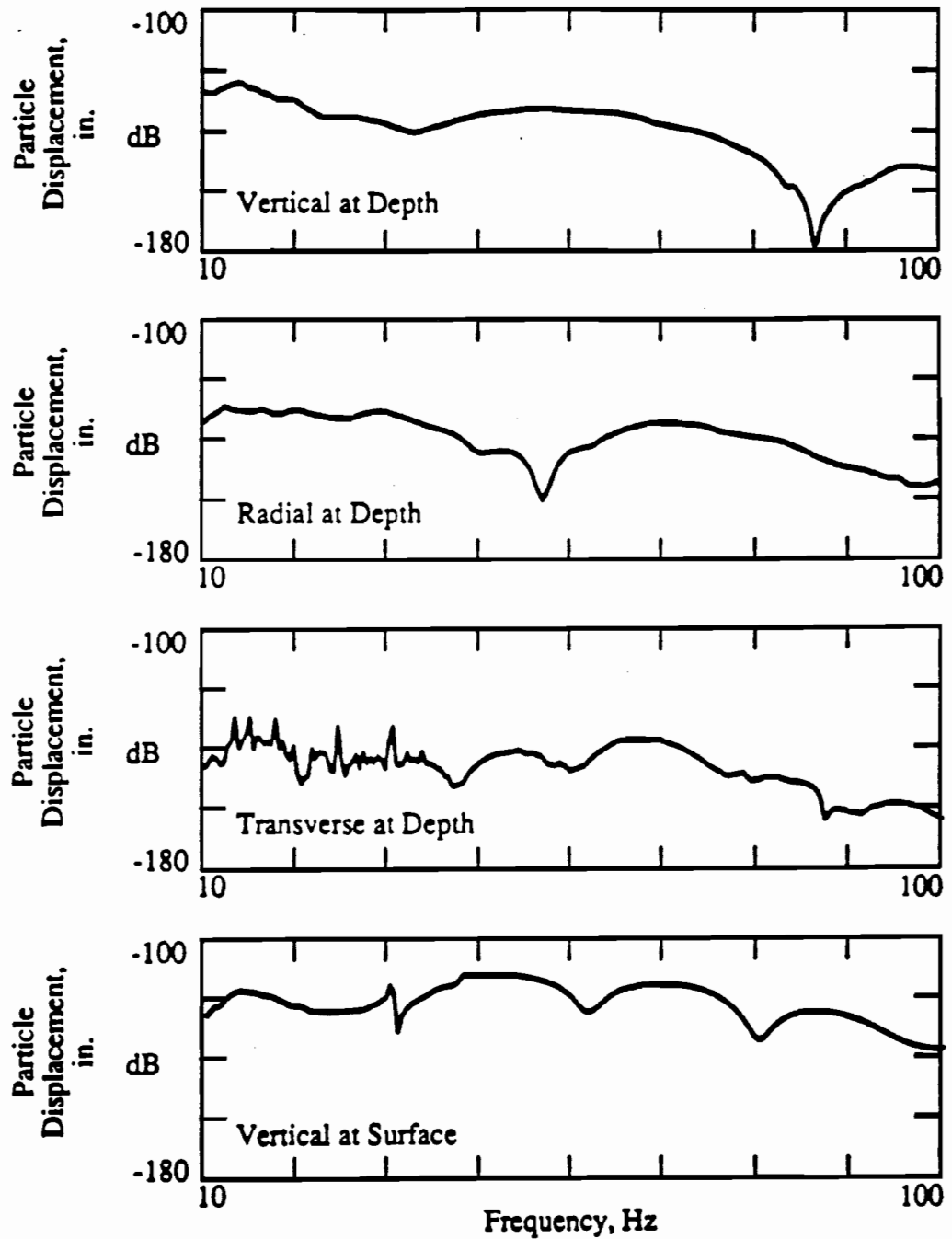


Fig. D16

Particle Displacement Spectra for Measurements at a Depth of 24 ft; (a) Vertical Component, (b) Radial Component, (c) Transverse Component, and (d) Vertical Component at the Surface

Appendix E
Spectral Functions Measured During Surface Wave Tests
on Curing Concrete

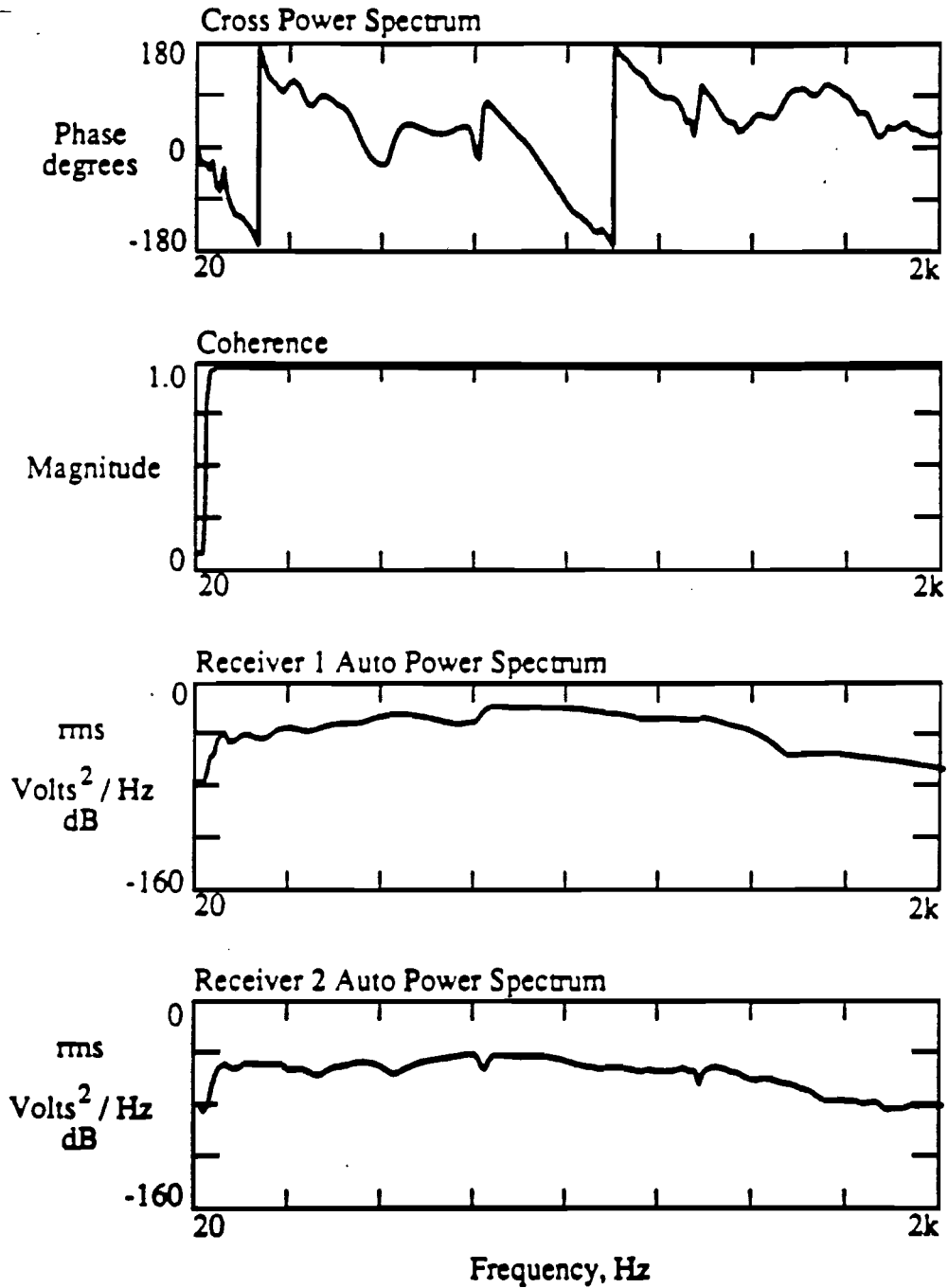


Fig. E1 Spectral Functions for the R2-R4 Receiver Spacing for Measurements Performed Prior to Placement of the Slab

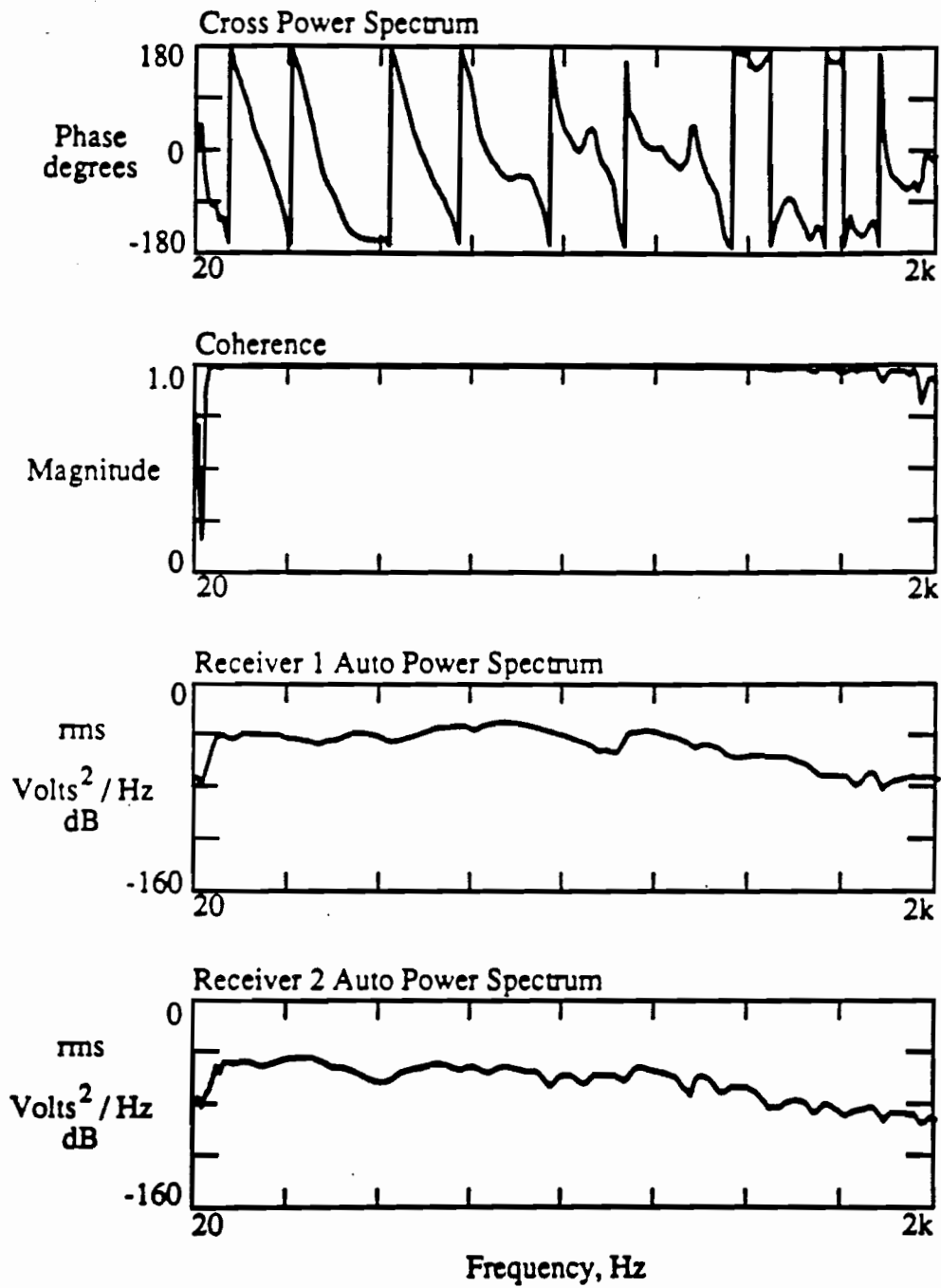


Fig. E2

Spectral Functions for the R1-R2 Receiver Spacing for Measurements Performed Prior to Placement of the Slab

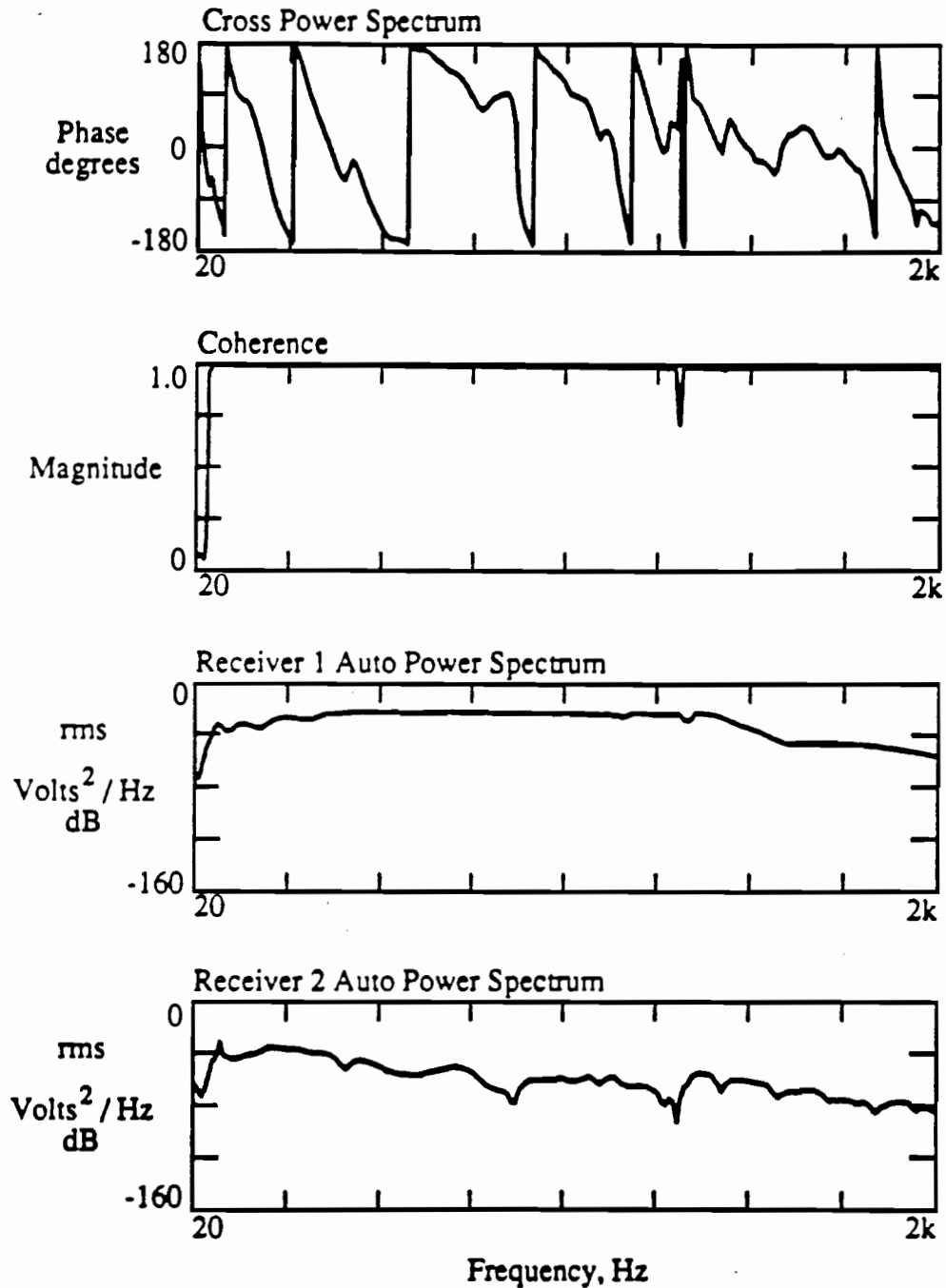


Fig. E3

Spectral Functions for the R1-R3 Receiver Spacing for Measurements Performed Prior to Placement of the Slab

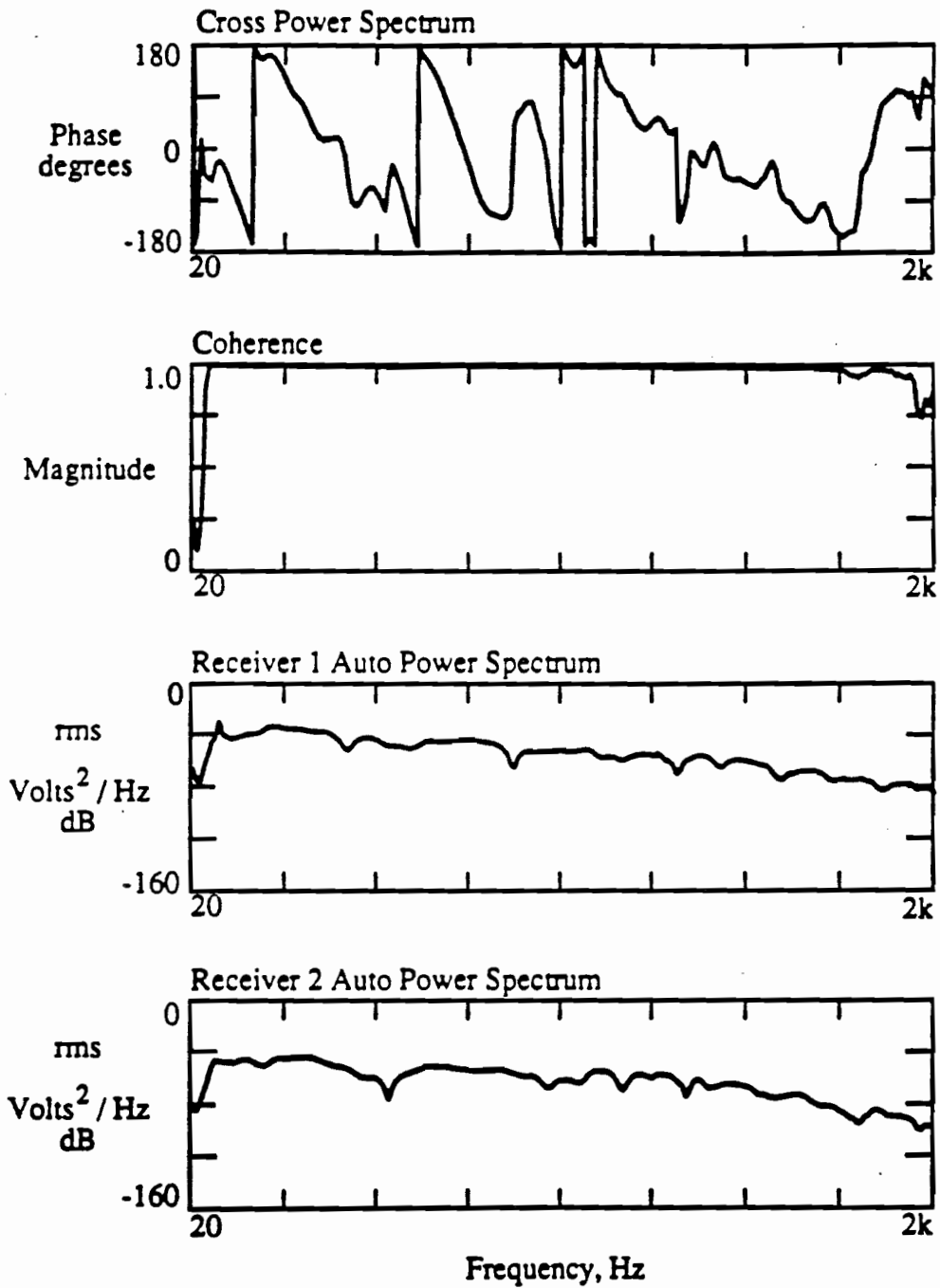


Fig. E4 Spectral Functions for the R3-R4 Receiver Spacing for Measurements Performed Prior to Placement of the Slab

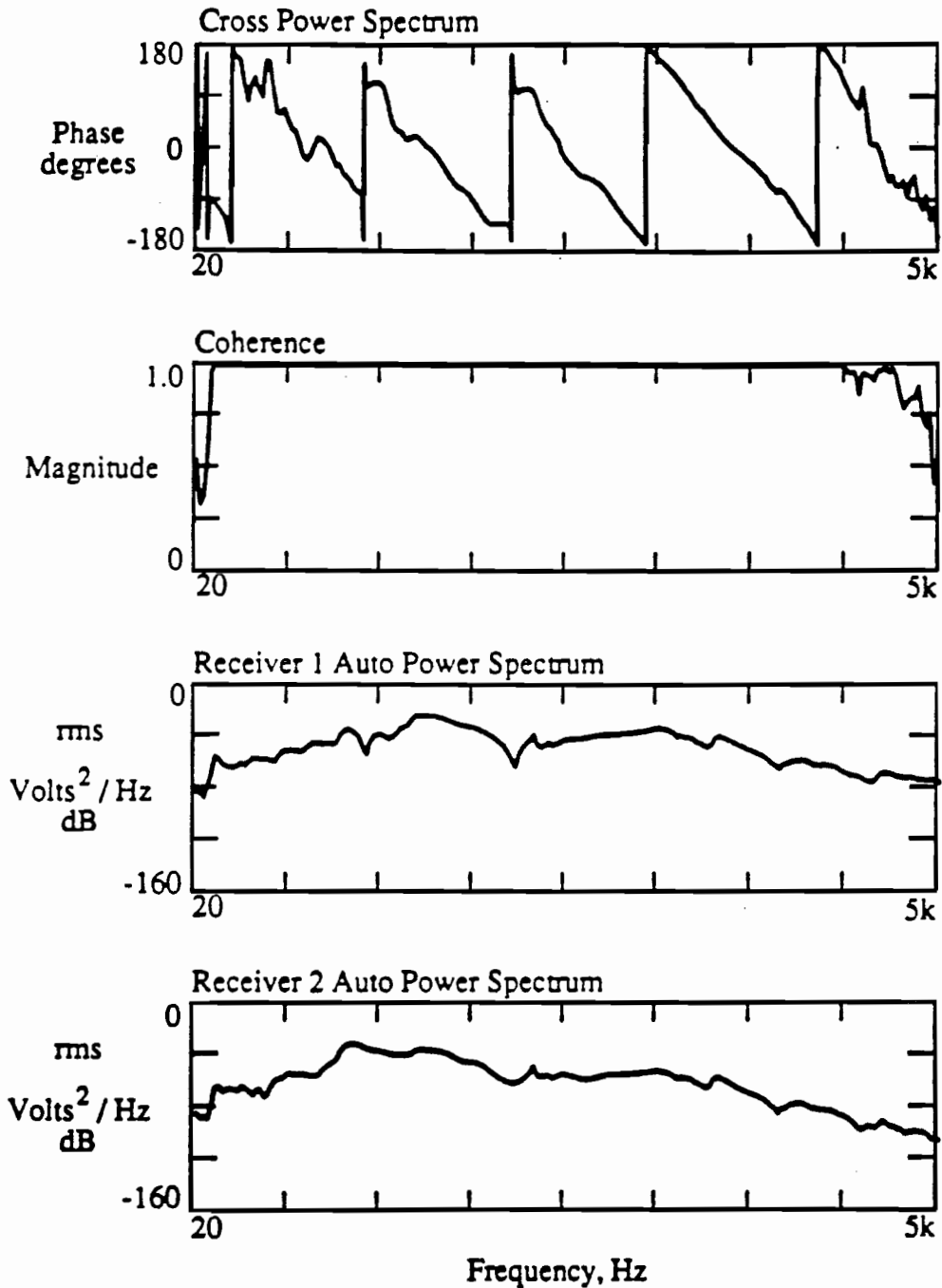


Fig. E5 Spectral Functions for the R2-R4 Receiver Spacing for Measurements Performed 207 Minutes After the Addition of Water to the Cement-Aggregate Mixture

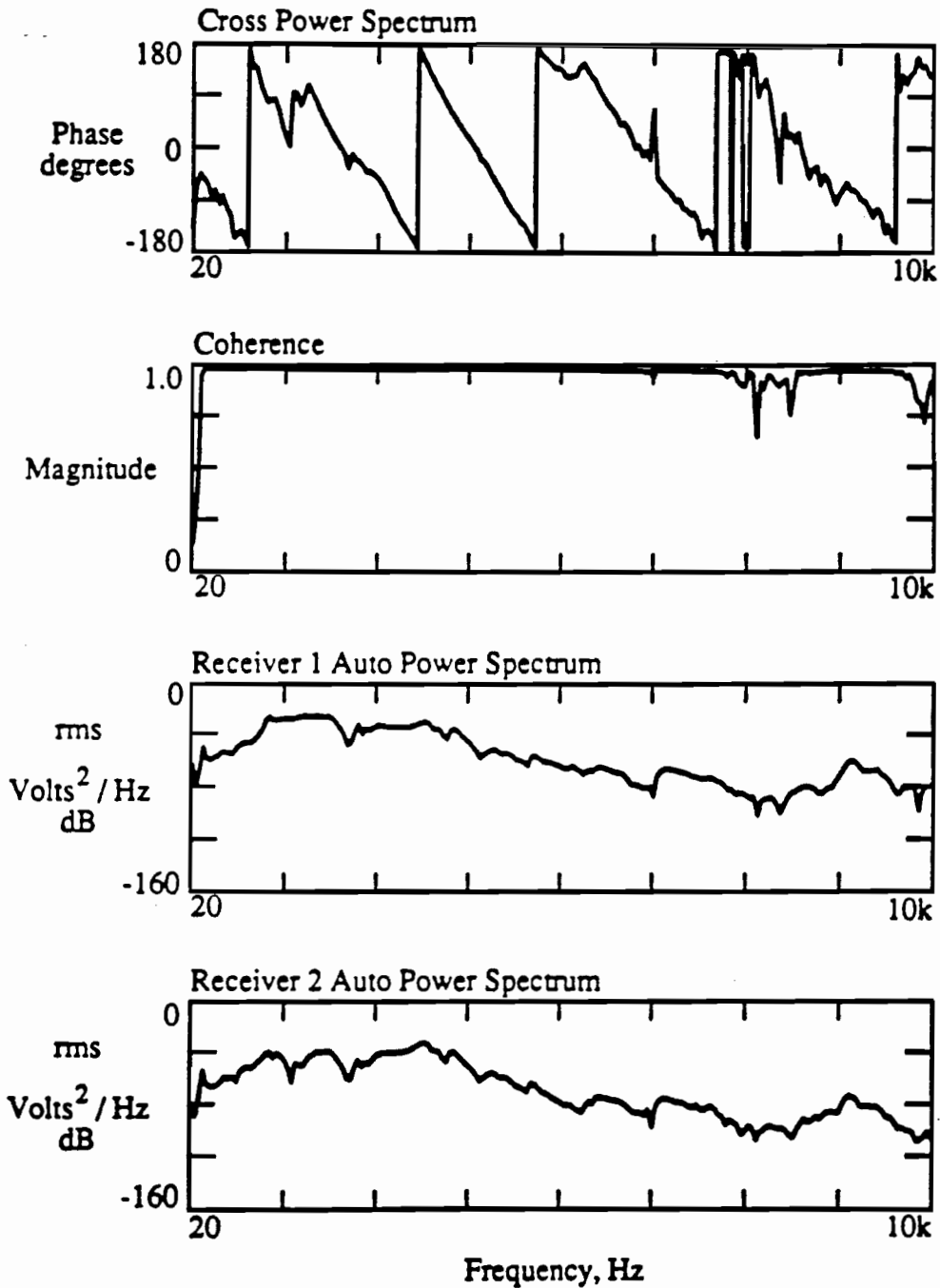


Fig. E6

Spectral Functions for the R1-R2 Receiver Spacing for Measurements Performed 217 Minutes After the Addition of Water to the Cement-Aggregate Mixture

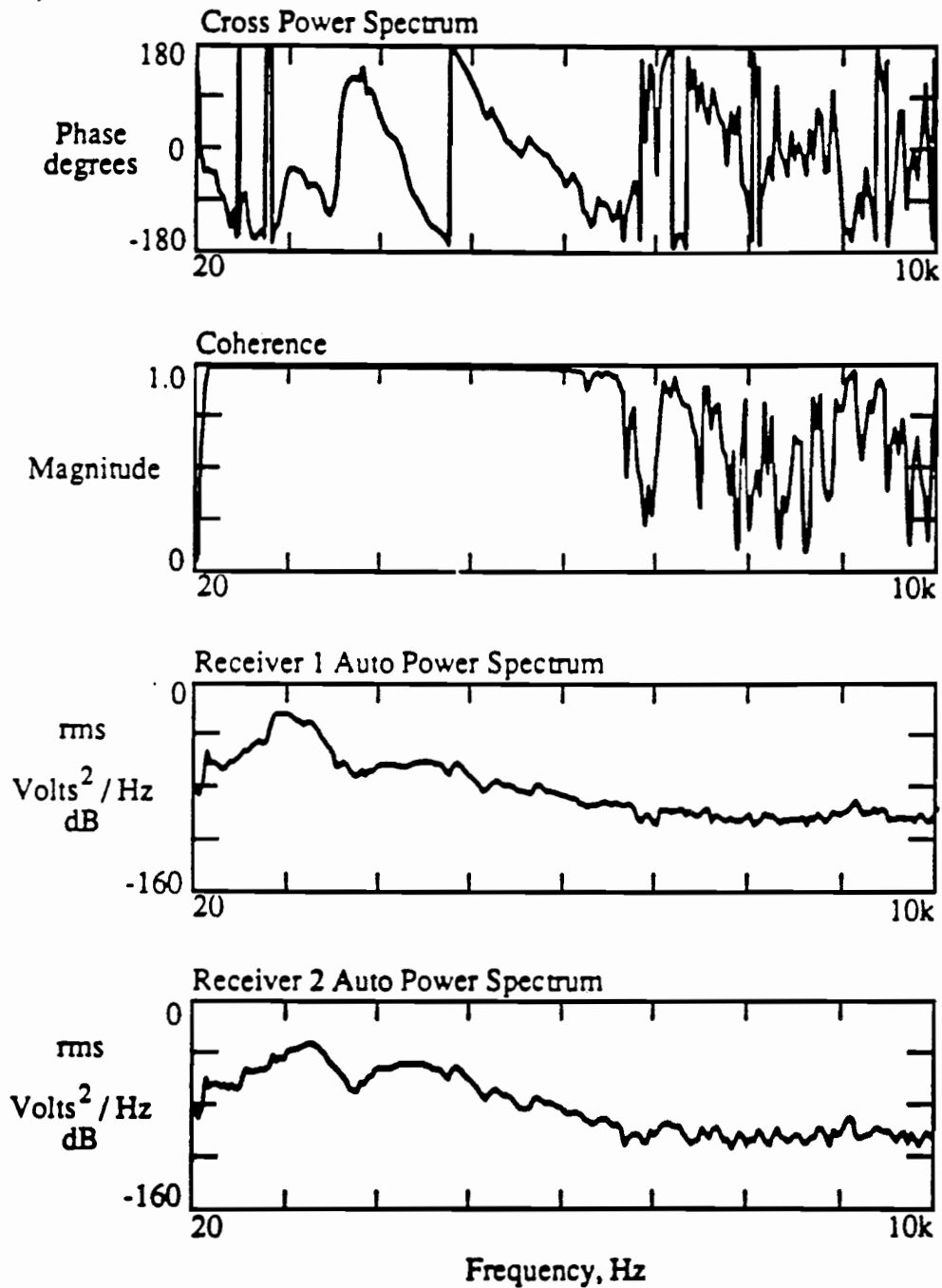


Fig. E7 Spectral Functions for the R3-R4 Receiver Spacing for Measurements Performed 222 Minutes After the Addition of Water to the Cement-Aggregate Mixture

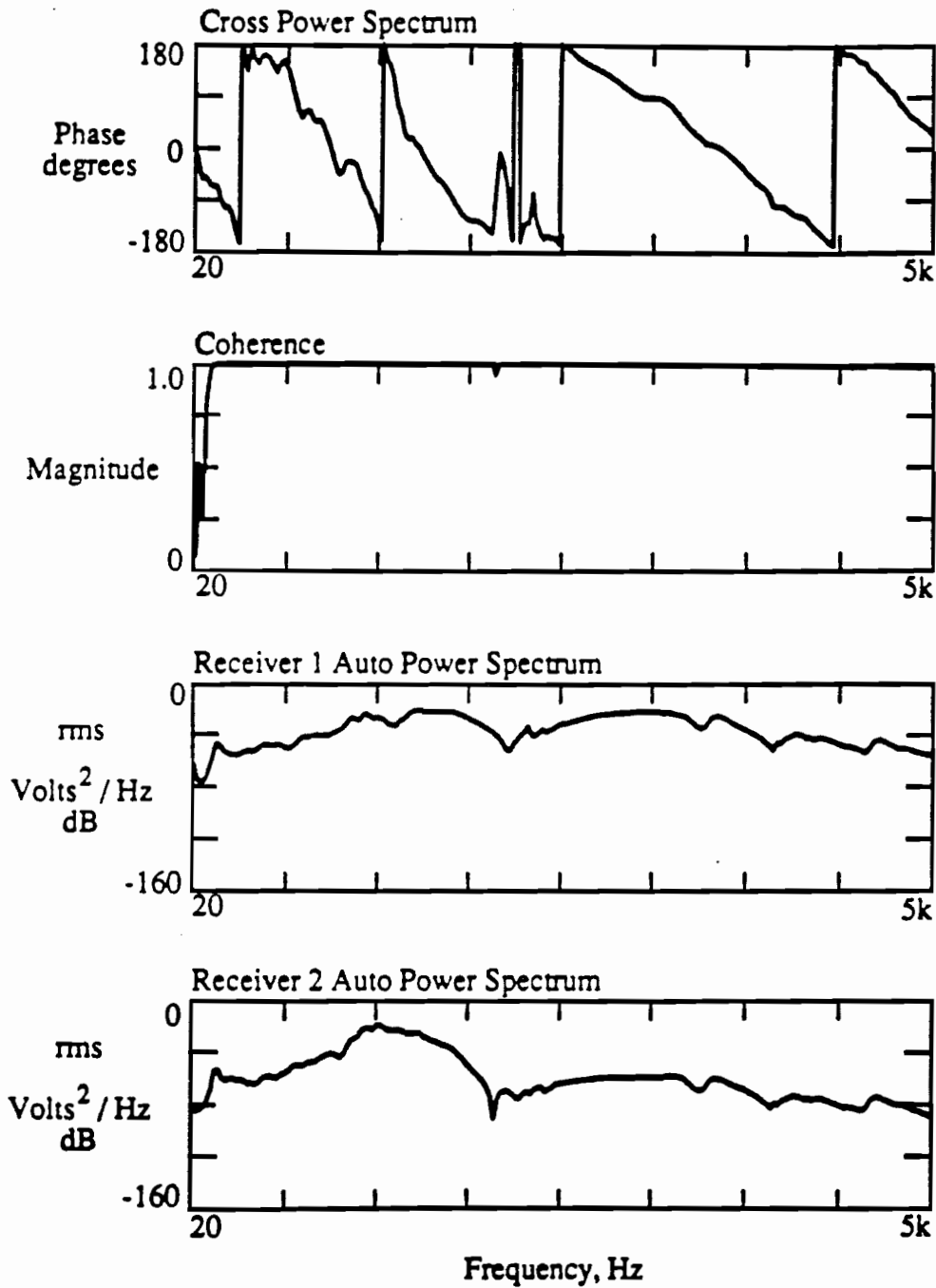


Fig. E8 Spectral Functions for the R1-R3 Receiver Spacing for Measurements Performed 227 Minutes After the Addition of Water to the Cement-Aggregate Mixture

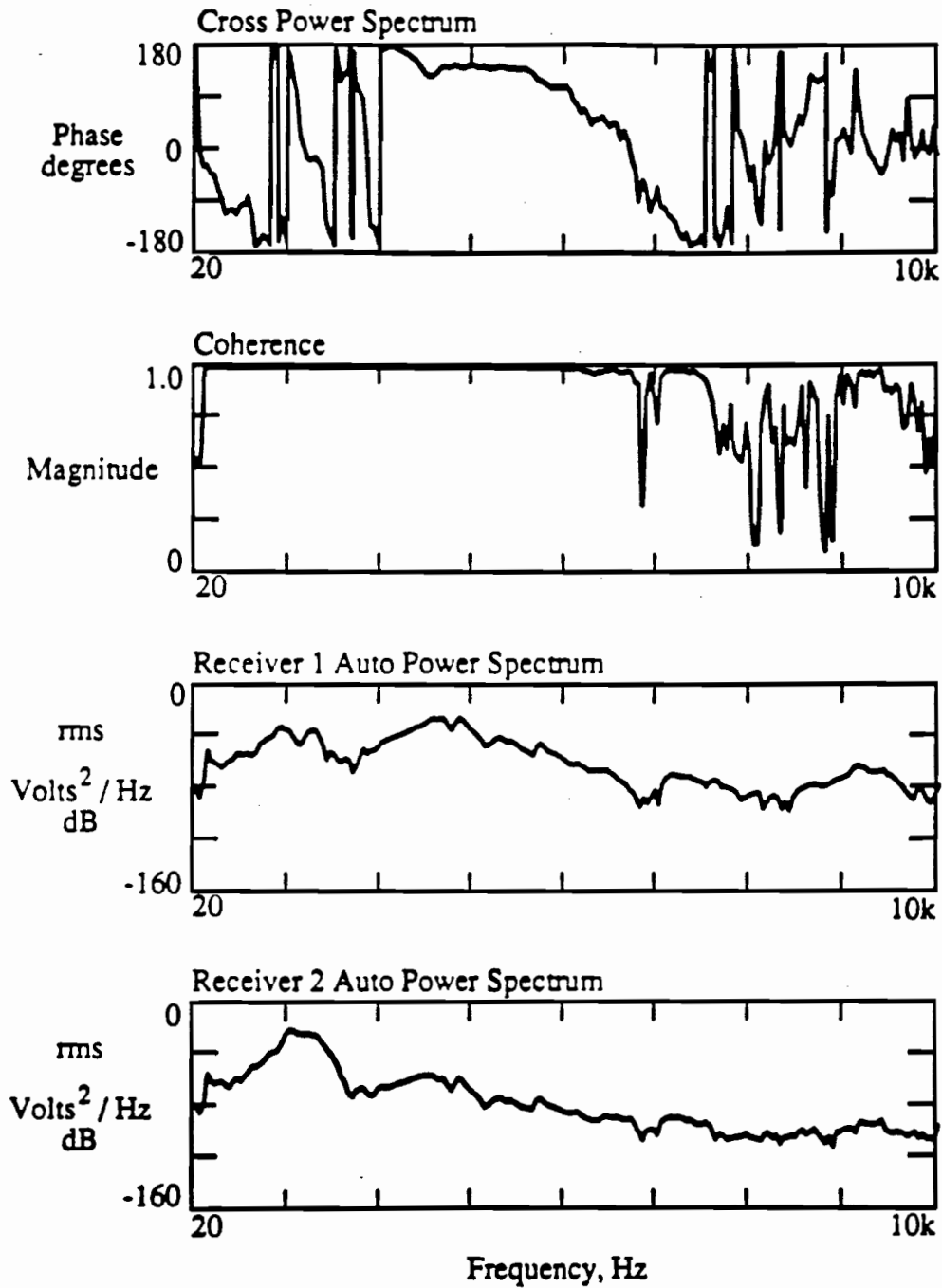


Fig. E9

Spectral Functions for the R2-R3 Receiver Spacing for Measurements Performed 232 Minutes After the Addition of Water to the Cement-Aggregate Mixture

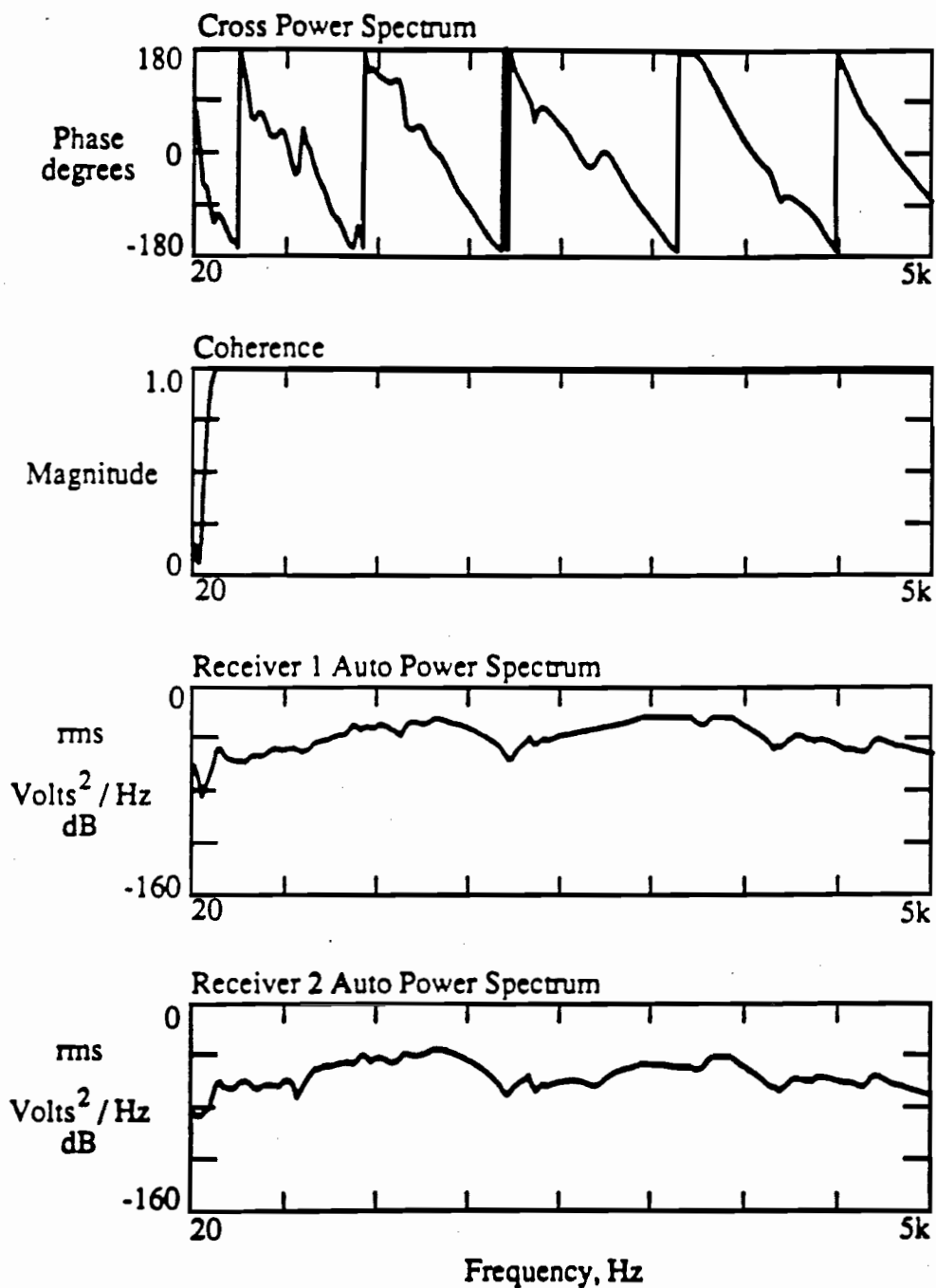


Fig. E10 Spectral Functions for the R1-R4 Receiver Spacing for Measurements Performed 237 Minutes After the Addition of Water to the Cement-Aggregate Mixture

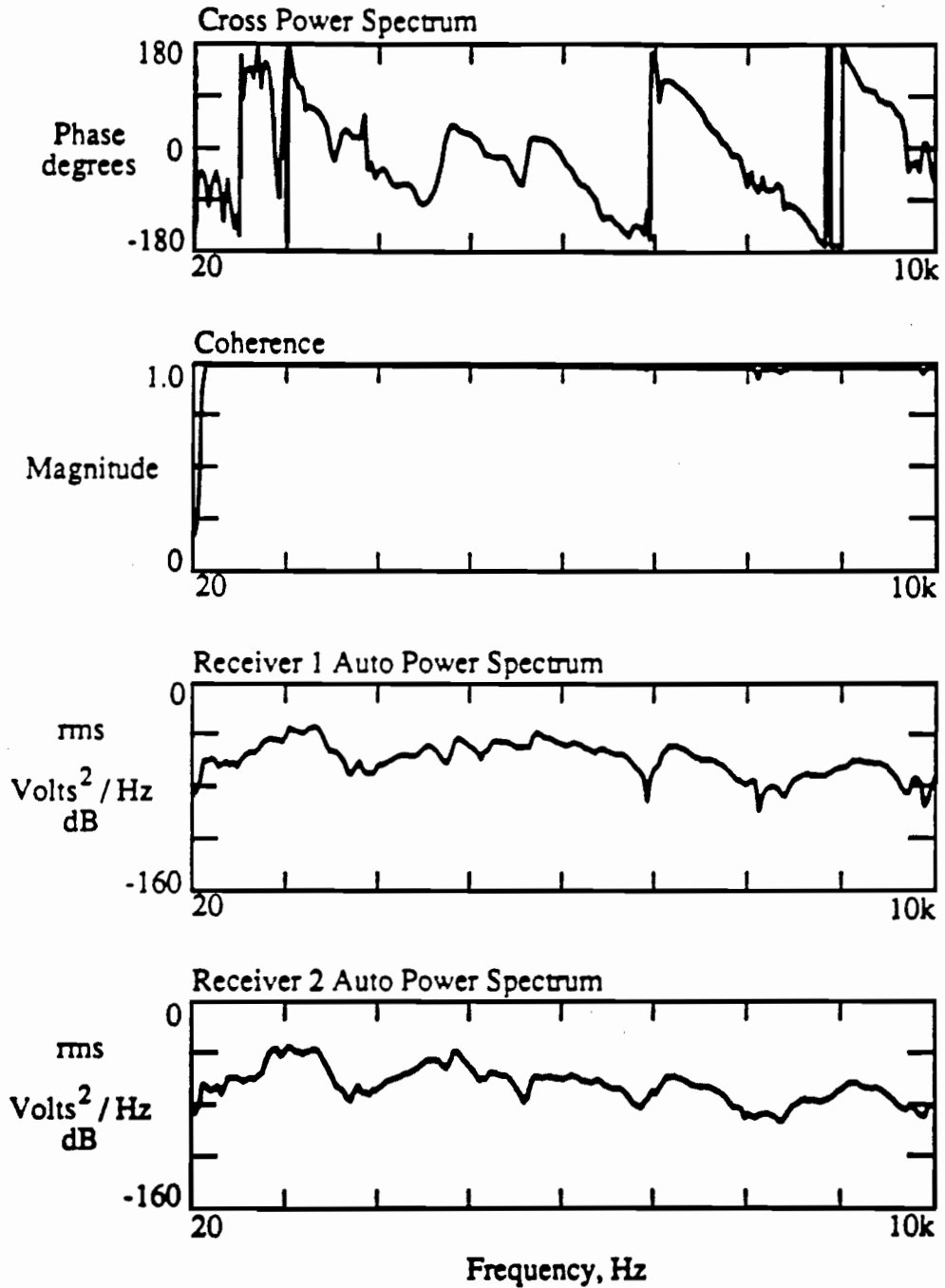


Fig. E11 Spectral Functions for the R2-R4 Receiver Spacing for Measurements Performed 287 Minutes After the Addition of Water to the Cement-Aggregate Mixture

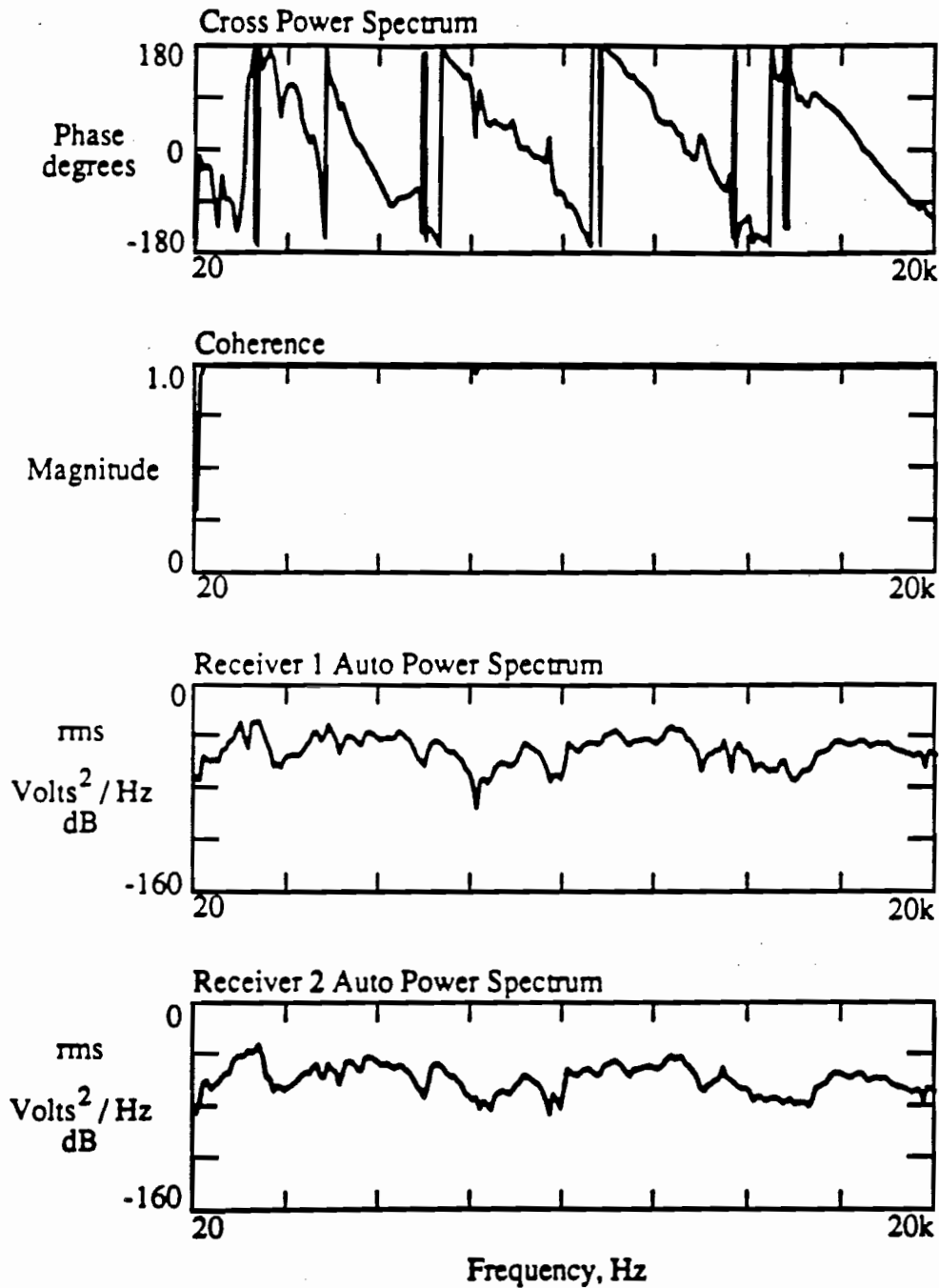


Fig. E12

Spectral Functions for the R1-R2 Receiver Spacing for Measurements Performed 292 Minutes After the Addition of Water to the Cement-Aggregate Mixture

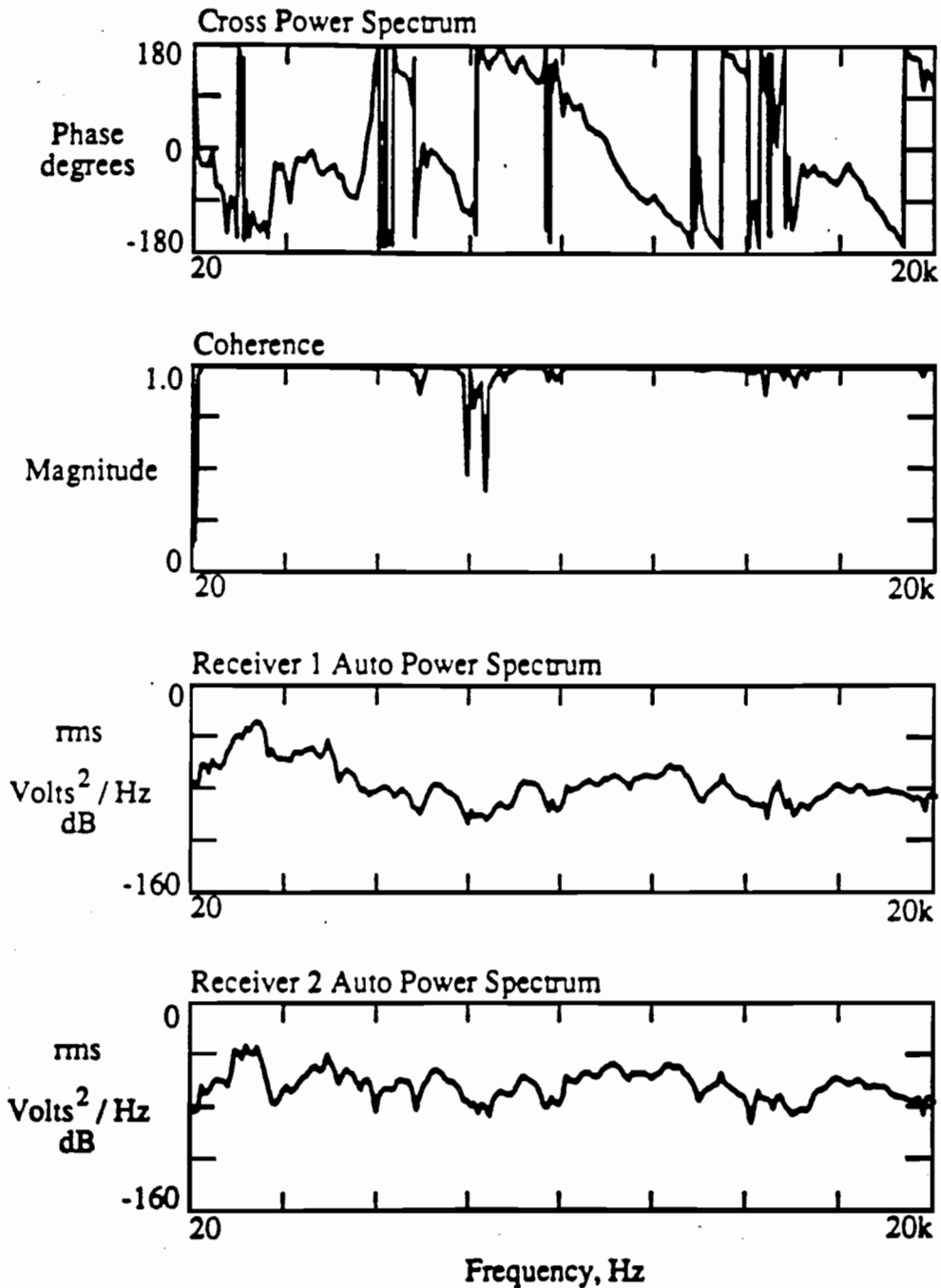


Fig. E13 Spectral Functions for the R3-R4 Receiver Spacing for Measurements Performed 297 Minutes After the Addition of Water to the Cement-Aggregate Mixture

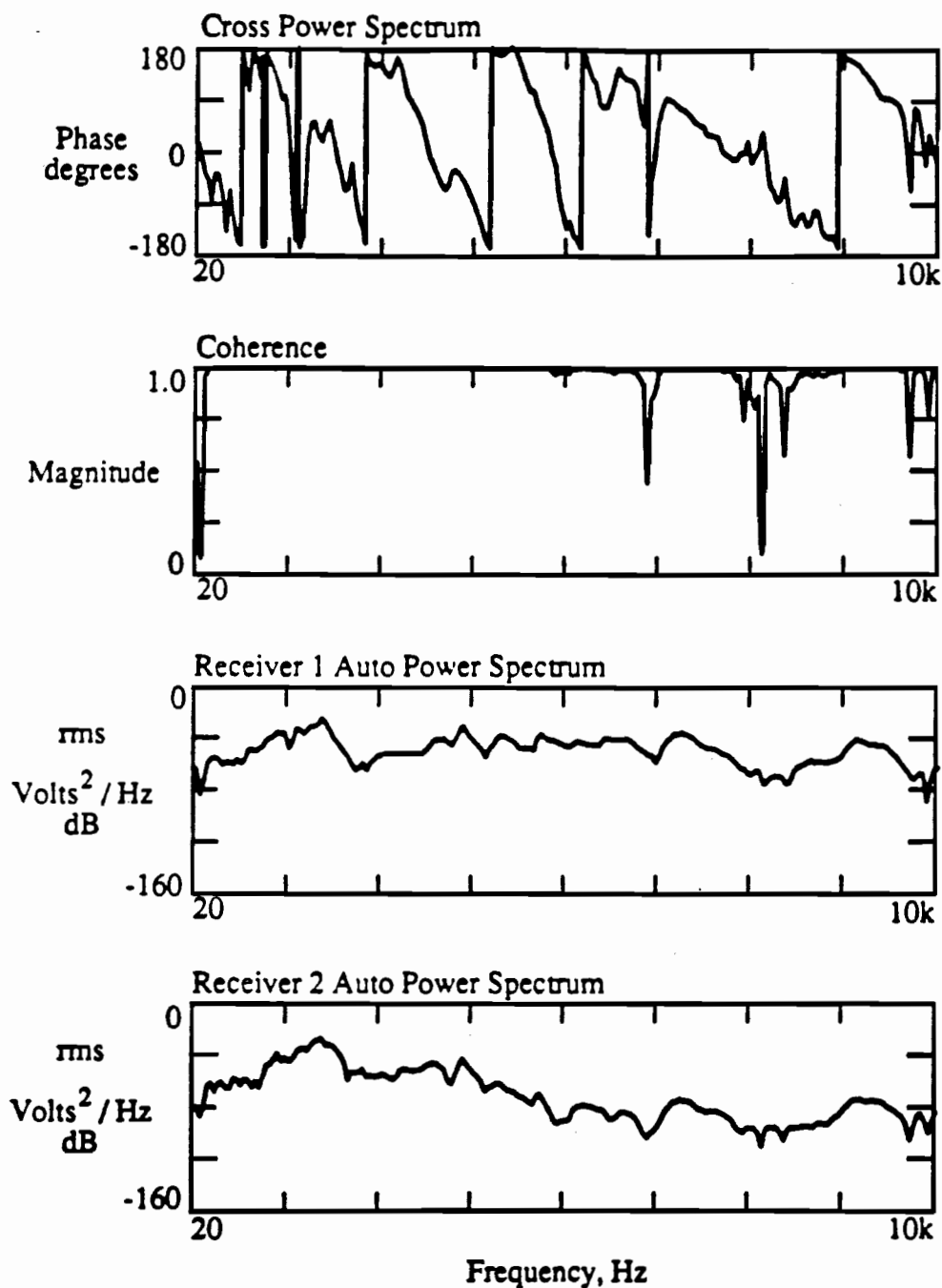


Fig. E14 Spectral Functions for the R1-R3 Receiver Spacing for Measurements Performed 302 Minutes After the Addition of Water to the Cement-Aggregate Mixture

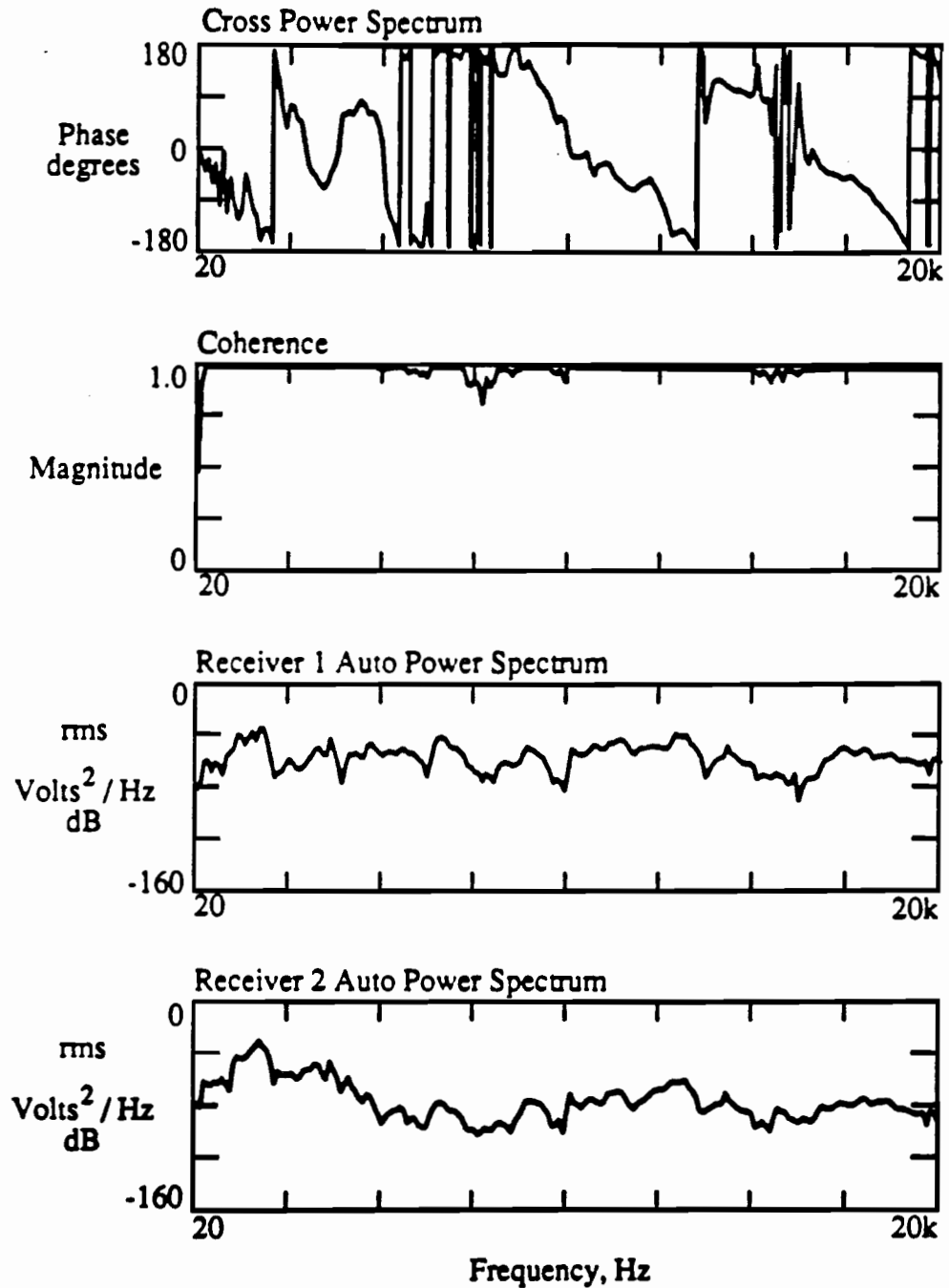


Fig. E15

Spectral Functions for the R2-R3 Receiver Spacing for Measurements Performed 312 Minutes After the Addition of Water to the Cement-Aggregate Mixture

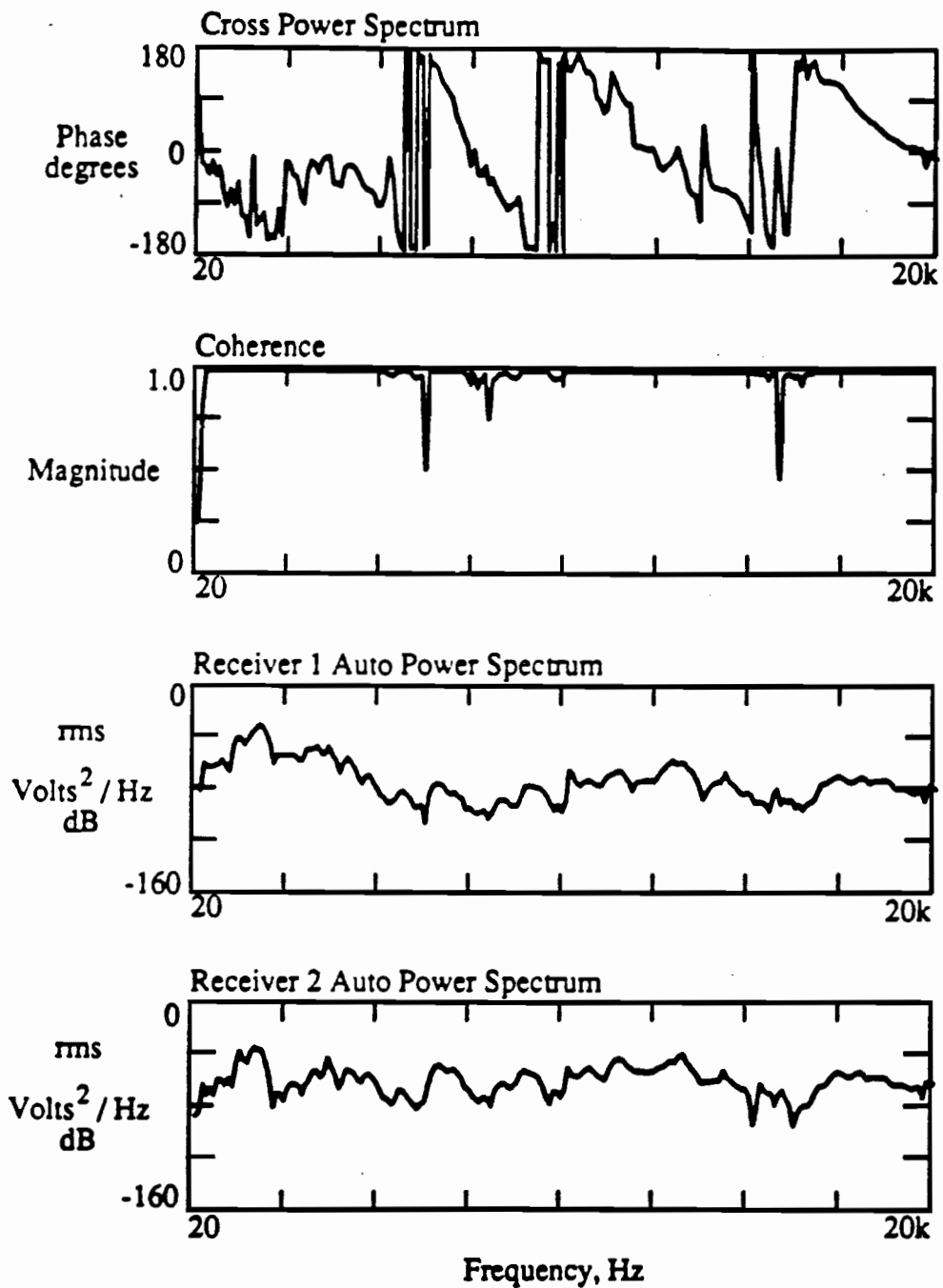


Fig. E16 Spectral Functions for the R1-R4 Receiver Spacing for Measurements Performed 317 Minutes After the Addition of Water to the Cement-Aggregate Mixture

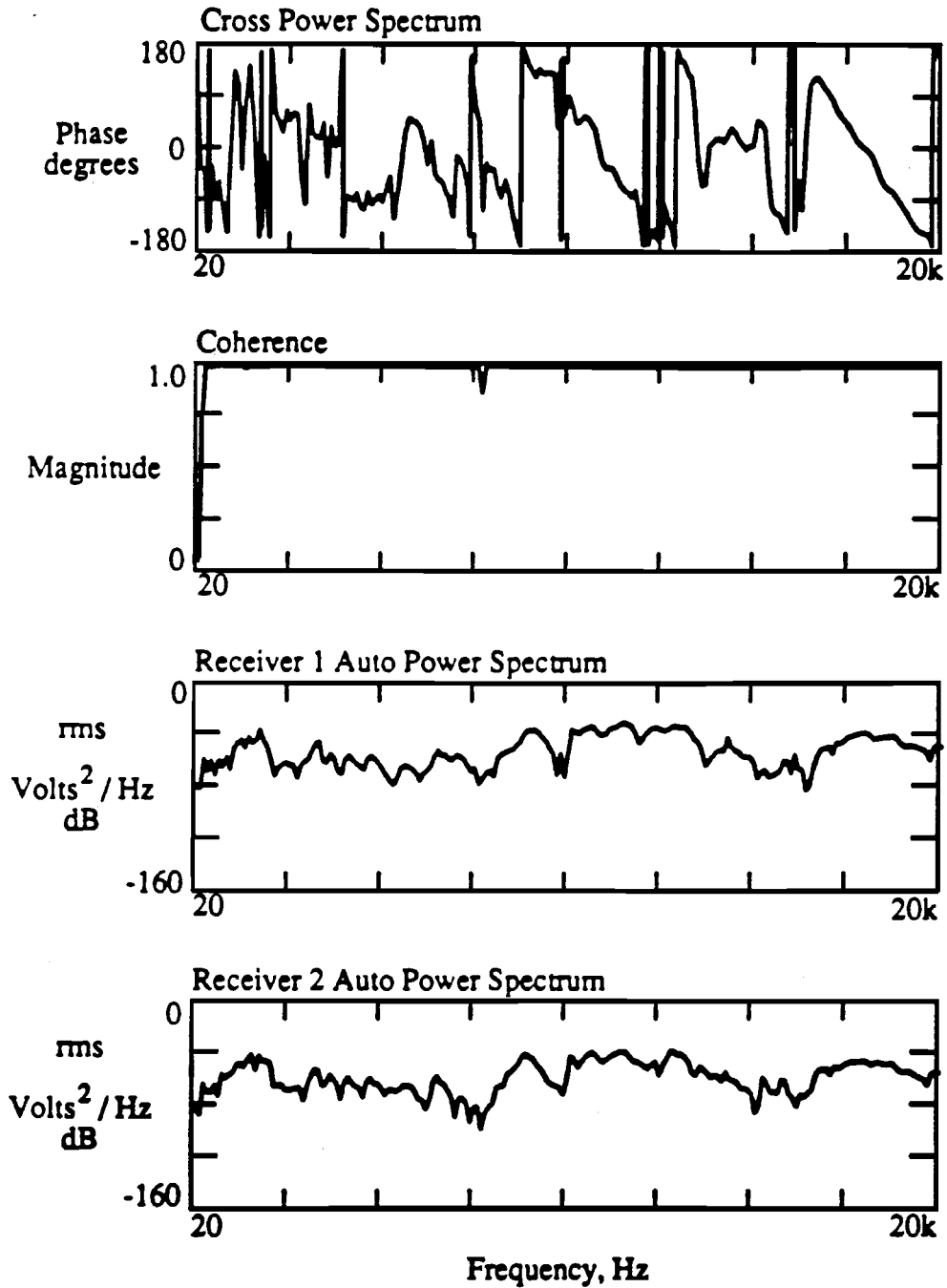


Fig. E17 Spectral Functions for the R2-R4 Receiver Spacing for Measurements Performed 377 Minutes After the Addition of Water to the Cement-Aggregate Mixture

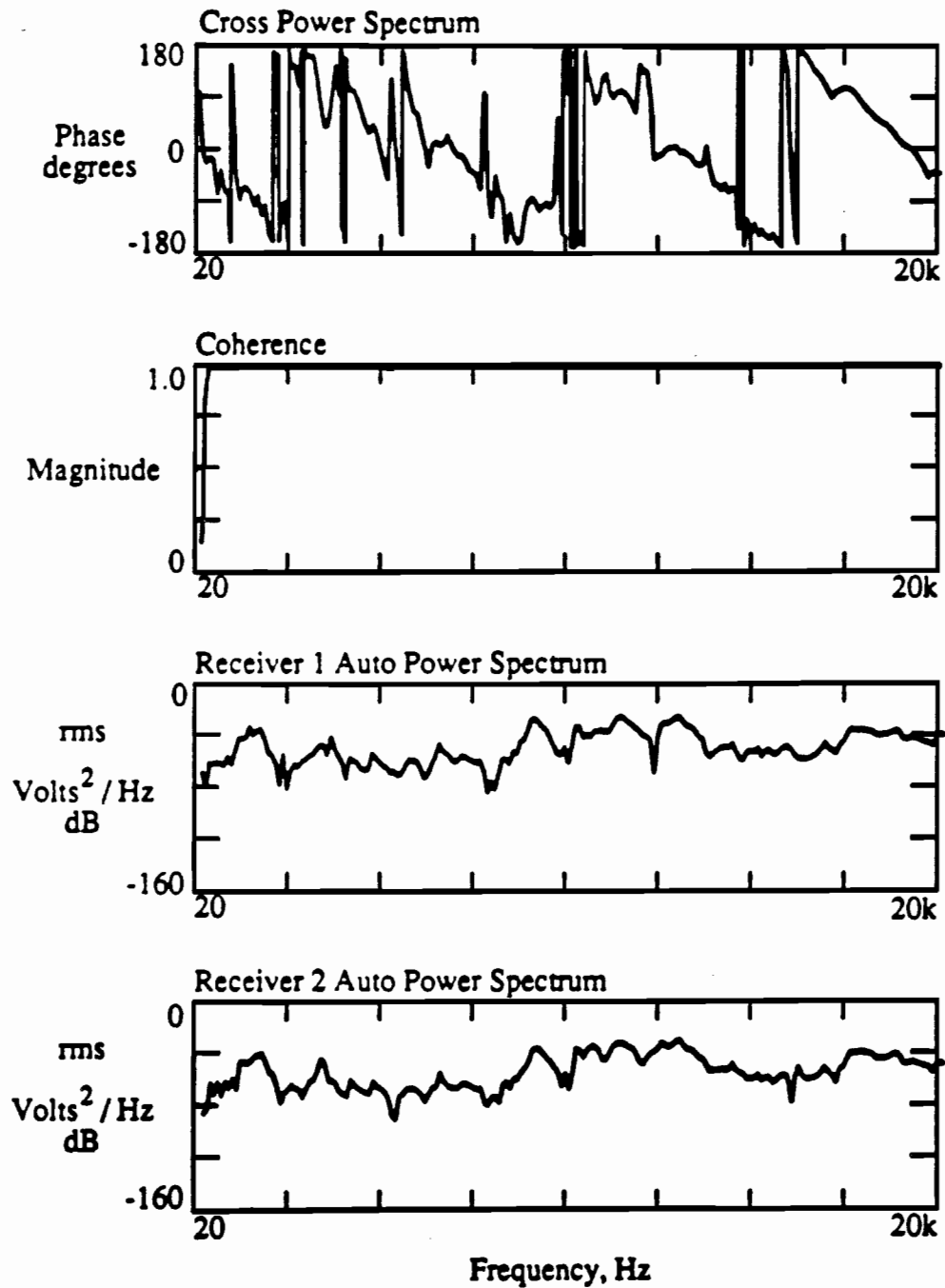


Fig. E18 Spectral Functions for the R1-R2 Receiver Spacing for Measurements Performed 382 Minutes After the Addition of Water to the Cement-Aggregate Mixture

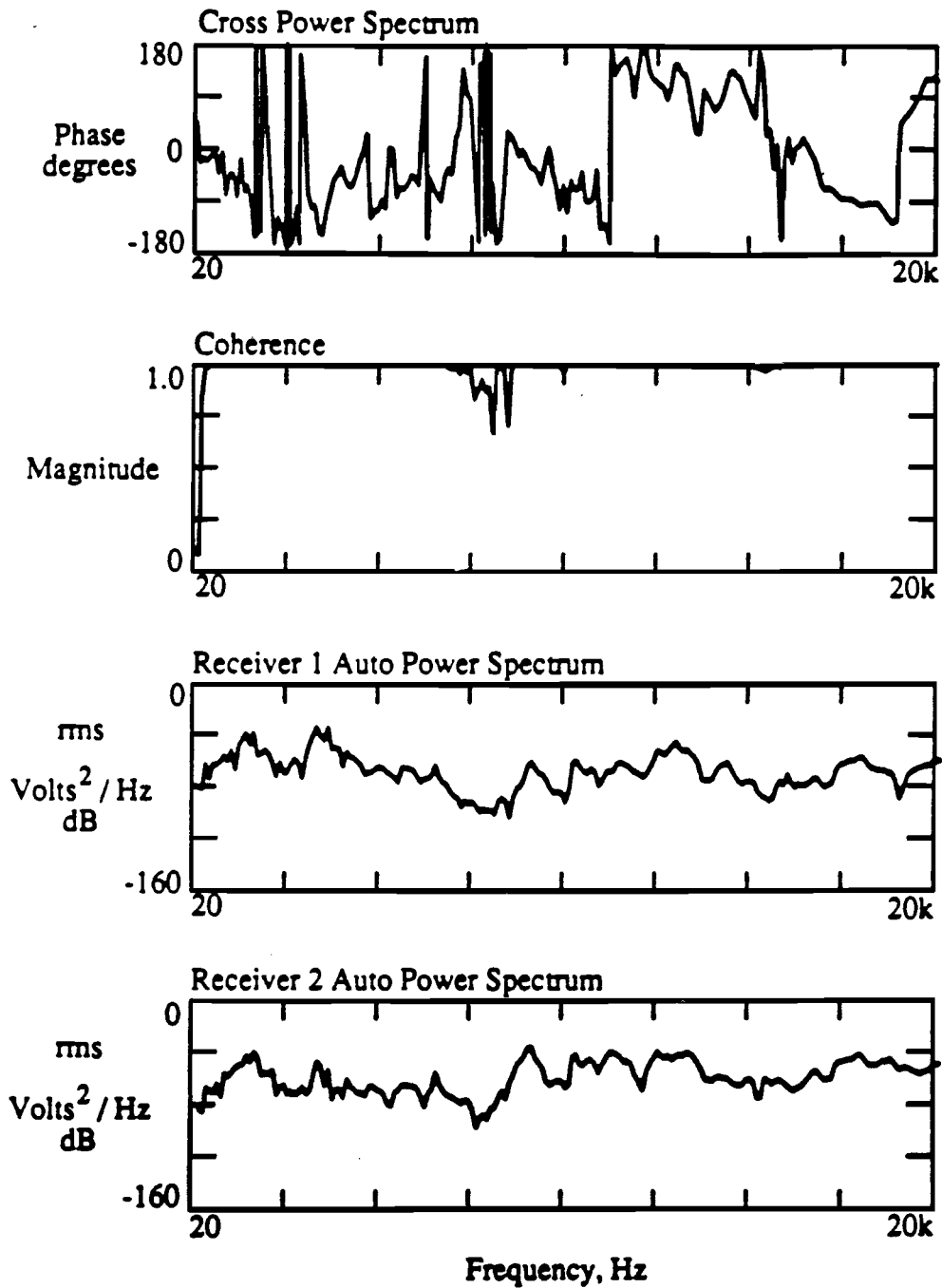


Fig. E19 Spectral Functions for the R3-R4 Receiver Spacing for Measurements Performed 387 Minutes After the Addition of Water to the Cement-Aggregate Mixture

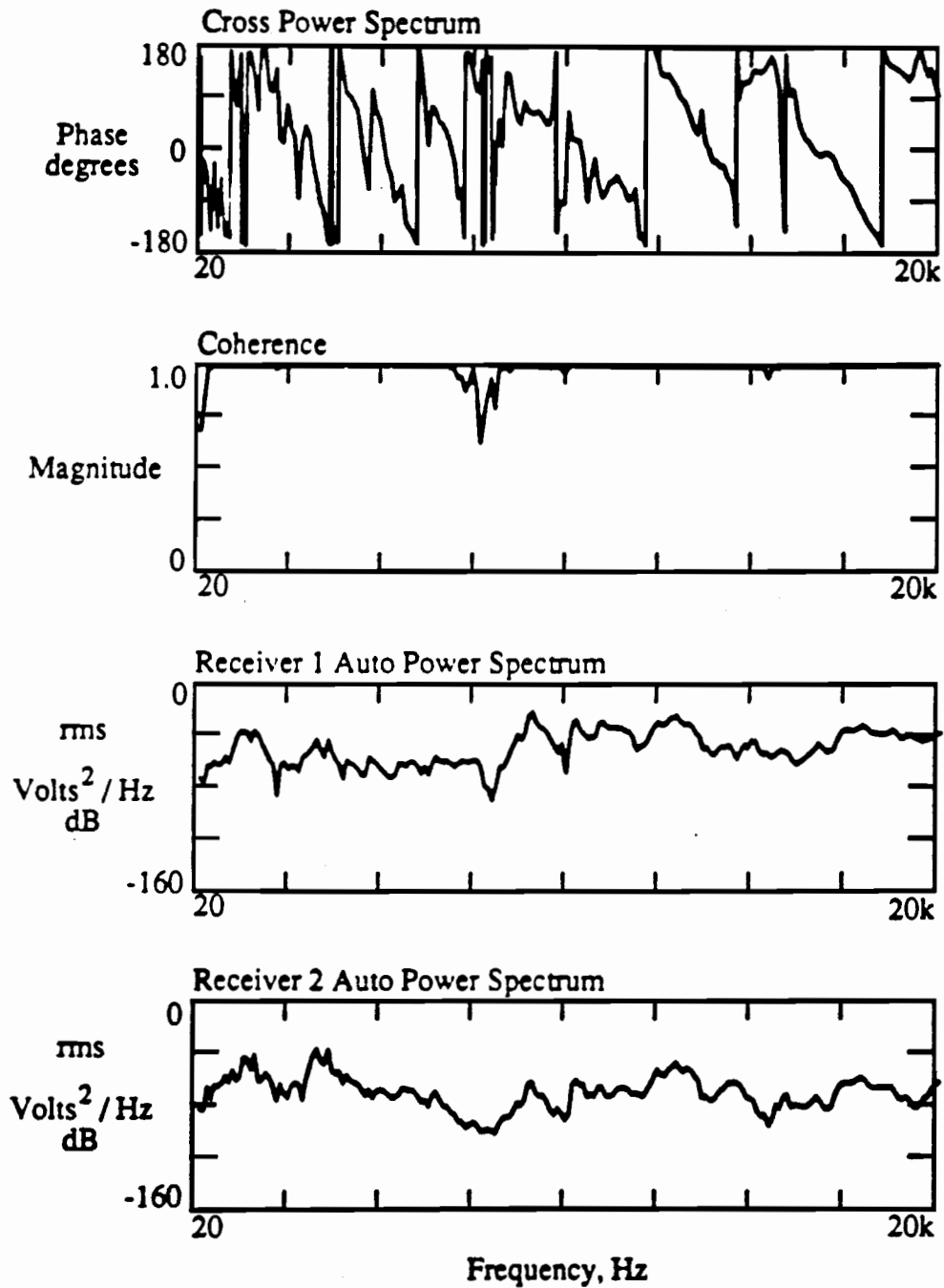


Fig. E20 Spectral Functions for the R1-R3 Receiver Spacing for Measurements Performed 392 Minutes After the Addition of Water to the Cement-Aggregate Mixture

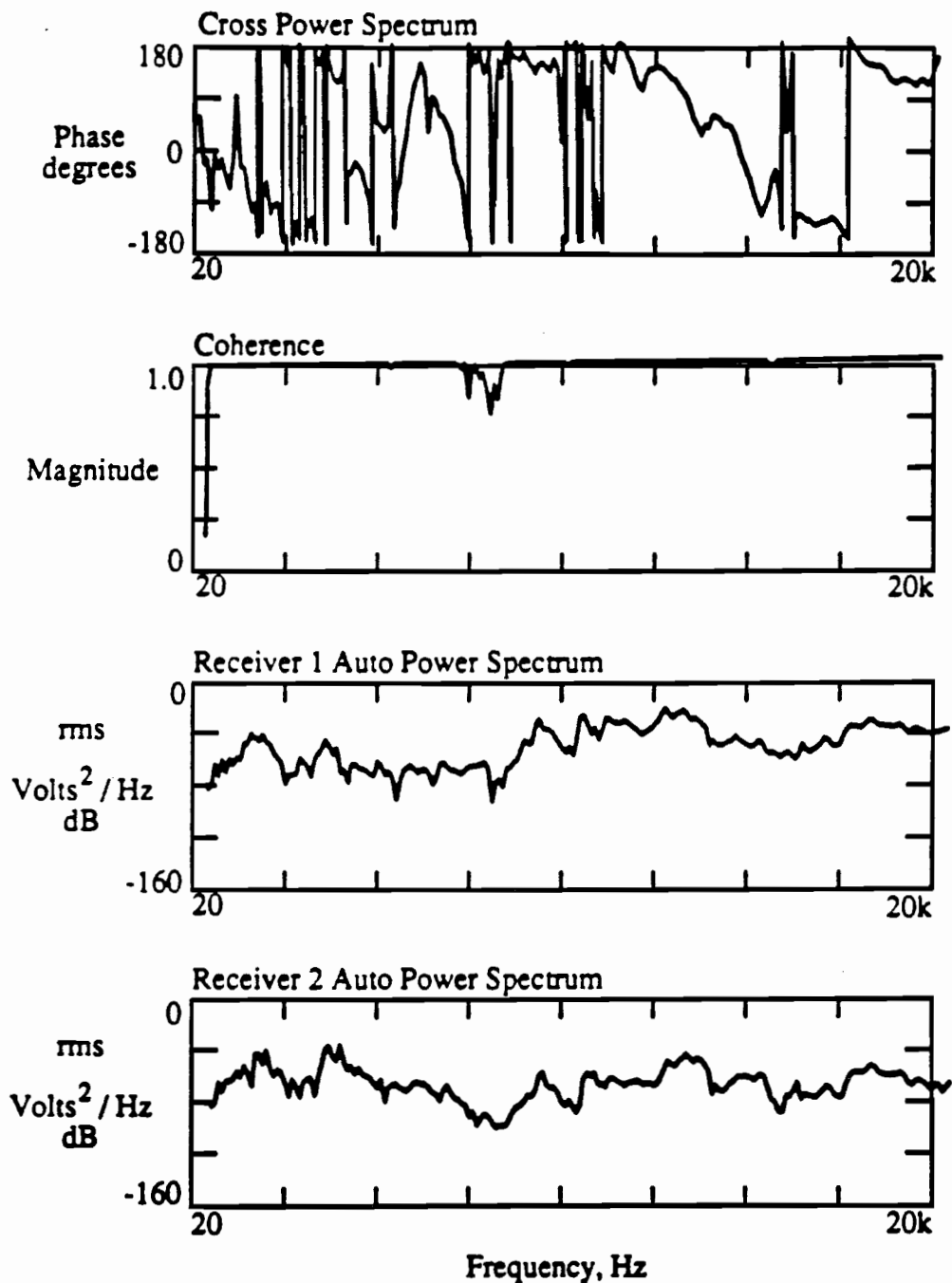


Fig. E21

Spectral Functions for the R2-R3 Receiver Spacing for Measurements Performed 397 Minutes After the Addition of Water to the Cement-Aggregate Mixture

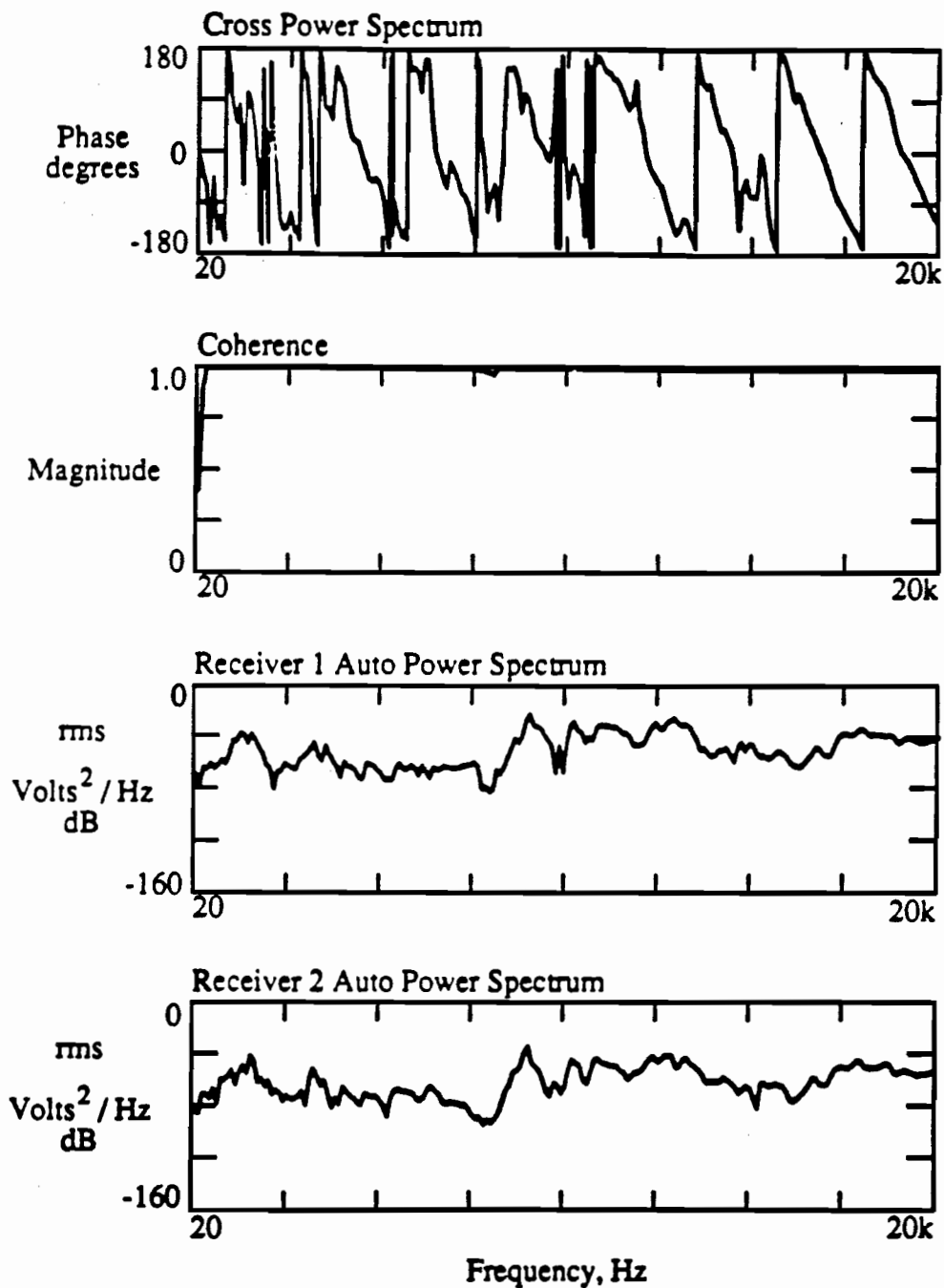


Fig. E22 Spectral Functions for the R1-R4 Receiver Spacing for Measurements Performed 402 Minutes After the Addition of Water to the Cement-Aggregate Mixture

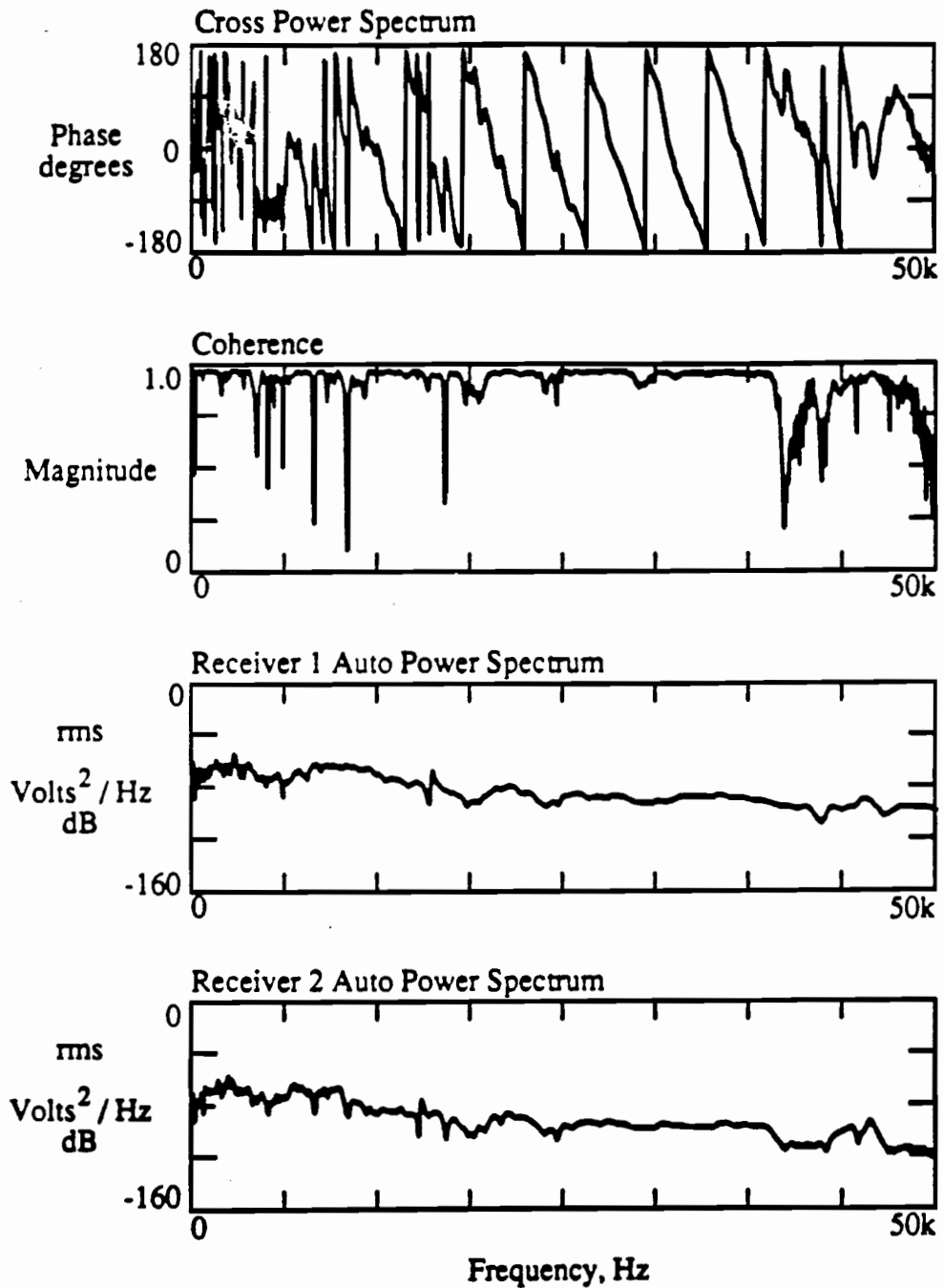


Fig. E23 Spectral Functions for the R2-R4 Receiver Spacing for Measurements Performed 517 Minutes After the Addition of Water to the Cement-Aggregate Mixture

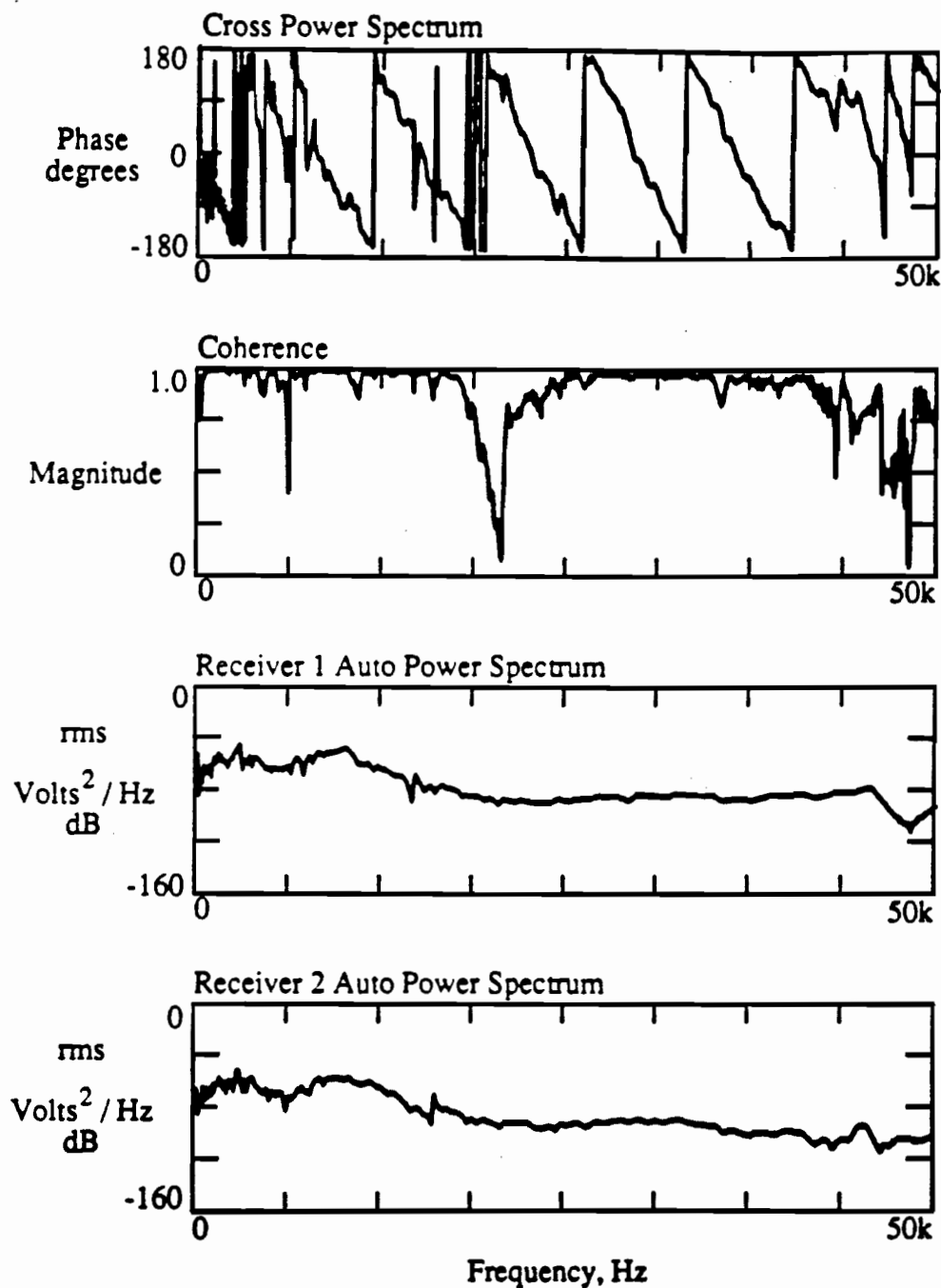


Fig. E24 Spectral Functions for the R1-R2 Receiver Spacing for Measurements Performed 522 Minutes After the Addition of Water to the Cement-Aggregate Mixture

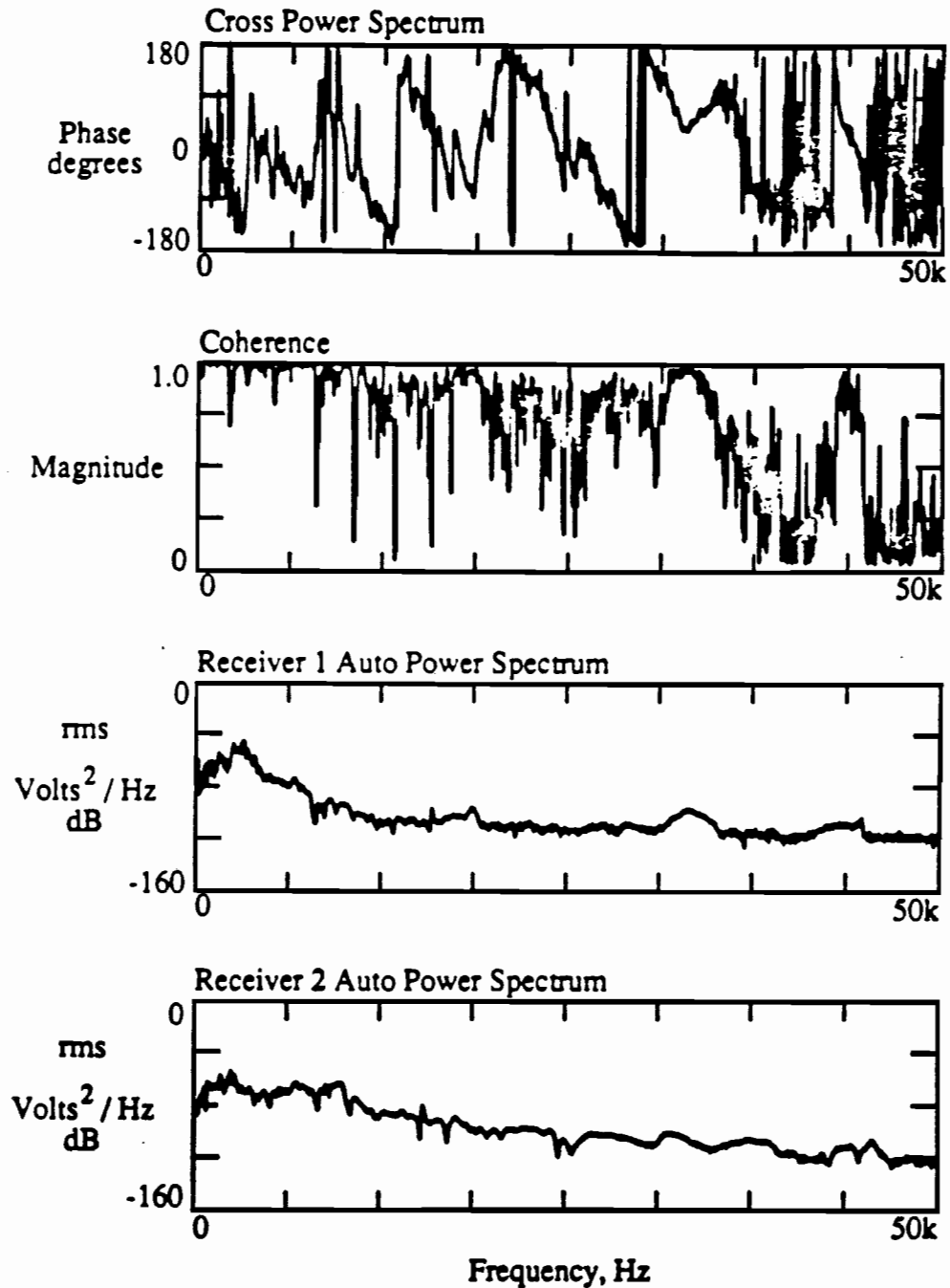


Fig. E25 Spectral Functions for the R3-R4 Receiver Spacing for Measurements Performed 527 Minutes After the Addition of Water to the Cement-Aggregate Mixture

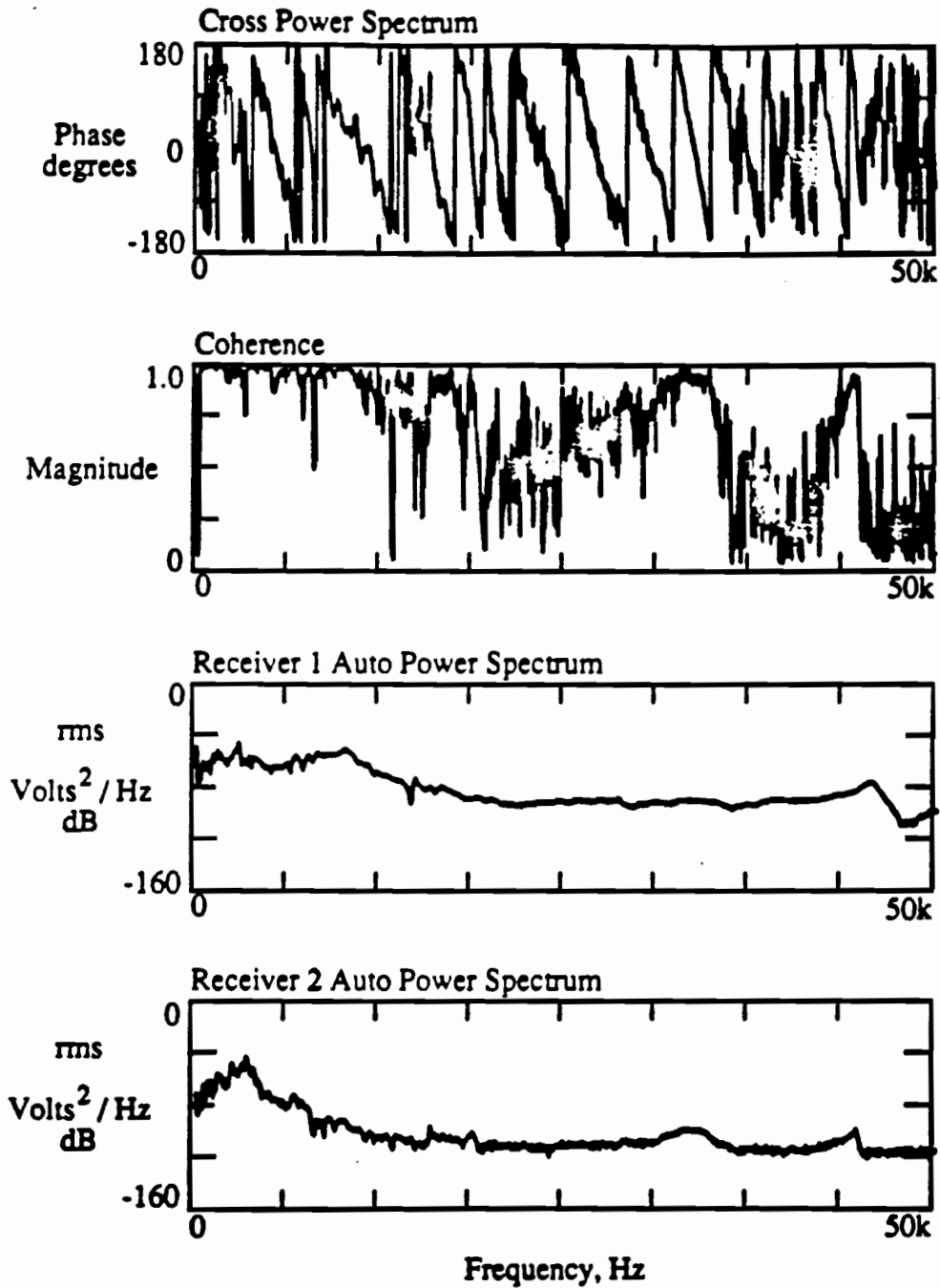


Fig. E26 Spectral Functions for the R1-R3 Receiver Spacing for Measurements Performed 532 Minutes After the Addition of Water to the Cement-Aggregate Mixture

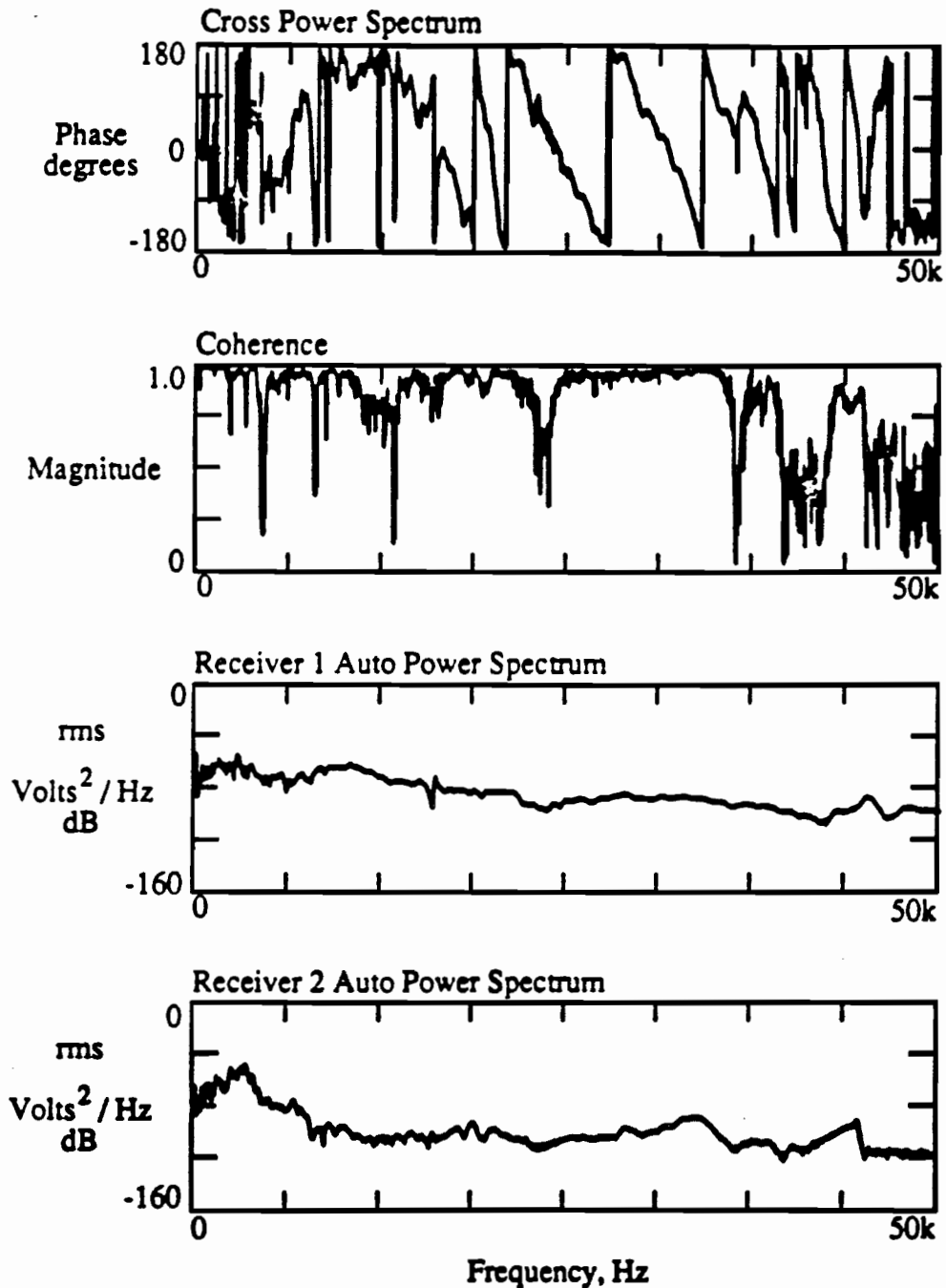


Fig. E27 Spectral Functions for the R2-R3 Receiver Spacing for Measurements Performed 537 Minutes After the Addition of Water to the Cement-Aggregate Mixture

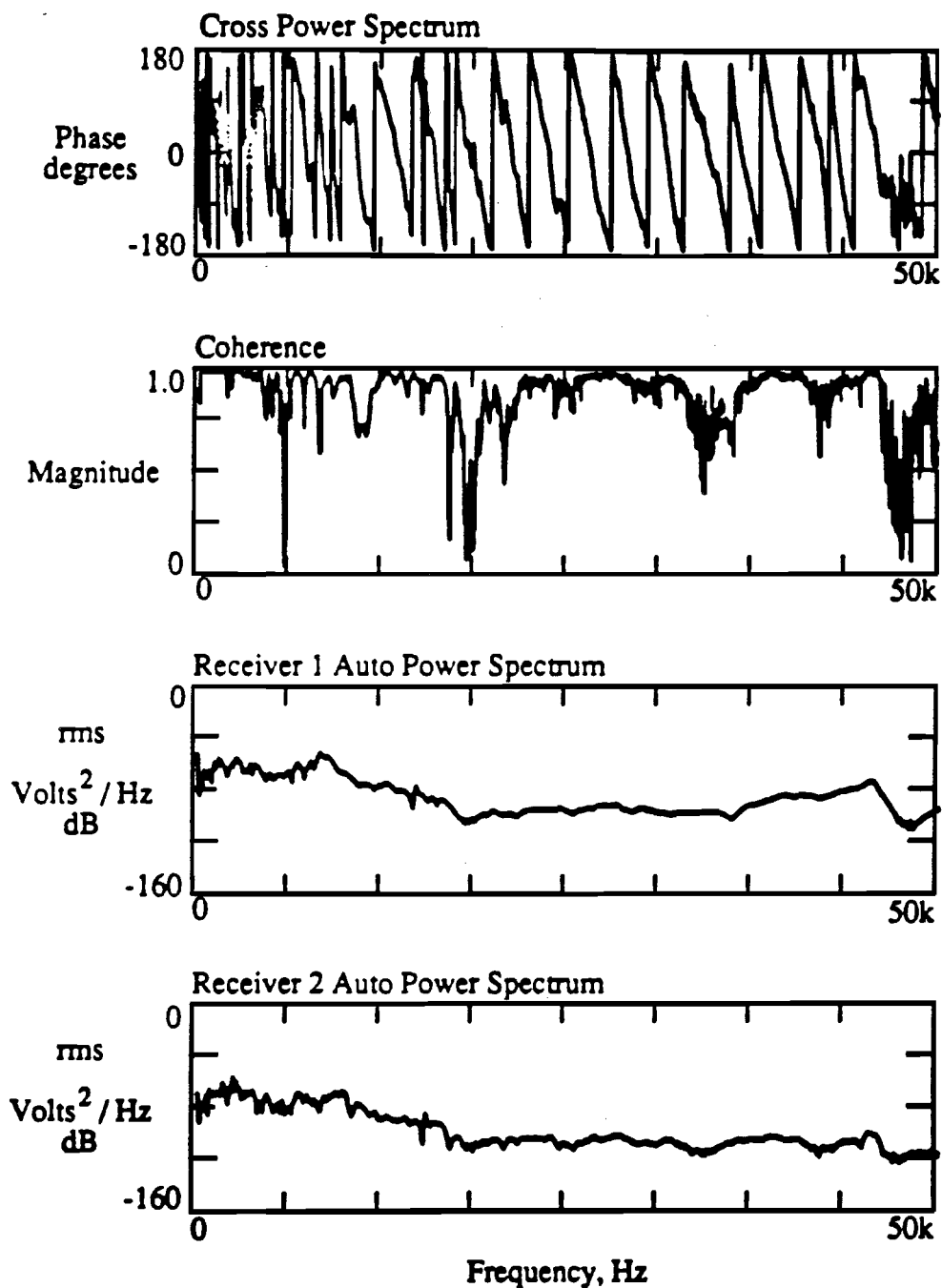


Fig. E28 Spectral Functions for the R1-R4 Receiver Spacing for Measurements Performed 542 Minutes After the Addition of Water to the Cement-Aggregate Mixture

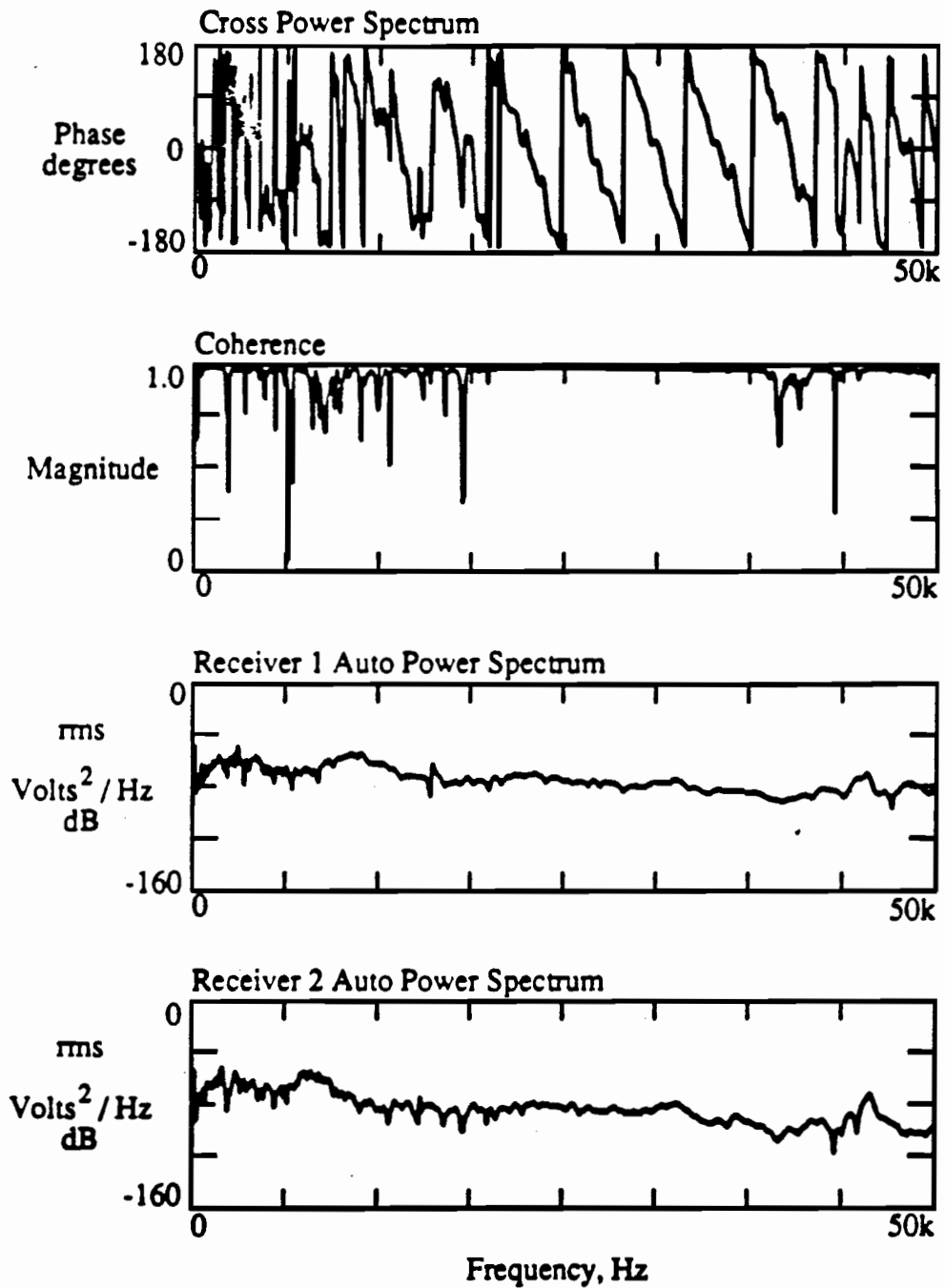


Fig. E29

Spectral Functions for the R2-R4 Receiver Spacing for Measurements Performed 1337 Minutes After the Addition of Water to the Cement-Aggregate Mixture

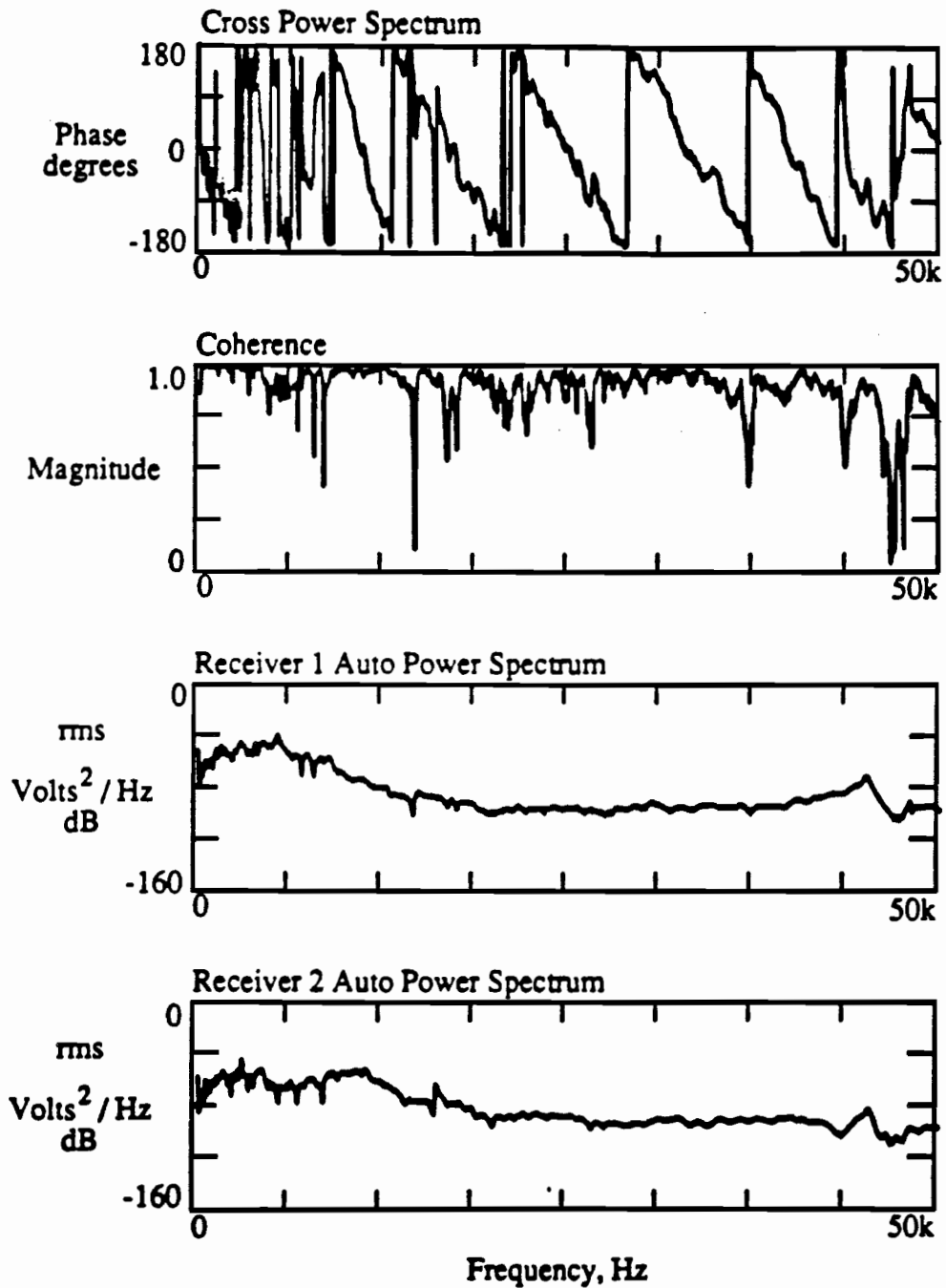


Fig. E30 Spectral Functions for the R1-R2 Receiver Spacing for Measurements Performed 1342 Minutes After the Addition of Water to the Cement-Aggregate Mixture

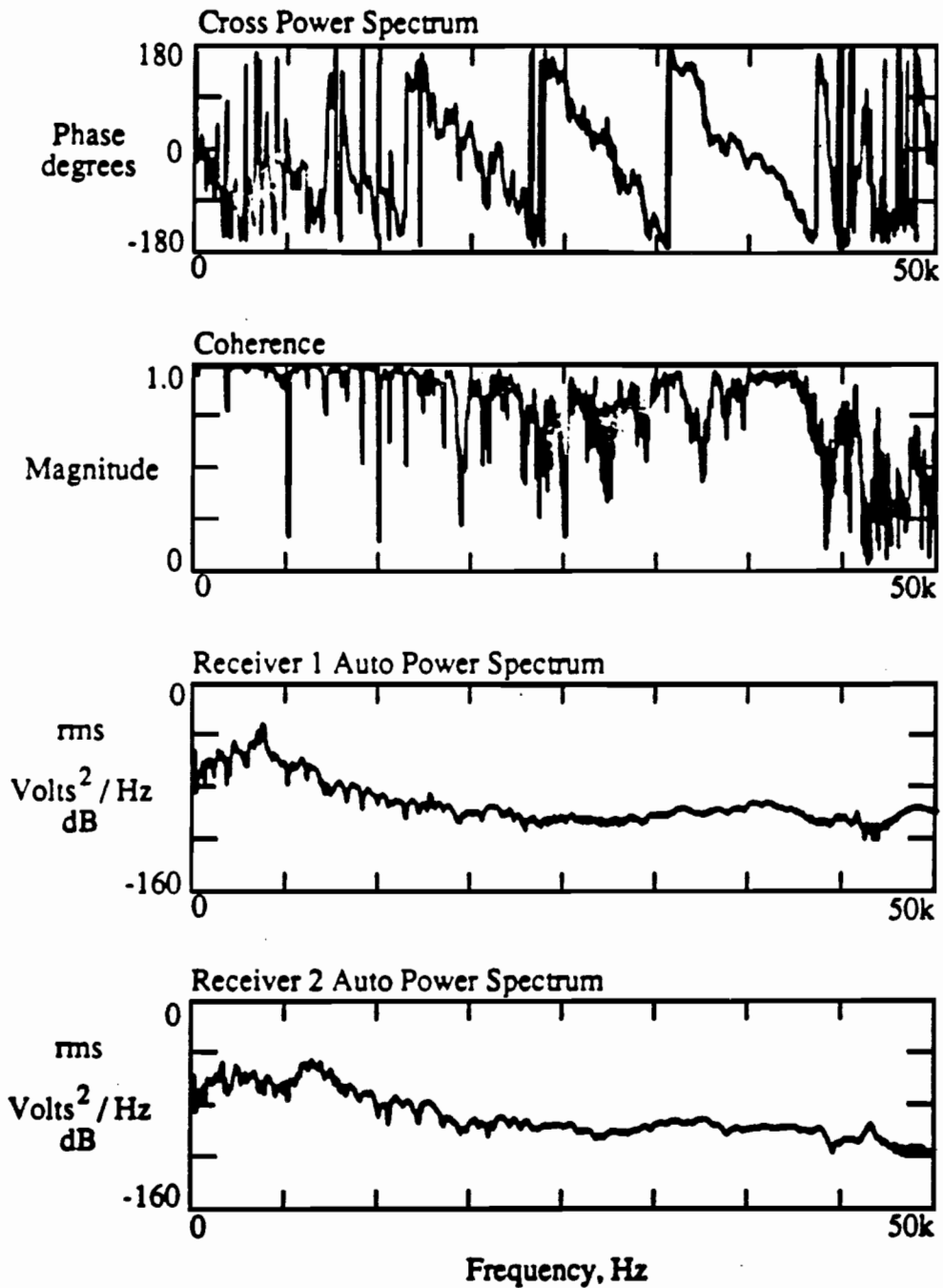


Fig. E31

Spectral Functions for the R3-R4 Receiver Spacing for Measurements Performed 1347 Minutes After the Addition of Water to the Cement-Aggregate Mixture

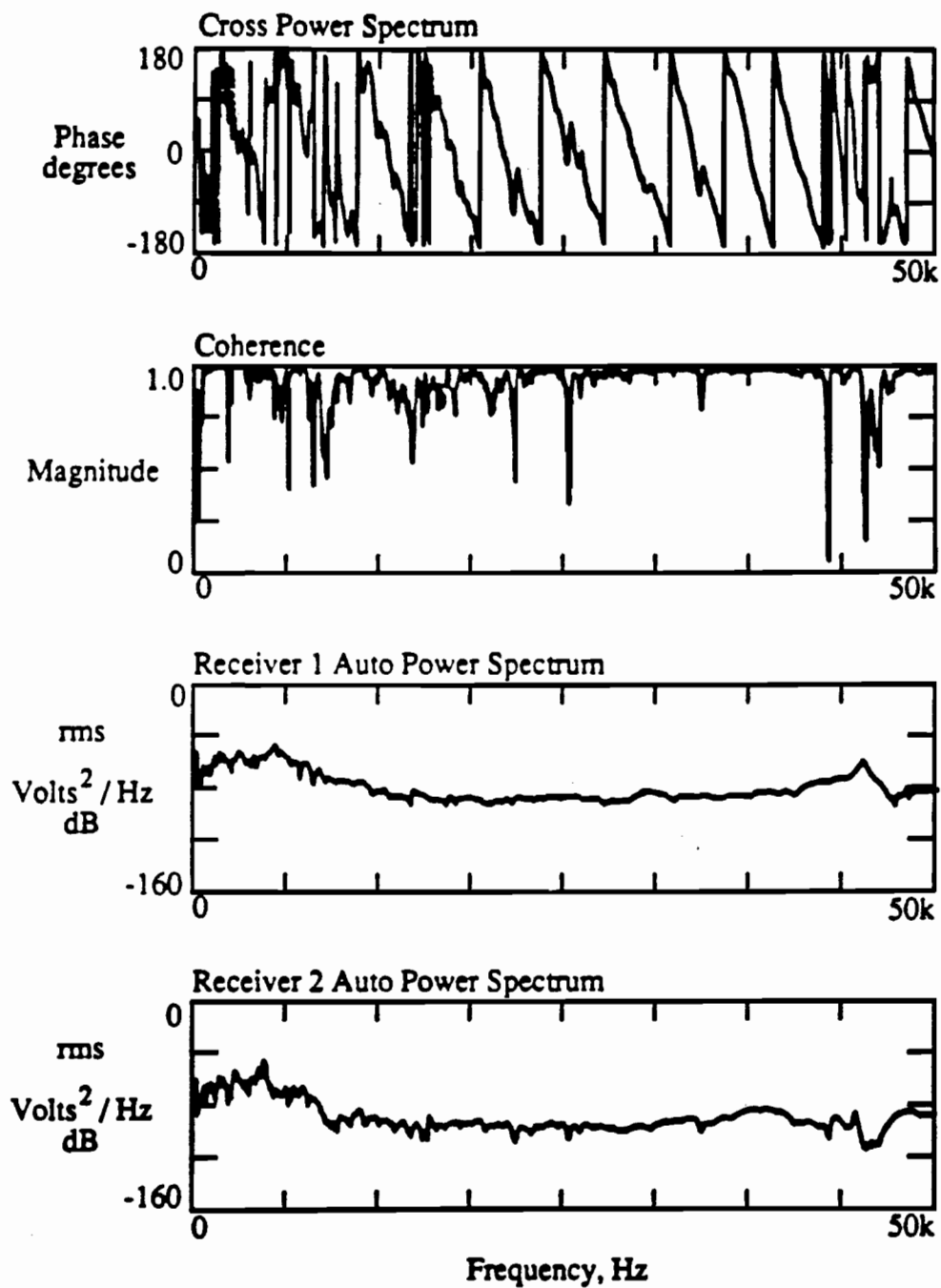


Fig. E32 Spectral Functions for the R1-R3 Receiver Spacing for Measurements Performed 1352 Minutes After the Addition of Water to the Cement-Aggregate Mixture

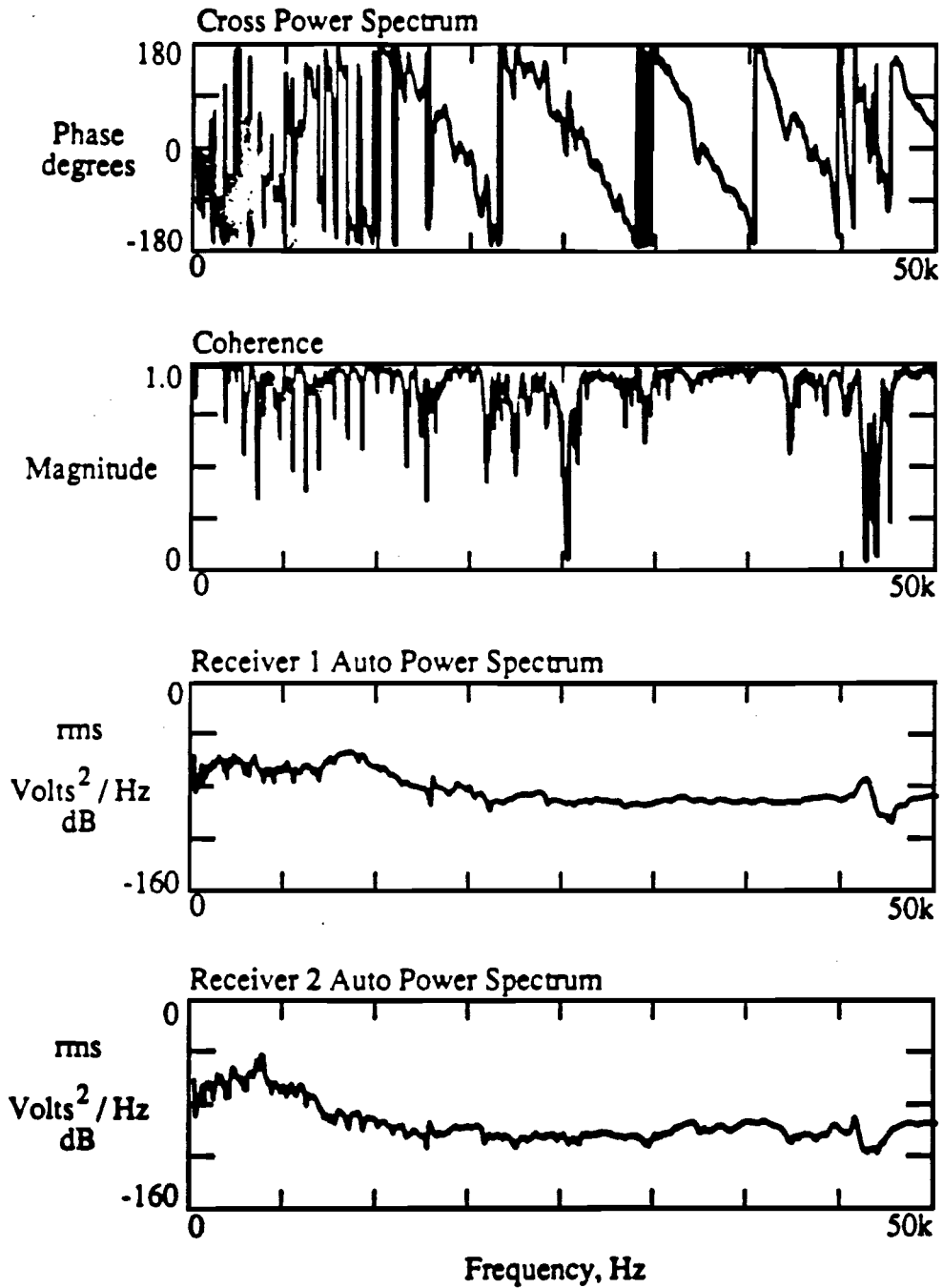


Fig. E33

Spectral Functions for the R2-R3 Receiver Spacing for Measurements Performed 1357 Minutes After the Addition of Water to the Cement-Aggregate Mixture

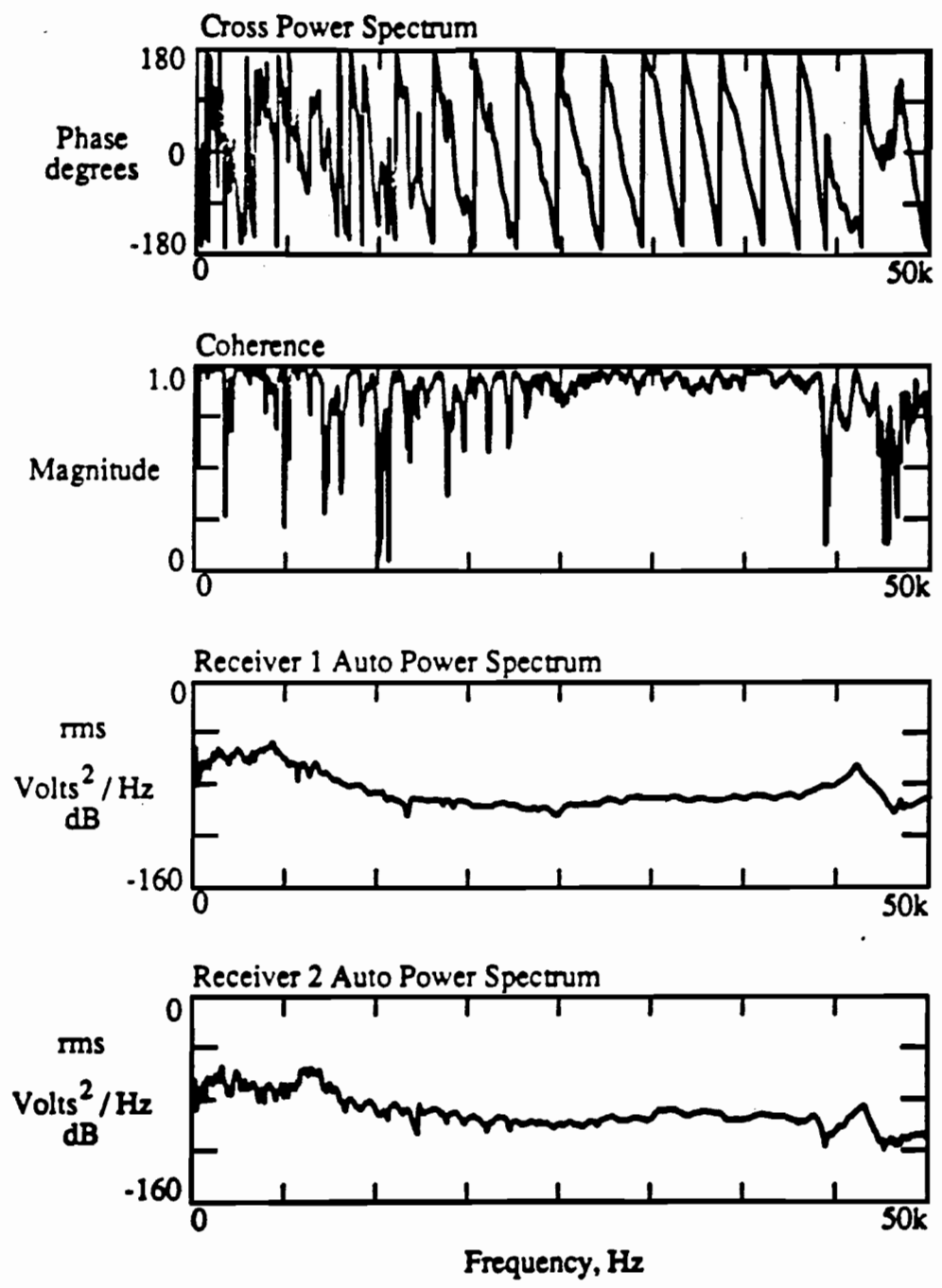


Fig. E34 Spectral Functions for the R1-R4 Receiver Spacing for Measurements Performed 1362 Minutes After the Addition of Water to the Cement-Aggregate Mixture

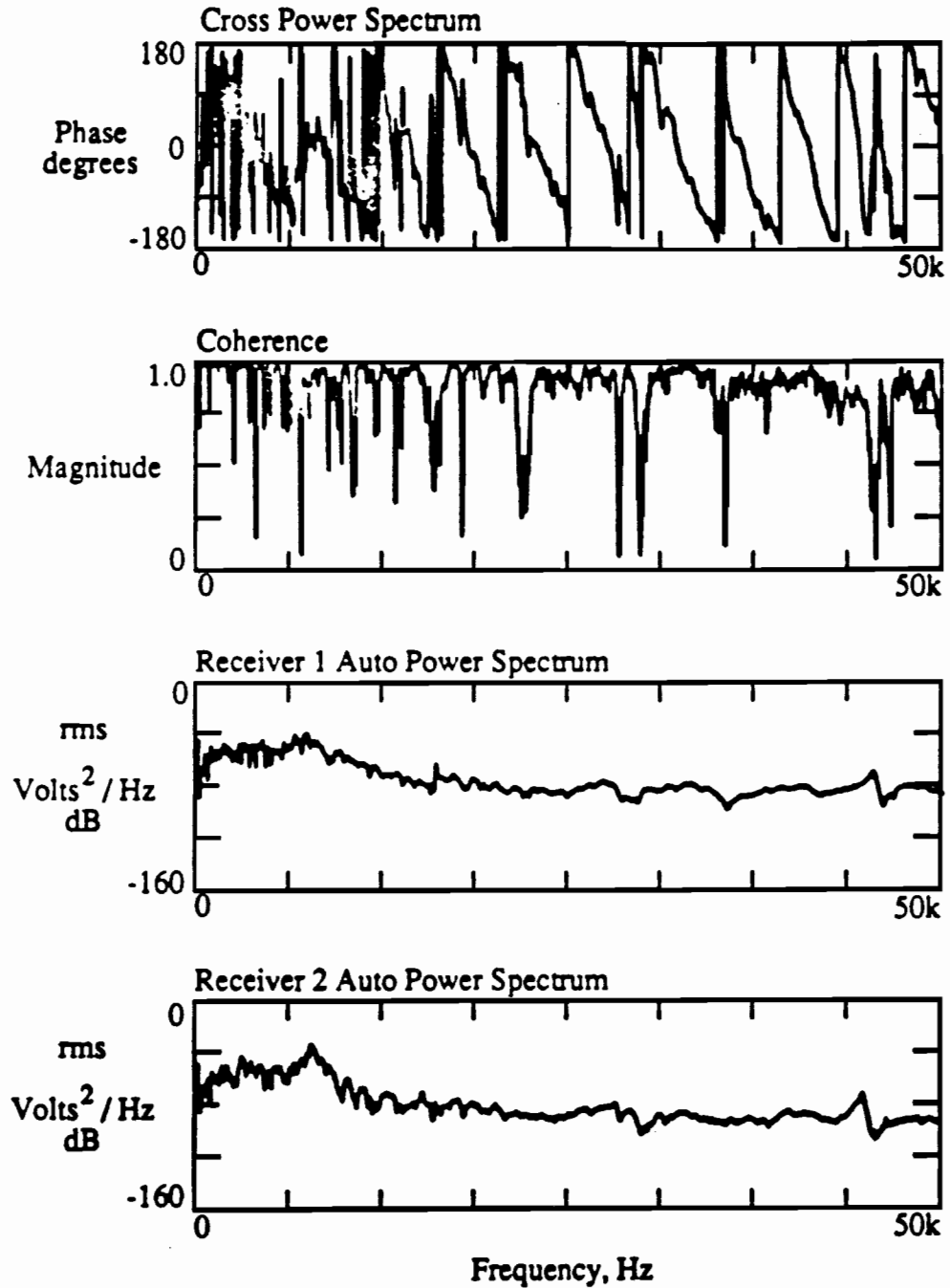


Fig. E35 Spectral Functions for the R2-R4 Receiver Spacing for Measurements Performed 6037 Minutes After the Addition of Water to the Cement-Aggregate Mixture

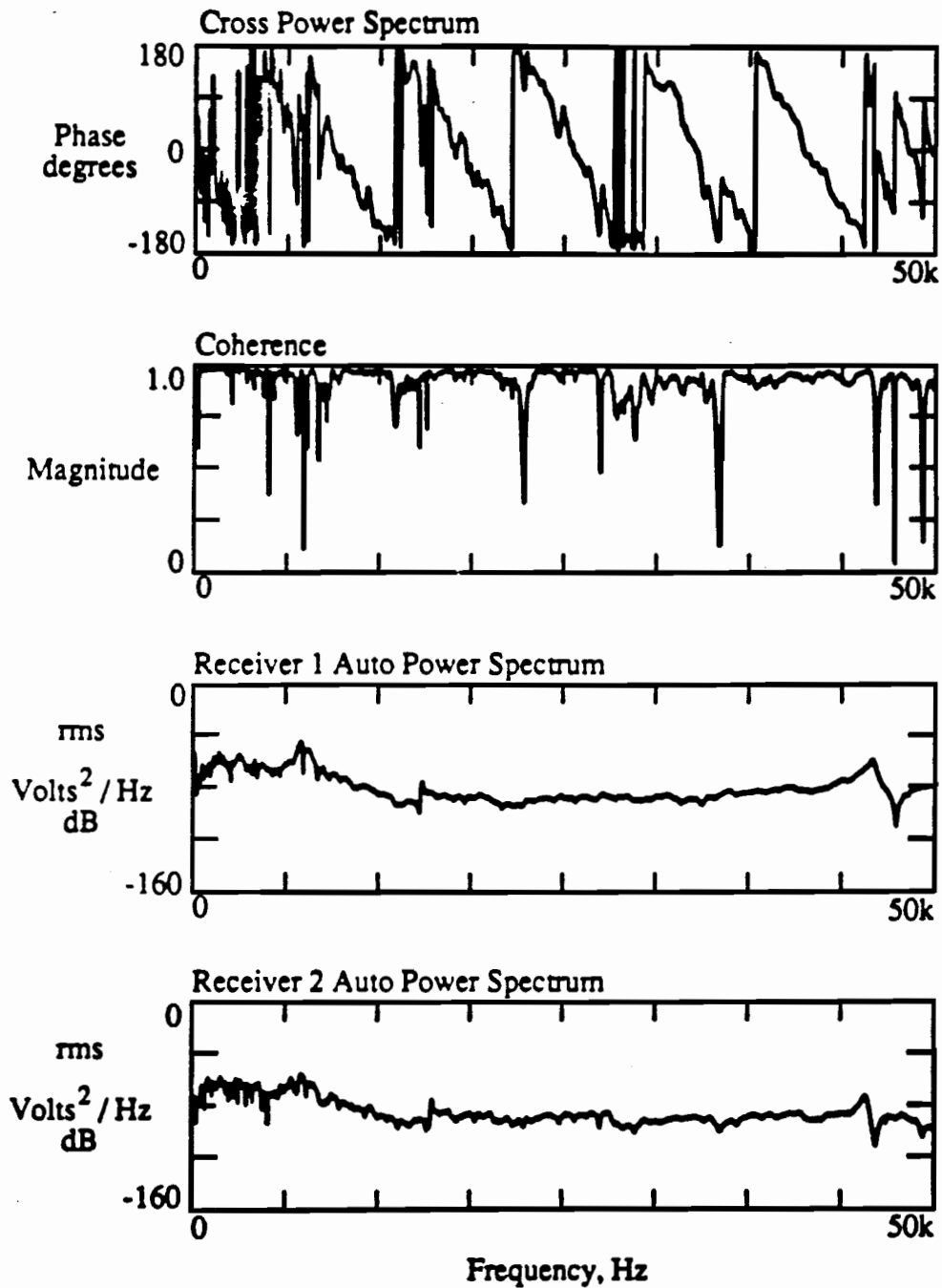


Fig. E36 Spectral Functions for the R1-R2 Receiver Spacing for Measurements Performed 6042 Minutes After the Addition of Water to the Cement-Aggregate Mixture

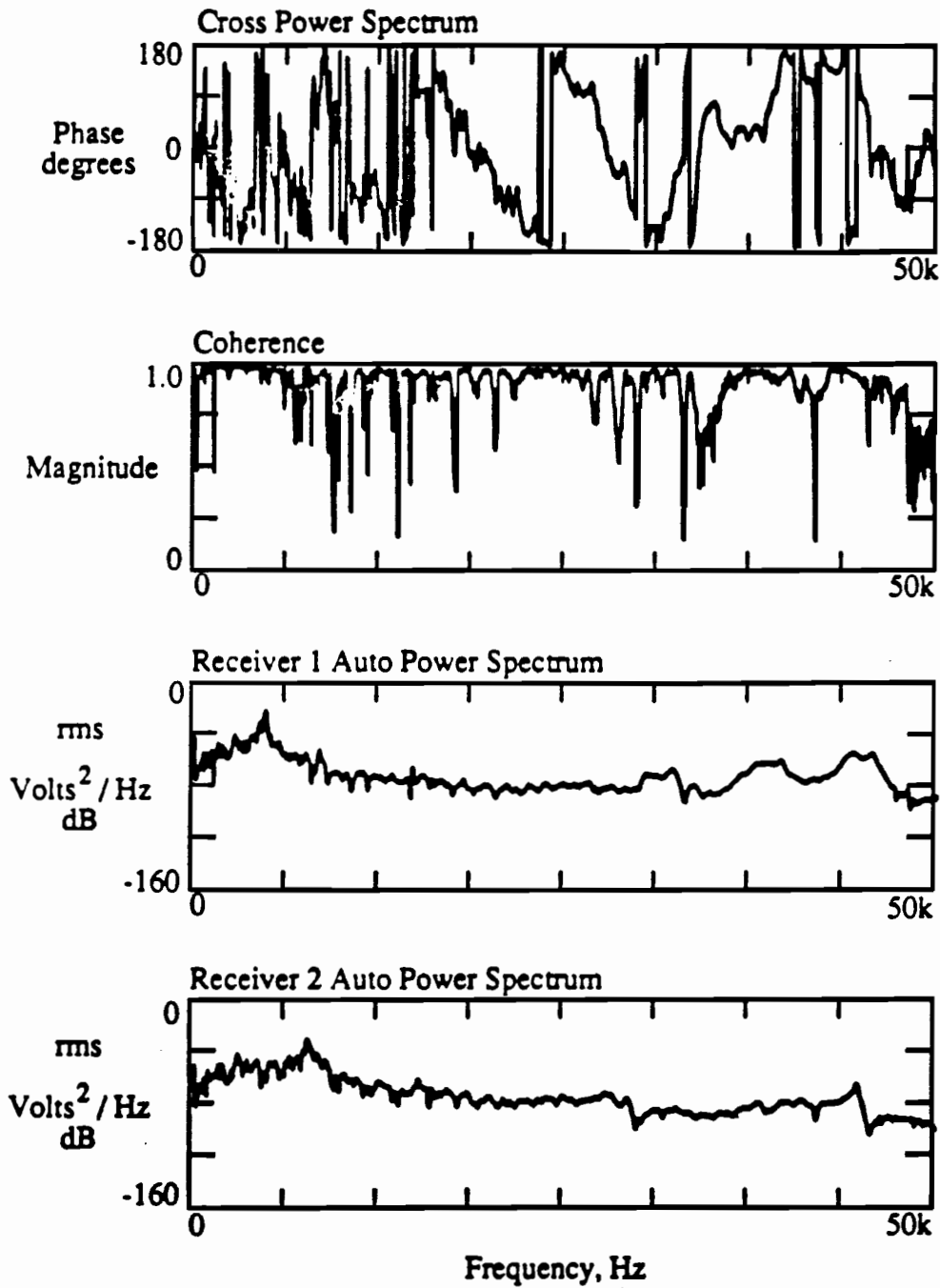


Fig. E37 Spectral Functions for the R3-R4 Receiver Spacing for Measurements Performed 6047 Minutes After the Addition of Water to the Cement-Aggregate Mixture

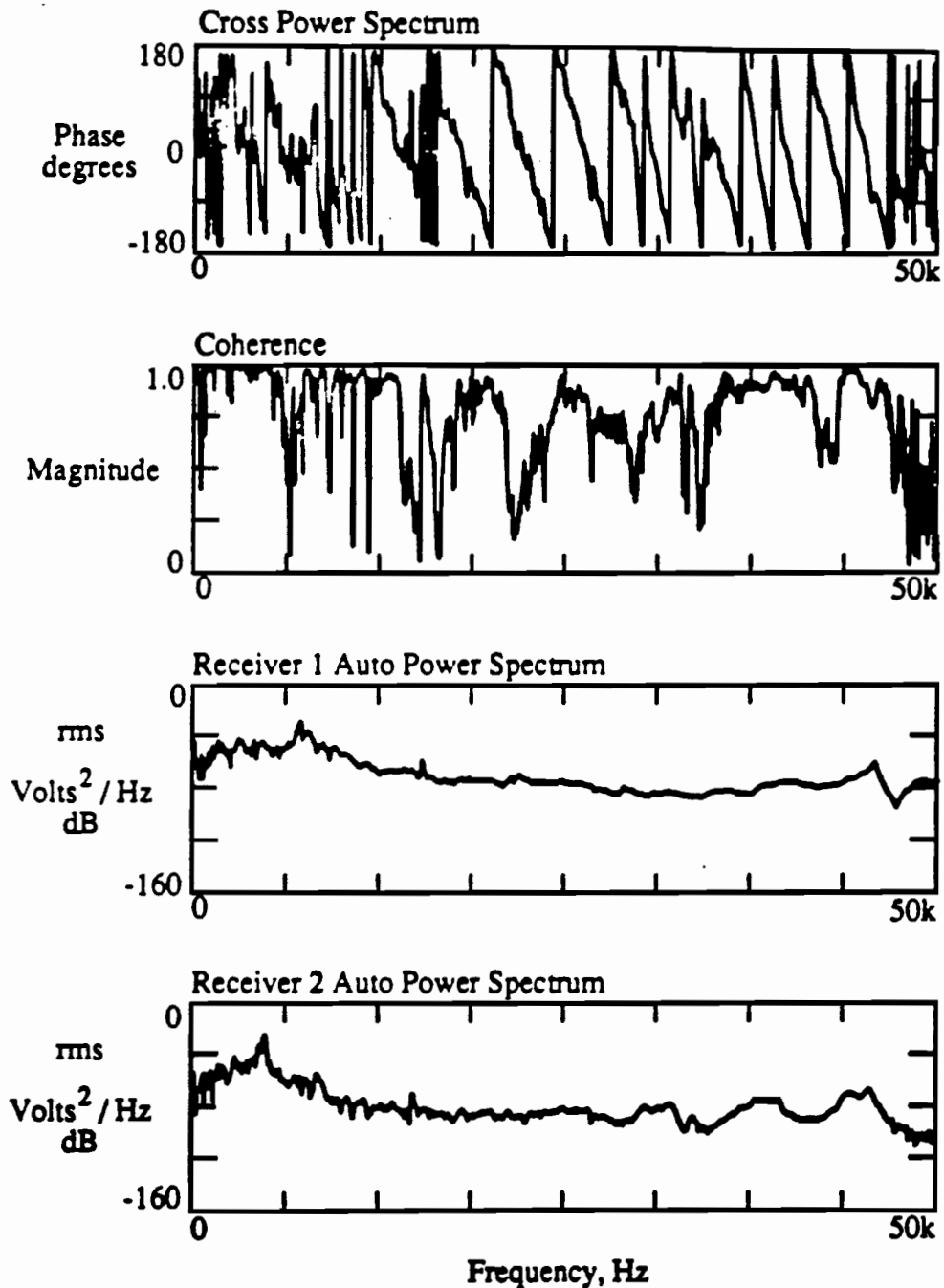


Fig. E38 Spectral Functions for the R1-R3 Receiver Spacing for Measurements Performed 6052 Minutes After the Addition of Water to the Cement-Aggregate Mixture

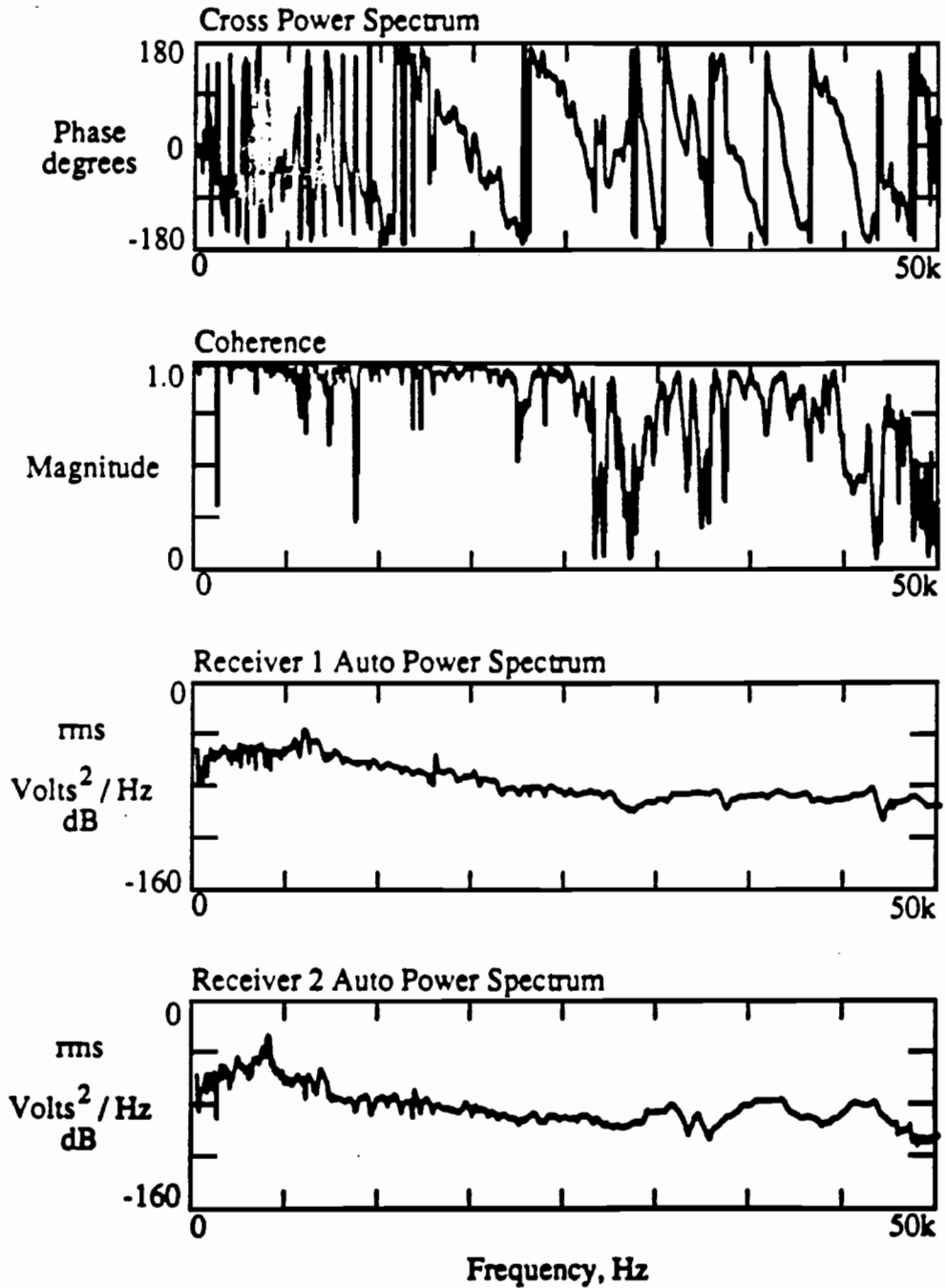


Fig. E39 Spectral Functions for the R2-R3 Receiver Spacing for Measurements Performed 6057 Minutes After the Addition of Water to the Cement-Aggregate Mixture

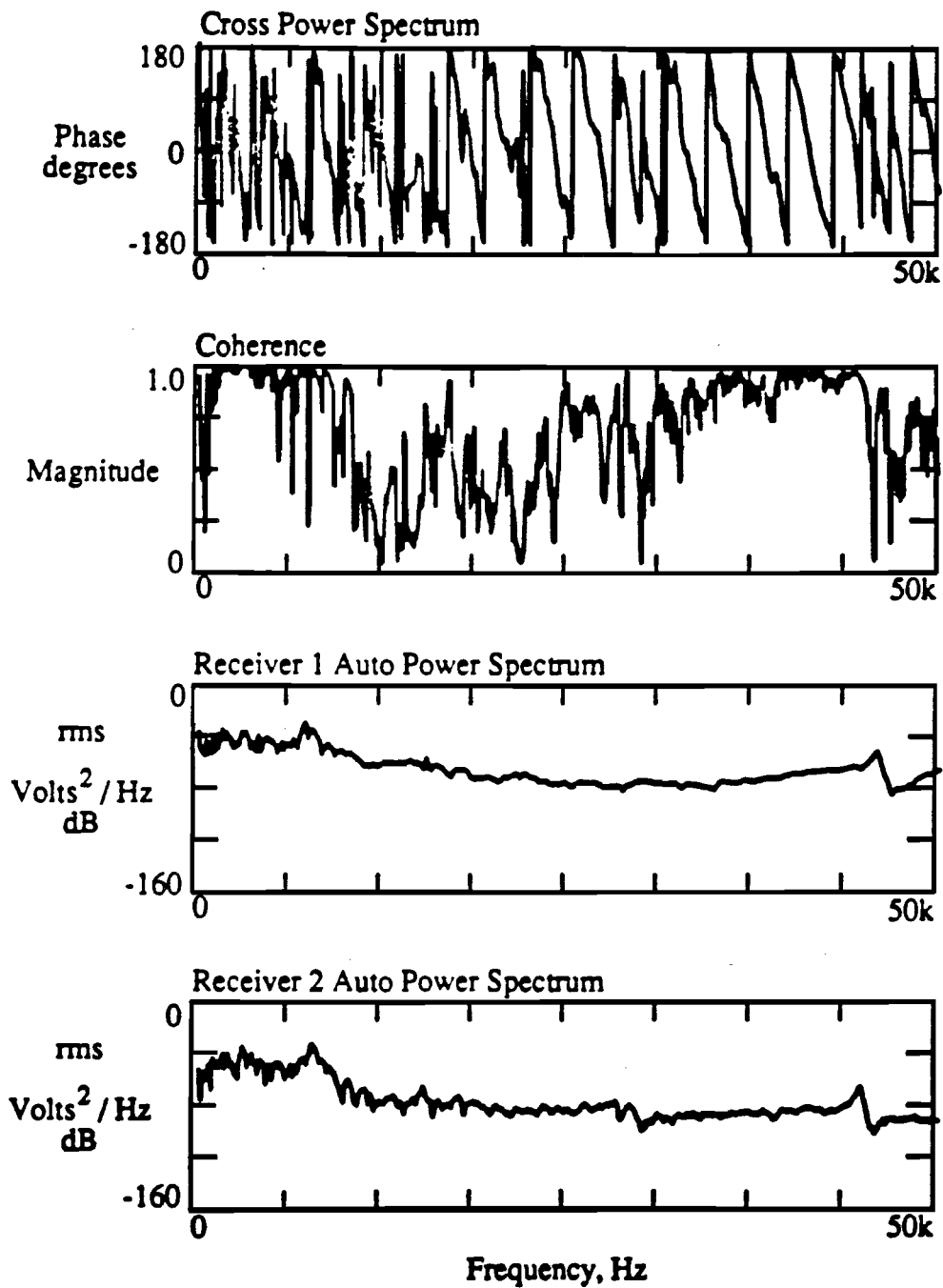


Fig. E40

Spectral Functions for the R1-R4 Receiver Spacing for Measurements Performed 6062 Minutes After the Addition of Water to the Cement-Aggregate Mixture